UNITED STATES DEPARTMENT OF COMMERCE
DANIEL C. ROPER, Secretary
NATIONAL BUREAU OF STANDARDS
Lyman J. Briggs, Director

✦

Journal of Research

of the

National Bureau of Standards

✦

Volume 21, No. 6

December 1938

[Published with approval of the Director of the Budget]

UNITED STATES
GOVERNMENT PRINTING OFFICE
WASHINGTON : 1938

For sale by the Superintendent of Documents, Washington, D. C. - - - - - - Price 30 cents
$3.50 per year on subscription

The prices of the separate Research Papers appearing in this JOURNAL are given on the front cover page. If 100 or more copies of any separate are ordered, a discount of 25 percent is allowed. Those who desire copies of separate Research Papers should send their orders and remittances without delay to the Superintendent of Documents, U. S. Government Printing Office, Washington, D. C. This will aid him to determine the number of copies to be printed for sale. Research Papers are not printed from electrotypes, and usually no more reprints can be had when the first and only printing is exhausted.

U. S. DEPARTMENT OF COMMERCE NATIONAL BUREAU OF STANDARDS

RESEARCH PAPER RP1151

Part of Journal of Research of the National Bureau of Standards, Volume 21, December 1938

LAWS OF TURBULENT FLOW IN OPEN CHANNELS

By Garbis H. Keulegan

ABSTRACT

The theoretical investigations of Prandtl and Kármán, and the experimental work of Nikuradse, have led to rational formulas for velocity distribution and hydraulic resistance for turbulent flow in circular pipes. With certain assumptions regarding the effects of secondary currents and of the free surface, and with the adoption of the hydraulic radius as the characteristic length, similar rational formulas are deduced for open channels. The validity and the applications of these formulas are illustrated by a study of Bazin's experiments. In this study the equivalent sand roughnesses of the channels used by Bazin are determined. The criterion for determining the conditions under which a channel with wooden-plank surfaces is to be considered hydrodynamically wavy or hydrodynamically rough is also evaluated. The rational formulas with constants determined from Bazin's experiments are expressed in the form of power laws. It is shown that Manning's empirical formula is a good approximation to the rational formula for rough channels when the relative roughness is large.

CONTENTS

	Page
I. Introduction	708
II. Development of the theory	709
1. Kármán law of velocity distribution	709
(*a*) General law of velocity distribution near a solid wall	709
(*b*) General equation of velocity distribution for smooth walls	711
(*c*) General equation of velocity distribution for wavy walls	712
(*d*) General equation of velocity distribution for rough walls	713
2. Derivation of resistance formulas	715
(*a*) Resistance formulas for circular and infinitely wide rectangular pipes	715
(1) Smooth walls	716
(2) Rough walls	717
(*b*) Resistance formulas for channels with polygonal cross sections	717
(1) Trapezoidal channels	718
(2) Channels of other shapes	720
(3) Error from neglect of the correction terms	720
(*c*) Equivalent sand roughness	722
III. Application to Bazin's experimental data	723
1. Description of Bazin's channel installation	723
2. Equivalent sand roughness for some of Bazin's channels	724
3. Surfaces of wood as examples of waviness	727
4. Effect of shape of cross section on mean velocity	730
5. Distribution of velocity in rough channels	732
6. Maximum velocity in rough rectangular channels	734
IV. Manning's formula for rough channels—power-law formulas	737
V. References	741

I. INTRODUCTION

The theoretical investigations of the phenomena of turbulent flow by Prandtl and by Kármán have prepared the way for rational interpretations of experimental results. In these investigations two distinct relationships of basic importance are expressed. First, in a unidirectional turbulent flow the apparent shear at any point depends on the square of the velocity gradient at that point. Second, the factor of proportionality in the relation of the apparent shear to the square of the velocity gradient is determinate once the similarity of turbulence is assumed. As a result of these two relationships, not only the velocity distribution, but also the hydraulic resistance factor for circular pipes, has been expressed in a rational form; that is, in a form derived by analytical methods involving only two constants to be determined by experiments. One of these constants is a universal constant, which is a characteristic of turbulence. The other constant is a characteristic of the surface of the pipe, which will be called the "surface characteristic" in this paper. In his classic experiments on circular pipes, Nikuradse [1, 2] [1] determined the universal constant of turbulence and the surface characteristics for smooth pipes and for pipes with one type of rough surface. These general results are well known and are presented in detail in recent works [3].

This paper is an attempt to apply these same principles to the problem of turbulent flow in open channels, mainly for the purpose of developing formulas for resistance or for mean flow in forms similar to those obtained for circular pipes. Two assumptions are made in developing the formulas. The first assumption is that Kármán's universal law of velocity distribution near a solid boundary is of general applicability. The second assumption is one in regard to the effects of secondary currents and of the free surface. It is assumed that the average result of these effects over the cross section of a channel is, in general, a small quantity which can be merged in the surface characteristics entering the flow formulas. Furthermore, it is found that when the hydraulic radius is adopted as the characteristic length of a channel cross section, the resulting formulas become practically independent of the shape of the channel except for a correction of geometrical origin which can likewise be merged with the surface characteristic. Thus the formulas for flow in open channels are identical in form with those for flow in circular pipes, the differences being in the values of the surface characteristics.

The necessary experimental data used in this paper are taken exclusively from Bazin's pioneer research [4] on flow in open channels, which constitutes an outstanding monument to early scientific work in this field. These experiments were carried out on a large scale near Dijon, France, in the years 1855 to 1860.

As a matter of convenience, the following definitions are adopted. A "pipe" is a conduit for carrying water in which the flowing stream is entirely bounded by solid surfaces. A "channel" is a conduit for carrying water in which the flowing stream is in part bounded by an air surface; that is, the stream has a free surface. The word "channel" is thus used as a synonym for the expression "open channel."

[1] Figures in brackets indicate the literature references at the end of this paper.

II. DEVELOPMENT OF THE THEORY

1. THE KÁRMÁN LAW OF VELOCITY DISTRIBUTION

The discussion here of the theory of velocity distribution relates to unidirectional flow in the neighborhood of a plane wall of large extent. When it is necessary to consider experiments for verification of the theoretical results, reference will be made to studies of flow in circular pipes, since numerous and reliable data are available for this case. These references are permissible because the flow in circular pipes is also unidirectional.

Again, in these discussions the thin laminar layer at the wall will be ignored, since the portion that it contributes to the total flow is negligible.

(a) GENERAL LAW OF VELOCITY DISTRIBUTION NEAR A SOLID WALL

Prandtl [5] has given the following expression for the turbulent shear stress at any point in a fluid moving past a solid wall (see fig. 1):

$$\sqrt{\tau/\rho}=l\frac{du}{dy} \tag{1}$$

where

τ = the shearing stress at the point,
ρ = the density of the fluid,
u = the velocity at the point,
y = the distance of the point from the wall, and
l = the so-called mixing length of momentum exchange.

For the purpose of finding an approximate law of velocity distribution in the neighborhood of the wall, we write eq 1 in the form

$$\sqrt{\tau_0/\rho}=l\frac{du}{dy}\sqrt{\tau_0/\tau}, \tag{2}$$

where τ_0 is the shear in the fluid at the wall.

The quantity in the left member of eq 2 has the dimensions of a velocity, and, because of its significance, has been called by Prandtl the shear velocity, denoted by the symbol u_*. To make the concept of shear velocity more concrete, it may be pointed out that it can be expressed in the following simple manner in terms of more customarily used quantities:

$$u_*=\sqrt{Rig}, \tag{3}$$

both for flow in circular pipes and for uniform flow in wide channels, where

R = the hydraulic radius,
i = the hydraulic gradient, and
g = the acceleration of gravity.

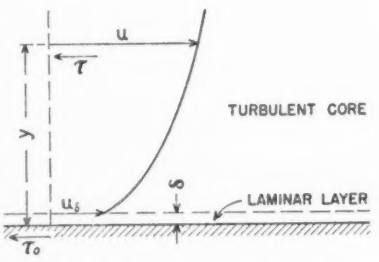

FIGURE 1.—*Diagram of velocity distribution in a stream flowing past a solid wall to illustrate notation.*

Introducing the notation for the shear velocity, we write eq 2 as

$$u_*=l\frac{du}{dy}\left(\frac{\tau_0}{\tau}\right)^{1/2}. \tag{4}$$

As a consequence of his principle of similarity of turbulence, Kármán derived the following expression for the mixing length l at any point y in terms of the velocity gradient at y:

$$l=\kappa\frac{u'}{u''}, \tag{5}$$

where the primes indicate differentiation with respect to y, and κ is a universal constant characterizing the turbulence [5]. This latter expression for l, however, requires a modification for the following reason. The two experimental determinations of l from the independent expressions, eq 4 and 5, using the velocity measurements in smooth or rough circular pipes, may be made to agree with each other for small values of y by selecting κ properly. But, then, for the same value of κ the two values of l show gradually increasing differences for increasing y, the largest difference occurring for $y=y_m$, y_m being the wall distance corresponding to $\tau=0$ [1]. Obviously, the agreement between the two determinations would be improved if now we select in the place of eq 5,

$$l=\kappa\left|\frac{u'}{u''}\right|\left[1+k_1\frac{y}{y_m}+k_2\left(\frac{y}{y_m}\right)^2+\ \ldots\ .\right], \tag{5a}$$

where k_1 and k_2 are constants.

Since in the types of flows we shall be considering, the component of acceleration normal to the direction of mean flow would be negligible,

$$\tau=\tau_0(1-y/y_m),$$

eq 4 then may be written also as

$$u_*=l\frac{du}{dy}\left[1+\frac{1}{2}\frac{y}{y_m}+\frac{3}{8}\left(\frac{y}{y_m}\right)^2+\ \ldots\ .\right]. \tag{4a}$$

When l from eq 5 is substituted in eq 4 there results, for values of y approaching zero,

$$u_*=\kappa\frac{(u')^2}{u''}, \tag{6}$$

which can be integrated, yielding

$$\frac{u}{u_*}=\frac{1}{\kappa}\ln\ (y/y_0), \tag{7}$$

where y_0 is a constant of integration. The other constant resulting from the first integration of eq 6 is put equal to zero as the consequence of the limiting value of u' at the wall. This is Kármán's law of velocity distribution in the neighborhood of a solid wall. The derivation is made for small values of y. Experience, on the other hand, shows that eq 7 is sufficiently accurate also for large values of y, even when y is as large as y_m. In the second approximate solution, the differential equation corresponding to eq 6 would contain y/y_m. The form of the resulting equation is necessarily complex and hardly suitable for the usual computations. Equation 7, being of a simpler form and also sufficiently accurate, will serve as the basis for the elementary mathematical development of this paper.

Theoretical considerations indicate that κ should be independent of the nature of the wall surface. This has been verified in the cases of flow in circular pipes and between parallel walls [6]. On the other hand, the constant of integration y_0, a length that we may term the "characteristic length of turbulence," varies with the shear velocity, and the roughness of the wall.

The next step is to consider the evaluation of y_0. Let δ be the minimum distance from the wall at which eq 7 holds. (See fig. 1.) That is, δ is the thickness of the boundary layer in which the viscous stresses either predominate or are of the same order as the apparent stresses due to momentum exchange. It can be shown easily that the rate of energy dissipation E in this layer per unit of surface is

$$E=\tau_0 u_\delta, \tag{8}$$

where u_δ is the velocity for $y=\delta$. From eq 7:

$$u_\delta/u_*=(1/\kappa)\ \ln\ (\delta/y_0),$$

and eliminating u_δ from the last two equations:

$$\ln\left(\frac{y_0}{\delta}\right)=-\frac{\kappa E}{\rho u_*^3}. \tag{9}$$

Unfortunately, in the present state of our knowledge of turbulence E and δ cannot be computed, so that eq 9 does not serve as a means of computing y_0.

In the absence of an adequate theory, the natural procedure is to resort to experience, using the method of dimensional reasoning as a guide. Based on the hydrodynamical effects that they produce, solid boundaries are usually classified as smooth, wavy, or rough. For these three types of walls, y_0 may be expressed in three distinct forms which will now be developed.

(b) GENERAL EQUATION OF VELOCITY DISTRIBUTION FOR SMOOTH WALLS

If the surface of the wall is smooth, y_0 will depend solely on u_* and ν, and dimensional reasoning then furnishes the relation

$$\frac{y_0 u_*}{\nu}=m, \tag{10}$$

where

m = a constant, and
ν = the kinematic viscosity.

Substitution of this value of y_0 in eq 7 yields

$$\left.\begin{aligned}\frac{u}{u_*}&=a_s+\frac{1}{\kappa}\ln\left(\frac{yu_*}{\nu}\right), \text{ or}\\ \frac{u}{u_*}&=a_s+\frac{2.30}{\kappa}\log\left(\frac{yu_*}{\nu}\right),\end{aligned}\right\} \tag{11}$$

which is the universal law of velocity distribution in the neighborhood of a smooth wall. The relation between the constants a_s and m is

$$a_s=\frac{1}{\kappa}\ln\left(\frac{1}{m}\right),$$

which may also be written in the form

$$m=e^{-\kappa a_s}. \tag{12}$$

The law expressed by eq 11 has been confirmed by Nikuradse [1], who obtained from experiments on smooth pipes the relation

$$\frac{u}{u_*}=5.5+5.75\log\left(\frac{yu_*}{\nu}\right) \tag{13}$$

Comparison of the experimentally determined values in eq 13 with the corresponding algebraic expressions in eq 11 gives

$$\kappa=0.40 \text{ and } y_0=\frac{1}{9}\frac{\nu}{u_*}. \tag{14}$$

This value of y_0 was first given by Prandtl.

Kármán gives for δ the experimentally determined value

$$\delta=11.5\frac{\nu}{u_*}. \tag{15}$$

(c) GENERAL EQUATION OF VELOCITY DISTRIBUTION FOR WAVY WALLS

When the wall surface is smooth but wavy in character (see fig. 2) and the wall shear is sufficiently low, y_0 is given by a relation of the form

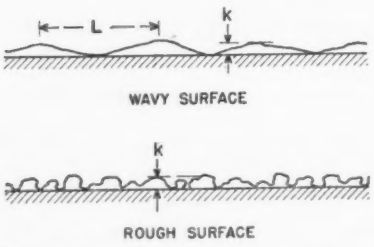

FIGURE 2.—*Diagrams of wavy and rough surfaces.*

$$\frac{y_0u_*}{\nu}=f\left(\frac{k}{L}\right), \tag{16}$$

where

L=the length of a wave, and
k=the height of a wave.

The ratio k/L may be called the "relative waviness." For a given ratio k/L, the function f may vary with the shape of the wavy projections, and hence surfaces with waves of different shapes must be treated separately.

If we introduce in eq 7 the value of y_0 from eq 16, there results

$$\left.\begin{aligned}\frac{u}{u_*}&=a_w+\frac{1}{\kappa}\ln\left(\frac{yu_*}{\nu}\right), \text{ or}\\ \frac{u}{u_*}&=a_w+\frac{2.30}{\kappa}\log\left(\frac{yu_*}{\nu}\right).\end{aligned}\right\} \tag{17}$$

This is the universal law of velocity distribution for wavy surfaces. The relation between a_w and the relative waviness is given by

$$f\left(\frac{k}{L}\right)=e^{-\kappa a_w}. \tag{18}$$

Our present very meager knowledge of wavy surfaces may be summarized by the statement that a_w decreases as k/L increases.

(d) GENERAL EQUATION OF VELOCITY DISTRIBUTION FOR ROUGH WALLS

When the wall surface is rough (see fig. 2), the expression for y_0 must be derived from k, the elevation of the roughness elements. The theory of dimensions then yields the relation

$$\frac{y_0 u_*}{\nu}=f\left(\frac{ku_*}{\nu}\right), \tag{19}$$

and accordingly the velocity distribution is given by substituting the value of y_0 thus obtained in eq 7:

$$\left.\begin{aligned}\frac{u}{u_*}&=a_r+\frac{1}{\kappa}\ln\left(\frac{yu_*}{\nu}\right), \text{ or}\\ \frac{u}{u_*}&=a_r+\frac{2.30}{\kappa}\log\left(\frac{yu_*}{\nu}\right).\end{aligned}\right\} \tag{20}$$

This is the universal law of velocity distribution for rough surfaces. The relation between a_r and the Reynolds number based on the height of the roughness elements is

$$f\left(\frac{ku_*}{\nu}\right)=e^{-\kappa a_r}. \tag{21}$$

The function f is known completely only for roughness produced by closely packed grains of sand, as determined by Nikuradse [2] by experiments on pipes of circular cross section. For the roughness of surfaces of the type used by Nikuradse, the symbol k_s will be adopted, to represent the mean height of the sand grains forming the roughness elements.

Nikuradse's data are given in figure 3, in which a_r is plotted as ordinate against log $(k_s u_*/\nu)$ as abscissa. Figure 3 shows that, when $k_s u_*/\nu$ is less than about 3.3, a_r is independent of u_* and has the value 5.5, which is the value of a_s for smooth surfaces. In other words, when $u_*<3.3\nu/k_s$, the surface behaves as if it were smooth.

Figure 3 also shows that when $k_s u_*/\nu$ is greater than about 67, a_r is given by the expression.

$$a_r=8.5-2.5\ln\left(\frac{k_s u_*}{\nu}\right)=8.5-5.75\log\left(\frac{k_s u_*}{\nu}\right). \tag{22}$$

Substitution of this result in eq 20 gives

$$\frac{u}{u_*}=8.5+5.75\log\left(\frac{y}{k_s}\right), \tag{23}$$

which is the law of velocity distribution in the vicinity of a surface covered with closely packed sand grains. Since the viscosity of the fluid does not enter eq 23, the equation applies to flow in the region where the hydraulic resistance varies with the square of the mean velocity.

The significant point of Nikuradse's investigation is the establishment of these two critical numbers for rough surfaces : $(k_s u_*/\nu)_1=3.3$ and $(k_s u_*/\nu)_2=67$. These critical numbers define a transition region in which both the kinematic viscosity and the relative roughness affect the friction. The complete generality of the results of Niku-

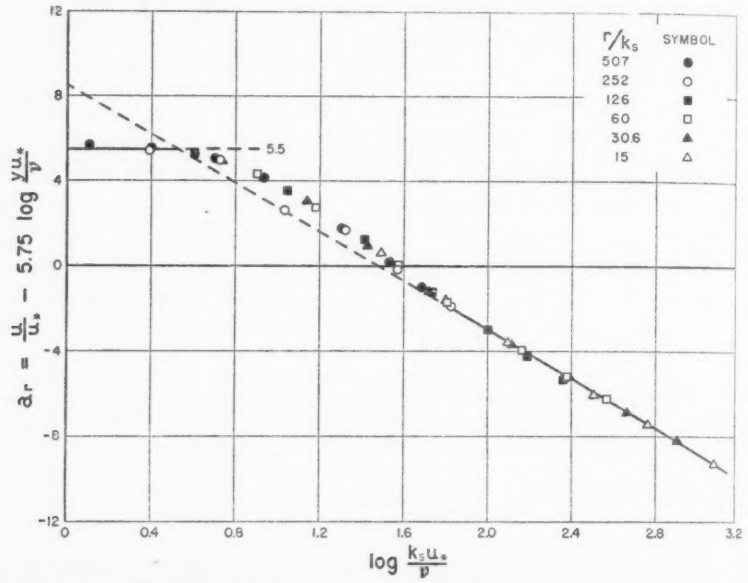

FIGURE 3.—*Surface characteristic a_r as a function of log $(k_s u_*/\nu)$ for circular pipes with surfaces of closely packed sand grains, according to Nikuradse.*

radse's investigation has been questioned on the grounds that the pipes which he used were not long enough. If this claim is valid, then we may expect to find lower values for the criteria if very long pipes are used, the effect being more pronounced for the higher critical number.

Schlichting's investigation [7] of roughness consisting of regular geometrical forms having a preassigned distribution has shown that in this case the velocity distribution law in the region where the quadratic resistance law holds is given by

$$\frac{u}{u_*}=a_{r0}+5.75 \log\left(\frac{y}{k}\right), \tag{24}$$

which is of the same form as eq 23. Here a_{r0} varies both with the shape and distribution of the roughness elements.

Thus the significant deduction to be derived from the results of experiments with rough surfaces in the region where the quadratic resistance law holds is that a_r in eq 20 satisfies the relation

$$a_r = a_{r0} - \frac{1}{\kappa} \ln \left(\frac{k u_*}{\nu} \right), \tag{25}$$

where a_{r0} has different values depending on the shape and distribution of the roughness elements of the surface under consideration. For a surface covered with sand $a_{r0}=8.5$.

Presumably wavy surfaces will also behave like rough surfaces if the velocity is high enough. The few investigations of wavy surfaces reported in the literature have involved relatively low velocities, and the results indicate that the resistance is independent of the relative roughness for such velocities. However, it seems reasonable to assume that, if the velocity is increased sufficiently, the conditions in the boundary layer will be changed so as to produce a resistance that will vary with the square of the velocity. This condition will exist for wall shears given by the inequality

$$(u_* k/\nu) > \phi(u_* L/\nu), \tag{26}$$

where ϕ is a function to be determined. When eq 26 is satisfied, then the velocity distribution for a wavy surface will be given by eq 20.

The constants a_s, a_w, a_r, and a_{r0} will be referred to hereafter in this paper as the "hydraulic characteristics of the surfaces," or more briefly, the "surface characteristics."

2. DERIVATION OF RESISTANCE FORMULAS

Careful experiments have shown that the resistance coefficient in pipes for a given Reynolds number R_e is not affected by the shape of the pipe, provided that in forming the Reynolds number the hydraulic radius R is used as the characteristic length of the pipe [8]. This can be explained by assuming that turbulent flow exhibits the following two properties. First, the velocity at a point in the vicinity of a wall depends solely on the shear at the wall element nearest to the point and not on the shear over the whole wall surface. Secondly, when the distance of the point from the wall is large enough, the increase in the velocity takes place at a rate much smaller than the rate of increase of the distance. This latter property is evident either from the $1/n$ power law or from the Kármán logarithmic velocity law. No such simplification exists for laminar flow, since the flow at a given point is affected by the whole wall. In fact, viscous uniform flow is a boundary-value problem.

These two properties of the law of velocity distribution permit its application to other cases of turbulent flow, once the constants involved in the law have been determined from tests on pipes of circular cross section. As examples of such applications there may be cited the analytical determination of the hydraulic skin friction of circular disk and flat plates [9, 10].

(a) RESISTANCE FORMULAS FOR CIRCULAR AND INFINITELY WIDE RECTANGULAR PIPES

As simple illustrations of the use of the hydraulic radius and of the Kármán law of velocity distribution, the coefficient of hydraulic resistance will be computed for two forms of pipes: (1) A pipe of circular cross section and (2) a rectangular pipe of infinite width. In the

first case, the wall shear τ_0 is the same over the entire perimeter of the section, and in the second case the variation in τ_0 at the two sides of the pipe can be neglected, since the pipe is infinitely wide. Hence, in both cases $\tau_0=\bar{\tau}_0$, the bar denoting the average value for the section.

Defining the friction coefficient λ in the usual way, the relation

$$\frac{\bar{\tau}_0}{\rho}=\lambda\frac{\bar{u}^2}{8} \tag{27}$$

in which $\bar{u}$ is the mean velocity of flow for the cross section, leads to the expression

$$\frac{\bar{u}}{\bar{u}_*}=2\sqrt{\left(\frac{2}{\lambda}\right)}, \tag{28}$$

where

$$\bar{u}_*=\sqrt{(\bar{\tau}_0/\rho)}.$$

Hence as a measure of the resistance, it is sufficient to consider the ratio $\bar{u}/\bar{u}_*$, which will be called the "mean flow ratio," instead of the resistance coefficient λ. This practice will be followed throughout this paper.

(1) *Smooth walls.*—Considering now a pipe of circular cross section, both sides of the expression

$$\frac{u}{u_*}=\frac{u}{\bar{u}_*}=a_s+b\ln\left(\frac{y\bar{u}_*}{\nu}\right), \qquad \left[b=\frac{1}{\kappa}\right],$$

which is the velocity distribution equation for a smooth surface, are multiplied by $2\pi r dr$, and then the resulting equation is integrated between the limits $(r_0-\delta)$ and 0, δ being the thickness of the laminar sublayer and r_0 the radius of the pipe. The flow in the laminar sublayer is negligible in comparison with the flow in the turbulent core, and hence the terms involving δ may be neglected. The resulting equation for the mean velocity of flow in a smooth-walled pipe of circular cross section is then

$$\frac{\bar{u}}{u_*}=\frac{\bar{u}}{\bar{u}^*}=a_s-1.5b+b\ln\left(\frac{r_0\bar{u}_*}{\nu}\right). \tag{29}$$

In a similar manner the equation for a smooth-walled pipe of rectangular section and of infinite width can be obtained, and is found to be

$$\frac{\bar{u}}{u_*}=\frac{\bar{u}}{\bar{u}_*}=a_s-b+b\ln\left(\frac{h\bar{u}_*}{\nu}\right) \tag{30}$$

where h is half the height of the section.

Introducing the hydraulic radius, $R=r_0/2$ and $R=h$, respectively, in the last two equations, they become

$$\frac{\bar{u}}{u_*}=\frac{\bar{u}}{\bar{u}_*}=a_s-0.81b+b\ln\left(\frac{R\bar{u}_*}{\nu}\right), \text{ and} \tag{31}$$

$$\frac{\bar{u}}{u_*}=\frac{\bar{u}}{\bar{u}_*}=a_s-b+b\ln\left(\frac{R\bar{u}_*}{\nu}\right), \tag{32}$$

respectively. It should be noted that this last equation applies also to a rectangular channel of infinite width and of depth h.

Now, introducing the experimentally determined values $a_s=5.5$. and $b=2.5$, and changing to common logarithms, the equations become

$$\frac{\bar{u}}{u_*}=\frac{\bar{u}}{\bar{u}_*}=3.5+5.75\ \log\left(\frac{R\bar{u}_*}{\nu}\right), \tag{33}$$

for smooth-walled pipes of circular cross section, and

$$\frac{\bar{u}}{u_*}=\frac{\bar{u}}{\bar{u}_*}=3.0+5.75\ \log\left(\frac{R\bar{u}_*}{\nu}\right) \tag{34}$$

for flow between smooth parallel walls of infinite extent. Thus, when the hydraulic radius is adopted as the characteristic length, it appears that the expressions for the average velocity become nearly identical in the two cases just considered.

(2) *Rough walls.*—To obtain the corresponding expressions for the mean velocity when the surfaces are rough, it is sufficient to replace a_s in eq 31 and 32 by the value of a_r given by eq 25. Hence when the walls are rough, eq 31 and 32 become

$$\frac{\bar{u}}{u_*}=\frac{\bar{u}}{\bar{u}_*}=a_{ro}-0.81b+b\ln\left(\frac{R}{k}\right) \tag{35}$$

for circular pipes, and

$$\frac{\bar{u}}{u_*}=\frac{\bar{u}}{\bar{u}_*}=a_{ro}-b+b\ln\left(\frac{R}{k}\right) \tag{36}$$

for parallel walls of infinite extent.

If the roughness is produced by closely packed sand grains, as in Nikuradse's experiments on rough surfaces, $a_{ro}=8.5$, and eq 35 and 36 become

$$\frac{\bar{u}}{u_*}=\frac{\bar{u}}{\bar{u}_*}=6.5+5.75\ \log\left(\frac{R}{k_s}\right) \tag{37}$$

for circular pipes, and

$$\frac{\bar{u}}{u_*}=\frac{\bar{u}}{\bar{u}_*}=6.0+5.75\ \log\left(\frac{R}{k_s}\right) \tag{38}$$

for parallel walls of infinite extent.

(b) RESISTANCE FORMULAS FOR CHANNELS WITH POLYGONAL CROSS SECTIONS

In passing from a circular pipe to a polygonal channel, a complication arises from the presence of secondary currents at the corners of the channel. Prandtl [5] has explained these currents as being due to the three-dimensional character of the turbulent velocity fluctuations. In consequence, the shear at the wall corners is reduced, since otherwise the resulting dissipation would be greater than that which can be maintained by the externally furnished energy. Thus in polygonal channels the shear at the wall is not uniform. Also the free surface acts as if it were a source of friction. The turbulent fluctuations near the surface, now only two-dimensional, again are a source of energy

dissipation, as the velocity at the surface is not uniform. If the extent of the free surface is decreased, a larger dissipation occurs, and the filaments of maximum velocity in any vertical are depressed. Accordingly, in applying Kármán's velocity law to channels, attention must be paid to these factors.

(1) *Trapezoidal channels.*—The expression for the mean velocity in a channel having a trapezoidal cross section will be derived next, and it will be demonstrated that the correction terms due to the variation in wall shear over the solid boundary and to the apparent shear at the free surface may be neglected without involving an error greater than a few percent. In other words, the hydraulic radius as customarily computed can be used as the characteristic length of the cross section of such a channel.

It is necessary to treat two cases; (1) when the bisectors of the internal angles intersect above the water surface, and (2) when they intersect below the water surface. (See fig. 4.)

Case 1.—Bisectors intersect above water surface. The internal angles of the cross section (see fig. 4) will be denoted by θ_1 and θ_2, the base width by B_0, and the depth of the water by h. For purposes of computation, the cross section will be divided into zones of infinitesimal width dy in such a way that all portions of any given zone are at the same minimum distance y from the wall.

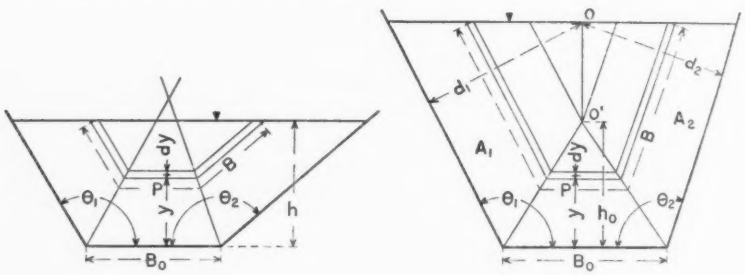

1. BISECTORS OF BASE ANGLES MEET ABOVE WATER SURFACE

2. BISECTORS OF BASE ANGLES MEET BELOW WATER SURFACE

FIGURE 4.—*Diagrams of trapezoidal channels to illustrate notation.*

The velocity u at a given point P in one of the zones can be written as

$$\frac{\bar{u}}{\bar{u}_*}=a+b\ln\left(\frac{yu_*}{\nu}\right)-\epsilon_f\frac{\bar{u}}{\bar{u}_*} \tag{39}$$

Here y is the normal distance of P from the wall and u_* is the shear velocity computed from the shear at the foot of the normal from P.

The term $\epsilon_f\bar{u}/\bar{u}_*$ is a correction applied to take account of the effect of the free surface.

The correction is expressed conveniently as a certain fraction ϵ_f of the ratio $\bar{u}/\bar{u}_*$, where $\bar{u}$ is the average velocity in the cross section, and $\bar{u}_*$ is the average shear velocity over the solid boundary. It is obvious that ϵ_f will be a function of the position of the point P. The relation of the local shear velocity u_* at an element of the wall to the mean shear velocity can be expressed by

$$u_* = \bar{u}_* (1 + \epsilon_*) \tag{40}$$

Replacing u_* in eq 39 by its value from eq 40, and discarding some small quantities involving ϵ_*, there results

$$\frac{u}{\bar{u}_*} = a + b \ln\left(\frac{y\bar{u}_*}{\nu}\right) - (\epsilon_f - \epsilon_*)\frac{\bar{u}}{\bar{u}_*}. \tag{41}$$

This may be referred to as the exact law of velocity distribution in a channel with smooth surfaces. If we neglect the flow in the laminary sublayer, the total flow through the cross section is given by

$$\bar{u}A = \int_\delta^h uBdy, \tag{42}$$

where A is the area of the wetted cross section and δ is the thickness of the laminar sublayer.

The length B of any zone is given by the relation

$$B = p - \alpha y, \tag{43}$$

where

p = the wetted perimeter, and
α = a function of the included angles of the form
$\alpha = ctn\ \theta_1 + ctn\ \theta_2 + 2csc\ \theta_1 + 2csc\ \theta_2$. (44)

Substituting in eq 42 the value of u from eq 41 and the value of B from eq 43, integrating, and neglecting the small quantities involving δ, there results

$$\frac{\bar{u}}{\bar{u}_*} = a_s - b + b \ln\left(\frac{hu_*}{\nu}\right) + \frac{bh^2\alpha}{4A} - \bar{\epsilon}\frac{\bar{u}}{\bar{u}_*}, \tag{45}$$

where $\bar{\epsilon}$ is defined as

$$\bar{\epsilon} = \frac{1}{A}\int (\epsilon_f - \epsilon_*) dA. \tag{46}$$

If the h in the logarithmic term is now replaced by the hydraulic radius R by the substitution $h = Rh/R$, and if β is used to represent the difference

$$\beta = \ln\left(\frac{h}{R}\right) - \frac{h^2\alpha}{4A}, \tag{47}$$

the expression for the mean velocity of flow in a channel of trapezoidal cross section with smooth walls becomes

$$\frac{\bar{u}}{\bar{u}_*} = a_s - b + b \ln\left(\frac{R\bar{u}_*}{\nu}\right) + b\beta - \bar{\epsilon}\frac{\bar{u}}{\bar{u}_*}. \tag{48}$$

The corresponding expression for wavy walls is obtained by substituting a_w for a_s in eq 48, and is

$$\frac{\bar{u}}{\bar{u}_*} = a_w - b + b \ln\left(\frac{R\bar{u}_*}{\nu}\right) + b\beta - \bar{\epsilon}\frac{\bar{u}}{\bar{u}_*}. \tag{49}$$

If the walls of the channel are rough, a_s in eq 48 should be replaced by a_r as given by eq 25 in which the value of a_{ro} depends on the roughness of the surface under consideration. The equation for the

mean velocity in a rough-walled channel of trapezoidal cross section then becomes

$$\frac{\bar{u}}{\bar{u}_*}=a_{ro}-b+b\ln\left(\frac{R}{k}\right)+b\beta-\bar{\epsilon}\frac{u}{u_*}. \tag{50}$$

Case 2.—Bisectors intersect below water surface. If the free surface is above the point of intersection of the bisectors of the internal angles, the value of β must be expressed differently. (See fig. 4.) Let the bisectors of the included angles meet at a point O', at a vertical distance h_0 from the bottom. The vertical line passing through O' meets the free surface at the point O. The two normals drawn from O to the side walls are of length d_1 and d_2. The vertical through O and O' divides the area A of the trapezoid into two portions A_1 and A_2. Then β will be given by the relation

$$\begin{aligned}2A\beta=&(2\cot\theta_1/2+\tan\theta_1)h_0^2\ln(h_0/d_1)+\\&(2\cot\theta_2/2+\tan\theta_2)h_0^2\ln(h_0/d_2)+\\&2A_1\ln(d_1/R)+2A_2\ln(d_2/R)-A,\end{aligned} \tag{51}$$

where R is the hydraulic radius.

The value of β thus determined can now be substituted in eq 48, 49 and 50 for this case.

(2) *Channels of other shapes.*—If the mean velocity in a channel of any other cross section is computed in the same manner, it will be found that the expressions for this velocity have the same form as those given for a trapezoidal cross section in eq 48, 49, and 50, except that the values of β and $\bar{\epsilon}$ vary from section to section. Hence these three equations are the rational equations for the mean velocity of uniform flow in channels of constant cross section and slope, since they are derived from a rational theory.

(3) *Error from neglect of the correction terms.*—Eq 48, 49, and 50 also enable us to compute the magnitude of the error that is involved if we neglect certain additive terms. If these general equations are compared with the corresponding equation for a channel of infinite width (see eq 32), it will be observed that they differ from it only in containing the additive terms $b\beta-\bar{\epsilon}\ \bar{u}/\bar{u}_*$. These terms may be interpreted as due to the combined effect of the existence of a free surface and of a nonuniform distribution of shear at the walls. The term $b\beta$ can be computed readily for any given shape of cross section, as this is a mere matter of geometry. Computation shows that for a triangular cross section β is independent of the depth of the water and has the value

$$\beta=0.19. \tag{52}$$

For a rectangular cross section it takes on the value

$$\beta=\ln\left(1+\frac{2h}{B_0}\right)-\frac{h}{B_0}, \tag{53}$$

as can be seen from eq 47.

For a semicircular cross section, β has the form

$$\beta=\int_0^h\left[\ln\left(\frac{y}{R}\right)\right]\frac{B}{R}\frac{dy}{p}+1, \tag{54}$$

Some computed values of β for rectangular and semicircular channels are given in table 1. The above formulas show that β varies with the hydraulic radius. Table 1 shows on the other hand that β in

itself is a small quantity. For polygonal channels other than rectangular, β is found to be of approximately the same magnitude as for a rectangular channel. For the sake of simplicity then, we may take $\beta=0.1$ for all polygonal channels irrespective of shape, since the error thus introduced is small.

Little is known as yet about the quantity $\bar{\epsilon}$. From the manner of formation, it can be inferred that $\bar{\epsilon}$ is small, particularly in those cases where the depression of the filaments of maximum velocity is small. It is conceivable that the magnitude of $\bar{\epsilon}$ will depend on the

TABLE 1.—*Values of β for rectangular and semicircular channels*

Rectangular		Semicircular	
R/B_0	β	R/r_0	β
0.05	0.049	0.05	0.178
.10	.098	.15	.200
.15	.143	.20	.210
.20	.175	.30	.227
.25	.193	.40	.244
		.50	.259

shape of the cross section. The exact determination of its value no doubt is connected with some parameter involving the ratio of the transverse length of the free surface to the wetted perimeter.

It is very likely that $\bar{\epsilon}$ can be evaluated best by means of experiments. The above expressions, eq 48, 49, and 50, indicate that in experiments for this purpose the surface characteristics of the channel wall will have to be determined in advance by tests on other forms of channels, or preferably on very wide rectangular pipes.

We leave the term $\bar{\epsilon}\ \bar{u}/\bar{u}_*$ out of consideration by assuming that it is small and can be merged with the surface characteristics a_s, a_w, or a_{r0}. We adopt 2.5 for the value of b and 0.1 for the value of β and put

$$A_s=a_s-2.5(1-\beta)=a_s-2.25,$$
$$A_w=a_w-2.5(1-\beta)=a_w-2.25,$$
$$A_{r0}=a_{r0}-2.5(1-\beta)=a_{r0}-2.25.$$

Thus, the general equations of mean flow, eq 48, 49, and 50, now become

$$\frac{\bar{u}}{\bar{u}_*}=A_s+5.75\log\left(\frac{R\bar{u}_*}{\nu}\right), \tag{55}$$

$$\frac{\bar{u}}{\bar{u}_*}=A_w+5.75\log\left(\frac{R\bar{u}_*}{\nu}\right), \text{ and} \tag{56}$$

$$\frac{\bar{u}}{\bar{u}_*}=A_{r0}+5.75\log\left(\frac{R}{k}\right), \tag{57}$$

for smooth, wavy, and rough surfaces, respectively. The experiments of Bazin will be examined in the light of these expressions. But prior to this examination it is permissible to effect a further simplification in the flow expression for rough channels, eq 57, by introducing the concept of "equivalent sand roughness."

(c) EQUIVALENT SAND ROUGHNESS

The hydraulic effect of roughness elements of arbitrary shape and of arbitrary distribution can be described very conveniently by comparing it with the effect of a rough surface consisting of closely packed sand grains of the type used by Nikuradse [2] in his studies of rough pipes. Such a comparison leads to the concept of equivalent sand roughness. The size of sand grains as a measure of roughness was first suggested and used by Kármán [11]. The basis of the comparison is the similarity of velocity distribution near a rough surface. In general

$$\frac{u}{u_*}=a_{r0}+5.75\log\left(\frac{y}{k}\right), \tag{24}$$

where k is a roughness height. In Nikuradse's results a_{r0} was found to have the value 8.5, so that

$$\frac{u}{u_*}=8.5+5.75\log\left(\frac{y}{k_s}\right), \tag{23}$$

where k_s is the size of the closely packed sand grains.
Eliminating u/u_* between these two equations,

$$5.75\log k_s=8.5-a_{r0}+5.75\log k. \tag{58}$$

This is the expression which gives the equivalent sand roughness k_s for the particular roughness k. Physically, if a velocity u is observed at a point distant y from a wall of an arbitrary roughness k under a known shear, the same velocity will be obtained at the same point and for the same shear if the particular roughness is replaced by sand grains of size k_s as given by eq 58.

If velocity traverses do not exist for a given roughness in a channel, let us say, the determination of the equivalent sand roughness can be made to depend on the mean flow. From eq 50 after combining the $\bar{\epsilon}$ term with a_{r0}, putting $b=2.5$ and $\beta=0.1$, we have

$$a_{r0}-5.75\log k=\frac{\bar{u}}{\bar{u}_*}-5.75\log R+2.25.$$

Substituting this in eq 58, there results

$$5.75\log k_s=6.25-\left(\frac{\bar{u}}{\bar{u}_*}-5.75\log R\right), \tag{59}$$

from which k_s can be computed. An advantage of this procedure is that it is not necessary to make a geometrical specification of roughness in any given case for the purpose of description. With k_s known, the expression for the mean flow in rough channels can now be written as

$$\frac{\bar{u}}{\bar{u}_*}=6.25+5.75\log\left(\frac{R}{k_s}\right) \tag{60}$$

III. APPLICATION TO BAZIN'S EXPERIMENTAL DATA

1. DESCRIPTION OF BAZIN'S CHANNEL INSTALLATION

The experiments of Bazin which are reviewed in this paper were made in an experimental channel located along the Bourgogne canal, near Dijon. [4] The channel was connected at the upper end with the canal which supplied the water and at the lower end with the river Ouche which received the discharge. It ran parallel with the canal for a distance of 450 m and then turned to the left toward the river for the remaining length of 146.5 m. It was built of poplar planks placed longitudinally and fixed to wooden frames spaced 1.5 m apart. The width of the channel throughout its entire length was 2 m. Rammed clay under the bed and cement mortar applied to the exterior of the vertical walls made the channel watertight. In the initial length of 200 m the slope of the channel was 0.0049; for the next 250 m to the bend the slope was 0.0084. When it was found necessary to experiment with slopes other than those given above and with different cross sections, these were invariably built of wood. To modify the slope a wooden floor was placed in the channel, and all spaces underneath were filled with clay.

The forebay at the upper end of the channel consisted of a rectangular chamber 5.40 m wide and 14 m long. The flow of water from the canal into the forebay chamber was regulated by means of four gates. Each had a width of 1 m and could be elevated to give a maximum opening of 0.4 m. The final control of the flow from the forebay chamber into the experimental channel was effected by means of 12 sharp-edged square orifices made of copper. With this arrangement a very uniform discharge was easily obtained.

An assistant stationed at the gates maintained the surface of the water in the forebay at a level of 0.80 m above the midpoint of the orifices, guided by the indications of a float gage. During calibration the discharge of the orifices was ascertained by putting a bulkhead in the initial portion of the channel and noting the time taken to fill the basin thus created. For determining accurately the volume of the water discharged through the orifices, the discharge was made into the isolated portion of the channel after the bottom of the latter was covered with water. Thus the volume to be measured was one between two horizontal water surfaces and the vertical walls of the channel.

The profile of the water surface in each test was measured as follows. Three metal studs were placed on the upper cross piece of each channel frame, one at the midpoint and one on each side, to serve as datum points. Their heights were measured from the bottom of the bed and also from the water surface, the difference yielding the depth of water. The depth gage was a graduated rod with a sharp metal edge at its lower end. This rod was movable in a block which was rested on one of the datum studs during measurements. An examination of the tables of data shows that in a great many tests the depth was measured continually over the entire length of channel investigated. Sometimes more than 100 such depth measurements were made—never less than 40. Again, the depth that was used for computing the hydraulic radius was usually the mean of some 20, 30, or 40 such determinations. These were selected from a reach where the depth was found to be uniform.

The profile of the channel bed was carefully determined at the commencement of each series of operations in the following simple and accurate manner. In each segment of the channel a bulkhead was placed downstream, and the section of the channel in which the slope was to be measured was filled with water. The profile of the channel bottom was then determined by depth measurements with reference to the still water surface.

The velocity traverses were made by means of a pitot-static tube of the type developed by Darcy. The constant of proportionality of the instrument was based on the results of the following two of the three methods used. In one method the surface velocities in the channel were measured both by a float and by the tube, and the results were compared. The comparison was restricted to measurements made in rectangular channels of large dimensions and great depth of flow. This comparison gave the value 1.006 for the constant. In another method the integrated discharge determined from velocity traverses by the tube was compared with the mean discharge. This method gave 0.993. The mean of the two results, or unity, was adopted.

2. EQUIVALENT SAND ROUGHNESS FOR SOME OF BAZIN'S CHANNELS

The first group of data to be considered is from the experiments which Bazin made to determine the effect of roughness on the mean

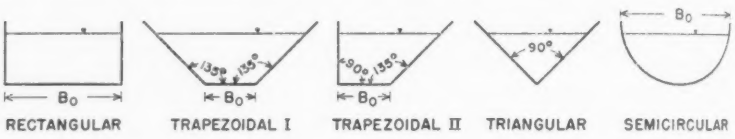

SHAPES OF CHANNELS

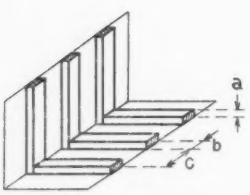

STRIPS	DIMENSIONS IN CM		
	a	b	c
CLOSELY SPACED	1	2.7	1
WIDELY SPACED	1	2.7	5

PLANK CHANNELS WITH WOOD STRIPS

FIGURE 5.—*Descriptive diagrams of Bazin's channels.*

velocity of flow. The experiments were made in rectangular channels, all of practically the same width. The types of rough surfaces, which were the same for the bottom and the vertical walls in each individual case, are listed in table 2, together with pertinent experimental data. Also see figure 5.

TABLE 2.—*Data from Bazin's tests on rough rectangular channels*

Series	Surface	Slope, i	Width, B_0	Hydraulic radius, R		Mean velocity, $\bar{u}$		Temperature, θ
				Minimum	Maximum	Minimum	Maximum	
			cm	*cm*	*cm*	*cm/sec*	*cm/sec*	° *C.*
2	Cement	0.0049	181.2	5.11	21.23	101.8	246.0	12.0
3	Brick	.0049	191.1	5.86	23.74	83.9	204.7	19.0
4	Fine gravel [1]	.0049	183.2	7.61	27.72	65.8	169.7	14.5
5	Coarse gravel [2]	.0049	186.1	8.88	30.09	54.7	149.3	16.0
8	Planks	.00824	199.0	4.47	19.19	107.4	261.2	8.5
12	Planks with closely spaced wood strips.[3]	.0015	196.6	9.21	32.81	50.2	127.8	8.5
13		.0059	196.1	6.26	24.09	76.2	197.4	7.0
14		.00886	195.2	5.56	22.14	86.8	221.2	14.0
15	Planks with widely spaced wood strips.[3]	.0015	196.0	11.53	39.60	39.0	94.9	16.5
16		.0059	196.0	8.05	29.42	58.1	149.8	7.5
17		.00886	195.1	7.06	26.99	67.3	169.8	16.5

[1] Gravel from 1 to 2 cm in diameter.
[2] Gravel from 3 to 4 cm in diameter.
[3] See figure 5.

To ascertain whether the mean velocity of flow in a channel of a given roughness k is affected by the kinematic viscosity, it is sufficient to investigate the relation between the quantities $(\bar{u}/\bar{u}_*-5.75 \log R)$ and $\log (\bar{u}_*/\nu)$.

In order to compute the principal quantities involved in the comparison, the following test data were taken from Bazin: The temperature of the water, θ; the hydraulic radius, R, in centimeters; the mean velocity of flow, $\bar{u}$, in centimeters per second; and the quantity $A=Ri/\bar{u}^2$, which is a measure of the hydraulic resistance. As A is not a dimensionless quantity, it was multiplied by g, the acceleration of gravity, to make it dimensionless.

In a channel the mean shear velocity is given by

$$\bar{u}_*=\sqrt{(Rig)}, \tag{61}$$

thus

$$\bar{u}/\bar{u}_*=1/\sqrt{(gA)}, \text{ and } \bar{u}_*=\bar{u}\sqrt{(gA)}.$$

The kinematic viscosity ν follows from the temperature θ.

The results of the computations are shown in figure 6, where $(\bar{u}/\bar{u}_*-5.75 \log R)$ is plotted as a function of $\log (\bar{u}_*/\nu)$.

It is seen that in these tests the observed points for each channel can be represented by a straight line parallel to the axis of $\log (\bar{u}_*/\nu)$. Hence, the quantity $(\bar{u}/\bar{u}_*-5.75 \log R)$ is a constant. Therefore, the quantity $(\bar{u}/\bar{u}_*-5.75 \log R/k)$ is also a constant and thus is independent of $k\bar{u}_*/\nu$, where k would be the actual roughness heights of any of the roughnesses employed. Thus in these tests the channels, including the channel with the cement walls, were hydrodynamically rough.

At this point attention may be invited particularly to the two groups of tests which were made with the channels having wooden strips using three different slopes. It is seen that, in this specific manner of presenting and analyzing the experimental material, the data taken with the different slopes are hardly differentiable from each other. Lindquist [11] in considering the same data compared the mean flow in these channels on the basis of Reynolds number, $R\bar{u}/\nu$. But this

method of treatment did not yield a simple correlation of the results. The underlying difficulty now can be readily understood, since the appropriate criterion of the hydraulic roughness is obtained by using $k\bar{u}_*/\nu$ and not $R\bar{u}/\nu$. The Blasius method of plotting the hydraulic friction factor λ against $R\bar{u}/\nu$ is satisfactory for rough pipes, as the relative roughness k/R remains the same for variable $\bar{u}$. In channels, on the other hand, a variable $\bar{u}$ signifies a variable k/R.

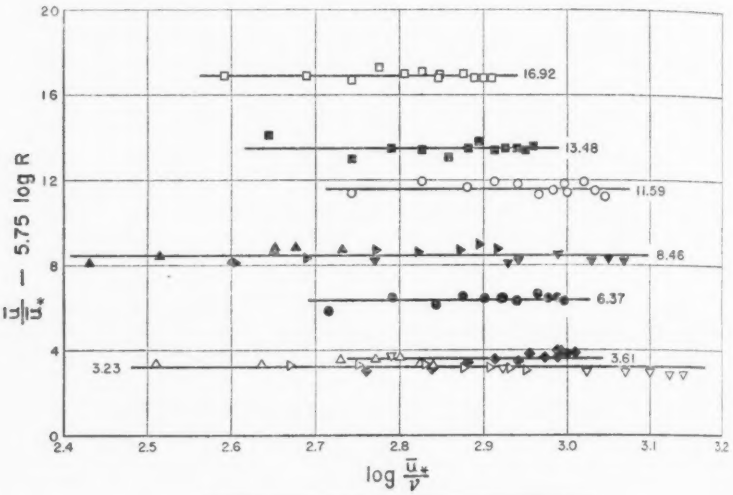

LEGEND			
SERIES	SYMBOL	SURFACE	SLOPE
2	□	CEMENT	.0049
3	○	BRICK	.0049
4	●	FINE GRAVEL	.0049
5	◆	COARSE GRAVEL	.0049
8	■	PLANKS	.00928
12	▲	PLANKS WITH	.0015
13	▶	CLOSELY SPACED	.0059
14	▼	WOOD STRIPS	.00886
15	△	PLANKS WITH	.0015
16	▷	WIDELY SPACED	.0059
17	▽	WOOD STRIPS	.00886

FIGURE 6.—*Quantity* $(\bar{u}/\bar{u}_* - 5.75 \log R)$ *as a function of* $\log (\bar{u}_*/\nu_*)$ *for rough rectangular channels.*

Basic data from Bazin.

The results shown in figure 6 indicate that the rational formulas for the mean flow which were assumed in the beginning are actually serviceable. To complete the examination it now remains to evaluate the equivalent sand roughness for each channel, using eq 59. The different quantities which are necessary for the computations are given in table 3. The values of the quantities R/B_0 and Y in table 3 are the averages from all the observations for a given channel. The resulting equivalent sand roughness is given in the next to the last column.

TABLE 3.—*Computation of equivalent sand roughness k_s for rough rectangular channels listed in table 2*

$(5.75 \log k_s = 6.25 - (\bar{u}/\bar{u}_* - 5.75 \log R) = 6.25 - Y_*)$

Series	Surface	R/B_0	Y	$6.25-Y$	$\log k_s$	k_s	R/k_s
						cm	
2	Cement	0.080	16.92	−10.67	−1.856	0.014	1,030
3	Brick	.084	11.59	−5.34	−0.928	.118	135
4	Fine gravel [1]	.106	6.37	−0.12	−.021	.952	20
5	Coarse gravel [2]	.116	3.61	+2.64	+.459	2.88	7.4
8	Planks	.067	13.58	−7.33	−1.275	0.053	253
12 13 14	Planks with closely spaced wood strips [3].	.090	8.46	−2.21	−0.384	.413	43
15 16 17	Planks with widely spaced wood strips.[3]	.110	3.23	+3.02	+.526	3.36	8.3

[1] Gravel from 1 to 2 cm in diameter.
[2] Gravel from 3 to 4 cm in diameter.
[3] See figure 5.

In this connection it is interesting to note that the equivalent sand roughness of the fine gravel, 1 to 2 cm in diameter, is 0.95, and that of the coarse gravel, 3 to 4 cm in diameter, is 2.9 (table 3). The difference between the equivalent sand roughness and the nominal size of the gravel is not very large. Bazin does not give the proportions of different sizes in his gravels. It is quite possible that the mean size of the gravel was close to 1 and 3 cm, respectively, in which case the agreement between the equivalent sand roughness and the actual gravel size is good. If this was not the case, the difference may be the result of the way in which the individual particles of gravel were distributed, or of the depth to which they were embedded in the supporting cement.

The analysis of Bazin's experiments on the effect of the roughness of channels, therefore, leads to the formula

$$\frac{\bar{u}}{\bar{u}_*} = 6.25 + 5.75 \log\left(\frac{R}{k_s}\right), \tag{60}$$

where k_s, the equivalent sand roughness, has the numerical values given in table 3.

Adopting this form of expression for the mean flow, Manning's formula, which is used extensively in engineering work, may be changed so as to contain the equivalent sand roughness in the place of the coefficient n. The advantage of such a change will be discussed later.

3. SURFACES OF WOOD AS EXAMPLES OF WAVINESS

In some of Bazin's experiments the effect of kinematic viscosity on the mean velocity of flow can be seen. From the experiments belonging to this category (see table 4), let series 28 and 29 be considered first. These tests were made in small rectangular channels 10 cm wide. The channels were prepared from four pieces of firwood, about 5 m long, hollowed out to a cross section of 10 by 10 cm. They were assembled end to end, and in the entire length there were only three joints. The surfaces were made as smooth as possible. The slopes used were 0.0047 and 0.0152. The data obtained from the

tests are shown in figure 7, in which $\bar{u}/\bar{u}_*$ is plotted against log $(R\bar{u}_*/\nu)$. It appears that the experimental points can be represented with sufficient accuracy by a straight line. This line has the same inclination as the two straight lines in the upper part of the figure, which represent the variation of the mean velocity of flow with kinematic viscosity in smooth circular pipes and in smooth rectangular pipes of very great width. The interpretation of this fact is that the polished

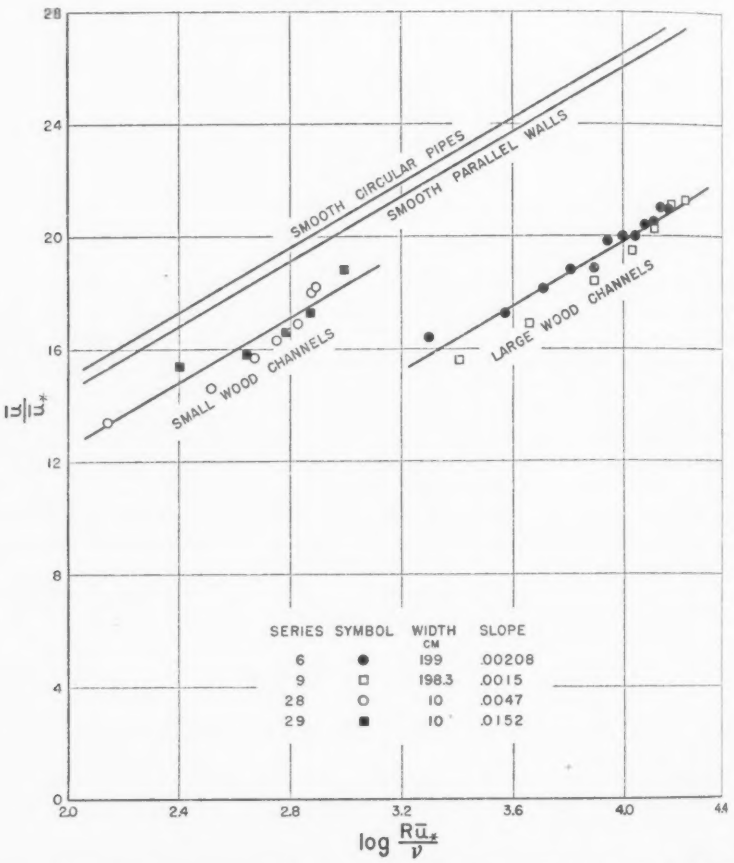

FIGURE 7.—*Mean flow ratio $\bar{u}/\bar{u}_*$ as a function of log $(R\bar{u}_*/\nu)$ for small and large rectangular wood channels, illustrating characteristics of channels with wavy surfaces as compared with smooth pipes.*

Basic data from Bazin

surface of firwood can not be considered as hydrodynamically smooth, since the indicated flow is less than that for a smooth surface. However, it is of a type classified customarily as wavy, since the effect of viscosity is similar to that obtained with a smooth surface. The formula for the flow as indicated by the line passing through the experimental points is

$$\frac{\bar{u}}{\bar{u}_*}=1.3+5.75\log\left(\frac{R\bar{u}_*}{\nu}\right), \tag{62}$$

which is of the same form as eq 56 with $a_w=1.3$.

TABLE 4.—*Rectangular wood channels with wavy surfaces*

[Data from Bazin]

Series	Surface	Slope, i	Width, B_0	Hydraulic radius, R		Mean velocity, $\bar{u}$		Temperature, θ
				Minimum	Maximum	Minimum	Maximum	
			cm	*cm*	*cm*	*cm/sec*	*cm/sec*	°*C*
28	Polished fir	0.0047	10.0	0.90	2.84	27.3	65.8	10.0
29	do	.0152	10.0	.92	2.25	57.1	108.6	10.0
6	Poplar planks	.00208	199.0	7.35	28.09	63.5	158.7	7.0
9	do	.0015	198.3	8.42	30.42	54.8	142.0	14.05

A similar effect of the kinematic viscosity is also noticeable in the results of the tests made in the larger channels of wooden planks at the smaller slopes. The data, which were obtained from the experiments of series 6 and 9 (table 4), that is, from the series of the smaller slopes, are reproduced in figure 7. Again in this case the distribution of the experimental points can be represented by a straight line with the same inclination as that of the lines corresponding to smooth circular pipes and smooth rectangular pipes of great width. In these tests with large wooden channels, then, the effect of kinematic viscosity is important when the slopes are small. Thus for the smaller slopes the surfaces are to be reckoned as hydrodynamically wavy.

Yet in the previous section a similar surface is interpreted as being hydrodynamically rough. The reason for this double designation of the same surface perhaps can be clarified if all the data for large rectangular wooden channels given in table 5 are considered as a whole. For this purpose it is preferable to study the relation between $(\bar{u}/\bar{u}_*-5.75\log R)$ and $\log(\bar{u}_*/\nu)$ as plotted in figure 8. Two straight lines are selected to represent the distribution of the experimental points, one horizontal and the other inclined. The horizontal line is taken from figure 6 and applies to the tests of series 8; the inclined line is taken from figure 7 and applies to the tests of series 6 and 9. The observed points, therefore, can be divided into two groups. In one group, all the points fall near the inclined line, which means that the associated flows vary with viscosity. In the other group all the points fall near the horizontal line, which means that the associated flows do not depend on viscosity. The lines intersect at a point given by $\log(\bar{u}_*/\nu)=2.9$. To derive a critical number representing this intersection, use may be made of the equivalent sand roughness already obtained for such wooden surfaces. See table 3. With $k_s=0.053$ cm, or $\log k_s=-1.275$, the criterion that is sought for is $\log(k_s\bar{u}_*/\nu)=1.625$ or $k_s\bar{u}_*/\nu=42.2$. Accordingly the unplaned wooden surfaces of the larger channels behave as wavy surfaces, when $k_s\bar{u}_*/\nu\leqslant 42.2$.

The mean velocity of flow for these channels with wavy surfaces, as derived from figure 7, is

$$\frac{\bar{u}}{\bar{u}_*}=-3.0+5.75\log\left(\frac{R\bar{u}_*}{\nu}\right). \tag{63}$$

TABLE 5.—*Data from Bazin's tests on large rectangular wood channels*

Series	Slope, i	Width, B_0	Hydraulic radius, R		Mean velocity, $\bar{u}$		Temperature, t
			Minimum	Maximum	Minimum	Maximum	
		cm	*cm*	*cm*	*cm/sec.*	*cm/sec.*	°C
6	0.00208	199.0	7.35	28.09	63.5	158.7	7.0
7	.0049	199.0	5.73	22.15	82.6	217.9	8.7
8	.00824	199.0	4.47	19.19	107.4	261.2	8.7
9	.0015	198.3	8.42	30.42	54.8	142.0	14.05
10	.0059	198.7	5.24	20.91	91.0	234.9	14.5
11	.00839	198.2	4.46	18.94	108.0	266.4	16.0

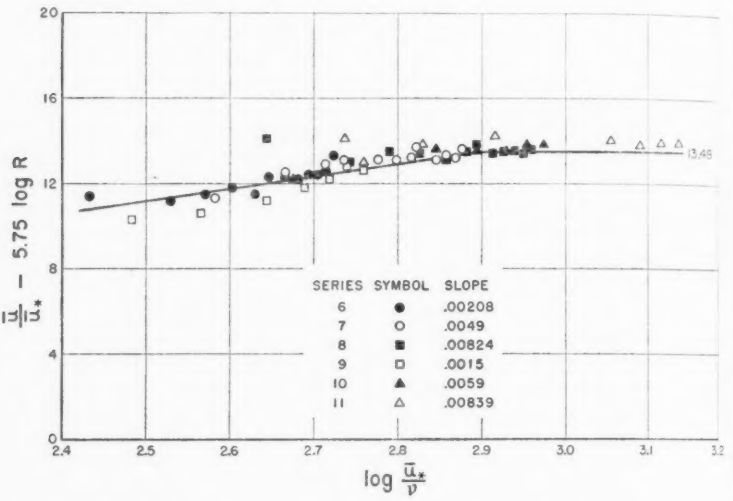

FIGURE 8.—*Quantity* $(\bar{u}/\bar{u}_* - 5.75 \log R)$ *as a function of log* $(\bar{u}_* R/\nu)$ *for large rectangular wood channels, illustrating transition from waviness to roughness.*

Basic data from Bazin

It is interesting to note that the value of the critical number given above for the transition of the surface characteristic from waviness to roughness is somewhat less than the upper criterion which Nikuradse found for his sand-covered surfaces, which was $k_s \bar{u}_* / \nu = 67$.

4. EFFECT OF SHAPE OF CROSS SECTION ON MEAN VELOCITY

Bazin was also interested in the possible effect of the shape of channels on the mean velocity of flow. The experiments to this end were carried out in channels with wooden walls. In what follows only those experiments in which the wooden surfaces have shown themselves to be hydrodynamically rough will be considered. These are listed in table 6. Also see figure 5.

TABLE 6.—*Data from Bazin's tests on wood channels of various shapes* [1]

Series	Shape [1]	Slope, i	Width, B_0	Hydraulic radius, R		Mean velocity, $\bar{u}$		Temperature, θ
				Minimum	Maximum	Minimum	Maximum	
			cm	*cm*	*cm*	*cm/sec*	*cm/sec*	°*C*
8	Rectangular	0.00824	199.0	4.47	19.19	107.4	261.4	8.5
11	do	.00839	198.2	4.46	18.94	108.0	266.4	16.0 to 21.0
18	do	.0049	119.7	7.17	25.57	102.6	231.3	8.0
21	Trapezoidal I	.0015	100.0	10.18	33.43	73.0	148.5	7.0
22	Trapezoidal II	.0049	94.5	7.85	25.51	109.0	241.6	24.5
23	Triangular	.0049	-------	9.97	25.57	125.8	236.3	22.0
26	Semicircular	.0015	140.0	11.89	35.11	79.5	168.9	22.5

[1] See figure 5.

From the test data of these series the quantity $(\bar{u}/\bar{u}_* - 5.75 \log R)$ was computed for corresponding values of $\log (\bar{u}_*/\nu)$. The results are plotted in figure 9. It is seen that $(\bar{u}/\bar{u}_* - 5.75 \log R)$ is practically independent of $\log (\bar{u}_*/\nu)$, except possibly for the semicircular section. The variation of $(\bar{u}/\bar{u}_* - 5.75 \log R)$ with $\log (\bar{u}_*/\nu)$ in the results for the semicircular section need not be interpreted as being necessarily due to the effects of kinematic viscosity. For, in the first place, if the correction term $2.5\,\beta$ is introduced using the values in table 1, the variation appears to be less pronounced; and in the

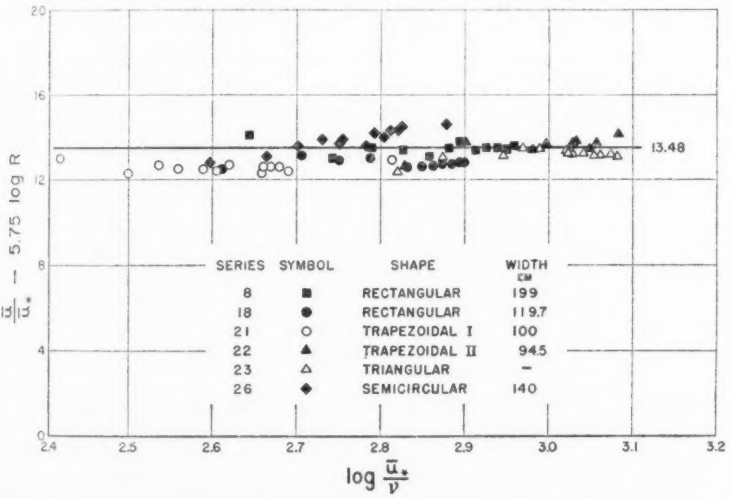

FIGURE 9.—*Quantity* $(\bar{u}/\bar{u}_* - 5.75 \log R)$ *as a function* $\log (\bar{u}_*/\nu)$ *for rough wooden channels of various shapes.*

Basic data from Bazin.

second place, the corrective term $\bar{\epsilon}\,\bar{u}/\bar{u}_*$ which was discarded in this discussion, is perhaps important in the case of the semicircular channel.

Table 7 has been prepared to show the effect of the shape of a channel on the mean velocity in these tests. The values given are the averages from the experiments of each series. In considering

these average values it is seen that the quantity $(\bar{u}/\bar{u}_*-5.75 \log R)$ varies but little in the channels of different shapes. If it is permissible to assume that the wooden material in every channel had the same equivalent sand roughness k_s, then the conclusion to be drawn is that the mean velocity of flow is practically independent of the shape of the channel; that is, in two channels of different shapes but of the same slope, the mean velocity of flow will be the same if the hydraulic radii are equal.

TABLE 7.—*Mean velocity of flow in wood channels of various shapes*

[Values of $Y=(\bar{u}/\bar{u}_*-5.75 \log R)$ for the channels listed in table 6.]

Series	Shape	Y
8	Rectangular	13.48
11	do	13.95
18	do	12.80
21	Trapezoidal I	12.59
22	Trapezoidal II	13.77
23	Triangular	13.15
26	Semicircular	13.86
Average		13.34

This conclusion will be in agreement with the theoretical formulation of the rational formulas for the mean velocity, provided that in these formulas the term $\bar{\epsilon}\ \bar{u}/\bar{u}_*$, expressing the effect of the secondary currents and of the free surface, is either negligible or is practically a constant for the shapes considered. Whether $\bar{\epsilon}\ \bar{u}/\bar{u}_*$ is negligible or a constant can be ascertained with certitude only from experiments where the surfaces of the walls have known hydrodynamic characteristics; that is, when a_{r0} is known previously.

5. DISTRIBUTION OF VELOCITY IN ROUGH CHANNELS

It was seen that the mean velocity of flow in the rough channels examined by Bazin is given with sufficient accuracy by the rational formula proposed. The reason for this must lie primarily in the assumption which is made regarding the distribution of velocity. Fortunately, Bazin also made measurements of velocity distribution. The velocity measurements which were made in large rectangular channels and at high velocities will be considered here. These are listed in table 8.

The velocity traverses best suited for examination are the following two: (1) A vertical traverse at the midchannel for the velocities in the neighborhood of the channel bottom; (2) a horizontal traverse about 3 to 5 cm below the water surface for the velocities in the neighborhood of the vertical walls. The examination that is desired consists in seeing how accurately the relation

$$\frac{u}{u_*}=8.5+5.75 \log \left(\frac{y}{k_s}\right), \tag{23}$$

which is the assumed relation for rough surfaces, is confirmed. Here u is the velocity at a distance y from the nearest point on the wall at which u_* is the shear velocity.

TABLE 8.—*Distribution of shear at the bottom of rough rectangular channels.*

S=distance from nearest corner.
h=depth of water.
B_0=width of channel.

Series 55, cement. $h/B_0=0.15$ $\bar{u}/\bar{u}_*=24.4$		Series 56, fine gravel. $h/B_0=0.28$ $\bar{u}/\bar{u}_*=14.7$		Series 57, coarse gravel. $h/B_0=0.21$ $\bar{u}/\bar{u}_*=11.5$	
$2S/B_0$	$\bar{u}_*/\bar{u}_*$	$2S/B_0$	$u_*/\bar{u}_*$	$2S/B_0$	$u_*/\bar{u}_*$
1.00	1.07	1.00	1.16	1.00	1.20
0.67	1.07	0.67	1.10	0.69	1.11
.34	0.98	.35	0.94	.37	0.93
.095	.87	.13	.88	.14	.82
.044	.89	.10	.82	.10	.76
		.05	.78	.06	.72

Series 59, plank. $h/B_0=0.13$ $\bar{u}/\bar{u}_*=21.4$		Series 61, plank.[a] $H/B_0=0.25$ $\bar{u}/\bar{u}_*=17.4$		Series 65, plank.[b] $h/B_0=0.21$ $\bar{u}/\bar{u}_*=11.5$	
$2S/B_0$	$u_*/\bar{u}_*$	$2S/B_0$	$u_*/\bar{u}_*$	$2S/B_0$	$u_*/\bar{u}_*$
1.00	1.00	1.00	1.14	1.00	1.15
0.80	1.07	0.80	1.12	0.80	1.12
.60	1.06	.39	0.98	.60	1.08
.40	1.04	.19	.92	.40	0.96
.20	0.92	.09	.85	.20	.86
.10	.88	.04	.79	.10	.78
.03	.78			.04	.63

[a] Widely spaced strips.
[b] Closely spaced strips.

Bazin gives the ratio $u/\bar{u}$ of the velocity at a point to the mean velocity in the channel for points in a horizontal section and in the midvertical section of the channel. An auxiliary computation is required to obtain the local shear velocity u_* which enters in eq 23. This may be obtained if the distribution of the shear velocity, that is the ratio $u_*/\bar{u}_*$, along the wall is known. The formula for this distribution is obtained by dividing each side of eq 23 by the quantity $(u/\bar{u})\ (\bar{u}/\bar{u}_*)$ which gives

$$\frac{\bar{u}_*}{u_*}=\frac{8.5+5.75\log\ (y/k_s)}{(u/\bar{u})(\bar{u}/\bar{u}_*)}. \tag{64}$$

By means of this relation the distribution of shear velocity in the various channels was determined. The results are given in tables 8 and 9. They show that the shear velocity, and therefore the shear, have minimum values at the corners. On the bottom of the channel the maximum shear occurs at the midpoint. On the vertical walls the maximum shear is found at a point slightly below the water surface, and its value is considerably less than the maximum shear on the bottom.

TABLE 9.—*Distribution of shear at the sides of rough rectangular channels*

S =distance from bottom corner
h =depth of water
B_0=width of channel

Series 55, cement. h/B_0= 0.15 $\bar{u}/\bar{u}_*$=24.4		Series 56, fine gravel. h/B_0= 0.21 $\bar{u}/\bar{u}_*$=14.7		Series 57, coarse gravel. h/B_0= 0.21 $\bar{u}/\bar{u}_*$=11.5	
S/h	$u_*/\bar{u}_*$	S/h	$u_*/\bar{u}_*$	S/h	$u_*/\bar{u}_*$
0.89	0.95	0.87	0.91	0.93	0.90
.60	.95	.62	.96	.67	.94
.39	.90	.38	.90	.41	.91
.17	.87	.13	.83	.15	.72
Series 59, plank. h/B_0= 0.13 $\bar{u}/\bar{u}_*$=21.4		**Series 61, plank.[a] h/B_0= 0.25 $\bar{u}/\bar{u}_*$=17.4**		**Series 65, plank.[b] h/B_0= 0.21 $\bar{u}/\bar{u}_*$=11.5**	
S/h	$u_*/\bar{u}_*$	S/h	$u_*/\bar{u}_*$	S/h	$u^*/\bar{u}_*$
0.88	0.97	0.92	0.92	0.95	0.75
.49	.93	.69	.96	.69	.91
.30	.92	.49	.93	.46	.87
.11	.78	.29	.91	.21	.75
		.09	.79	.09	.63

[a] Widely spaced strips.
[b] Closely spaced strips.

Now, the ratio u/u_* may be computed from the product

$$u/u_*=(u/\bar{u})(\bar{u}_*/u_*)(\bar{u}/\bar{u}_*),$$

where the first factor in the product is obtained directly from Bazin's data, the second from eq 64, and the third from Bazin's data using eq 61. The values of u/u_* thus obtained for various channels are plotted as ordinates against the quantity log (y/k_s) as abscissas in figures 10 and 11. The distribution of the points, both for the horizontal and the vertical velocity traverses, is given quite satisfactorily by the straight line representing eq 23.

6. MAXIMUM VELOCITY IN ROUGH RECTANGULAR CHANNELS

Bazin observed that, when the width of a channel is about five times or more the depth of water, the velocity distribution in the middle vertical is the same as in the verticals of a channel of infinite width. From measurements at the middle verticals in eight different channels he derived the velocity formula for wide channels in the form

$$\frac{u_{max}-u}{\sqrt{(hi)}}=20\left(\frac{z}{h}\right)^2, \tag{65}$$

where u is the velocity at a point distant z from the surface of the water and h is the depth. Introducing the shear velocity $u_*=\sqrt{(hig)}$, this law can be expressed in dimensionless form as

$$\frac{u_{max}}{u_*}-\frac{u}{u_*}=6.3\left(\frac{z}{h}\right)^2, \tag{66}$$

It can be shown, however, that this is an approximation to the equation

$$\frac{u_{max}-u}{u_*}=5.75 \log\left(\frac{h}{h-z}\right), \tag{67}$$

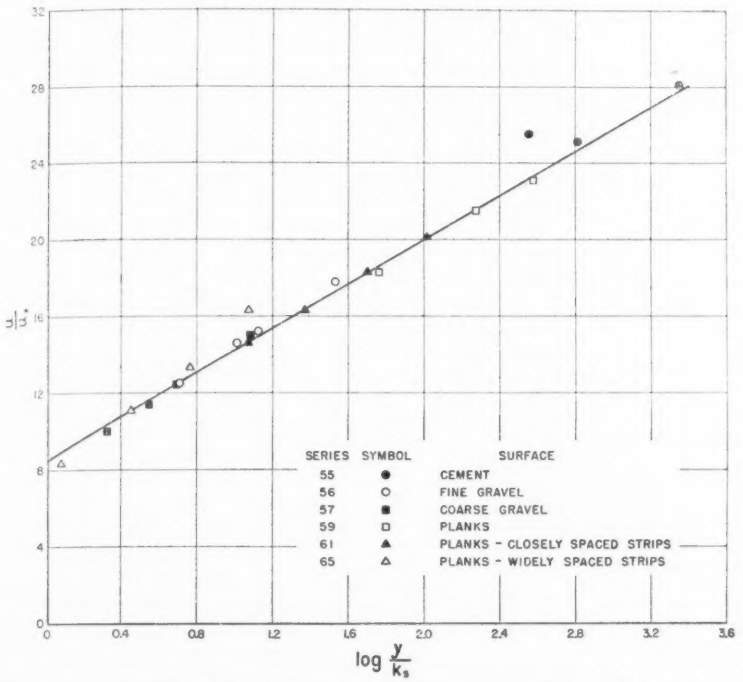

FIGURE 10.—*Velocity distribution for a vertical traverse at the center line of rough rectangular channels.*

The straight line represents eq 23. Basic data from Bazin.

which is deduced from the Kármán velocity law and is usually referred to as the velocity deficiency equation for the turbulent core. On the basis of eq 65, Bazin obtained the relation between the mean velocity and the maximum velocity in very wide channels in the form

$$u_{max}-\bar{u}=\frac{20}{3}\sqrt{(hi)}, \text{ or } u_{max}-\bar{u}=2.13u_*. \tag{68}$$

In channels of finite width, on the other hand, the difference between the maximum and the mean velocity is larger, and for such cases Bazin gives on empirical grounds the relation

$$u_{max}-\bar{u}=14\sqrt{(hi)}. \tag{69}$$

After introducing the shear velocity, eq 69 becomes

$$u_{max}-\bar{u}=4.5u_*. \tag{70}$$

Evidently, this formula for channels of finite width lacks generality in that it does not contain the width of channel. To correct this defect the following procedure may be used if we assume that the maximum velocity occurs at the surface. First, it is necessary to find a relation between $u_{*\max}$, the maximum shear velocity at the midpoint of the channel, and the mean shear. By definition

$$\frac{u_{*\max}}{\bar{u}_*}=1+\sigma, \tag{71}$$

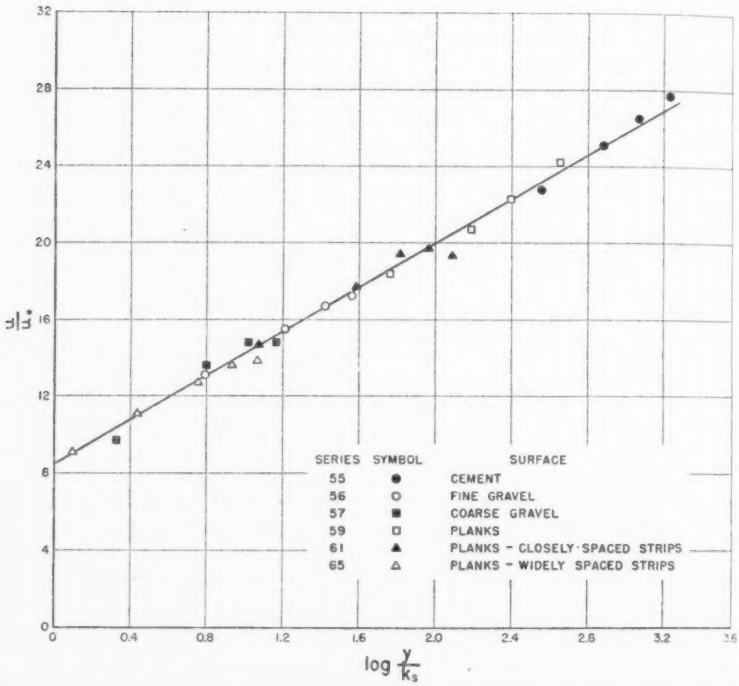

FIGURE 11.—*Velocity distribution for a horizontal traverse slightly below the water surface in rough rectangular channels.*

The straight line represents eq 23. Basic data from Bazin.

where σ is a function of the depth of the water, the size and roughness of the channel, and the velocity. It will be supposed that for small values of h/B_0, where h is the depth and B_0 is the bottom width,

$$\sigma=\alpha_1\frac{h}{B_0}\frac{\bar{u}_*}{\bar{u}}, \tag{72}$$

where α_1 is a constant which may be determined by using some of the results of Bazin. The data to be considered are given in table 8, and also in table 10, together with the value of α_1 computed on the basis of eq 72. It is seen that α_1 for different channels varies between 8.2

and 13.2. The mean of all the determinations, 11, is perhaps a good value to adopt, since σ is a small quantity.

The velocity law given by eq 23 and the resistance law given by eq 60 lead to

$$\frac{u_{max}}{u_{*max}}-\frac{\bar{u}}{\bar{u}_*}=2.25+5.75\log\left(\frac{h}{R}\right). \tag{73}$$

As $h/R=1+(2h/B_0)$, the logarithmic term in eq 73 can be expressed in the series form. Neglecting powers of h/B_0 higher than the second, eq 73 now becomes

$$\frac{u_{max}}{u_{*max}}-\frac{\bar{u}}{\bar{u}_*}=2.25+5\frac{h}{B_0}-5\left(\frac{h}{B_0}\right)^2, \tag{74}$$

or from eq 71

$$\frac{u_{max}-\bar{u}}{\bar{u}_*}=\left[2.25+5\frac{h}{B_0}-5\left(\frac{h}{B_0}\right)^2\right](1+\sigma)+\sigma\frac{\bar{u}}{\bar{u}_*}. \tag{75}$$

Inroducing σ from eq 72,

$$\frac{u_{max}-\bar{u}}{\bar{u}_*}=2.25\left[1+C_1\frac{h}{B_0}+C_2\left(\frac{h}{B_0}\right)^2\right], \tag{76}$$

where

$$C_1=7.1+11\frac{\bar{u}_*}{\bar{u}}, \text{ and}$$

$$C_2=24.5\frac{\bar{u}_*}{\bar{u}}-2.25.$$

This is a formula which gives the relation of the mean velocity to the maximum velocity in rough rectangular channels where the ratio of the depth of water to the width of channel does not exceed 1:5.

TABLE 10.—*Computation of the constant* α

Series	$\bar{u}_{*max}/\bar{u}_*=1+\sigma$	h/B_0	$\bar{u}/\bar{u}_*$	α
55	1.07	0.15	24.4	11.4
56	1.16	.21	14.7	11.2
57	1.20	.21	11.5	11.0
59	1.08	.13	21.4	13.2
61	1.14	.25	17.4	9.8
65	1.15	.21	11.5	8.2
Average				10.8

IV. MANNING'S FORMULA FOR ROUGH CHANNELS—POWER—LAW FORMULAS

Manning's formula for mean velocity of flow in rough channels is widely used in engineering practice, mainly because of its simple form. It will be of considerable interest, therefore, to examine this formula

in the light of the formulas which have been deduced in this paper. The formula as ordinarily written is

$$\bar{u}=\frac{1.476}{n}R^{1/6}\sqrt{(Ri)},$$

where $\bar{u}$ and R are expressed in terms of feet and seconds. Introducing the acceleration of gravity, $g=32.2$ ft/sec^2, the formula becomes

$$\bar{u}=\frac{0.263R^{1/6}}{n}\sqrt{(Rig)},$$

or, in the notation of this paper,

$$\frac{\bar{u}}{\bar{u}_*}=\frac{0.263}{n}R^{1/6}.$$

The quantity n is generally called "Manning's n," and is interpreted as a measure of roughness. Obviously, if the formula is to be dimensionally complete, the factor $0.263/n$ must have the dimensions $[L]^{-1/6}$. A dimensionless formula results when the equivalent sand roughness k_s is introduced as follows:

$$\frac{\bar{u}}{\bar{u}_*}=C(R/k_s)^{1/6}, \tag{77}$$

where

$$C=\frac{0.263k_s^{1/6}}{n},\ (k_s \text{ in ft}), \tag{78}$$

or

$$C=\frac{0.00863k_s^{1/6}}{n},\ (k_s \text{ in cm}). \tag{79}$$

Eq 77 is then a power law for the mean velocity of flow in the form

$$\frac{\bar{u}}{\bar{u}_*}=C\left(\frac{R}{k_s}\right)^m.$$

Lindquist [12] has determined the value of m, using the Kármán form of the law of resistance for sand-coated pipes and finds that 1/6 is a satisfactory value. A proper value of C may be obtained by a similar comparison. From eq 60 and 77,

$$C\left(\frac{R}{k_s}\right)^{1/6}=6.25+5.75\log\left(\frac{R}{k_s}\right).$$

Assigning to R/k_s the successive values 500, 250, 120, 60, 30 and 15, the corresponding values of C are found to be 7.72, 7.98, 8.20, 8.32, 8.36, and 8.30. Adopting for C the mean value 8.12, the dimensionless form of Manning's formula will be

$$\frac{\bar{u}}{\bar{u}_*}=8.12\left(\frac{R}{k_s}\right)^{1/6}. \tag{80}$$

The relation between the equivalent sand roughness and Manning's n, according to eq 79, now is

$$n=0.00106k_s^{1/6}, \tag{81}$$

where k_s is expressed in centimeters. This last equation, however, is not suitable for determining the equivalent sand roughness k_s when Manning's n for a channel is known.

The value of the exponent m of the power law formula is related to the roughness factor (R/k_s). This is readily seen from a study of the velocity distribution for flows near rough surfaces. The velocities for fully developed turbulence with sand-coated surfaces are shown in figure 12, where log (u/u_*) is plotted against log (y/k_s) in accordance with eq 23. The line thus obtained is decidedly curved, indicating

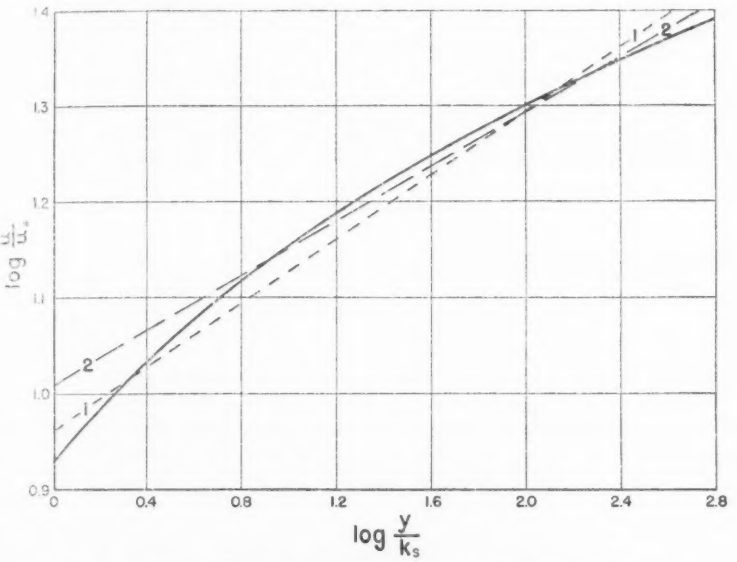

FIGURE 12.—*Log (u/u_*) as a function of log (y/k_s) for rough channels.*

The curve represents the rational formula given by eq 23. The line 1-1 represents the power-law formula with exponent $n=1/6$, which is equivalent to Manning's formula. The line 2-2 represents the power-law formula with exponent $n=1/7$.

that the value of m in a power law formula depends on R/k_s. If then it is desired to arrive at a mean flow formula of the power law type, it is necessary to select a straight line which will approximate the curve of eq 23 for large values of y/k_s. A practical range of R/k_s is from $R/k_s=15$ to $R/k_s=500$. With this range in mind, two straight lines are drawn in figure 12 as fairly good approximations to actual observations. The line 1–1 represents the velocity distribution

$$\frac{u}{u_*}=\frac{u}{\bar{u}_*}=9.15\left(\frac{y}{k_s}\right)^{1/6},$$

corresponding to eq 80. The line 2–2 which conforms to the relation

$$\frac{u}{u_*}=\frac{u}{\bar{u}_*}=10.2\left(\frac{y}{k_s}\right)^{1/7}, \tag{82}$$

is especially useful for reasons that will now be explained.

It was mentioned earlier in the paper that the velocity distribution near a rough surface consisting of imbedded sand grains is identical with that near a smooth surface when the velocity of flow is sufficiently small. It is to be expected that this will be true also for roughnesses represented by cement either plain or mixed with sand, by brick, and by ashlar masonry. The departure from smoothness begins when $\bar{u}_*k_s/\nu$ reaches the value 3.3, according to figure 3. This number, which is of considerable interest, may be referred to as the criterion of smoothness. It is seen from figure 3 that the criterion is given by the intersection of two lines, one representing the velocity distribution law for smooth pipes, and the other the corresponding law for rough pipes. This is an important result which must be involved also in the power law formulas of velocity distribution for smooth and for rough surfaces. The appropriate law for the smooth surface results from the Blasius law of resistance, [13] which, in the notation of this paper, is

$$\frac{\bar{u}}{\bar{u}_*}=6.99\left(\frac{r_0\bar{u}_*}{\nu}\right)^{1/7}.$$

This form implies the velocity distribution

$$\frac{u}{u_*}=\frac{u}{\bar{u}_*}=8.62\left(\frac{y\bar{u}_*}{\nu}\right)^{1/7}. \tag{83}$$

As the exponents of y in eq 82 and 83 have the same value, the desired criterion of smoothness can be obtained by equating to each other the right-hand members of these two equations. Then the elimination of y gives

$$\left(\frac{k_s\bar{u}_*}{\nu}\right)^{1/7}=1.18, \text{ or}$$

$$\left(\frac{k_s\bar{u}_*}{\nu}\right)=3.26,$$

which is in good agreement with the value 3.3 obtained from figure 3.

It is now clear that the power law with exponent $m=1/7$ is sufficiently accurate when $R\bar{u}_*/\nu$ or R/k_s, is large, and the law with exponent $m=1/6$ when $R\bar{u}_*/\nu$ or R/k_s is small. The formulas of the logarithmic type are free from this restriction. As a matter of possible interest, the results of Bazin's experiments on mean flow in channels will be given also in the form of power laws.

In rough channels the mean flow is given by

$$\frac{\bar{u}}{\bar{u}_*}=9.1\left(\frac{R}{k_s}\right)^{1/7}, \text{ or } \frac{\bar{u}}{\bar{u}_*}=8.12\left(\frac{R}{k_s}\right)^{1/6} \tag{84}$$

The formula holds for concrete, brick, and gravel when $k_s\bar{u}_*/\nu>3.3$ and for planed wood when $k_s\bar{u}_*/\nu>42.2$. Some values of k_s are given in table 3.

In smooth channels, or in rough channels with $k_s\bar{u}_*/\nu<3.3$,

$$\frac{\bar{u}}{\bar{u}_*}=7.6\left(\frac{R\bar{u}_*}{\nu}\right)^{1/7}. \tag{85}$$

In wooden channels with polished surfaces

$$\frac{\bar{u}}{\bar{u}_*}=6.8\left(\frac{R\bar{u}_*}{\nu}\right)^{1/7}. \tag{86}$$

In channels of planed wood, when $k_s\bar{u}_*/\nu<42.2$,

$$\frac{\bar{u}}{\bar{u}_*}=5.2\left(\frac{R\bar{u}_*}{\nu}\right)^{1/7}. \tag{87}$$

The numerical coefficients in these formulas result from the rational formula once the exponent $m=1/7$ is selected.

The author acknowledges gratefully the numerous suggestions and extensive editorial assistance in the preparation of this paper furnished by K. Hilding Beij of the Bureau's staff, and also helpful criticisms by Herbert N. Eaton.

V. REFERENCES

[1] J. Nikuradse, Gesetzmässigkeiten der turbulenten Strömung in glatten Rohren. Ver. Deut. Ing., Forschungsheft 356 (1932).
[2] J. Nikuradse, Strömungsgesetze in rauhen Rohren. Ver. Deut. Ing., Forschungsheft 361 (1933).
[3] B. A. Bakhmeteff, The Mechanics of Turbulent Flow. Princeton University Press (1936).
[4] H. Bazin, Recherches hydrauliques. Mém. divers savants, Sci. Math. et Phys., **19**, Paris (1865).
[5] L. Prandtl, *Ueber die ausgebildete Turbulenz.* 2d Int. Congress Applied Mechanics, Zurich, p. 62 (1926).
[6] Th. v. Kármán, Mechanische Aehnlichkeit und Turbulenz. Nachr. Ges. Wiss. Göttingen, Math.-phys. Klasse, 58 (1930).
[7] H. Schlichting, *Experimentelle Untersuchungen zum Rauhigkeitsproblem.* Ing.-Archiv, **7**, 1 (1936).
[8] J. Nikuradse, *Untersuchungen über turbulente Strömungen in nicht kreisformigen Rohren;* Ing.-Arch. **1**, 306 (1930).
[9] L. Prandtl, Zur turbulenten Strömung. Aero. Versuch. Göttingen, **4**, Lief., 18 (1932).
[10] Th. v. Kármán, *Über laminare und turbulente Reibung.* Z. ang. Math. Mech. **1**, 233 (1921).
[11] Th. v. Kármán, *Turbulence and skin friction.* J. Aeron. Sci. **1**, 1 (1934).
[12] E. Lindquist, On velocity formulas for open channels and pipes. Special report, Third World Power Conference, Stockholm (1933).
[13] H. Blasius, Das Aehnlichkeitsgesetz bei Reibungsvorgängen in Flüssigkeiten, Ver. Deut. Ing., Forschungsheft 131 (1913).

WASHINGTON, July 13, 1938.

U. S. Department of Commerce National Bureau of Standards

RESEARCH PAPER RP1152

Part of Journal of Research of the National Bureau of Standards, Volume 21, December 1938

OBSERVATIONS ON CRYSTALLINE SILICA IN CERTAIN DEVITRIFIED GLASSES

By Arthur Q. Tool and Herbert Insley

ABSTRACT

Samples of a borosilicate glass having a relatively high silica content were devitrified at temperatures in the range between 625° and 950° C by heat treatments of various durations. The crystals in these samples, and in certain other devitrified siliceous materials, were studied by examining their form and general appearance and by comparing the characteristics of their endothermic and exothermic effects which develop in heating and cooling curves, respectively, as a result of "rapid" inversions. In general agreement with the experience of other investigators, it was found that the devitrification developed approximately as follows: Heat treatments at points above 700° C caused cristobalite to appear within a month or less and in considerable quantities. Increasing the duration of treatment caused this material to disappear while tridymite developed coincidentally at a fairly rapid rate. When the duration of a treatment approached 6 months at temperatures near 800° but below 870° C, quartz in turn almost completely displaced the tridymite.

The results indicate that ultimately wedge-shaped twins always displace the earlier formed plates as the tridymite development is advanced by increasing the duration of treatment at any reasonable temperature below a point which may greatly exceed 1,000° C, and that coincidentally the inversion effects are shifted from the 150° to the 100° C range. The fact that the crystalline plates and practically all inversion effects at temperatures above the lower range were made to disappear almost completely by imposing relatively long heat treatments suggests the possibility that each of the two recognized inversion ranges of tridymite belongs to one of two low-temperature tridymite types, each of which possesses but one inversion range. It would also seem that the type inverting in the 100° C range was the stable form from 870° C to well above 1,000° C at least.

[Vol. 21

CONTENTS

	Page
I. Introduction	744
II. Observations on the general effects of devitrification in certain borosilicate glasses	745
III. Treatment and testing of glass	746
IV. Experimental results	747
Sample 1	747
Sample 2	749
Sample 3	751
Sample 4	752
Sample 5	753
Sample 6	754
Sample 7	756
Sample 8	757
Sample *A*	760
Sample *B*	761
Sample *C*	761

IV. Experimental results—Continued. Page
Sample *D* 762
Sample *E* 762
Sample *F* 762
Sample *G* 763
V. General coordination and possible significance of results 763
VI. Incidental discussion 766
VII. Summary 772

I. INTRODUCTION

Many glasses when heated in certain temperature ranges for any considerable time will show some evidences of devitrification, although the extent and nature of the crystal development and the temperatures at which the rate of this development is highest may vary greatly with the composition. If the "devitrification range" of a glass is defined as the temperature range within which noticeable evidences of devitrification develop during heat treatments of appropriate duration, this range will usually be found to lie entirely above the normal annealing range. That is, most of the glasses in common use devitrify very slowly or not at all during ordinary annealing treatments, and their devitrification proceeds at an appreciable rate only when the viscous deformability exceeds that required for such treatments. In other words, lowering the temperature into or below the annealing range so reduces the mobility of the glass that a sort of physical stability is imposed upon the more or less accidental molecular space pattern which developed during the melting process.

In order to gain certain desirable changes in the properties of glass it is occasionally necessary to depart from those compositions yielding this stability which prevents a massing of any of the constituents into possible crystal formations. Such departures may not only affect the rate of devitrification and its ultimate extent but may also change very greatly the breadth and position of the devitrification range. The composition is naturally the chief factor in determining the type of crystals developed, but often the treating temperature and the duration of the treatment are additional factors.

Certain borosilicate glasses present examples of this use of compositions which result in very desirable properties at the expense of stability; and some of these glasses devitrify rather extensively when heated for moderately long periods at any temperature in a rather wide range above 600° C. Temperature not only determines the necessary duration of a treatment required to produce obvious devitrification in a given glass, but it also limits the ultimate extent of the devitrification, and together with the duration of a treatment it often determines the type of crystals found in a devitrified material. For example, treatments lasting several days at 700° C will in many cases develop cristobalite as practically the only crystalline product in these glasses, while an equal period at 800° C will yield tridymite as the chief product. Actually cristobalite appears first in both cases, and if the treatments are prolonged sufficiently at these temperatures, quartz ultimately appears and becomes practically the only form present.

II. OBSERVATIONS ON THE GENERAL EFFECTS OF DEVITRIFICATION IN CERTAIN BOROSILICATE GLASSES

This paper [1] deals chiefly with results obtained by the devitrification of certain specimens of borosilicate glasses at temperatures between 650° and 950° C. The first visual evidences of devitrification in many of the samples were very fine surface cracks, which probably developed during the period of cooling from the treating to the observing temperature. The best examples of such surface cracks appeared in the polished surfaces of some samples that were being intermittently treated for a total duration of several days near 700° C in the course of some experiments designed to demonstrate that the refractive index and density reach stable values after not more than a few hours' treatment. The surface effects did not appear until long after the desired stability was reached, but extending the treatments beyond 3 or 4 days often developed them rapidly without causing detectable changes in the properties being studied. At this stage the glass was soon encased in a thin translucent film which usually could be ground and polished away leaving apparently only clear undeteriorated glass. Occasionally, however, in some of the more inhomogeneous samples certain cords developed a cloudiness throughout their extent during these treatments; and the surface deterioration often appeared first at the polished ends of some of these cords.

In samples such as rods made by the gathering process, these nonuniformities in the deterioration rate at different points were especially noticeable. That is, the devitrification often developed more rapidly and to a greater extent in one or two than in the rest of the concentric cylindrical shells that are often apparent in glass rods. Probably because of the occasional coolings required for close observation and test, these shells sometimes separated during a series of treatments at temperatures near and below 700° C. These separations usually occurred early in such a series and before any visible evidence of devitrification developed. Their detection occurred only after the samples were immersed in oil and then reheated. This caused the shells to be outlined by very thin carbon films or mirrors within the body of the rod. Later it was noted that in other rods, apparently similar inner shells often were outlined by films of crystals which developed rapidly and were among the first to appear. On some occasions these films even preceded those developing on the outer surface. Ultimately the devitrification spread throughout the mass of the glass, but these observations indicate that the distribution of the crystals probably never became uniform. Moreover, it is apparent that the rates of development of the various crystalline phases at any efficacious treating temperature were not likely to be the same in all parts of the glass at any time. Consequently, well-developed quartz crystals might often appear in certain shells while cristobalite was still predominant in others.

[1] The greater part of the results presented here were included in an informal progress report entitled "Some Observations on a Devitrified Glass," which was read at the Washington meeting of the American Ceramic Society on February 9, 1932.

Numerous preliminary tests showed that the devitrification of such glass rods developed much more rapidly at 800° C than at 700° C. After 3 days a rod would often be encased in a dense white crystal-rich shell approximately 0.5 mm thick. At this time some of the inner shells might remain practically clear, while others would be highly devitrified. When rods in this condition were cooled, the outer shell broke away from the remainder of the glass as 200° C was approached. This happened because of the relatively large contraction of cristobalite at its inversion point. A treatment of 14 days entirely devitrified such rods and the cristobalite was to a great extent transformed into tridymite. Cooling the samples under these conditions caused no breaking up of the glass, and its hardness and density seemed to be greater than originally. In one case, for example, the density of the original glass was 2.2407 and after 2 weeks of treatment it was 2.2684. Regardless of the possible density changes occurring at the treating temperature because of devitrification, the change [2] noted here should be attributed chiefly to the difference between the expansivity coefficients of the residual and original glasses and to the contraction of the tridymite at its inversion points.

III. TREATMENT AND TESTING OF GLASS

The samples used in the major portion of the tests described in section IV were cut from a glass rod [3] (approximately 1 cm in diameter) that was procured from the general glass supply of the National Bureau of Standards. Placed in a platinum boat, these samples were treated in an electric furnace, the treating temperatures in which were maintained within 10° C of the desired point. Extended treatments at temperatures above 700° C caused the glass to adhere more or less to the container, and above 800° C. considerable deformation developed.

The devitrification changes in the samples were followed closely by making frequent heating and cooling curve tests, and also by examination with a petrographic microscope. Occasionally X-ray patterns were procured and in certain cases expansivity measurements [4] were included in the tests. In the heating and cooling curve tests, the heating rate was usually somewhat in excess of 3° C per minute throughout the test range, but the cooling rate dropped from about 5° at 500° C to about 1° per minute at 90° C. The test sample, reduced to small granules by cracking, weighed 1.5 g and the neutral body required in differential pyrometry consisted of granular Al_2O_3. The difference in temperature between neutral body and sample and the temperature of the latter were determined at intervals ranging, respectively, from ¼ to 2 minutes and from 5 to 10 minutes by the usual combined differential and simple thermocouple system in which one wire was platinum and the other two were 90 Pt–10 Rh. The differences in temperature were indicated by galvanometer deflections. A 1° difference at 500° C corresponded to a double deflection of about 46 mm. A potentiometer was used in determining the sample temperature.

[2] This density increase at room temperature caused by devitrification is somewhat larger than the unrelated density change that (as shown in a previous paper, Trans. Soc. Glass Tech. **9**, 185 (1925)) can be produced in undevitrified glasses of the same type by reducing the annealing temperature from 700° to 450° C and that can be reversed by reannealing at 700° C.

[3] According to an analysis made by the Chemistry Division of this Bureau, the percentages of the chief constituents of this Pyrex glass were: SiO_2, 80.6; B_2O_3, 11.9; Al_2O_3, 2.2; Na_2O, 3.9; and K_2O, 0.07.

[4] *Expansion effects on the inversion of silica crystals in certain devitrified glasses*, A. Q. Tool and J. B. Saunders, J. Research NBS **21**, 773 (1938) RP1153.

IV. EXPERIMENTAL RESULTS

SAMPLE 1

This sample was treated for 25 days at 725° C. Contrary to earlier experiences described in the preceding section, the resulting devitrification was reasonably uniform throughout the glass. The treatment caused some deformation and the two pieces of rod comprising the sample adhered strongly at their points of contact. During the cooling after removal from the furnace the sample broke into several large pieces as it passed through the range of the high-low inversion of cristobalite.

All of the observed heat effects which could be ascribed to crystalline inversions in this sample fell in the temperature range (80° to 300° C) covered by the heating and cooling curves represented in figure 1. The curves *A* (heating) and *A'* (cooling) were obtained on the glass previous to any heat treatment. Neglecting the depression [5] just

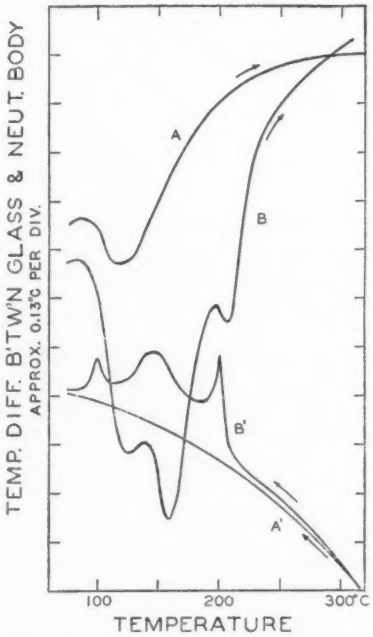

FIGURE 1.—*Curves showing inversion effects of tridymite and cristobalite in a devitrified glass.*

Curves *A* and *A'* are the heating and cooling curves obtained before devitrification. Curves *B* and *B'* are the corresponding curves obtained after devitrification. Curves were obtained by differential thermocouple method. On the average, observations were taken at intervals of 2° C or less. All observations are covered by the breadth of the curves in this and the following graphs with the exception of figure 5 where the individual points are shown. In figures 1 and 2 the heating curves for the undevitrified and particularly for the devitrified glass are greatly distorted in the range just above 100° C by an endothermic effect which is supposedly caused by the vaporization of moisture from the surfaces of the glass dust particles which remained after the samples were crushed and sifted for test.

above 100° C in *A*, they show no inversion or other heat effects. In the heating curve *B*, obtained on the devitrified glass, the depression is so unusually deep that a large part of it must be ascribed to endothermic effects resulting from crystalline inversions. The three minima falling near 120°, 160°, and 210° C indicate that a large por-

[5] This depression is unimportant in this connection because it is presumably a moisture effect and is usually observed in the first heating curve of any granular sample of undevitrified glass from which the fine dust formed by crushing has not been carefully sifted out. The similar endothermic effect in curve *B* has an even greater magnitude, which seems excessive even after a reasonable allowance is made for the probable contribution from a low-high inversion of the tridymite present. Probably the combined effect was excessive because the partial crystallization of the silica had so increased the alkali content of the residual glass that its dust absorbed more moisture than did that of the original glass. Whenever a crushed sample of the glass was re-treated at high temperatures the supposed moisture effects were markedly diminished in the later tests. This reduction may have been caused by a decrease in the free dust after the sintering.

tion of the depression was the result of three inversions. The cooling curve B′ shows three corresponding exothermic effects; but because of the test conditions and the nature of such inversions, the temperatures determined by the maxima in *B′* are somewhat lower than those determined by the minima in *B*.

The low-high inversions causing the minima near 120° and 160° C may be ascribed to tridymite, while the inversion causing a minimum near 210° C indicates the presence of a considerable quantity of cristobalite. It may seem that the cristobalite inversion should have been expected near this temperature because of the relatively low developing temperature.[6]

The heating curves for both the undevitrified glass [7] (curve *A*) and the devitrified sample (curve *B*) are extended in figure 2 to tempera-

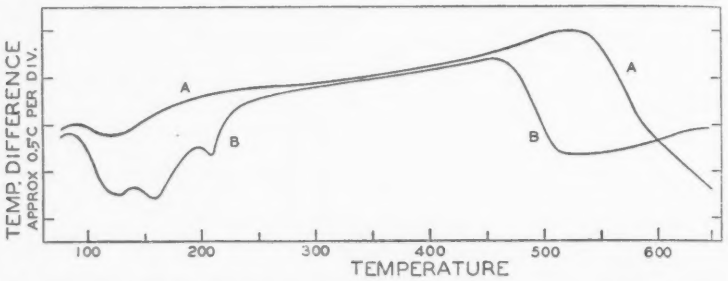

FIGURE 2.—*Heating curves extended into the softening range of the glasses.*

Curve *A* is the same as that in figure 1. The curves designated by *B* in the two figures were not obtained on the same portion of sample 1. This extension of the curves shows that devitrification shifts the normal endothermic effect of the glass to a lower-temperature range and that no appreciable quartz-inversion effect appeared in the tests of sample 1. As in figure 1, the ordinates were adjusted for temperatures near 300° C. The deviation at lower temperatures is indicated approximately in figure 8.

tures well above 573° C, which is the approximate inversion point of quartz.[8] Evidently the heat treatment imposed on this sample developed no appreciable quantity of quartz, since there is no evidence in either curve of a thermal effect corresponding to an inversion of this material. Both curves, however, do show the presence of endothermic effects in relatively high temperature ranges, and in the case of the undevitrified glass the range includes the quartz inversion point. These are the normal effects always found in temperature ranges just below those of softening whenever glasses are subjected to heating-curve tests.

Because of the silica depletion suffered by the glass phase from devitrification, the temperature range of this glass-effect in *B* is lowered considerably with respect to that in *A*. Judging from the beginning temperatures of the effects, this lowering amounts to approximately 60° C (approximately from 530° to 470° C), but the actual lowering is even greater because (as should be expected) the width of the range was materially reduced by the devitrification. The lowering of the range of the endothermic effect indicates an approximately equivalent lowering of the softening range, while the reduction in its width indicates a material increase in the rate of softening with

[6] Fenner, Am. J. Sci. **36**, 331 (1913), procured data which indicate that the low-high inversion point of this material decreases from 277° to 220° C as the developing temperature is reduced from 1,600° to 1,025° C, approximately.

[7] Heating curves extending to still higher temperatures have been obtained on similar glasses and were presented in a previous publication (J. Am. Ceram. Soc. **8**, 1 1925").

[8] Bates and Phelps. Phys. Rev. [2] **18**, 115 (1921).

temperature. These results explain the unexpectedly large deformation sometimes obtained by devitrification treatments. They also agree with the common experience that devitrifiable glass tubes or bulbs subjected to continued heating at temperatures approaching their softening ranges ultimately lose their normal ability to withstand pressure at those points where devitrification develops.

To the unaided eye this devitrified sample had a uniform milky appearance throughout the body of the glass, except that one cylindrical layer parallel to the axis of the rod was much more opaque than the remainder of the glass. This condition suggested not only a greater but also a more advanced degree of crystalline development in this layer. By microscopic examinations of powdered samples and of a thin section cut normal to the axis of the rod so that a ring of the more highly devitrified layer was included, tridymite occurring usually as plates, but sometimes as wedge-shaped twins, was readily identified in all parts of the sample. Because of the small size of these crystals and the presence of the enveloping glass their index of refraction could not be determined with precision, but it was near that given in the literature for tridymite. In the main body of the glass, cristobalite appeared to be predominant although it was identified with difficulty. It was found on examining the material with an oil-immersion objective that cristobalite occurred as very minute rounded pellets or as short rods in which no double refraction could be observed, and that its index of refraction was near the accepted value for cristobalite. In the layer showing the greatest devitrification, tridymite, associated with a few quartz crystals, was the major product. Some of these quartz crystals reached a length of 10 microns, their pyramidal faces were well developed, and the prismatic faces, although not so large, were also present.

An X-ray diffraction pattern obtained from a powdered sample contained faint lines of both cristobalite and tridymite. Those of the former were more intense, and this indicated a possible predominance of this form. None of the characteristic quartz lines could be detected, presumably because the amount of this material in the sample was very small.

SAMPLE 2

This sample of the glass rod was treated twice at 675° C, once for 18 days and again for 19 days. After the first treatment a marked devitrification such as developed in the first sample had appeared only in the outer shell to a depth of possibly 1 mm. This shell in peeling while cooling naturally caused the whole sample to shatter. The heat effects near 200° C in the heating and cooling curves obtained on this shell were very large and sharp with respective minima and maxima at 214° and 199° C. There were no indications of heat effects at lower temperatures.

After the second treatment, during which the shell and relatively clear core were kept separate, both parts appeared from a visual examination to have reached about the same stage of devitrification. The magnitude of the cristobalite heat effects by being almost equal for the two parts (although 25 percent smaller than that obtained on the shell after the first treatment) supported the visual observation. In the case of the core, the minimum and maximum of the effects were at 218° and 201° C, respectively, and these values were duplicated

within one degree after 2 weeks on another part of the sample. In the cooling curve (curve 1, fig. 3) very slight indications of heat effects were detectable near 160° and 100° C. In the case of the shell, the minima and maxima were at 216° and 200° C, respectively, and there was some indication of a moderately large and closely bound subordinate member on the low-temperature side of the endothermic effect. A similar and less pronounced indication was noted in only one of the heating curves obtained on the core.

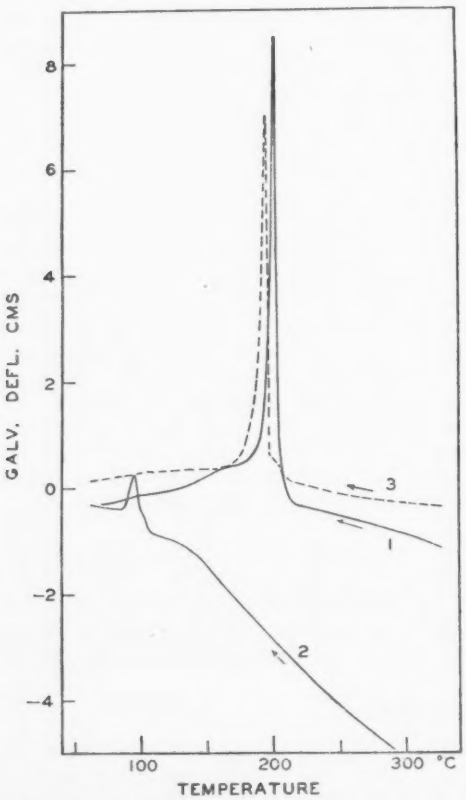

FIGURE 3.—*Cooling curves showing cristobalite and tridymite inversion effects.*

Curve 1 obtained on sample 2 after 37 days at 675° C. Large cristobalite effect followed by very small tridymite effect. Curve 2 obtained on same sample after six additional days at 800° C. Indefinite tridymite effect centering on 136° C followed by definite effect near 95° C. Curve 3 obtained on sample 3 after 33 days at 625° C. Ordinates are double galvanometer deflections.

By microscopic examination after the second treatment, the core was found to contain (in addition to the residual glass) both cristobalite and tridymite, although the former was by far the more abundant. Cristobalite occurred as long thread-like chains of minute beads with threads radiating in many places from a common center. The double refraction of these crystals was extremely weak and their index of refraction was normal for cristobalite, although determinations of the usual precision were impossible because the crystals were so small. The tridymite occurred as plates which were clearly visible only when on edge. They had the index of refraction and other optical properties (double refraction and character of elongation) of such tridymite crystals, and seemed to be concentrated in certain parts of the sample. No quartz could be found. An X-ray diffraction pattern showed clearly defined critobalite lines which were more intense than those found in sample 1. Besides these lines there were two extremely faint lines corresponding to the strongest lines in a pattern obtained on relatively pure tridymite.

The outside shell when examined microscopically after the second treatment was found to contain cristobalite, tridymite, and quartz. Cristobalite was the most abundant and occurred either as fine fibers often radiating from centers or as short rods arranged along branching fibers. The shape of the rods could be distinguished only with the oil-immersion objective, and while the index of refraction of the fibers

could not be determined accurately, it was 1.48 ±0.01. Tridymite, present only in small amounts, was in the form of hexagonal plates. The quartz occurred as aggregates of interlocking grains. In an X-ray pattern (see fig. 4 (A)) the cristobalite lines were well developed and only slightly fainter than those obtained from the reference material (cristobalite obtained by heating quartz at 1,500° C). Only two extremely faint lines corresponding to the strongest lines in the quartz pattern were present.

After these treatments and examinations, a portion of the core was further heat treated for 6 days at 800° C. The cooling curve then obtained (curve 2, fig. 3) indicated a very definite inversion effect with its peak or maximum at 95° C and its beginning at 108° C. The latter temperature was somewhat lower than that of the minimum of a relatively small and indefinite effect which appeared in the heating curve and may have been caused by moisture.[9] There was also an indication of a broad indefinite effect between 150° and 120° C in the cooling curve but no corresponding effect of even that weak character appeared in the heating curve. There was also no indication of cristobalite effects in any of the heating or cooling curves nor was there any definite evidence of quartz-inversion effects. In a superficial microscopic examination at this stage the tridymite crystals appeared to be plates turned on edge, but a more careful examination with an oil-immersion objective (1.9 mm) showed an abundance of wedge-shaped twins which may have been composed of parallel growths of plates. Skeleton twins and interpenetration twins were also common.

SAMPLE 3

A 33-day treatment at 625° C devitrified only a very thin outer layer of this sample of the rod, and the greater part of this layer cracked into small flakes during the cooling. These were easily peeled from the clear inner glass which was broken up by the bursting of the outer layer at 200° C. Heating and cooling curves obtained on this outer shell indicated no inversion effects except those of cristobalite. The respective minimum and maximum of the low-high and high-low effects were at 207° and 194° C, which are 7° and 5° lower than the corresponding temperatures obtained on sample 2 after the first of the 675° C treatments. This again is a result that seems to agree with the usually reported experience that reducing the devitrifying temperature lowers the inversion temperature. A slight hump on the high-temperature side of the base of the principal effect (curve 3, fig. 3) indicated the presence of a subordinate effect which in regard to temperature coincided rather more closely than its principal to the cristobalite effect shown in curve 1, figure 3. The smallness of this hump suggests that it was accidental, but its persistence in duplicate curves tended to remove this possibility. Moreover, such evidences of possible satellites were often noted in other samples (see fig. 5) on one side or the other of both cristobalite and tridymite effects. In almost every case such evidences indicated two or more

[9] It was found later that the definite endothermic effect which usually appears at, or near, 115° C and corresponds to the exothermic effect occurring below 100° C often did not develop to a detectable magnitude at any temperature. Apparently this happened when the tridymite crystals were only partially transformed from plates to wedge-shaped twins. In fact, the magnitude of the exothermic effect appears under such conditions to increase in a more or less erratic manner as the preheating temperature preceding cooling tests is increased. This suggests that the endothermic effect is distributed over a wide range of temperatures which may reach almost 400° C as long as the transformation to wedge-shaped twins is in its initial stages. This occasional nonappearance of a clear-cut endothermic effect in a restricted range just above 100° C is likely to be overlooked in the presence of the moisture-dust effect.

effects which were separated by intervals of several degrees. Possibly this separation may be explained by a difference in the devitrification development in different portions of the sample. At times it also appeared that increasing the period of treatment erased a satellite on the high-temperature side, and at others that it shifted a major effect into the approximate position previously occupied by a satellite. Such shifts were usually toward lower temperatures.

When a portion of the shell was examined microscopically under the highest power available, minute branching fibers with an average width of less than 1 micron could be distinguished. Their index of refraction could not be determined but they showed an extremely weak double refraction and a positive elongation, both of which are properties of cristobalite. An X-ray pattern (fig. 4 (B)) gave faint but characteristic cristobalite lines. No other lines were present.

SAMPLE 4

This sample when cooled after a treatment of 11 days at 800° C did not disintegrate, presumably because the cristobalite was almost completely converted to tridymite. The heating curve had a large endothermic effect with a minimum at 152° C, but there were no significant indications of cristobalite effects. There was also strong evidence of an effect near 120° C, but a definite inversion temperature was not indicated. The general appearance of the cooling curve indicated effects much like those shown in figure 6 for sample 8 after a 12-day treatment. The main exothermic effect with a maximum at 144° C was broad although quite pronounced. Its breadth was exaggerated by a small hump near 160° C. There was also a small and very definite effect with a maximum at 99° C. No indication of quartz or cristobalite was detected.

Only three phases (glass, tridymite, and quartz) were identified in this sample by the petrographic examination. Because of being mixed with so much tridymite the index of refraction of the glass could not be determined definitely.

Tridymite plates were scattered throughout the sample and probably constituted the most abundant crystalline phase. In general, the plates were small but were considerably larger than those in sample 1 treated at 725° C. A layer of plates larger than the average occurred in a thin cylindrical coaxial layer having a radius which was about two-thirds that of the rod. The characteristics of the plates were negative elongation on upturned plates, low double refraction, and refractive index slightly less than that of the surrounding glass. A reexamination of powdered and thin section specimens of this sample showed a few forms like the skeleton and interpenetration twins found in sample 2.

The quartz crystals occurred in two localities, on the surface of the rod, and in the cylindrical layer containing the larger tridymite plates. They were small (30 microns or less in the largest dimension) but larger than those in sample 1, and appeared microscopically as six-sided figures.[10] The determined index agreed with that of quartz, and the form was essentially that of a rhombohedron.

[10] Dana, System of Mineralogy, 184, figure 4. Sixth edition (1911).

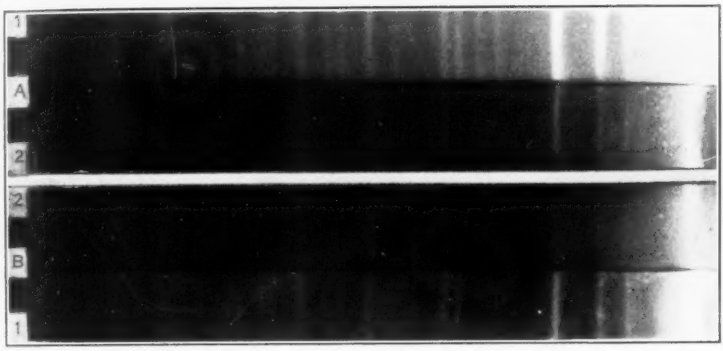

FIGURE 4.—*X-ray patterns of samples 2 and 3.*

A1 is a pattern of the reference material. *A2* is a pattern of sample 2 after 37 days at 675° C. The original photograph shows both cristobalite and quartz lines, although the latter do not appear in the reproduction. *B1* is a pattern of the reference material. *B2* is pattern of sample 3. Cristobalite a lines are relatively faint in the reproduction.

UNIV. OF MICH.

SAMPLE 5

This sample of the rod was treated 10 days at 750° C and on cooling broke up more completely near 200° C than sample 1. Moreover, the devitrification was concentrated to a somewhat greater extent near the outer surface. After separating the core from the thick and more densely devitrified shell as well as possible, heating and cooling curves were taken on them individually. For both portions these curves showed large definite inversion effects near 200° C, and much smaller ones near 150° C, while only the cooling curve indicated a very slight effect near 100° C. The minima for the largest effect fell at 214° for both shell and core and the maxima fell, respectively, at 201° and 203° C. These temperatures agree reasonably well with those obtained for the same inversion in sample 2 after its first treatment at 675° C. The minima for the intermediate effect were at 164° and 162° C and the maxima at 155° and 150° C, respectively, for core and shell.

After these tests the two parts of the sample were subjected to a second treatment of 12 days at 750° C and retested. Neither the heating nor the cooling curves now gave any clear indication of the cristobalite effect near 200° C and in general, the results for the shell and core were almost identical. The cooling curves corresponded roughly to those obtained on sample 8 after 18 days of treatment at 800° C (fig. 6), although the effect near 100° C for sample 5 was somewhat broader and consequently less definite. Furthermore, a comparison of the magnitude of this effect with that of the effect near 150° C in the two cases indicated that the low-temperature effect in sample 5 was relatively smaller than that in sample 8 after 18 days. This suggests that the devitrification of the latter sample was somewhat further advanced than that of the former. For the shell the minimum and maximum were, respectively, at 154° and 145° C for the upper tridymite effect, and the maximum for the lower effect was at 96° C; for the core the corresponding temperatures were 152°, 144°, and 96° C. The minima for the lower effect (if such existed) were submerged to some extent by the moisture effect, although in these particular tests this spurious effect could not have been large.

Finding from these tests that the two parts of the sample were in almost identical stages of devitrification, the core was again treated at 750° C for 10 days and the shell at 800° C for 6 days. In neither case did the heating and cooling tests indicate a definite effect near 150° C, although there was a trace of a small broad effect between 150° and 120° C in the cooling, and within a slightly higher range in the heating curves. Apparently the portion treated at the lower temperature now lagged somewhat in its stage of devitrification since it was noted that its tridymite effect (that obtained near 100° C by cooling) was broader and less pronounced than that of the portion treated at 800° C. In the latter case the effect indicated a stage between that represented by curve 2, figure 3, and that by the curve for sample 8 after 30 days of treatment at 800° C (fig. 6). The maxima for this effect now fell at 92° and 94° C, respectively, for shell and core. The tests were not carried into the quartz range.

107462—38——4

In comparing these samples under the microscope after the second treatment no perceptible difference was noted in the degree of crystalline development. The material of the shell, for example, consisted of tridymite, glass, and quartz. Quartz was present in small amounts, but the crystals were fairly large (20 to 30 microns in length) and had well developed faces. The tridymite crystals generally appeared as flat plates in random orientation, but these plates sometimes appeared to be so joined as to form the semblance of wedge-shaped twins.

SAMPLE 6

This sample was treated six successive times at 900° C and was tested after each treatment. The treating periods totaled 1, 2, 4, 9,

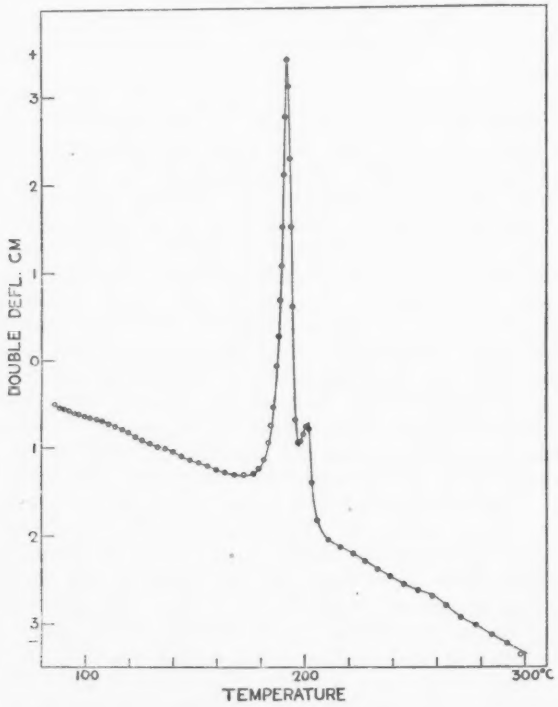

FIGURE 5.—*Cristobalite inversion effect with satellite.*

Cooling curve obtained on sample 6 after 1 day at 900° C.

51, and 251 days for the respective tests in the series. Heating and cooling curves after the first day of treatment (when the crystal concentration was much greater near the surface than in the core) showed large inversion effects with corresponding minima and maxima at 201° and 192° C, respectively. No indications of other effects were

present except that the cooling curve definitely indicated a satellite [11] on the high-temperature side of the high-low inversion effect (fig. 5). The heating curves gave no evidence of a corresponding satellite, but this may be explained on the assumption that a large heat effect closely followed by a much smaller one usually masks the latter completely. It will also be noted that the values obtained here for the temperatures of the cristobalite effects are lower than those obtained on either sample 2 or 3. It seems unlikely that these differences in position are a matter of uncertainty in the determinations because all duplicate tests indicated that the maximum deviation should not exceed ±2.0° C when the effects are (as they were in these cases) nearly the same in magnitude. Consequently, it no longer appears that increasing the developing temperature in this range (below 1,000° C) necessarily raises the cristobalite inversion point.

After the second day of treatment a cooling curve only was procured, and it indicated a still larger exothermic effect with a maximum at 195° C. There was no evidence of other effects except that the satellite, which apparently had also grown in magnitude, had practically merged with the main effect. It was estimated that the satellite, if it had not been followed by the larger effect, would have produced a maximum near 201° C.

The first cooling curve test after the fourth day of treatment yielded a maximum at 195° C and a definite hump on the high-temperature side still persisted; but a second test on another part of the sample gave an effect with a maximum at 198° C and a hump on the low-temperature side at approximately 192° C. These results point to the possibility that the sample contained two slightly different types of nonuniformly distributed crystalline materials. Both cooling tests indicated very small inversion effects with maxima between 160° and 150° C.

At the end of the ninth day of treatment the exothermic effect near 200° C was very small. There were, however, two additional effects, a small and rather indefinite one extending from 170° to 120° C with a maximum near 136° and a small but more definite one with a maximum near 88° C. Except that their magnitude was much smaller, these effects apparently corresponded closely to the devitrification stage represented by the curve in figure 6 for the 18-day treatment at 800° C. During this series of tests it was noted that treatments at temperatures well above 800° C never produced as large an upper tridymite effect (with a maximum near 150° C) as treatments of a proper duration at points below that temperature almost invariably produced.[12]

---

[11] Effects of this nature and the small effects which sometimes develop in the range between 170° and 190° C would presumably be ascribed to the influence of certain impurities by some investigators. R. Weil (Compt. rend. 183, 753; 1926), for example, believed that the position of the inversion ranges of portions of certain cristobalite crystals which he studied was affected by the presence of impurities in the form of the oxides of the alkali and some other metals.

[12] Possibly this difference in the effects produced can be ascribed to the relatively excessive fluxing effect of the residual glass on the transformation of the intermediate stages at the higher temperatures. That is, under such conditions certain intermediate stages may transform into final or succeeding stages at almost the same rate as they develop from preceding or initial stages. In consequence, no great concentrations of crystals of such intermediate types appear. The persistence of crystals in the preceding (or final) cristobalite stage will not be so seriously affected by this fluxing effect because a relatively large concentration of cristobalite must develop, presumably, before the silica depletion is sufficient to cause the fluxing effect to become excessive.

The treatment of 51 days caused the effect near 200° C to disappear and practically erased the one or more effects between 170° and 120° C, but it developed very considerably the low-temperature effect which had now become quite sharp and definite with its maximum at 82° and its beginning just above 90° C. Increasing the treatment to 251 days did not materially alter the results except that it broadened and possibly increased slightly the height of the effect occurring below 100° C. Two cooling curves obtained on the same charge gave 82° and 85° C as the temperature of the maximum of this effect. In both cases it began at 100° and ended at 75° C.

When examined petrographically at this stage tridymite appeared to be the only crystalline constituent. The crystals were moderately large and wedge-shaped and interpenetration twins were common.

Following these treatments at 900° C the sample was treated twice at 950° C, and the total treating periods for the two tests following these treatments were 4 and 52 days. In neither case was there an indication of any effect above 100° C in the cooling curves, and the effect below that point was practically unchanged except that the maximum was raised to 88° C.

SAMPLE 7

The results from the cooling tests after a 9-day treatment of this sample at 900° C were, in general, similar to those obtained on the previous sample after the same period of treatment. That is, the cristobalite effect was practically nonexistent, there was a small effect with a maximum near 88° C, and an indefinite effect of small magnitude extending from 170° to 120° C, which, in this case, appeared to have maxima at 156° and 127° C. Corresponding to these, the heating curve possessed a minimum at about 145° C. As before, the results of both the heating and cooling curve tests indicated that the intermediate effects near 150° C were relatively much smaller after treatments near and above 900° C than they were after treatments near and below 800° C. On the other hand, the greatest magnitude ultimately attained by the effect occurring below 100° C in the cooling curves was practically the same after long treatments in either range. Assuming that the original samples were identical, this would indicate that the ultimate quantity of the crystalline phase which could be developed did not vary materially with the treating temperature for this range between 750° and 950° C. Naturally, this is based on the assumption that the rate of transformation from tridymite to quartz below 800° C was relatively quite low as compared with that from cristobalite to tridymite.

After a total of 22 days at 900° C, a cooling curve on this sample indicated no effects above 100° C. The lower inversion effect of the cooling tridymite began at this point, was relatively broad, and reached a maximum at 86° C. At this stage the material was examined petrographically in both powder form and in thin section. Under crossed nicols it was found to be faintly birefringent, and areas with the same extinction position (representing presumably sections of single crystals) were elongate in shape with very poorly defined limits. More sharply defined needles were scattered through this cloudy material, and they, together with the less well defined areas, had a negative character of elongation. No wedge-shaped twins were positively

identified, but it was impossible to determine the exact character and shape of indefinite birefringent areas.

SAMPLE 8

The tests so far described were undertaken chiefly to ascertain the results of changing the treating temperature. These results indicate that for this glass 800° C is a favorable treating temperature for following the course of the changes in the "prompt" inversions from

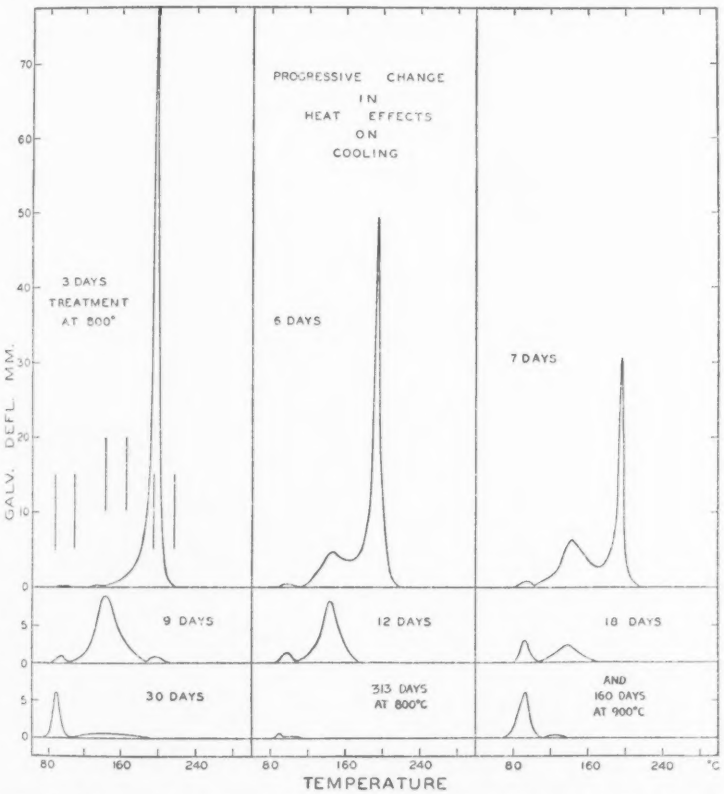

FIGURE 6.—*Progressive changes in exothermic effects as duration of devitrifying treatments increased.*

Only those portions of the cooling curves are presented which were affected by inversions occurring below 300° C. The procedure followed in procuring these portions was equivalent to the subtraction of curve *A'* from curve *B'* in figure 1. The three pairs of vertical lines in the first section show the approximate limits of the ranges within which the maxima of the three major effects usually occurred. At its greatest magnitude the intermediate heat effect is relatively indefinite since it covers a rather broad range in comparison to its height. It will be noted that the last effect to appear after the treatment at 900° C is about 50 percent greater than the similar effect after 30 days at 800° C, although the heights are almost the same in terms of double galvanometer deflections.

the time of the development of cristobalite until quartz becomes predominant. In consequence, this sample was subjected to a series of treatments at that temperature, and cooling curves (and occasionally heating curves) were obtained when the duration of the series of heat treatments totaled 3, 6, 9, 12, 18, 30, 55, 116, and 313 days. The

cooling curves obtained after the first six and the ninth total periods are represented in figure 6, and the indicated inversion temperatures are presented in table 1. These are difference curves procured by

TABLE 1.—*Cristobalite and tridymite inversions* [a]

Sample No.	Test No.[b]	Treatment		Portion of sample tested	Indicated inversion temperature						Approximate relative height of cristobalite high-low effects	Approximate range of cristobalite effects	
					Cristobalite		Tridymite						
							First		Second				
		Temperature[c]	Total duration[d]		Low-high	High-low	Low-high	High-low	Low-high	High-low		Low-high	High-low
		°C	Days		°C	°C	°C	°C	°C	°C		°C	°C
1	1	725	25	All	210	201	160	145	[e] 120	101	2½	175 to 200	220 to 175
					209	201	160	146	120	106	2½	175 to 200	220 to 175
2	1	675	18	Shell	214	199	------	------	------	------	12	180 to 250	217 to 180
				Shell	216	200	------	------	------	------	9	175 to 250	217 to 180
	2	675	37	Core	218	201	------	------	------	------	8	185 to 260	220 to 180
				do	217	201	------	------	------	------	9	182 to 260	220 to 175
				Shell	------	------	------	------	(g)	92	------	------	------
	3	800	6	Core	------	------	------	------	(g)	95	------	------	------
				do	------	------	------	------	(g)	95	------	------	------
3	1	625	33	Shell	207	194	------	------	------	------	7	182 to 240	212 to 170
4	1	800	11	All	------	------	152	144	[e] 120	99	------	------	------
	1	750	10	Shell	214	201	162	150	------	------	6	180 to 260	216 to 170
				Core	214	204	164	155	------	------	6	180 to 260	216 to 170
				do	214	202	164	155	------	------	6	180 to 250	220 to 170
5	2	750	22	Shell	------	------	154	145	110	96	------	------	------
				Core	------	------	152	144	110	96	------	------	------
	3	750	10	Core	------	------	------	------	(g)	94	------	------	------
	3'	800	6	Shell	------	------	------	------	105	92	------	------	------
	1	900	1	All	201	192	------	------	------	------	5	170 to 228	212 to 174
	2	900	2	do	(g)	195	------	------	------	------	7½	(g)	212 to 170
	3	900	4	do	(g)	195	------	------	------	------	2	(g)	210 to 175
					(g)	198	------	------	------	------	3½	(g)	212 to 174
	4	900	9	do	------	------	(g)	136	(g)	88	------	------	------
6	5	900	51	do	------	------	------	------	(g)	82	------	------	------
	6	900	251	do	------	------	------	------	109	82	------	------	------
					------	------	------	------	(g)	85	------	------	------
	7	950	4	do	------	------	------	------	(g)	88	------	------	------
	8	950	52	do	------	------	------	------	109	88	------	------	------
7	1	900	9	All	------	------	145	127	------	------	------	------	------
	2	900	22	do	------	------	------	------	(g)	86	------	------	------
	1	800	3	Shell	208	198	------	------	------	------	7	180 to 225	214 to 170
				Core	207	198	------	------	------	------	3	186 to 225	214 to 182
	2	800	6	All	201	194	155	145	------	------	4	175 to 225	213 to 174
	3	800	9	do	------	------	155	143	------	------	------	------	------
	4	800	12	do	------	------	152	143	------	------	------	------	------
	5	800	18	do	------	------	(g)	140	(g)	94	------	------	------
8	6	800	30	do	------	------	------	------	107	89	------	------	------
	7	800	55	do	------	------	------	------	107	90	------	------	------
	8	800	116	do	------	------	------	------	109	91	------	------	------
	[f] 9	800	313	do	------	------	------	------	------	------	------	------	------
	[f] 10	900	4	do	------	------	------	------	------	------	------	------	------
	11	900	59	do	------	------	------	------	114	92	------	------	------
	12	900	160	do	------	------	------	------	114	93	------	------	------
8'	1	800	7	All	205	197	155	143	------	------	2½	184 to 228	214 to 180

[a] The more prominently indicated inversion points found in the glass samples devitrified during this investigation.

[b] Test numbers also signify the number of treatments received previous to test.

[c] After each treatment the samples were cooled to room temperature and prepared for test. Consequently, a sample was whole only during the first treatment.

[d] The duration of the second and all additional treatments at a given temperature is shown by the difference between the corresponding value tabulated and the next preceding for the same sample portion.

[e] Values uncertain because of added effect from vaporization of moisture.

[f] Quartz effects only were appreciable.

[g] Necessary heating curves not procured or effects were of doubtful origin.

subtracting the ordinates of curves obtained on the untreated glass from those obtained on the treated glass; that is, a similar curve would have been obtained if the differences between the ordinates of curves A' and B', figure 1, had been plotted. The curve for a treatment of

7 days was obtained on the companion sample of No. 8 and was introduced to fill a rather wide gap in the stages of the disappearance of the cristobalite effect. A close correspondence between these companions cannot be expected, however, because one was broken up after 3 days, while the other was whole during its entire treatment (7 days).

During the treatment of these samples quartz probably began to develop quite soon, but the quantity did not become sufficient to produce significant effects in either heating or cooling curves until approximately the 30th day of treatment. After 55 days the quartz-inversion effect (fig. 7) had nearly reached the magnitude of the cristobalite effect after 6 days and its height was approximately doubled and tripled after 116 and 313 days, respectively. For these last three periods of treatment its maxima in the cooling curves were between 570° and 572° C and its minima in the heating curves fell between 574° and 576° C.

The tridymite effect which has its maximum between 100° and 80° C still maintained approximately the same magnitude after the 55th day that it had had after the 30th, but after the 116th day it had noticeably diminished and after the 313th day it had almost disappeared, as shown in figure 6. There were no observable exothermic effects in the range between 120° and 300° C after any of the last three treating periods.

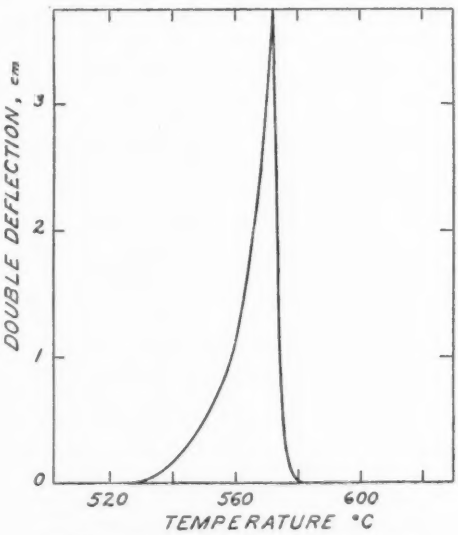

FIGURE 7.—*Quartz-inversion effect in cooling curve.*

At this stage (55th day of treatment) the effect in sample 8 was increasing very rapidly with duration of treatment, and after the treatment totaled 313 days at 800° C the height was tripled.

Examination with the microscope after the 3d day disclosed two fairly well defined internal zones of devitrification. The inner one centered on the axis of the cylinder and the outer one was about midway between the axis and periphery. The remainder of the glass was fairly clear. Most of the crystalline material occurred as minute rounded and faintly birefringent particles which were arranged along lines radiating from centers. This material which occurred in the characteristic habit of cristobalite was so interspersed with glass that no good determinations of the refractive index could be made, but it was in the vicinity of 1.48. A small amount of material was crystallized in roughly quadrangular forms. Possibly this was tridymite but no optical properties distinguishing it from cristobalite could be obtained.

After the 30th day, quartz was an abundant crystalline constituent, and although its crystal habit was difficult to determine, it apparently occurred as rhombohedrons with perhaps additional short prismatic faces. Tridymite was also relatively abundant and a number of wedge-shaped twins (more frequently the skeleton wedge-shaped forms) were present, but individual plates could also be observed. No cristobalite was identified. After the 313th day no tridymite or cristobalite was found and the crystalline material appeared to be entirely quartz.

Since quartz after these treatments was the only crystalline phase present in sufficient quantity to register very appreciable effects in heating and cooling curves or to be observed petrographically, the sample was now treated at 900° C in order to change this phase ultimately to tridymite, and curves were procured after the 4th, 59th, and 160th day of treatment. The first of these reduced the quartz effect very materially but developed no effects in the range between 60° and 470° C. The normal residual glass effect appeared at this upper limit (see curve *B*, fig. 2) and would have masked any small effect that might have been present between that point and 520° C. After the 59th day the quartz effect had almost completely disappeared and a rather broad but pronounced effect beginning at 116° and ending at 80° C appeared in the cooling curves. The maximum of this effect was near 92° C and the magnitude was almost as great as that shown in figure 6 for the 30th day of treatment at 800° C. No other effect appeared below 300° C except possibly a very small one near 120° C. After 160 days the effect between 116° and 80° C was somewhat larger and more definite than it was after the 59th day and its maximum fell at 93° C. The corresponding minimum in the heating curve was at 114° C. It is possible that the failure of the cristobalite and intermediate tridymite effects to appear can again be ascribed to the excessive fluxing effect of the residual glass.

As shown by microscopic examination, the sample after the last treatment consisted of tridymite, glass, and quartz. The latter was present in very small amounts, its grains showed no crystalline faces, and were much corroded, and embayed (possibly owing to the inversion to tridymite). The tridymite was present very largely as wedge-shaped twins which often showed additional polysynthetic twinning. The composition planes of the polysynthetic twins were apparently parallel to the edges of the wedge-shaped crystals.

The following results were obtained on materials that contained crystalline silica and were gathered from various sources. These results are presented for comparison with those described above.

SAMPLE *A*

This sample, developed from fused quartz under unknown conditions, contained a high percentage of cristobalite. Being fine powder, it was not so suitable for heating and cooling curve tests as the previously described samples containing much lower percentages of cristobalite. Only about 0.4 g could be used as a charge without increasing the volume that was ordinarily employed and considered rather large for satisfactory work. Nevertheless, the cristobalite inversion effects (curves *A* and *A'*, fig. 8) were relatively large with a maximum on cooling at 218° and a minimum at 260° C on heating. Both effects started at approximately 240° C. These large effects were respectively followed and preceded by small trailing effects which

by some might be ascribed to final and initial adjustments which accompany the real inversion. No other indications of inversions were noted.

No tridymite could be seen when the material was examined petrographically. The cristobalite occurred as minute rounded pellet which showed a very low but easily perceptible birefringence. In many cristobalite samples this birefringence is not discernible.

SAMPLE *B*

This was reported to be a powdered flint treated 5 hours at 1,400° C, and its inversion effects were broad and about one-fourth as large as those of sample *A*. The effect on heating appeared to be more definite than that on cooling, because the latter seemingly approached the doublet form with the larger member on the low-temperature side. (Curves *B* and *B'*, fig. 8.) In the heating curve the inversion effect began at approximately 210° and the curve minimum fell at 236° C. In the cooling curve it began at 260° and the curve maximum fell at 222° C with a possible secondary near 240° C. No other inversion effects were observed below the quartz range.

As shown by microscopic examination, the sample was composed largely of quartz but also contained some cristobalite which was usually on the borders of the quartz grains. The refractive index of the cristobalite was just above 1.48 but there was no perceptible birefringence. No tridymite could be identified.

SAMPLE *C*

This sample was reported to be silicic acid treated for 5 hours at 1,400°. It had an even finer texture than samples *A* and *B*. The inversion effects were again broad and had about the same magnitude as those of sample B, but unlike them, the effect on cooling was more definite than that on heating because the latter had a slight likeness of a doublet. On heating, the effect began at about 160°, the curve minimum was reached at 220° C, and

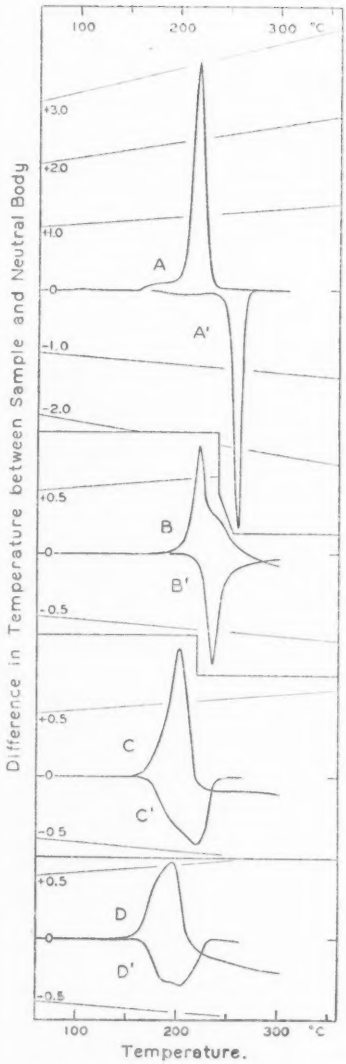

FIGURE 8.—*Inversion effects of various silica materials.*

The original ordinates, double galvanometer deflections, have been transformed into the corresponding temperature differences in order to give a suggestion of the relative temperature change developed during the inversions. The indicated temperature differences are approximately correct at 100° and 300° C where the necessary factors for the transformations were experimentally determined. Elsewhere, the ordinates are also within the probable error of the determinations, although the relation between the deflections and temperature differences is nonlinear, particularly in this range. The primed and unprimed letters indicate heating and cooling curves respectively. Only those portions of the curves near the effects are shown. Some of the curves show peculiarities which possibly signify an approaching transformation of cristobalite into tridymite.

there was a marked change in curvature as 200° C was approached. On cooling, the effect began just above 220° and the curve maximum fell at 203° C. (Curves *C* and *C'*, fig. 8.) No other effects were noted below 300° C.

Under the microscope the material seemed to be composed of grains containing clouds of very minute inclusions which obscured observation. The refractive index of these inclusions or particles was much less than 1.48. With the exception of these low-index particles the material seemed to be structureless, and it showed no perceptible birefringence where they were absent.

SAMPLE *D*

This sample was reported to have been developed from silicic acid by a treatment at 1,300° C for an unspecified time. Its texture was similar to that of sample C, but its inversion effects (especially on cooling) were even broader with blunted tops and bottoms instead of the usual sharp-pointed maxima and minima. In fact, their character was such that they appeared to be made up of two almost equal effects which might have been separated by approximately 20° C. (Curves *D* and *D'*, fig. 8.) If the effects were doublets the smaller members were on the low-temperature side. In the heating curve the effect began just above 160°, reached its greatest depth at about 204°, and ended slightly above 230° C. In the cooling curve the effect began at about 230°, reached its maximum at approximately 195°, and ended just below 150° C. The general appearance of curve *D* approached that of the curve obtained by the second test on sample 6 after the 4th day of treatment. The effect in *D*, however, was smaller, was in a slightly lower temperature range, and gave less indication of a secondary peak.

The appearance of this sample under the microscope was very similar to that of sample *C*, especially with regard to the character of the inclusions.

SAMPLE *E*

This was part of a nodule caused by the devitrification of a soda-lime glass, and it contained tridymite plates and considerable cristobalite. The concentration of the crystalline phases in the glass was very low. Consequently, only very small effects were obtainable in the heating and cooling curves. These consisted of minima in the heating curve at 166°, 198°, and 214° C, and corresponding maxima in the cooling curve at 150°, 184°, and 209° C. Tests on another charge changed the position of these points in no case by more than 2° C. In addition to these three possible effects, no others were indicated in the range from 80° to 300° C.

SAMPLE *F*

This was another specimen of a devitrified glass, but it came from a different and unknown source. It contained chiefly thin flat tridymite plates, but each plate was composed of a number of small tridymite individuals. (See reproduction of photomicrograph, fig. 9.) A large number of these individuals were twinned, either polysynthetically, in a wedgelike form, or both. The outer form of the wedge twins was never displayed. The concentration of the crystalline phase in the glass was again very low and the possible heat effects detected near 115° and 166° and near 150° and 80° C in the heating and cooling curves, respectively, were extremely small. A second cooling test confirmed the 150° and 80° C points.

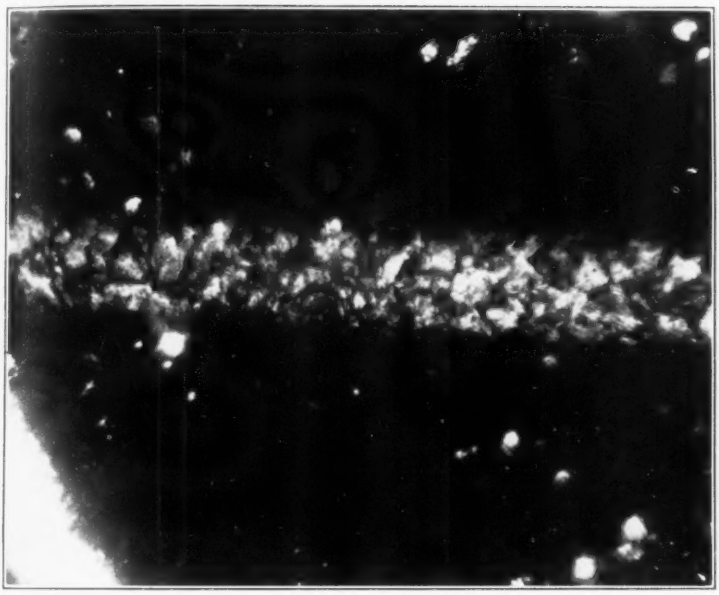

FIGURE 9.—*Reproduction of photomicrograph of tridymite crystal.*

Crossed nicols, magnification × 80. With unpolarized light this crystal from sample *F* appeared as a homogeneous plate.

UNIV. OF MICH.

SAMPLE G

This was a portion of a silica brick transformed by use and was composed largely of tridymite in the form of wedge-shaped twins. The nature of the sample was excellent for making heating and cooling-curve tests and there was only one significant effect in each curve. The effect in the cooling curve was relatively large and definite. It began at 110° and ended at 84° C. The curve maximum was at 98° C, while the minimum in the heating curve developed at 124° C. The effect in the heating curve was, however, not so clear-cut and there was some indication that it was followed by a small effect which extended to about 160° C. These temperatures for the maxima and minima are among the highest obtained for the low-temperature tridymite inversion effect during this investigation.

V. GENERAL COORDINATION AND POSSIBLE SIGNIFICANCE OF RESULTS

From the experience obtained in performing the various series of tests described above as representative examples of more numerous tests, it seems that the results may be coordinated as follows:

1. Borosilicate glasses with a relatively high silica content when held at treating temperatures near or within a considerable range below 800° C first develop a cristobalite that yields inversion effects at points usually somewhat above 200° C, both when heated and cooled. If the duration of the treatment is increased after these effects reach their maximum, they then decrease with a rapidity that depends on the treating temperature.

2. Increasing the duration of the heat treatments at these temperatures causes the temperatures, indicated respectively by the maxima and minima of the cristobalite effects in the cooling and heating curves, to shift over intervals which are greater than the probable error of determination.

3. Even before the cristobalite effects begin to decrease, tridymite plates appear in considerable numbers and small heat effects make their first appearance in the range between 190° and 150° C. Curve 1, figure 3, gives some evidence of one of the smaller effects noted in this range.

4. If the duration of the heat treatments is further increased, the number of plates multiplies rapidly and the small heat effects continue to grow into large but broad and rather indefinite tridymite effects, the maxima and minima of which usually indicate high-low and low-high inversion temperatures between 140° and 160° C. In the meantime, the cristobalite effects dwindle toward insignificance.

5. As these effects near 150° C approach their maximum size, wedge-shaped tridymite twins also begin to develop rapidly and a high-low inversion with its maximum usually somewhat below 100° C coincidently appears. The corresponding low-high effect with its minimum at a somewhat higher temperature is not so easily and consistently located, possibly because some remnants of the moisture effects supposedly associated with glass dust interfere, although such dust should now be eliminated by sintering. For another possibility see footnote 9.

6. Continuing the treatments causes the effects near 150° C to diminish steadily and also greatly reduces the number of plates, so

that they are few in comparison to the number of twins. At the same time, the tridymite effects near 100° C grow rather rapidly and become so definite in comparison to the earlier and much larger effects near 150° C that the maximum of the high-low and the minimum of the low-high inversion can be easily and precisely located. These effects and also those near 150° C shift their positions, however, as the duration of the treatments increases.

7. Still longer treatments practically eliminate the tridymite plates and almost completely destroy the tridymite effects near 150° C, leaving only very small seeming remnants of those effects near 120° and 140° C in the heating and cooling curves, respectively. (The 30-day treatment brought sample 8 into about the middle of this stage.) There are, therefore, at this stage no really manifest inversion effects from these points to approximately 570° C where the quartz effects have now begun to grow with relative rapidity. As the duration of the treatments of various samples is increased, the indicated temperatures of the effects near 150° and also of those near 100° C shift about over ranges which appear to be appreciably larger than should be expected in view of the estimated probable uncertainties of determination. The relatively narrow and consequently definite tridymite effects in the cooling curves occur almost wholly within the range between 80° and 100° C with maxima near 90° C, while the almost equally definite effects in the heating curves have minima near 110° C.

8. Greatly increasing the duration of the heat treatments almost completely removes the inversion effects near 100° C and transforms practically all of the wedge-shaped tridymite twins into quartz. The quartz now yields very large and definite effects with maxima and minima (in cooling and heating curves, respectively) between 570° and 576° C.

9. Subjecting the material at this stage to heat treatments at 900° C (as in the case of sample 8, for example) transforms the quartz with relative rapidity into wedge-shaped tridymite twins. The inversion effects near 100° C reappear with a greater magnitude than they had previously since they are now at least equally high (or deep) and definitely broader. The cristobalite effects apparently fail to develop, and the intermediate tridymite effects near 150° C, if present, are too small to be located with any certainty. (See paragraph 11 also.)

10. Treatments of the original glass at 900° C develop cristobalite as the first crystalline product, and its large definite inversion effects occur at temperatures which are at least as low as those usually obtained after treatments at lower temperatures.

11. The development of tridymite from the cristobalite at 900° C follows much the same course as in the case of treatments at 800° C or lower, except that the inversion effects near 150° C are usually no more than barely detectable. Consequently, they never reach that prominence they attain as a result of the treatments at lower temperatures. This difference in prominence must, it would seem, be ascribed to an increase at the higher temperature in the transformation rates of intermediate crystalline forms. Possibly the increased fluxing power of the residual glass at 900° C causes these rate increases almost entirely.

12. The effects near 100° C, when the original glass is treated at 900° C, ultimately become larger than those appearing at any time as a result of treatments at 800° C and lower; presumably, because tridymite becomes the end product as soon as 870° C is exceeded. (Also see paragraph 9 and fig. 6.) That is, the absence of any loss to quartz must more than offset the possible increase in the solubility of crystalline silica in the residual glass as the temperature rises through this range near 870° C.

13. Occasionally the inversion effects occurring near 200° C when the cristobalite is developed at 900° C or lower appear to be double or to cover unusually broad ranges (see last column, table 1). Similar conditions often develop in the tridymite inversion effects near 150° C and possibly to some extent in the more definite effects near 100° C.

It seems further that the significance of these results may be outlined as follows:

1. The results indicate that the shift in prominence from the tridymite effects near 150° C to those near 100° C is related to the change in crystal habit from plates to wedge-shaped twins. In any case it would seem that the "high-temperature" inversion effects are predominant only when the tridymite is "young" and that they are displaced in this role by the "low-temperature" effects as the material becomes more "mature" (age being measured in terms of the duration of treatment and the effectiveness of the other conditions which enter into the development of the crystals).

2. The above suggests that there are at least two kinds of low tridymite which may exist normally at room temperatures, and that each kind has a rapid inversion range in which it transforms to a high form that has no rapid inversions at still higher temperatures. That is, it appears that these high forms can only change into other high forms through very sluggish transformations which probably occur in most cases at relatively high temperatures as compared with those of the rapid inversions. Verification of this would signify that a sample is a composite of two kinds of tridymite whenever (as is usual) both of the established inversions occur in it.

3. If two such low temperature types of tridymite exist, the high form of the one inverting near 150° C is not an end product at treating temperatures between 870° and 950° C. Whether it is such a product at higher temperatures may also be doubtful.

4. If both inversions, the one near 150° and that near 100° C, should ever be found in what appeared to be a single crystal, such a crystal, as well as the whole sample, would then assume the character of a composite. In that case it would seem that similar conditions might appear in cristobalite or in any other silica crystals if a sluggish transformation has caused only a partial change from one form of crystal to another. Presumably, such composites would resemble some of those crystals in which multiple inversions were investigated optically by Weil. (See footnote 11, page 755.)

5. If close association of two or more forms within the same crystal should influence the inversion characteristics of the forms, it may well be that this influence in the suspected composites would be the cause of minor shifts such as were observed in the indicated inversion temperatures of many of the samples and which were often larger than the estimated errors in locating such temperatures. This possibility, if

established, would also explain some of the wide divergences in the published results of other investigators for the various inversion points. Moreover, it should throw some light on the cause of the rather large temperature hysteresis effects which have been observed in certain cases.

VI. INCIDENTAL DISCUSSION

Certain of the variations in the results outlined in the preceding sections can no doubt be ascribed to two kinds of inhomogeneity in the original material. The most evident of these inhomogeneous conditions caused the devitrification to develop and to proceed through the mass in more or less well defined waves. These waves corresponded to the crystal growths in various portions of the glass sample that were differentiated by the cords or striae contained.

The other condition, which also can be considered as a type of inhomogeneity, existed at the air-glass surfaces, and it usually so hastened devitrification there that it was often more potent than any of the cords in causing an early wave of crystal development. Moreover, this potency was greatly enhanced and other complications were probably introduced whenever the glass was broken up. Such a multiplication of the air-glass surface was introduced whenever a sample was prepared by crushing, and the sample was always crushed for the test made between the first and second of a series of treatments. As a result of the fragmentation the second treatment probably developed a relatively pronounced second wave of newly developed crystals which followed the older crystals of the first treatment through the various transformations. When the lag was sufficient, these waves probably remained more or less distinct even after the development of tridymite and the practical disappearance of cristobalite.

To a certain degree these inhomogeneities and the resultant waves of devitrification may account for the lack of definiteness in some of the heat effects of inversion and for the occasional satellites of these effects. This possibility requires, however, that the indicated inversion temperatures (of cristobalite, for instance) changed either with the duration of treatment at the temperatures employed or with the position of the crystals in the sample. In either case it would seem that the changes in the indicated inversion temperatures were caused by the same factors that influence growth and sluggish transformations of the crystals. Consequently, it appears logical to suppose that both inversion temperature and temperature hysteresis change as the crystals grow or proceed through some sluggish transformation which is induced by continued heat treatment. Since the treating temperatures were all below the cristobalite stability range in the heat treatments described above, the cristobalite-tridymite transformation was probably proceeding continuously from the appearance and until the disappearance of the cristobalite. At such treating temperatures there is, however, the possibility that other transformations or changes also develop and affect the inversion characteristics. These changes may or may not have something of the nature of those postulated by Sosman[13] in seeking an explanation for the apparent decrease in the inversion temperatures of cristobalite as its formation temperature is reduced.

[13] The Properties of Silica. Page 259 (1927).

According to Sosman's hypothesis the proportion of oxygen atoms in undefined or haphazard positions increases and decreases with the treating (or formation) temperature of the cristobalite. It is then further postulated that the inversion temperature of the crystals increases and decreases with the relative number of such haphazard atoms. To account for still other peculiarities of the crystals he also postulates that there is a certain type of heterogeneity in the structure of cristobalite. Granting these highly speculative possibilities, it seems reasonable to suspect that the relative number of haphazard atoms and the degree of heterogeneity are to some extent not only coordinate but related; or at least, that they are both affected by practically the same factors. At any rate uniformity in the proportion of such atoms should scarcely be expected to exist throughout even a single crystal. Any lack of such uniformity would of itself constitute heterogeneity. Moreover, it would seem that a heterogeneity of whatever nature should affect the inversion temperature.

If changes developed in the proportion of haphazard atoms by treatments at high temperatures are to affect the inversion temperatures, it is necessary that the proportion established by any treatment shall be susceptible to preservation during a cooling of the material to the inversion points or lower. Presumably this preservation is accomplished by cooling through the higher temperature ranges at comparatively rapid rates. As a matter of fact, however, a drastic rate does not seem to be required anywhere except possibly within the cristobalite range. This, at least, is the impression one would gain from certain of Fenner's experiments. The susceptibility to preservation suggests that the changes in the relative number of haphazard atoms must have the nature of sluggish transformations.

It is possible therefore that at most temperatures the duration of treatment is, along with the temperature of treatment, a real factor in determining the inversion temperature of the resulting cristobalite crystals. It may as a matter of fact be the more important of the two. At least, it may easily be so when the treating temperature is below the cristobalite range, and, especially, when the condition of the material is such that all transformations develop slowly. That is, the duration of treatment required to develop any condition may be considered as always depending on the nature of the silica material as well as on its temperature. In view of the nature of the material and of the treatments employed, this consideration of the experimental factors which may determine the inversion temperature of cristobalite suggests that the variations observed in the cristobalite inversions—as noted at various points in the previous discussion—are to be expected since undoubtedly the age of the crystals even in a single sample varied greatly. It also corroborates the belief that the obvious inhomogeneities of the original glass and the consequent waves of devitrification may account for the satellites of some of the inversion effects. Furthermore, variations in the effective duration of treatment becomes a possible explanation for the occasional marked deviations in Fenner's [14] data from the general trend on which the dependence of the inversion temperature on that of formation or treatment is chiefly based.

[14] Am. J. Sci. 36, 369 (1913). Some of the inversion temperatures deviate from 5° to 30° C from any curve which might reasonably represent the supposed dependence of these temperatures on those of formation or treatment.

In the formation and treatment of crystals there are two possibilities which should be considered. That is, the crystals may be formed and treated at the same or at different temperatures. In the latter case, treatment will produce a change in the relative number of haphazard atoms if the hypothesis fits the actual conditions. In the other case, however, it may be a matter of uncertainty as to whether or not any such change takes place. The proportion of such atoms and the degree of heterogeneity corresponding to the formation temperature may be attained immediately at incipiency and remain unchanged throughout the growth and any further treatment of the crystal at that temperature. As a matter of conjecture, it seems more likely, however, that the conditions in incipient crystals are, regardless of the temperature, much the same unless there are two or more kinds of high cristobalite. Even in that event the incipient form would usually be the same if the usual course of the transformations of crystalline silica when heated is followed. Conceding that the incipient condition is independent of the formation temperature and that the condition corresponding to that temperature is gradually developed, it follows that the mass of crystals in a sample at any intermediate stage of devitrification would represent a wide range of development stages and a correspondingly broad interval of inversion temperatures. This may account for the rather peculiar effects of samples *B*, *C*, and *D* in figure 8.

At this point it should be noted that Greig [15] has reported that the heat effects of inversion in certain samples containing cristobalite did not develop sharply at any temperature when the samples were cooled through the inversion range. He also observed that many of the small crystals, when mechanically attached to the surrounding glass, failed to invert and consequently reached atmospheric temperatures in the high form. Other investigators have also reported observations which suggest that in certain cases the cristobalite inversions may be very lethargic and that such persistence of the high form is not uncommon. There is no doubt some similarity between such observations and certain of those presented in the previous pages. These observations include the broad inversion ranges, the variability of the indicated inversion temperature, marked temperature hysteresis, and certain peculiarities noted in the cristobalite crystals when the samples were examined microscopically.

If the chief cause of the lethargy of inversion lies in the surrounding or attached materials, it seems obvious that the incipient or very small crystals would be most affected, especially since they should be the least capable of breaking away from those materials. Such a crystal with its attached material may be considered as a very heterogeneous structure. A structure of this sort may well be incapable of inverting sharply at a definite temperature and any delay in the inversion should depend on the degree of heterogeneity. Since there is in the usual artificially prepared sample a great variety of crystal sizes and degrees of attachment it follows that the inversion ranges should be correspondingly broad. Obviously, the attached material may be crystalline as well as glassy. Consequently, this broadening of inversion effects should appear whenever any transformation is only partially accomplished. To what extent the restraint exerted by

[15] J. W. Greig, Am. J. Sci. **13**, 40 (1927); J. Am. Chem. Soc. **54**, 2846 (1932).

attached materials on the inversions of small newly developed crystals is mechanical (as has been suggested) is, however, a matter for further consideration.

Whatever may be the nature of the changes which cause the variations in the inversion effects of cristobalite, it seems possible that the development of tridymite also includes changes of a somewhat similar nature since it was noted that within certain limited temperature ranges its inversion points also appeared to be variable especially when either the treating temperature or period was changed. At least two distinct tridymite inversion ranges [16] are known to exist and these may be considered as centering on 150° and 100° C when both the low-high and high-low effects are considered. As stated before, the sequential appearance (and disappearance) of the effects in these two ranges as the treatments were prolonged leads to the possibility that each inversion range belongs to a more or less distinct crystalline type that has but two modifications (high and low). Of these types only the one inverting in the vicinity of 100° C appears to possess a high modification that is stable in the lower part of the tridymite stability range. Whether the high modifications of the possible two or more tridymite types divide this range between them will require further study since it may well be that the types appearing first and inverting at the higher temperatures are never really stable.

The indication that there is a sluggish development of one tridymite from another suggests that this transformation is the source of the suspected heterogeneity of tridymite crystals. Even so, this heterogeneity might have something of the nature of that postulated by Sosman, or of that suggested as a possibility by Fenner who, in discussing the significance of his results took cognizance of Smits' theory of allotropy in this connection. This idea that sluggish transformations cause the possible tridymite heterogeneity suggests further, however, that any apparently individual tridymite crystal can be considered as a more or less heterogeneous and intimate mixture of decadent (or disappearing) and of immature (or developing) forms which are unevenly distributed throughout not only the sample as a whole but also the seemingly individual component crystals.

Certain parts of any such mixed crystal should, however, be relatively homogeneous in their structure and, consequently, each of these probably resembles rather closely in its structure some one of the various crystalline forms entering into the series of transformations undergone by the crystal as a whole. In that case these fragmentary parts are presumably cemented together by layers of less homogeneous material which has its disorganized and more or less haphazard structure because all of the various intermediate stages of the transformations are represented in it. Granting the existence of such composites, it seems probable that the very different but more homogeneous parts exert through this cementing layer considerable mutual influence upon their individual inversion characteristics.

On the basis of this mixture hypothesis several relatively large inversion effects appearing at points separated by more or less definite temperature intervals would show the presence of a corresponding

[16] It will be presumed for the time being that only these two particular inversion ranges are involved although some indication of another range centering on approximately 130° C was noted. Furthermore, another possible range near 440° C has been reported by Travers and Goloubinoff, Rev. Metall. **23**, 27, 100 (1926).

number of distinct and rather persistent crystalline types within the sample. Minor variations in the inversion temperatures from their normal position and any exceptional broadening of the inversion effects would be the result of a mutual influence exerted by the various types within composite crystals upon the inversions of the components. Presumably, such variations would be relatively insignificant in the case of very predominant types having large inversion effects, but these variations should increase if the predominance of the type waned as the sluggish transformations continued. Masses of heterogeneous crystals containing a predominant type with inversions that are easily influenced should, if all possible degrees of heterogeneity are present, yield rather broad inversion effects such as those of tridymite near 150° C. Exceptional broadening of this nature may cause the observable effects to be unexpectedly small in many cases, just as they were in sample F for instance.

Experience with these materials would seem to show that crystals or crystalline fragments must ordinarily be exceedingly small before their inversions can be materially modified by the nature of their surroundings. Conceivably, however, the inversions in composites made up of closely associated fragments may be materially modified by such association if the fragments do not too greatly exceed the submicroscopic scale. Moreover, the fragments may not possess the uniformity of structure suggested by their appearance, and elements of the transition layers may permeate them to some extent. The crystal shown in figure 9 may be an example of such a composite of tridymites if elements of the plate structure still persist in the transition layers or elsewhere. Presumably, the transformation in this crystal is well advanced, but in the beginning of a transformation the heterogeneous regions may be even less obvious and constitute little more than a film over the surface of an otherwise perfectly uniform crystal.

Composites with modified inversions may also be formed during the cristobalite to tridymite transformation. Possibly the crystals studied by Weil [17] possessed a heterogeneity of this kind, although he ascribed the observed differences in the inversion ranges of various portions of the same crystal to the effect of impurities. With respect to such effects from impurities, the results of Fenner's experiments [18] testing this point indicate that cristobalite from specially purified silica yields practically the same variations in its inversions as does cristobalite from melts containing considerable impurities or flux.

Obviously, the development of the original crystalline growth and of any other later sluggish transformations must proceed much more slowly in relatively pure than in fluxed silica unless the developing temperatures for the purer material are considerably higher. Consequently, Weil [19] in subjecting cristobalite crystals to alkali vapors probably caused regions of incipient tridymite to develop very rapidly but only on the crystal surfaces during that time when the temperature was below the cristobalite range. Such an action would presumably cause inversion changes very similar to those he observed. This suggests that he may have been dealing with composite crystals of the type discussed in the previous paragraphs rather than with a direct effect of impurities on the inversions as he assumed.

[17] Compt. rend. **180**, 1949 (1925).
[18] Am. J. Sci. **36**, 363, 370 (1913).
[19] Compt. rend. **183**, 754 (1925).

Moreover, it is clear that the acid treatments which he later applied [20] should in most cases have removed any such possible incipient tridymite from the surfaces of the vapor-treated cristobalite almost as easily as it would have removed the film of alkaline glass that was undoubtedly formed. On account of this action the temperature of the inversion effects should have been raised by the acid treatment. In general, however, the acid treatment would fail in this action if the tridymite was more deeply embedded, since any dissolving away of probable surface films of glass would normally release only those tridymite structures that were on the surfaces. The development of deeply embedded structures would presumably require relatively long treatments and fairly large original cristobalite crystals. Some of the natural crystals with two inversion ranges did not entirely lose their apparent inhomogeneity on being subjected to the acid treatment. Weil ascribed this resistance to the protection which a deeper permeation into the crystals afforded the impurities. He apparently did not consider the possibility that the displaced inversion effects were caused by deep seated regions of incipient tridymite although some of the natural crystals which showed peculiar inversion effects were classed as tridymite.

If by any chance impurities were not the direct cause of the nonuniformity of the inversions of these crystals, it would seem that the evidences of heterogeneity actually observed by Weil in what appeared to be relatively large individual crystals may be as well explained on the basis of composite crystals of cristobalite and small portions of incipient tridymite as on any other. Moreover, some of the crystals classed as tridymite may have contained small amounts of decadent cristobalite especially when their inversion effects extended to comparatively high temperatures. Granting that the crystals were composites of this nature, his results on various individual crystals then give a much clearer insight as to the possible structure of such composites than can be obtained by experiments which require large masses of crystals where the masses presumably include crystals representing all of the possible stages of heterogeneity which may be developed during a sluggish transformation.

The possibility that decadent fragments of cristobalite may enter into tridymite composites and influence the tridymite inversions makes the comparative indefiniteness and the relatively great breadth of the inversion effect of that tridymite form which appears to be intermediate between cristobalite and the final tridymite even less surprising. This follows, since some of the crystals of this intermediate form will invert at abnormally low temperatures because of the influence of the final tridymite, while other crystals will invert at abnormally high temperatures because of the influence of cristobalite. Finally, there is a possibility that the medium which transmits this influence is made up of the silica threads or chains which are discussed by Sosman. That is, such chains may in many cases lead through several incomplete structures at certain times during the progress of any transformation or series of transformations. Between the more regular incomplete structures, the threads at such times would presumably be tangled and twisted to a considerable extent. This condition in some cases may actually approach that of silica glass. If

[20] Compt. rend. **183**, 753 (1926).

this picture is at all representative of actual conditions, it seems, when the persistence usually ascribed to these chains is considered, that it may be along them that a structure exerts the influence which resists or abets the inversion of its intimate neighbors.

VII. SUMMARY

1. A series of tests was made for the purpose of following in a devitrifying glass the well-known series of transformations—noncrystalline silica to cristobalite to tridymite to quartz—which can be completed under proper conditions at temperatures below 870° C.

2. The devitrifying or transformation temperatures employed ranged from 625° to 950° C, and the material treated consisted of a high silica borosilicate glass which devitrified readily at temperatures above 750° C.

3. The devitrification products were studied mainly by procuring heating and cooling curves which extended over the whole temperature range of possible rapid inversions. In addition, several of the samples were examined microscopically, and X-ray patterns were also obtained occasionally.

4. The apparent inversion points of the cristobalite ranged from 201° to 218° on heating and from 192° to 240° C on cooling (as indicated by the endothermic and exothermic effects).

5. The points similarly determined for the upper inversion of the tridymite ranged from 145° to 164° C and from 127° to 155° C on heating and cooling, respectively.

6. The corresponding points for the lower inversion of the tridymite fell between 107° and 120° C and between 82° and 101° C.

7. The inversion points of the quartz as determined in the same way, all fell between 570° and 576° C, and it appears that much of this spread can be ascribed to the relatively high rates (approximately 5° C per minute) employed in this range both on heating and cooling.

8. The inversion effects in the upper tridymite range were usually broad and often indefinite, and they always disappeared completely soon after the effects in the lower inversion range of this material reached their maximum.

9. Ordinarily, the interval between the complete disappearance of the effects in the upper inversion range and the full growth of those in the lower range seemed to coincide with the period within which the tridymite crystals were transformed from plates to wedge-shaped twins.

10. Certain speculations concerning the significance of this coincidence and of the results, in general, are incorporated in a discussion.

WASHINGTON, July 1, 1938.

U. S. Department of Commerce National Bureau of Standards

RESEARCH PAPER RP1153

Part of Journal of Research of the National Bureau of Standards, Volume 21, December 1938

EXPANSION EFFECTS ON THE INVERSION OF SILICA CRYSTALS IN CERTAIN DEVITRIFIED GLASSES

By Arthur Q. Tool and James B. Saunders

ABSTRACT

Expansion curves are presented which show the inversion effects of the cristobalite, tridymite, and quartz that were present in a devitrified glass having a relatively high silica content. These results agree in practically every respect with results presented in a previous paper and obtained from the exothermic and endothermic effects caused by the same inversions. So far as these results are concerned with the nature and changes of inversion effects as tridymite is developed from cristobalite and quartz, they substantiate the previously suggested possibility that there are, at room temperature, two or more forms of tridymite instead of only one, such as has been generally supposed.

CONTENTS

	Page
I. Introduction	773
II. Method of measurement	773
III. Results	774
IV. Conclusion	778

I. INTRODUCTION

This paper deals with the expansion effects of inversion that were obtained on some of the samples discussed in a previous paper [1] which describes the heat effects and some of the characteristics of the crystals found in a devitrified borosilicate glass having a rather high silica content. A description of the glass and fuller details concerning the heat treatments causing its devitrification will be found in that paper. The chief purpose in obtaining the expansion data was the corroboration of previously described results on the progressive changes in the characteristics of the "prompt" inversions of the crystalline silica. Such changes developed as the various "sluggish" inversions proceeded at treating temperatures in the devitrification range of the glass.

II. METHOD OF MEASUREMENT

The expansion data (curves) were procured by means of the interferometric method and the apparatus used has been described in previous papers.[2] The test samples (three pyramidal spacers) were, however, smaller (height, 1.78 mm in one case) than usual because

[1] Tool and Insley, J. Research NBS **21**, 743 (1938) RP 1152.
[2] Tool, Lloyd, and Merritt, BS J. Research **5**, 627 (1930) RP219. Saunders and Tool, BS J. Research **11**, 799 (1933) RP626.

larger pyramids were likely to crack during the repeated heatings and coolings required by a series of tests. While this reduction in size made long series of tests possible, it materially reduced the precision of the measurements. This, however, was no great handicap because the expansion changes sought were ordinarily much greater than the uncertainties in the measurements. Moreover, the principal purpose was to locate inversion effects rather than to make highly accurate expansivity measurements. In general, the samples used in the expansion tests were subjected to devitrifying treatments along with the corresponding samples employed in the heating and cooling curve tests mentioned above.

Interferometer plates of fused silica were used in these expansivity tests because the measurements were carried to relatively high temperatures. Moreover, it is evident that it would be impossible to match the extremely variable expansion of the devitrified samples with that of any material suitable for these plates, although such a match is very desirable in making precise measurements on ordinary samples. The lower interferometer plate on which the pyramidal spacers rested was so constructed and calibrated that it served as an interferometric thermometer for determining the temperature changes during the required heatings and coolings of the tests. When properly assembled and mounted in the test furnace and observed through a viewing apparatus, the interferometer system presented two sets of fringes separated by a narrow boundary. As the temperature changed, the passage of the fringes over fiducial points was recorded by means of a chronograph. From the resulting record the changes in temperature and the corresponding length changes per unit length of sample could be computed. The number of fringes was such that the approximate average expansivity over small temperature intervals never exceeding 5° C could easily be determined for each such interval in the range between room temperature and 625° C. In obtaining these data the heating rate throughout this range was approximately 3.5° C per minute.

III. RESULTS

The results presented here include only those obtained on two samples. These were numbered 1 and 8 in the first paper cited above. The first of these samples was treated for 25 days at 725° C, after which it contained considerable cristobalite and tridymite plates, some wedge-shaped twins of the latter, and a little quartz. A petrographic examination of this sample indicated that cristobalite was probably the main crystalline phase, but the thermal expansion, as well as the other heat effects, seem to show that tridymite was predominant. That is, the expansion curve (*B*, fig. 1) indicates relatively large inversion effects near 115° and 150° C in the tridymite range and another effect between 500° and 600° C. The latter is probably a composite of "rapid" expansion effects in both the residual glass and the quartz.

Curves *A* and *A'* in figure 1 are the expansion and contraction (heating and cooling) curves of the original glass, and a comparison of these curves with curve *B* shows the great change in the expansion caused by the devitrification. The change in the trend of curve *A* near 450° C indicates that the unannealed glass was entering the

annealing range at these temperatures, and the rise starting near 550° C corresponds to the beginning of the rapid-expansion range of this glass previous to its devitrification. The drop to curve *A'* at 625° C, where the glass was held for a time preparatory to starting the cooling curve, corresponds not to a deformation but to an actual though relatively slow contraction which this type of glass invariably shows in this temperature range. In the case of the devitrified sample, the beginning of the rapid-expansion range of the residual glass (curve *B*) apparently occurs near 470° C, and there is some indication of a quartz effect just above 550° C. The rate of deformation of the devitrified glass was appreciable at temperatures above 600° C and this shows that devitrification greatly softened the material.

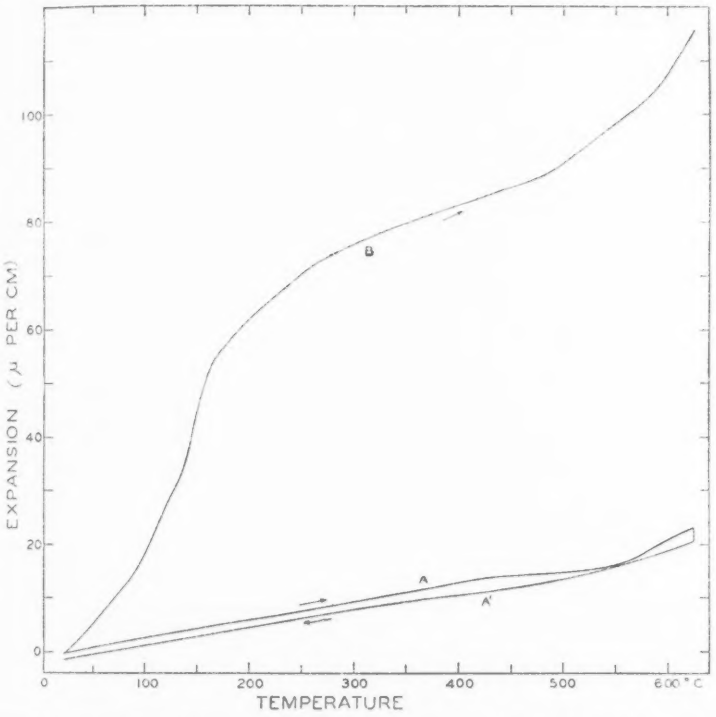

FIGURE 1.—*Expansion curves of devitrified (B) and undevitrified (A and A') samples.*
The change in expansion was caused by the devitrification of a borosilicate glass containing a relatively high percentage of silica.

The first eight of the series of curves in figure 2 show the changes in the apparent expansivity with temperature (between 50° and 300° C) after the glass had been subjected to various periods (ranging from 3 to 313 days) of devitrifying treatment at 800° C. After 3 days of treatment the cristobalite effect near 200° C was very large, and there was some indication that a tridymite effect near 150° C was developing. After the sixth and seventh days the cristobalite effect had practically disappeared, and it was practically nonexistent after the ninth day. From the sixth and through the twelfth days the

intermediate tridymite effect near 150° C, being quite large, was predominant, but by the eighteenth day it had yielded this dominance to the tridymite effect which had been slowly developing near 100° C since the sixth day of treatment. After the thirtieth day the tridymite effect near 100° C was practically the only one remaining and it had also practically disappeared when the treatment totaled 313 days

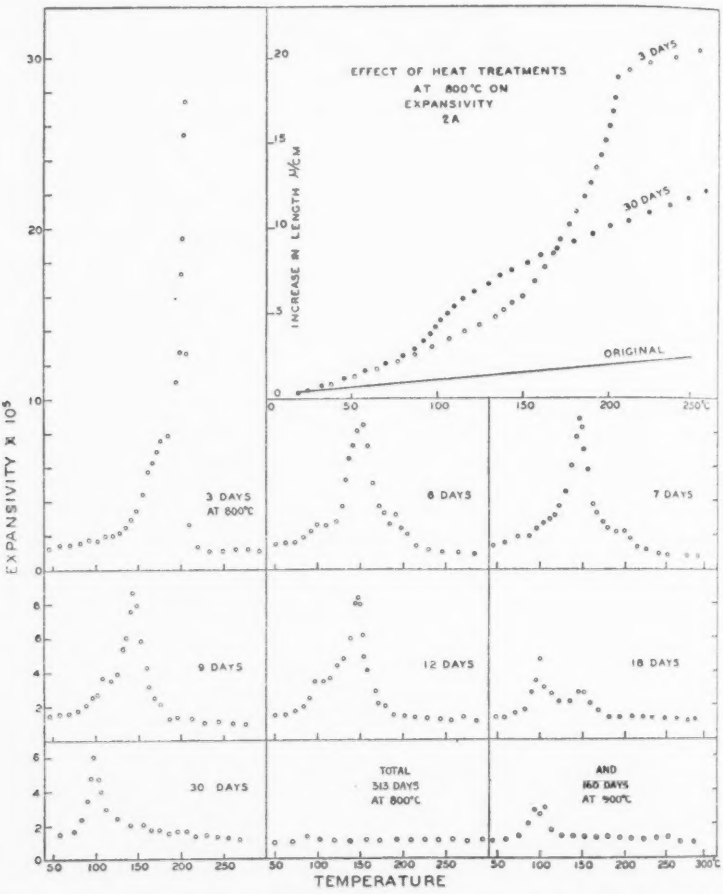

FIGURE 2.—*Approximate apparent expansivities of the devitrified glass after treatments of various duration at 800° C.*

These curves show the change in apparent expansivity with temperature and the progressive change in the inversion effects as the duration of the heat treatment was increased. Figure 2A presents some of the expansion curves from which the apparent expansivities were computed.

because the tridymite had been transformed into quartz. Throughout most of the time that the intermediate tridymite effect was dominant, tridymite plates appeared to be the predominant crystalline phase; but these plates were displaced by wedge-shaped tridymite twins at about the time that the effect near 100° C became dominant.

The results derived from expansion curves indicate that as the duration of the heat treatment increased the cristobalite and tridymite

effects, respectively, disappeared and developed sooner than the corresponding exothermic effects derived from cooling curves obtained on the same sample, No. 8, as described in a previous paper. (Tool and Insley, footnote 1.) These differences appear because the expansion samples were selected from parts of No. 8 which were uniformly devitrified and in consequence practically free from clear glass at the end of the first 3 days of treatment, whereas the samples used in obtaining the exothermic effects were representative of the whole of No. 8.

Figure 2 (*A*) presents two examples of the expansion curves from which the approximate expansivities shown by the curves in figure 2

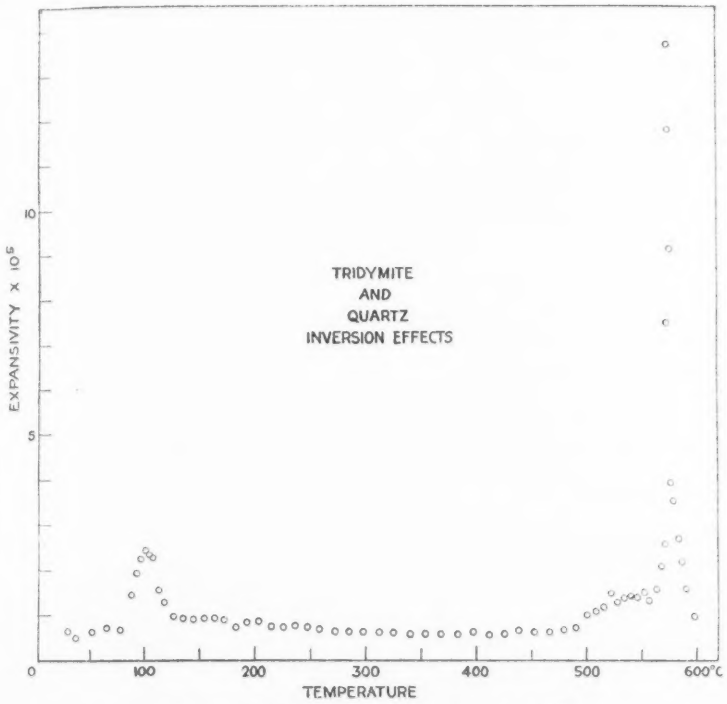

FIGURE 3.—*Tridymite and quartz inversion effects.*

This curve was obtained after a heat treatment of 55 days at 800° C. The small effect beginning at about 470° C and just preceding the quartz effect was caused chiefly by the normal increase in the apparent expansivity of the residual glass in this range, although adjustments preliminary to the quartz inversion probably add to this increase.

were computed. For comparison the expansion curve of the original glass is also included.

The curve presented in figure 3 shows the apparent expansivities of sample 8 after it had been treated for 55 days at 800° C. Two inversion effects were found at this time, the tridymite effect near 100° C and the quartz effect near 575° C. After the 313th day of treatment the quartz effect was more than six times as large as that shown here, and the tridymite effect had practically disappeared, as shown in figure 2. To reduce this quartz to tridymite the treating temperature was raised to 900° C and after 160 days the completion

of this reduction was being approached. Tests made at intervals during this treatment showed no indications of the cristobalite and intermediate tridymite effects, but the tridymite effect near 100° C soon appeared and grew slowly as the quartz effect diminished. The effect obtained near 100° C as the result of a test following the 160th day of treatment at 900° C is shown in the last of the series of curves in figure 2.

The fact that the cristobalite and intermediate tridymite effects were not detected during the development of the effect near 100° C as the quartz was transformed into tridymite wedge-shaped twins [3] by the 900° C treatments is not proof that the agents causing these effects did not develop and take their part in the transformation. That is, it is always possible that the fluxing effect of the residual glass at that treating temperature was so great that it was impossible for cristobalite and certain intermediate forms of tridymite to develop in sufficient concentrations to cause detectable inversion effects. It should be remarked, however, that the intermediate tridymite effect near 150° C often fails to reach any prominence during the transformation of cristobalite into tridymite when materials containing a much lower percentage of fluxing agents are treated at such developing temperatures.

IV. CONCLUSION

The results on the expansion effects caused by the various inversions found in the devitrified glass agree very well with those on the endothermic and exothermic effects of the same inversions, as a comparison of figure 2 with figure 6 of a previous paper [4] shows.

Consequently, they yield supporting evidence that either of the tridymite inversions, which are usually considered to occur near 117° and 160° C, on heating may appear without the presence of the other in this material.

WASHINGTON, August 19, 1938.

[3] During the investigation it was found that wedge-shaped twins of tridymite replaced the earlier developed tridymite plates when the devitrifying treatments of this glass were sufficiently prolonged at 800° C or below. Moreover, the exothermic and endothermic inversion effects centering on 100° C increased in magnitude as the number of twins increased, whereas the magnitude of the effects centering on 150° C decreased as the number of plates decreased. When the devitrification was developed by treatments at 900° C or above, the number of plates and the effects near 150° C were at all times relatively insignificant, but the number of twins and the prominence of the effects near 100° C were undiminished.

[4] Tool and Insley, J. Research NBS **21**, 743 (1938) RP 1152.

U. S. Department of Commerce National Bureau of Standards

RESEARCH PAPER RP1154

Part of Journal of Research of the National Bureau of Standards, Volume 21, December 1938

PORTABLE GEIGER COUNTER UNIT

By Leon F. Curtiss

ABSTRACT

A readily portable unit with entirely self-contained power supply, for operation of a low-voltage Geiger-Müller tube counter is described. The Neher-Harper circuit is incorporated in an integrating circuit which yields one pulse for approximately 60 counter pulses. The output pulse operates a Cenco counter. The sensitivity is such that 1 microgram of radium can be measured at 1 meter or 1 milligram at about 30 meters. This unit can therefore be used for measuring the gamma-ray activity of feebly active samples and also to detect slight contamination due to spilled or broken radium preparations. It also makes a very sensitive device for locating lost radium. Since it is operated entirely from dry batteries mounted in the case it can be used anywhere. The total weight is 13 pounds.

CONTENTS

	Page
I. Introduction	779
II. Description of circuit	779
III. Geiger-Müller tube	780
IV. Mounting for the unit	781
V. Sensitivity	782

I. INTRODUCTION

Situations frequently arise where it is desirable to measure feeble gamma-ray activity under conditions where alternating-current mains are not available for power supply for Geiger-Müller tube counters. Examples are measurement of radium ores in their original location, detection of lost radium, and in surveys of radium dial painting establishments to detect concealed deposits of luminous powder which have accumulated over long periods of operation and may become a hazard to the health of the workers. A simple, compact, and sensitive device of this kind is described below, which is operated entirely from dry batteries contained in the case of the instrument.

II. DESCRIPTION OF CIRCUIT

The wiring diagram of the control circuit for operating the counter is shown in figure 1. The Neher-Harper [1] circuit is incorporated in the first stage to permit the use of a large counter to increase the sensitivity and decrease the time required for observations, which is secured by the high counting rate which this circuit permits. The counter pulses from the Neher-Harper circuit are amplified and leveled in amplitude in the second stage. The third stage is a rectifier

[1] Phys. Rev. 49, 940 (1936).

which enables the condenser, C_3, to be charged by the rectified pulses. As soon as the voltage on this condenser reaches the flashing voltage of the neon lamp, N, shunted about it, the condenser is discharged, which impresses a voltage pulse on the grid of the last tube actuating the Cenco counter, Z. Thus the circuit serves to integrate the pulses and a wide range of ratios between the number of Geiger-Müller pulses and counts registered by the Cenco counter can be obtained by adjusting the constants of the input to the last stage.

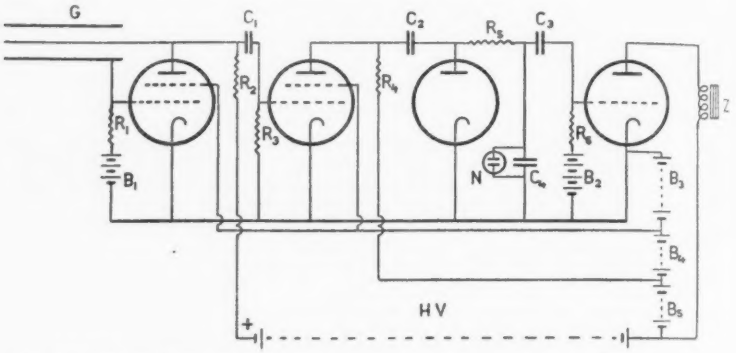

FIGURE 1.—*Wiring diagram of integrating amplifier for Geiger-Müller counter.*

G, Geiger-Müller tube; *Z*, Cenco counter; *N*, T4½ lamp.

Circuit constants are as follows:

R_1, R_4=20 meg.	C_1, C_2=0.0001 mf.	B_1=6 v.
R_2=5 meg.		B_2=10 to 15 v.
R_3=1 meg.	C_3, C_4=0.01 mf	B_3=15 to 30 v.
R_4=1 meg.		B_4=90 v.
R_5=10 meg.		B_5=45 v.
		HV=405 to 450 v.
		(Eveready X-180)

Since observations must be continued over a considerable time to secure reasonably accurate measurements, the natural variations of the flashing voltage of the neon lamp are averaged out quite adequately since at most these variations are of the order of 1 percent. Thus the neon lamp introduces no noticeable error into the final results, which from their nature under usual conditions do not exceed an accuracy of 2 or 3 percent.

III. GEIGER-MÜLLER TUBE

One obstacle to the satisfactory design of portable counter units with self-contained power supply in the past has been the high voltage, usually about 1,200 volts, required for operation of the Geiger-Müller tube counter. Recent work in this laboratory has shown that it is possible to operate counters up to 5 or 6 cm in diameter, containing gas at 6- or 7-cm Hg pressure, at voltages between 450 and 650 volts. This reduction in voltage has been obtained by using a mixture of argon and hydrogen in the tube. There seems to be a fairly critical ratio of hydrogen to argon at which the counting voltage is much lower than for either gas alone at the same pressure. This condition has been obtained by trial in the counters we have made so that we have no exact information as to the proper proportions of the two gases.

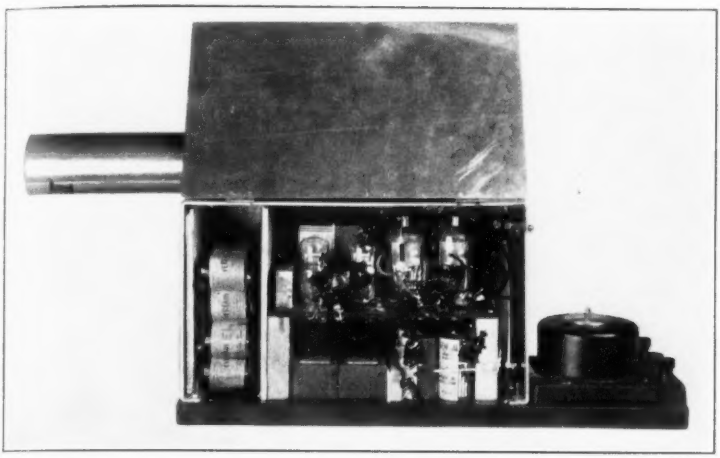

FIGURE 3.—*Interior view of case, showing the location of batteries and integrating amplifier.*

Ceneo counter at right.

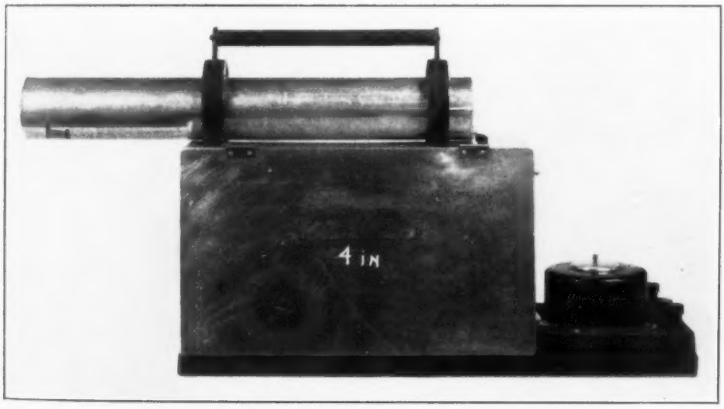

FIGURE 4.—*External view of completely assembled instrument with Geiger-Müller tube mounted in lighttight cylinder on top of the case.*

UNIV. OF MICH.

Another recent development due to Duffenback, Lifschutz, and Slawsky [2] has made possible the production of tube counters with exceptionally stable characteristics and remarkably flat "plateaus." Our procedure has varied somewhat from that recommended by these authors. We find it sufficient to pass a feeble alternating-current discharge between the wire and cylinder of individual counters using hydrogen which is frequently changed, as recommended by them.

An example of the operating characteristics of a counter prepared in this way and filled with a hydrogen-argon mixture at 7-cm Hg pressure is shown in figure 2, which shows the variation of counting rate with voltage. The diameter of the outer cylinder, made from 100-mesh copper gauze, as recommended by Evans,[3] was in this case 4.5 cm. Tests made in the Bureau's laboratory have verified the increase in sensitivity over a smooth metallic cylinder, which Evans reports. Referring to the curve in figure 2, it can be seen that the flat part of the curve from about 500 to 650 volts is very nearly horizontal. The counting rate in this range is therefore practically independent of voltage. This is equally a test of the linearity of the integrating circuit since pulses delivered to the integrating condenser must be sensibly equal to obtain a plateau of this type.[4]

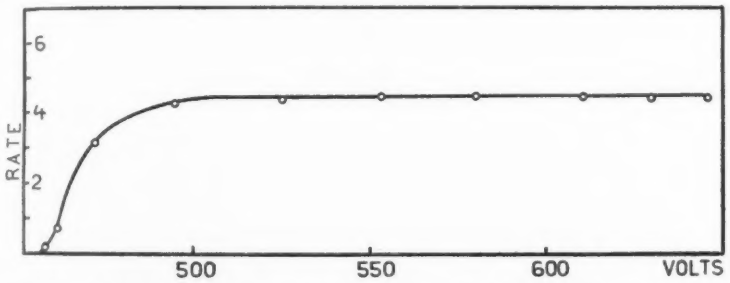

FIGURE 2.—*Curve showing variation of counting rate with voltage for Geiger-Müller tube when used in the integrating circuit shown in figure 1.*

Counters of this type, sealed in Pyrex, have been in use over a year without appreciable change in sensitivity or operating characteristics.

IV. MOUNTING FOR THE UNIT

Recent developments in commercial dry batteries have provided 45-volt units of exceptionally light weight, in the neighborhood of 2 ounces. Consequently, it is quite possible to inclose the batteries indicated in figure 1 within the case for the integrator circuit. The mounting and inclosure used for one of our units is shown in figures 3 and 4, which are photographs of the complete unit. Figure 3 shows the compartment inclosing the batteries and integrating circuit open, and figure 4 shows the compartment closed ready for use. The counter is mounted horizontally inside a tubular aluminum shield. The total weight is 13 pounds.

[1] Phys. Rev. **52**, 1231 (1937).
[3] Rev. Sci. Instr. **7**, 444 (1936).
[4] Attention must of course be given to the batteries, as they deteriorate with age. Instead of checking them by a voltmeter, which does not necessarily indicate their open circuit voltage, it is better to test the instrument as a unit by a radioactive preparation of known magnitude. The National Bureau of Standards is prepared to issue feeble standards for this purpose.

V. SENSITIVITY

The sensitivity of this unit, using a 100-mesh gauze counter 4.5 by 25 cm, is such that 1 microgram of radium at 1 meter increases the rate of the Cenco counter by about 12 counts per hour. Thus this instrument can readily be used to detect radium ores and stray deposits of luminous powder in radium dial painting plants. It also may serve as a very sensitive detector for lost radium preparations of the type used for cancer treatment. An unshielded preparation of 1 milligram of radium can be detected at 25 to 30 meters. Therefore, the presence of lost radium can be determined readily, even when lodged in inaccessible locations. The complete portability of the instrument makes its use convenient and enables explorations over large areas to be made with ease.

The author acknowledges the help of A. V. Astin in connection with the details of the integrating circuit, and the assistance of B. W. Brown and L. L. Stockmann in constructing and testing the complete unit.

WASHINGTON, September 30, 1938.

U. S. Department of Commerce National Bureau of Standards

RESEARCH PAPER RP1155

Part of Journal of Research of the National Bureau of Standards, Volume 21, December 1938

CONCRETE AS A PROTECTIVE MATERIAL AGAINST HIGH-VOLTAGE X-RAYS [1]

By George Singer, Lauriston S. Taylor, and Arvid L. Charlton

ABSTRACT

A description is given of relative X-ray-transmission measurements on a group of especially prepared concrete specimens and commercial building blocks selected to sample the concrete mixes and cover the range of concrete densities in common use. It was found that the lead equivalent of any concrete was an increasing function of its mass per unit area and independent of the nature of the mix. Relations between lead equivalence, density, mass, and thickness are given, from which the thickness of concrete necessary for adequate protection can be calculated for any voltage in the voltage interval 200 to 400 kv.

CONTENTS

	Page
I. Introduction	783
II. Method	785
III. Description of concrete	785
1. Prepared specimens	786
2. Building blocks	787
IV. Results	788
1. Variation of lead equivalent with X-ray voltage and thickness of concrete	788
2. Variation of protection coefficient with density	788
3. Thickness of concrete required for protection	790
4. Variation of lead equivalent of concrete with mass per unit area	793
5. Concrete-lead mass ratio	793
V. Conclusion	793

I. INTRODUCTION

Within the past few years the highest excitation potentials commonly used in X-ray therapy have been raised considerably above the 200-kv limit of 15 years ago; 400-kv equipment is now commercially available, and there are numerous X-ray generators of various types operating at potentials between 400 and 1,000 kv. There has been a corresponding extension in the application of X-rays to the inspection of metals, and in the use of X-radiation as a scientific tool in the physical laboratory. With this trend, the need for adequate protection of personnel against very penetrating radiation has become more urgent than ever.

Lead has been the most commonly used protective material, both in metallic form as sheet lead and lead shot and in combination with other materials, as in lead-rubber and X-ray protective glass. For the most penetrating X-radiation available a few years ago, no other

[1] Preliminary report presented at Fifth International Congress of Radiology, Chicago, September 1937.

protective material compared at all favorably with lead except barium, and the usefulness of the latter was limited by practical difficulties in making a homogeneous barrier. For this reason, the Advisory Committee on X-ray and Radium Protection has made all recommendations for X-ray protection [2] in terms of lead and has recommended that the effectiveness of all other materials be measured by their lead equivalents. In table 1 are given the recommended lead barriers for direct X-radiation excited by potentials up to 600 kv—the present voltage limit of the recommendations. The recommendations of the committee are given in columns 1 and 2 of table 1. Column 3 has been added to show the approximate weight per square foot of lead barrier recommended in column 2. The weight of the required barrier is seen to increase so rapidly with increasing excitation potential that above 200 kv the cost of lead for such a barrier becomes very high and the problem of supporting the required lead mass becomes serious.

TABLE 1.—*Mass of lead barrier for adequate protection*

Potential	Recommended minimum equivalent lead thickness	Weight of barrier [1]
1	2	3
kv	*mm*	*lb/ft²*
75	1.0	2.4
100	1.5	3.5
150	2.5	5.9
175	3.0	7.1
200	4.0	9.5
225	5.0	14
300	9.0	21
400	15.0	35
500	22.0	52
600	34.0	80

[1] Approximate.

One possible solution is to make the protective barrier of a material which is self-supporting. Concrete suggests itself at once. In any case, however, for radiation of a given quality, the mass of an adequate concrete barrier will always be greater than that of a corresponding lead barrier; but since the concrete is self-supporting and relatively inexpensive, this increase in weight is not particularly objectionable except in the case of installations in existing buildings unable to withstand the additional loading.

Such data [3] as have been published on the lead equivalence of concrete are old and are confined to X-ray excitation potentials not exceeding 200 kv. It is the purpose of the present paper to give the results of measurements on a series of concrete samples and commercial building blocks for X-ray potentials ranging from 200 to 400 kv.

[2] Handb. BS (1936) H20.
[3] G. W. C. Kaye, Roentgenology (Paul B. Hoeber, Inc., 1923), p. 95; Brit. J. Radiol. **23**, 158 (1937).
Kaye and Owen, Proc. Phys. Soc. **35**, 33D (June 1923).
C. B. Braestrup, Am. Architect (September 1929).

II. METHOD

The lead equivalent of each concrete sample was obtained by direct comparison with sheet lead, 99.9 percent pure, meeting Federal specifications for grade *A* lead. The method used is essentially that previously described for determining the lead equivalence of X-ray glass.[4] The experimental arrangement is shown in figure 1; for complete constructional details of the X-ray tube, ionization chamber, and current-measuring system, the original paper describing this apparatus should be consulted.[5]

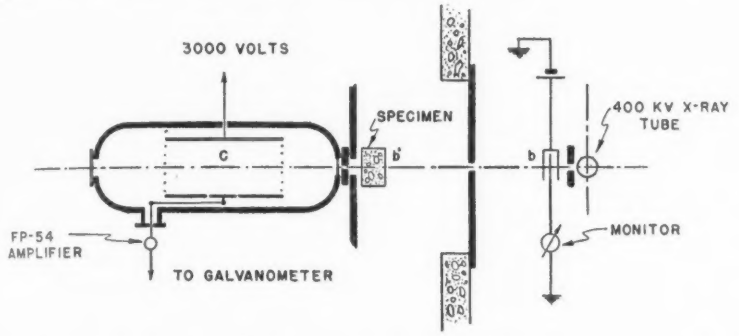

FIGURE 1.—*Diagram of apparatus used in determining the lead equivalent of concrete.*

The beam of radiation, *bb'*, emerges from the tube at an angle of 90 degrees to the tube axis, and after passing through the concrete test cylinder shown, enters the ionization chamber, *c*. The cross-section of the beam is limited by the four diaphragms shown. The resulting ionization current, after amplification, is measured by direct deflection of a high-sensitivity galvanometer in the output of the amplifier. When measuring radiation through heavy protective barriers the residual ionization current due to scattering, radioactive contamination, and cosmic radiation, is a considerable fraction of the total current measured. For such measurements requiring the highest sensitivity, a rate-of-drift method is used in order to get the benefit of a time average for this background radiation; this average remains fairly constant and affects alike the measurements of the standard filters and test specimens, so that, as a rule, no zero correction in the ionization readings is necessary.

III. DESCRIPTION OF CONCRETE

The concrete specimens on which tests were made were selected so as to cover adequately the types of mixes and range of densities most commonly used. These specimens fall into two classes, (*a*) the first consists of a group of especially prepared test specimens;[6] (*b*) the second consists of a group of solid building blocks which were obtained on the market. Tables 2 and 3 give data on all specimens.

[4] George Singer, J. Research NBS **16,** RP 870, 1936.
[5] L. S. Taylor, G. Singer, and A. L. Charlton, J. Research NBS **21,** 19 (1938) RP 1111.
[6] We are indebted to John Tucker, Jr., of the Cement Section of the National Bureau of Standards, who selected the test samples and under whose supervision they were prepared.

TABLE 2.—*Prepared concrete specimens*

Specimen	Proportions (cement to sand to gravel)	Approximate dimensions		Density of specimens at 24 hours		C/W[a] ratio	Consistency, expressed as approximate slump
		Height	Diameter				
GRAVEL CONCRETE							
		Inches	*Inches*	*lb/ft³*	*g/cm³*		*Inches*
G1	1:2.2:3.8	4¼	6.0	148	2.37	1.60	6
G2	1:2.2:3.8	6⅛	6.0	145	2.34	1.60	6
G3	1:2.2:3.8	8½	8.0	147	2.36	1.60	6
G4	1:2.2:3.8	4¼	6.0	152	2.47	1.75	3
G5	1:2.2:3.8	6⅛	6.0	147	2.36	1.75	3
G6	1:2.2:3.8	8¼	8.0	150	2.40	1.75	3
G7	1:2.2:3.8	4⅝	6.0	150	2.40	1.90	1
G8	1:2.2:3.8	6½	6.0	150	2.40	1.90	1
G9	1:2.2:3.8	8⅛	8.0	148	2.37	1.90	1
LIMESTONE CONCRETE							
L1	1:3.6:2.4	4⅛	6.0	144	2.31	1.75	3
L2	1:3.6:2.4	6⅛	6.0	147	2.36	1.75	3
L3	1:3.6:2.4	8⅛	8.0	144	2.31	1.75	3
N	(b)	4⅛	6.0	132	2.12	4.17	(c)
NN	(b)	4⅛	6.0	132	2.12	4.17	(c)

[a] Cement-water ratio. [b] Neat cement. [c] Normal consistency.

TABLE 3.—*Solid building blocks*

Specimen	Dimensions	Density
	Inches	*g/cm³*
B4	3¾×7½×11¾	2.02
B6	5½×6×9	2.01
B8	7½×8×13	2.10

1. PREPARED SPECIMENS

Three types of specimens were prepared. Specimens *N* and *NN* were made of neat cement of normal consistency (24 percent of water). Specimens *G* were nominal 1:2:4 mixes, the exact cement-sand-gravel proportions being 1:2.2:3.8, respectively, by weight. Potomac River sand (quartz), fineness modulus 3.1, was used as fine aggregate. Potomac River gravel (quartz), size No. 4 to 1½ inches, was used as coarse aggregate in mix *G*, and Potomac River sand and West Virginia limestone in mix *L*. In mix *L* the sand–coarse-aggregate ratio was adjusted to give maximum density for the mix with the size limestone (No. 4 to ⅜ in.) that was available. The proportions of mix *L* were 1:3.6:2.4.

The specimens were cylinders 6 or 8 inches in diameter and approximately 4, 6, or 8 inches in thickness, the thickness in all cases was not more than the nominal diameter. They were kept in molds for 24 hours, then stored in a moist room for 3 weeks, after which they were permitted to dry slowly in laboratory air until tested. The gravel concrete was made in three wetnesses. The wettest specimen had as much water as should be used in ordinary construction; the driest was of a consistency that could be used for very special work, in which the extra cost of spading, rodding, and tamping the concrete into the form would be justified by the increase in desirable properties which could be obtained by this rather dry concrete.

2. BUILDING BLOCKS

In addition to the prepared samples, three different building blocks were tested. These are listed in table 4. These blocks were part of a purchase of several hundred made from a manufacturer and contractor in the vicinity of Washington for use in the construction of protective barriers for the 400-kv X-ray generator of the National Bureau of Standards. Block *B4* was a solid block of rectangular cross section; blocks *B6* and *B8* had the horizontal cross section of the usual three-web building block but were solid, that is, the two cylindrical cores ordinarily used in making three-web blocks were omitted. The nature of the mix was not known except that in accordance with the usual commercial practice the mix was made sufficiently dry to permit prompt removal of the blocks from the machine molds, the ideal mixture for blocks being that which will barely retain its shape when the forms are removed immediately after the concrete has been deposited and pressed into shape. This is a great deal drier than the mixtures ordinarily used in poured concrete.

TABLE 4.—*Lead equivalent of concrete*

Sample	Thickness	Diameter	Density	Lead equivalent at—					Mass per unit cross section
				200 kv	250 kv	300 kv	348 kv	400 kv	
	cm	*cm*	*g/cm³*	*mm*	*mm*	*mm*	*mm*	*mm*	*g/cm²*
G1A	10.5	15.3	2.37	1.60	2.26	3.01	3.82	4.88	24.9
G1B	10.9	15.3	2.37	1.66	2.33	3.13	3.91	4.64	25.8
G2A	15.4	15.3	2.34	2.60	3.86	5.09	6.18	7.42 7.32	36.0
G2B	15.4	15.3	2.34	2.58	3.96	5.12	6.23	7.45 7.42	36.0
G3	20.4	20.4	2.36	----	5.97	8.03	9.86	11.00	48.1
G4A	10.9	15.3	2.47	1.70	2.40	3.17	3.97	4.73	26.9
G4B	10.7	15.3	2.47	1.70	2.37	3.12	3.98	4.66 4.68	26.4
G5A	15.4	15.3	2.36	2.63	4.01	5.13	6.30	7.40	36.3
G5B	16.0	15.3	2.36	2.77	4.20	5.44	6.66	7.97 7.92	37.8
G6A	20.6	20.3	2.40	----	5.80	7.73	9.59	11.59	49.4
G6B	21.4	20.3	2.40	----	6.06	8.11	9.97	12.16	51.4
G7A	10.8	15.3	2.40	1.70	2.34	3.12	3.98	4.68	25.9
G7B	10.1	15.3	2.40	1.58	2.21	2.90	3.64	4.31	24.2
G8A	16.3	15.3	2.40	2.90	4.42	5.64	6.93	8.22	39.1
G8B	16.4	15.3	2.40	2.93	4.40	5.77	6.92	8.32	39.4
G9A	20.4	20.3	2.37	----	5.59	7.47	9.23	11.29	48.3
G9B	20.3	20.3	2.37	----	5.76	7.70	9.48	11.58	48.1
G10A	10.1	----	----	1.49	2.00	2.70	3.47	4.02	----
G10B	10.6	----	----	1.58	2.16	2.95	3.69	4.33	----
G11A	15.1	----	----	2.36	3.74 3.73	4.89	5.97	7.02 7.06	----
G11B	15.5	----	----	2.55	3.92	5.10	6.23	7.42 7.33	----
L1A	10.7	----	2.31	1.67	2.30	3.07	3.80 3.78	4.49	24.7
L1B	10.3	----	2.31	1.57	2.13	2.85	3.50 3.55	4.19	23.8
L2A	15.9	----	2.36	2.77	4.22	5.40	6.56	7.80	37.5
L2B	15.8	----	2.36	2.78	4.19	5.39	6.57	7.76	37.3
L3A	20.4	----	2.31	----	5.61	7.45	9.19	11.10	47.1
L3B	20.2	----	2.31	----	5.57	7.38	9.02	10.92	46.7
NA	10.2	----	2.12	1.52	2.03	2.69	3.34	3.92	21.6
NNA	10.3	----	2.12	1.52	2.00	2.68	3.34	3.90	21.8
X	20.7	----	----	----	5.72	7.67	9.44	11.52	----
B4	----	----	----	1.33	1.48	1.99	2.53	2.99 2.98	19.5
B6	----	----	----	1.80	2.74 2.76 2.89	3.80	4.65 4.60 4.70	5.76 ---- 5.73	29.7
B8	----	----	----	----	4.58	6.03 6.07	7.52 7.50	9.04	41.6

IV. RESULTS

1. VARIATION OF LEAD EQUIVALENT WITH X-RAY VOLTAGE AND THICKNESS OF CONCRETE

The lead equivalent of each sample was determined at each of the following excitation potentials: 200, 250, 300, 348, and 400 kv. No beam filter was used, the only filter being 2 mm of copper and 10 mm of aluminum inherent in the X-ray tube.

The results of these tests are tabulated in table 4 and are plotted in figures 2, 3, and 4. It is apparent from these data that the lead

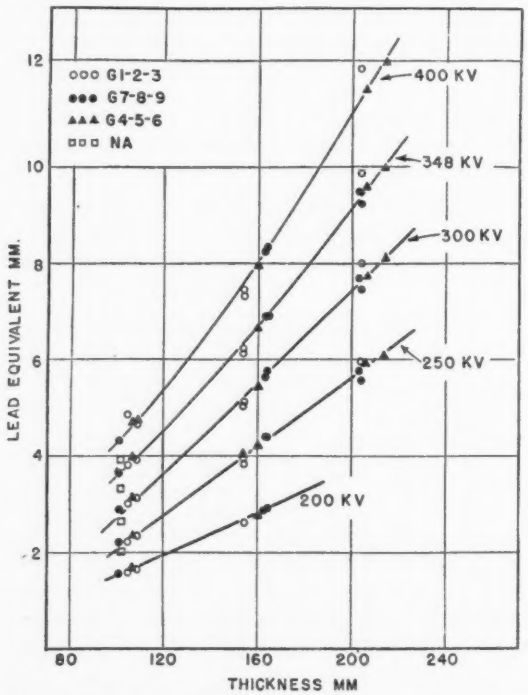

FIGURE 2.—*Variation of lead equivalent of a concrete barrier with thickness.*

See table 4 for description of specimens.

equivalent of a sample of given density depends not only on its thickness but also on the X-ray excitation potential as well, and above 200 kv.[7] increases with both.

2. VARIATION OF PROTECTION COEFFICIENT WITH DENSITY

Figure 5 is a typical plot of the protection coefficients [8] as a function of density for samples of approximately equal thickness. The samples of figure 5 were cylinders approximately 4 inches thick;

[7] The complete curve showing the lead equivalent of concrete as a function of the excitation potential has a minimum at approximately 200 kv and a low maximum at about 100 kv. However, the portion of the curve below 200 kv is of little practical value.

[8] "Protection coefficient" has been defined as follows by the American Advisory Committee on X-ray and Radium Protection:

"The protection coefficient of a material is the ratio of the thickness of lead to the thickness of the material which absorbs a given X-ray beam to the same extent."

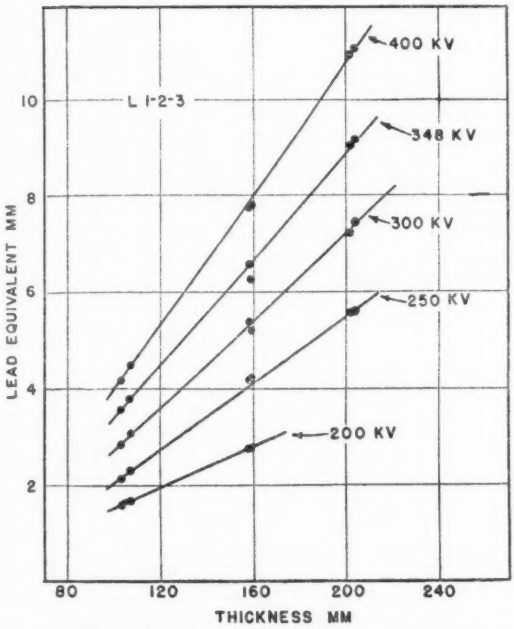

FIGURE 3.—*Variction of lead equivalent of a limestone concrete barrier with thickness.*

See table 4 for description of specimens.

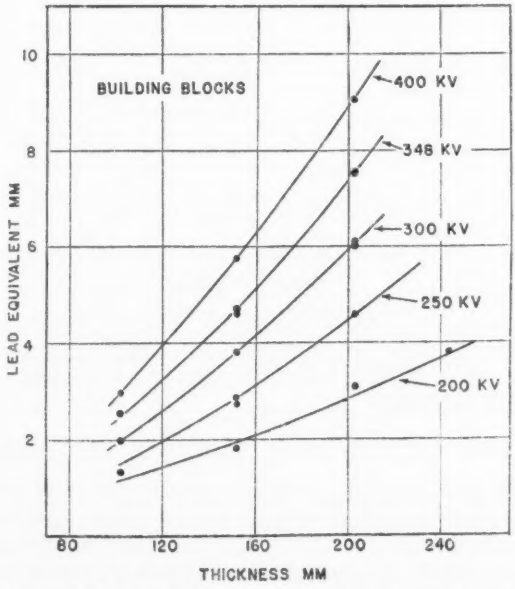

FIGURE 4.—*Lead equivalent of concrete building blocks plotted against thickness of blocks.*

See table 5 for description of specimens.

similar plots were made for samples 6 and 8 inches thick. The lines were drawn so as to pass through the origin of the coordinate system as they would do if the protection coefficient varied linearly with the density of the concrete. It appears that within the experimental error of the measurements the points do fall on the lines so drawn, and we may, therefore, conclude that within this quality range the protection coefficient of concrete is directly proportional to the density of the concrete. It follows that in this range the components of the concrete mix do not directly affect the protective quality of the material aside from their effect on the concrete density. In figure 5, four different concrete mixes are included: Two specimens are neat

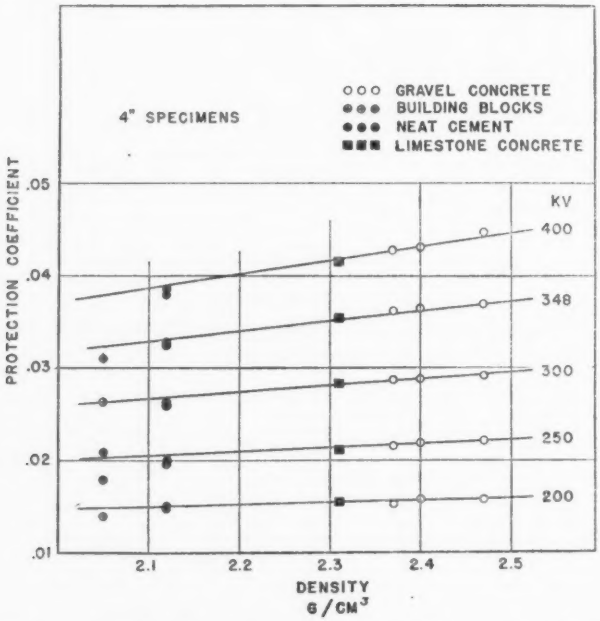

FIGURE 5.—*Variation of protection coefficient of 4-inch concrete test cylinders with density of specimens.*

cements, one is a limestone concrete, three are gravel concretes, and two are building blocks of unknown composition; yet the observed differences in their protective coefficients can be explained simply in terms of their densities.

3. THICKNESS OF CONCRETE REQUIRED FOR PROTECTION

Since there are no striking differences in the lead equivalents of samples of equal density but varying composition, there is no particular advantage in making tests on many different samples; and, therefore, all subsequent measurements extending these tests to lead equivalents greater than the recommended lead thicknesses were con-

fined to two groups of samples designated as *G* (density 2.36) and *B* (building blocks, density 2.0 to 2.1$_0$). These data are summarized in table 5 and are plotted in figures 6 and 7. In these figures the intersection of the dotted curve with the full-line curves gives the thickness of this concrete required to give the degree of protection recommended by the Advisory Committee on X-ray and Radium Protection. For concrete of some slightly different density, the required thickness can be obtained if its density is known, since for

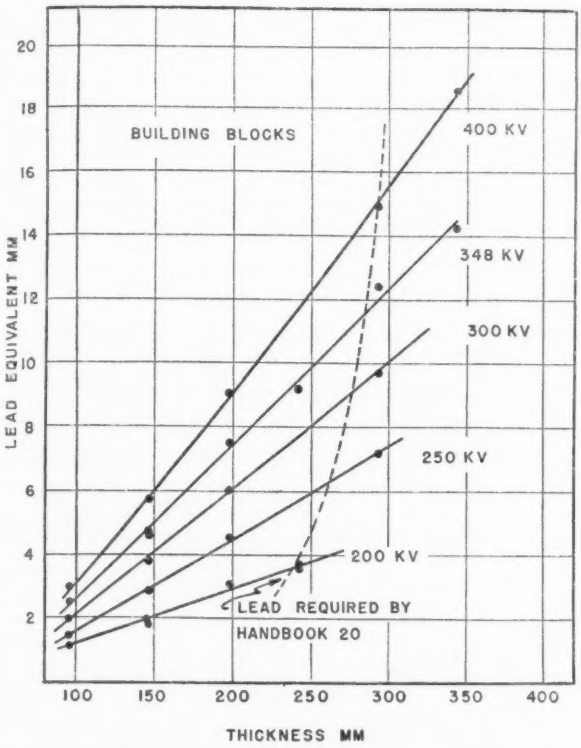

FIGURE 6.—*Curves for obtaining required thickness of barrier made of building blocks of average density 2.05 g/cm³.*

samples of approximately equal thickness the lead equivalent varies linearly with density. However, in using figures 6 and 7 to compare concretes of widely different densities, it should be remembered that the protection coefficient of a sample depends also on the sample thickness. Therefore, to determine the required thickness of any concrete it should be compared with a concrete of greater rather than with one of smaller density; by making this determination in this way a thickness somewhat greater than that required will be obtained and the error resulting will be on the safe side.

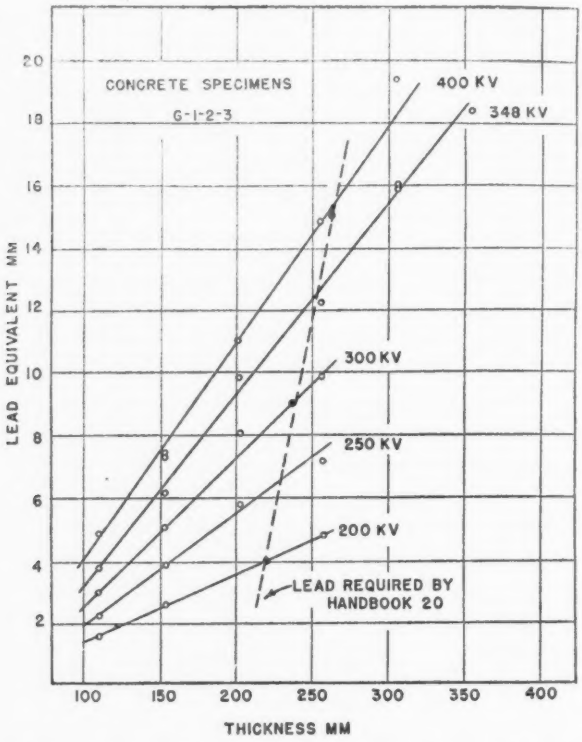

FIGURE 7.—*Curves for obtaining required thickness of concrete barrier of average density 2.35 g/cm³.*

TABLE 5.—*Lead equivalent of concrete*

Sample	Average density	Thickness	Lead equivalent					Mass per unit cross section
			200 kv	250 kv	300 kv	348 kv	400 kv	
	g/cm³	cm	mm	mm	mm	mm	mm	g/cm²
G1A	2.37	10.5	1.59 1.60	2.26	3.01	3.82	4.88	24.9
G2A	2.34	15.4	2.60	3.86	5.09	6.18	7.42 7.32	36.0
G3	2.36	20.4	.....	5.97	8.03	9.86	12.00	48.1
G1A+G2A	2.35	25.9	4.79	7.14	9.81	12.2 12.2	14.8	61.1
G1A+G3	2.36	30.9	.....	.....	.....	15.9 15.8	19.3	72.9
G2A+G3	2.35	35.8	.....	.....	.....	18.3	.....	84.1
B4	2.0_2	9.6	1.15 1.33	1.48	1.99	2.53	2.99 2.98	19.5
B6	2.0_2	14.7	1.89 1.80	2.74 2.76 2.89	3.80	4.65 4.60 4.70	5.76 5.73	29.7
B8	2.1_0	19.8	3.0_7	4.58	6.03 6.07	7.52 7.50	9.04	41.6
B4+B6	2.0_9	24.3	3.58 3.90 3.67	.....	.....	9.14	10.5	49.1
B4+B8	2.0_7	29.4	.....	7.1_8	9.6_8	.....	14.2 14.9	61.2
B6+B8	2.0_8	34.5	.....	.....	.....	14.2	18.5	71.7
Required for adequate protection	.....	.....	4.0	.....	9.0	.....	15.0	.....

4. VARIATION OF LEAD EQUIVALENT OF CONCRETE WITH MASS PER UNIT AREA

All absorption data on concrete given above for various mixes, densities, and thicknesses are conveniently summarized in figure 8, in which the lead equivalent of a concrete barrier is plotted against the mass of the barrier per unit cross-sectional area. For a given voltage all samples in this graph fall on a single curve no matter what the composition, density, or thickness of the individual samples may be. For this reason the thickness of a concrete barrier required for adequate protection can be most conveniently obtained from figure 8 by use of the relation $L=M/D$, where L is the thickness of concrete barrier; M is the mass of barrier per unit area required to give the desired degree of protection—obtained from figure 8; and D is the density of the concrete used.

As has already been noted, the curves in figures 6 and 7 must be used with caution when the density of a given concrete is widely different from those used as standards in these two graphs. It is clear that no such precautions are necessary in making the same determination by means of figure 8 and for this reason its use is recommended.

5. CONCRETE-LEAD MASS RATIO

In figure 8 the dotted curve is for metallic lead; this is included for the purpose of comparing the mass of a concrete wall with that of a lead barrier providing equivalent protection. Table 6 contains a summary of such a comparison for 200-, 300-, and 400-kv radiation.

In column 5 of table 6 there are given the ratios of the mass of a concrete barrier to the mass of its lead equivalent. The ratio is high at the lower excitation potentials; at 200 kv an adequate concrete barrier has about 12 times the mass of its lead equivalent, while at 400 kv the concrete barrier has only 3.5 times the mass of an equivalent lead shield.

TABLE 6.—*Concrete-lead mass ratio*

Potential	Recommended lead equivalent	Mass per unit area		Mass of concrete / Mass of lead
		Lead	Concrete	
1	2	3	4	5
kv	*mm*	*g/cm²*	*g/cm²*	
200	4.0	4.5	53	11.8
300	9.0	10.2	57	5.6
400	15.0	17.0	60	3.5

V. CONCLUSION

Since the protection coefficient of concrete increases rapidly with increasing excitation potential, the thickness of the concrete barrier which will provide adequate protection at, say 400 kv, is not very much greater than that required to give the same degree of protection at a much lower voltage. So, from figure 6, we see that for the building blocks tested, a barrier about 30 cm (11.8 in.) is adequate at 400 kv, while at 200 kv the thickness required is about 22 cm (8.7 in.). Similarly, from figure 7, the thickness of concrete required at 400 kv is about 26.5 cm, while the required thickness at 200 is 22 cm.

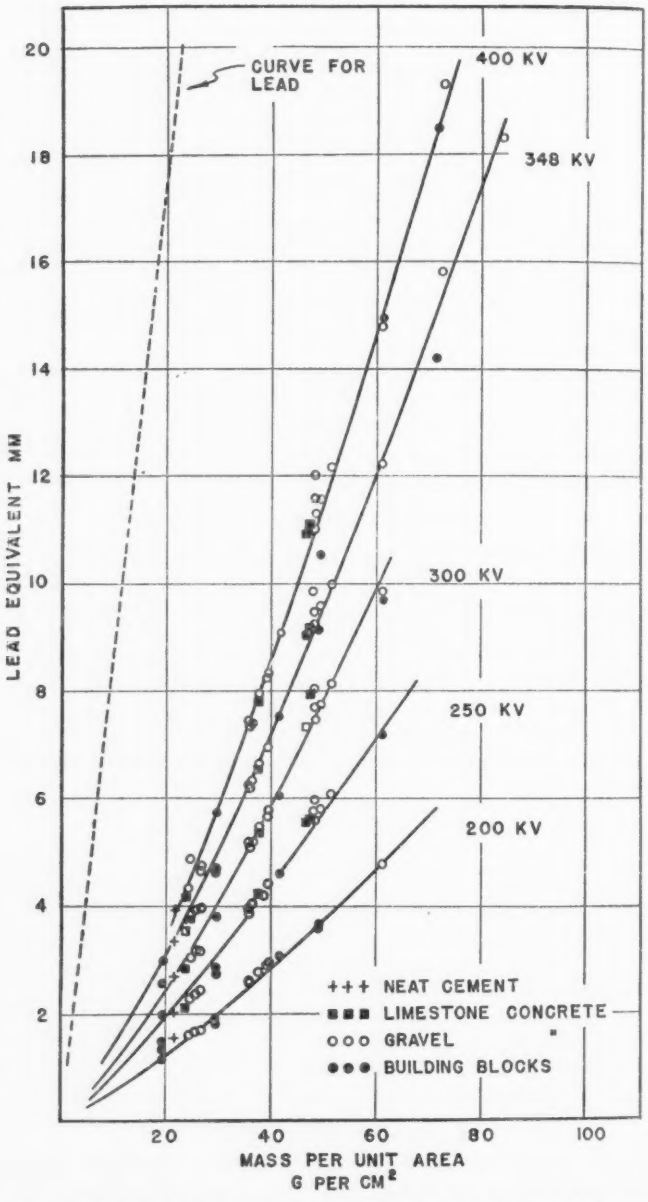

FIGURE 8.—*Lead equivalent of any concrete barrier as a function of the mass of the barrier per unit cross-sectional area.*

In both cases the additional thickness required in going from 200 to 400 kv is small and a barrier providing adequate protection at a given excitation potential will also be adequate at a lower voltage.

WASHINGTON, July 20, 1938.

U. S. Department of Commerce National Bureau of Standards

RESEARCH PAPER RP1156

Part of Journal of Research of the National Bureau of Standards, Volume 21, December 1938

ON THE ACCURACY OF RADIO FIELD-INTENSITY MEASUREMENT AT BROADCAST FREQUENCIES

By Harry Diamond, Kenneth A. Norton,* and Evan G. Lapham

ABSTRACT

This paper presents a discussion of errors commonly encountered in radio field-intensity measuring sets operating at broadcast frequencies. Data are given to indicate the magnitudes of the different errors existing in typical commercial measuring sets, and an estimate is presented of the probable accuracy of measurement attained. Of the several errors, the one resulting from the simplifying assumption that a loop antenna has the same voltage step-up for a distributed induced voltage as for a lumped voltage introduced at its center is often the most serious. An analysis is given to show how this error arises and an expression is derived for taking it into account. A method for eliminating this error, suggested by Baker and Huxley, is discussed, and data are given illustrating the efficacy of this method. Other means for limiting this error are also discussed.

CONTENTS

		Page
I.	Introduction	795
II.	Magnitudes of errors in typical commercial equipment	797
III.	Analysis of effect of distributed capacitance of loop antenna	799
IV.	Analysis of experimental data on distributed-capacitance effect	806
V.	ΔC method for eliminating the distributed-capacitance effect	807
VI.	Untuned loop antenna	809
VII.	Shielded loop antenna	810
VIII.	Precautions for attaining maximum accuracy	812
IX.	Conclusions	817

I. INTRODUCTION

The increasing interest in the quantitative determination of the service area of broadcast stations, coupled with a more rigorous approach to the derivation of radio-wave attenuation formulas, has resulted in a twofold interest in the accuracy of radio field-intensity measurements at broadcast frequencies. This interest has been reflected in the increased number of measuring sets calibrated at the National Bureau of Standards during the past few years. In general, the sets tested employed one of three methods of measurement and were found to be subject to typical errors, characteristic of these methods. This paper presents the results of a critical study of the magnitude of the errors encountered with the three different methods; consideration of these errors is restricted to operating frequencies below 1,600 kc/s, and to field intensities ranging from 100μv/m to 0.1 v/m.

* Associate Engineer, Federal Communications Commission.

The nature of the errors likely to be involved may best be understood from consideration of the manner in which the measurement of the field voltage induced in the loop antenna is made in the three methods. In one method, the first detector of a superheterodyne receiver, used in conjunction with a voltage-attenuator connected between the detector and the intermediate amplifier, constitutes the voltage determining means. The detector is first calibrated at high-voltage level in a low-frequency calibrating circuit. A comparison is next made between the voltages developed across one-half of the loop antenna by the field being measured and by a local voltage of identical frequency inserted at the center of the loop antenna and adjusted to give the same current in the plate circuit of the detector as that given by the low-frequency calibrating voltage. The voltage step-up, or Q-factor, of the loop antenna is then measured by a similar comparison between the local voltage applied directly to the detector input and the voltage it develops across one-half the loop antenna by virtue of resonance. From these two measurements, the field voltage induced in the antenna may be computed.

In the second method of measurement, the voltage-determining means consists of a voltage generator and attenuator for introducing at the center of the loop antenna a known voltage of the same radio frequency as the field voltage. Equality of the two voltages is determined by using the receiving set as an uncalibrated vacuum-tube voltmeter, usually connected across one-half of the loop antenna. The third method of measurement differs from the second in that the calibrating voltage is of fixed value (high level) and is compared with the induced field voltage by means of the first detector of a superheterodyne receiver used in conjunction with a voltage attenuator connected between the first detector and the intermediate amplifier. In a commercial equipment employing this method the gap between successive steps of the voltage attenuator is spanned by a linear output-indicating system comprising a half-wave rectifier and indicating meter.

It will be evident that the following factors may influence the correctness of the measured field voltage in one or all of the three methods considered: (a) incorrect calibrating voltage; (b) nonlinearity of the detector and of the output indicating system; (c) incorrect voltage-attenuator design; (d) stray voltages induced in the loop antenna by the calibrating oscillator or from other portions of the set; (e) regeneration in various portions of the set; and (f) inaccurate introduction of the calibrating voltage because of unbalance of the loop antenna. The accuracy of field-intensity measurements will be affected by the cumulative error in the voltage determination and, in addition, by two other possible errors which we shall term: (g) the proximity effect, and (h) the distributed-capacitance effect. The proximity effect consists in the distortion of the measured field caused by the set container or by other objects near the loop antenna; for example, a portion of the automobile in which the set may be installed. The distributed-capacitance effect consists in the difference produced by the distributed capacitance of the loop antenna in the effective voltage step-up of the tuned loop-antenna circuit for the distributed field voltage and for the lumped calibrating voltage.

The distributed-capacitance effect appears to have been given scant consideration in the design of commercial apparatus. The error

in the measured value of the Q-factor, caused by the distributed capacitance, is a function of the ratio of the operating frequency to the natural frequency of the antenna. In some commercial sets, in which the loop antennas operate near their natural frequencies when in the upper portions of their frequency ranges, the distributed-capacitance error is of the order of 15 percent. An analysis of this error is given in the paper together with a derived expression for the correction factor to be applied in order to compensate for it. The computed factor agrees well with experimental results.

II. MAGNITUDES OF ERRORS IN TYPICAL COMMERCIAL EQUIPMENT

In this section are presented data on the magnitudes of the several errors as measured in commercial equipment typical of the three methods of field-intensity measurement described. Based on these data, an estimate is given of the absolute accuracy of apparatus representative of each of the three methods.

In the measurement of several sets of a commercial type employing the first method, the following errors were detected. An error of up to 6 percent was caused by harmonics in the 1,000-cycle calibrating voltage and by a change in the detector grid bias (from its operating value), when the calibrating circuit was turned "on." An error of up to 16 percent was caused by nonlinearity of the detector; the departure from linearity was found to vary with operating frequency in several sets because of the variable voltage introduced in the detector plate-circuit by the heterodyne oscillator. In one set, faulty neutralization of the detector (produced by an unbalance in the modulating circuit due to a poor electron tube) caused an error of up to 5 percent. Leakage from the local oscillator was of negligible order unless an attempt was made to use low-level calibration of the detector; in the latter case an error of up to 5 percent was produced in the measurement of the Q-factor, depending upon the orientation of the loop antenna. An error of up to 8 percent was introduced by the effect of the distributed capacitance of the antenna upon the measurement of its Q-factor; in this particular design the limited operating frequency range of each loop antenna (2.2 to 1) resulted in limiting the maximum value of this error to 8 percent. The distortion of the field by the set container was found to be responsible for an error ranging from 0 to 10 percent as the orientation of the loop antenna was varied from a plane perpendicular to the longitudinal axis of the container to a plane containing this axis. Errors of types (c) and (f) were found to be negligible.

In estimating the absolute accuracy of measurement for this method, consideration must be given to the difference in sign of several of the errors and the variation of several with the operating frequency. The absolute accuracy appears to be not greater than 20 percent for stock equipment. However, an accuracy of 5 percent may be attained if the following precautions are taken: correction of possible maladjustments of set; positioning of the set to provide for optimum orientation of the loop antenna or use of an extension fitting to raise the loop antenna appreciably above the set: measurement and application of a correction factor for the nonlinearity of the first detector; and application of a correction factor for the distributed-capacitance effect.

The accuracy of the second method of field-intensity measurement discussed, depends largely upon the accuracy of the calibrated voltage generator. Since commercial equipment of this type is available with an accuracy of ±3 percent up to 3,000 kc/s, this method combines simplicity of manipulation with accuracy of the voltage-determining means. Other possible sources of error with this method are (d), (e), (f), (g), and (h) of the enumeration in section I. The error of type (h) is present in this method, even though a Q-factor measurement is not explicitly made, because the distributed field voltage and the lumped calibrating voltages are stepped-up differently by resonating the loop antenna prior to comparison.

In a number of sets employing this method which were tested, errors of types (d), (e), and (f) were generally found of negligible order. In several sets, mounted on automobiles with the loop antennas extending above the top, errors of type (g) were up to 20 percent in magnitude and varied with the orientation of the loop antenna with respect to the automobile. One set which employed a single loop antenna to cover a frequency range of from 550 to 1,550 kc/s had an error of type (h) equal to 12 percent at the upper frequency. In general, sets of this type have a probable over-all absolute accuracy of not better than 15 percent. (This neglects the proximity error caused by installation in an automobile.) When a correction factor is applied for the effect of distributed capacitance of the loop antenna, a probable absolute accuracy of about 5 percent appears reasonable.

The sets tested, representative of the third method of field-intensity measurement, were of identical manufacture. The following errors were detected. Errors in the calibrating voltage ranged up to 5 percent. One set showed an error caused by nonlinearity of the first detector up to 5 percent; the other sets were free from this error. The voltage attenuator was in general accurate to within the limits of measurement, that is, 2 percent. However, individual steps of the attenuator were found to be in error up to 10 percent in two of the sets. The output indicating system was in general linear within 2 percent, provided that the lower sixth of the indicator scale was not employed. However, in two sets, aging of the output meter produced errors up to 8 percent. Errors of the types (d) and (e) were found to be of negligible order. Incorrect setting of the antenna balancing condenser in one set produced an error of type (f) ranging up to 6 percent at 1,500 kc/s. This type of equipment employs a single loop antenna to cover the frequency range of from 550 to 1,550 kc/s and hence is subject to a material distributed-capacitance error at the upper frequencies; the magnitude of this error was found to be 15 percent at 1,500 kc/s in all of the sets tested.

The over-all absolute accuracy of this equipment may be estimated at not better than 20 percent. After application of a correction factor for the distributed-capacitance effect, the probable accuracy becomes about 10 percent. An absolute accuracy of 5 percent may be attained by correcting for such errors as may be present in the calibrating voltage, in the introduction of the calibrating voltage, in possible nonlinearity of the detector, in individual steps of the voltage attenuator, and in the output indicating system.

III. ANALYSIS OF EFFECT OF DISTRIBUTED CAPACITANCE OF LOOP ANTENNA

The importance of the difference in the Q-factor of the loop antenna for a distributed induced voltage and for a lumped voltage at its center has been indicated in the previous section. The availability of an exact correction factor which could be employed to take this effect into account would increase the absolute accuracy of commercial radio field-intensity measuring sets to an appreciable degree. An analysis of the underlying phenomenon leading to the derivation of the correction factor follows.

As already indicated, the difference in the Q-factor arises from the distributed capacitance of the loop antenna. Because of the distributed capacitance, the current is different in different portions of the loop antenna. The nature of the effect of the distributed capacitance upon the current distribution in a tuned loop antenna (and upon the distribution of the equivalent effective resistance) was given in several papers by Breit [1] in 1921 and 1922.

Breit showed that the current distribution at resonance is independent of the distribution of voltage and is the same as if the system were nondissipative. The latter point leads to the conclusion that the current distribution is also independent of resistances introduced at various points along the loop antenna and enabled Breit to measure the current distribution in several loop antennas by the resistance-variation method. In an unpublished thesis submitted to the University of Minnesota in 1928, Bailey [2] proved this conclusion experimentally.

Proceeding with Breit's theory, the currents at any two points, 1 and 2, along a loop antenna are related by eq 1 below, which is based on the equality of power at the two points. (The resistances R_1 and R_2 may be defined as the equivalent resistances at points 1 and 2).

$$\frac{i_1}{i_2}=\frac{\sqrt{R_2}}{\sqrt{R_1}}. \tag{1}$$

Placing $e_2=R_2 i_2$, and substituting for i_2 in eq 1, we have

$$i_1=\frac{e_2}{R_2}\cdot\sqrt{\frac{R_2}{R_1}}=\frac{e_2}{\sqrt{R_1R_2}}. \tag{2}$$

Hence, the relation between the current (i_0) which enters the effective tuning condenser as a result of a lumped voltage (e_m) inserted at the center of the loop antenna is given by eq 3,

$$i_0=\frac{e_m}{\sqrt{R_0R_m}}. \tag{3}$$

In this equation, R_0 is the equivalent resistance of the loop antenna at its grid end and R_m is the equivalent resistance at its center. (The significance of the terms i_0 and e_m will appear from figure 1(a), which corresponds substantially to the circuit arrangement employed in each

[1] G. Breit, *The distributed capacitance of inductance coils*, Phy. Rev. 17, 649 (1921).
G. Breit, *High-frequency resistance of inductance coils*. BS Sci. Pap. 17, 569 (1922) S430.
[2] Stuart L. Bailey, *The characteristics of the coil aerial as used with radio signal intensity measuring apparatus*. Thesis for degree of Master of Science, submitted to University of Minnesota (June 1928).

of the three methods of field-intensity measurement discussed.) For a uniformly distributed voltage ($e_x \cdot dx$) induced per elementary length (dx) of wire

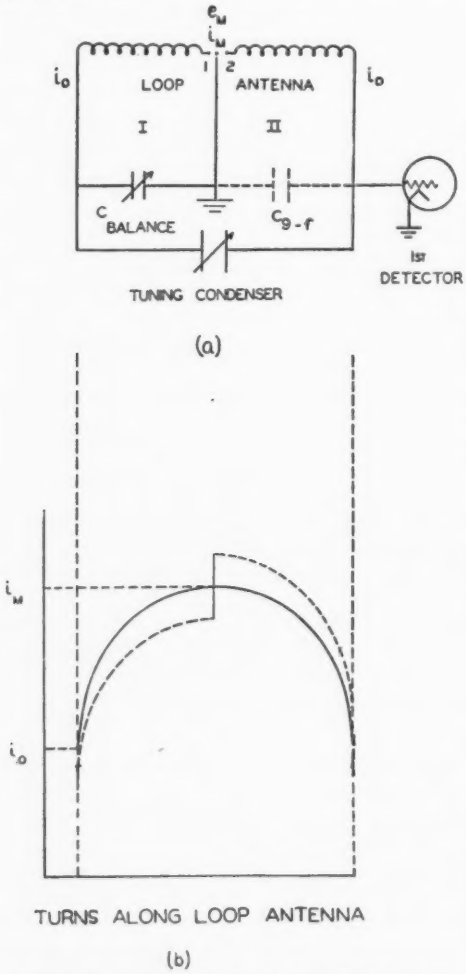

FIGURE 1.—*Arrangement of balanced loop antenna in the methods of field-intensity measurement considered, and current distributions for two conditions of antenna balance.*

$$i_0 = \frac{1}{\sqrt{R_0}} \int \frac{e_x \cdot dx}{\sqrt{R_x}}, \quad (4)$$

where R_x is the equivalent resistance at the point x along the wire.

Now, in each of the methods of measuring field intensity discussed in the foregoing section, i_0 corresponding to the lumped and distributed voltages is adjusted to equality and the assumption is made that for this condition, writing h_e for the effective height of the loop antenna and ϵ for the field intensity

$$e_m = [\int e_x \cdot dx = h_e \epsilon] \quad (5a)$$

instead of the actual relationship from eq 3 and 4, namely,

$$e_m = \int e_x \sqrt{\frac{R_m}{R_x}} \cdot dx. \quad (5b)$$

Therefore, a certain factor must be applied to the value of e_m in order to determine the true value of the induced voltage. This correction factor, derived from the approximate expression (eq 5a) and the correct expression (eq 5b), is defined by F in the following equation:

$$\frac{1}{F} = \frac{\int e_x \cdot \sqrt{\frac{R_m}{R_x}} \cdot dx}{\int e_x \cdot dx}, \quad (6)$$

which may be written by using eq 1:

$$\frac{1}{F} = \frac{\int e_x \cdot \frac{i_x}{i_m} \cdot dx}{\int e_x \cdot dx}. \quad (7)$$

Now, if the induced voltage per elementary length is assumed independent of x (that is, is uniformly distributed), we have

$$\frac{1}{F}=\frac{e_x \cdot \frac{1}{i_m}\int i_x \cdot dx}{e_x \int dx}=\frac{i_{ave}}{i_m} \tag{8}$$

and

$$F=\frac{i_m}{i_{ave}}. \tag{9}$$

The correction factor is seen to be intimately tied up with the current distribution along the loop antenna. The factor F differs from unity to the extent that the distributed capacitance of the loop antenna causes the current at resonance to vary throughout the antenna.

So far in our analysis, no consideration has been given to the actual current distribution along the loop antenna. To evaluate the correction factor an exact knowledge of the current distribution is required. Referring to figure 1(b), the solid curve shows qualitatively the current distribution when the loop antenna is exactly balanced. The symmetry of the distribution curve is lost if any unbalance of the loop antenna occurs. Thus, the dotted curve corresponds to the current distribution when the balancing condenser is reduced below its value for exact balance. It should be emphasized that the distribution curves shown apply independently of the voltage distribution; the latter may be uniformly distributed or introduced as a lumped voltage at points 1 or 2, figure 1(a). In the following derivations, exact symmetry of the current-distribution curve is assumed and, hence, exact antenna balance. The effect of antenna unbalance will be treated later in this paper.

A summation relationship equivalent to eq 6 was derived by Bailey (see footnote 2), in an extension of Breit's work carried on to derive an expression for the correction factor with which we are dealing. Bailey chose to work with resistance distribution because of the possibility of measuring the effective resistance directly. He found that the resistance distribution could be represented by an inverse parabolic curve and derived the following expression

$$R_x=\frac{R_m}{1-\left(1-\frac{R_m}{R_0}\right)x^2}, \tag{10}$$

where $x=2n/N$, N being the total number of turns in the loop antenna and n indicating the number of turns from the center. By measuring the terminal resistances of a loop antenna at several frequencies and averaging $\sqrt{(R_m/R_x)}$ along only the vertical portions of the loop antenna to take account of the fact that the field voltage is not actually uniformly distributed along the entire loop antenna, Bailey obtained several values for the correction factor. Actually, the error introduced by assuming the voltage uniformly distributed is small for even a two-turn loop antenna of any shape and becomes negligible as the turns are increased to about six. Since Bailey used a six-turn loop antenna, his

factor may be calculated by using eq 6 and 10, with a negligible error, giving

$$\frac{1}{F}=\frac{1}{2}\left\{\sqrt{\frac{R_m}{R_0}}+\frac{\sin^{-1}\sqrt{1-\frac{R_m}{R_0}}}{\sqrt{1-\frac{R_m}{R_0}}}\right\}. \tag{11}$$

However, the utility of eq 11 is limited in the practical case, since it is not usually convenient to measure either R_0 or R_m in commercial field-intensity measuring sets. A second method of attack is made possible by considering the following relation derived by Breit

$$\frac{i_0}{i_{ave}}=1-\left(\frac{f}{f_0}\right)^2, \tag{12}$$

where (f/f_0) is the ratio of the operating frequency to the natural frequency of the loop antenna. Assuming a current distribution to correspond with the inverse parabolic resistance distribution found by Bailey, it is possible to determine from eq 1, 10, and 12 the relationship between i_z and i_m as a function of the argument (f/f_0) and thus from eq 8 to derive a general expression for F in terms of (f/f_0). Thus, we have the factor expressed in terms of an argument which may be readily measured. The relationship for the current distribution and the corresponding expression for F are given, respectively, in the first line of the second and third columns of table 1.

Working independently, Baker and Huxley [3] derived an expression for F as a function of the ratio of the distributed capacitance to the tuning capacitance of the loop antenna on the basis that the loop antenna may be represented as a uniform transmission line. Expressions for the current distribution corresponding to this assumption and for the factor F in terms of the argument (f/f_0) are given, respectively, in the second line, second and third columns, of table 1.

Still another possible workable assumption is to proceed from eq 8 and 12, assuming a parabolic current distribution. Breit stated in his papers that this distribution corresponded approximately to his measured values. The derived expressions for current distribution and the factor F, corresponding to this assumption, are given, respectively, in the third line, second and third columns, of table 1.

However, none of the three relations for the correction factor was found to agree with many experimental determinations made in the process of calibrating field-intensity measuring sets at the National Bureau of Standards. An orderly examination of the data showed that the correction factor should be of the order of one-half that given by the transmission-line theory, and materially lower than given by the other two theories, particularly for the larger values of (f/f_0). Accordingly, a further examination of the underlying theory was made. Studying Breit's analysis, it became apparent that his mathematics pointed to an elliptical current distribution even though he had suggested from his measured values that the distribution was approximately parabolic. An expression for F derived on the basis of elliptical current distribution, was found to fit the data rather nicely. The

[3] W. G. Baker and L. G. H. Huxley, Correction to Field Strength Measurements with Loop Antennae. Radio Research Board of Australia Bulletin 47, Report 1, Melbourne (1931).

expressions for the current distribution and for the correction factor, corresponding to this assumption of an elliptical current distribution, are given, respectively, in the fourth line, second and third columns, of table 1.

It should be noted in connection with table 1, that the correction factors tabulated are based on an assumption of uniformly distributed field voltage along the wire of the loop antenna and hence are not exact. However, as has already been noted, the departure from exactness is quite small and decreases with an increasing number of turns in the loop antenna. In the case of the elliptical current distribution, a two-turn square-loop antenna mounted on a side would have as its exact correction factor the value

$$F=\frac{1+\left(\frac{4}{\pi}-1\right)\alpha}{1+0.030\alpha}, \tag{13a}$$

while for a two-turn square-loop antenna mounted on a corner, the exact factor would be

$$F=\frac{1+\left(\frac{4}{\pi}-1\right)\alpha}{1+0.020\alpha}. \tag{13b}$$

TABLE 1.—*Expressions for current distribution and correction factor corresponding to the four assumptions considered*

[$\alpha=(f/f_0)^2$ and $x=2\pi/N$]

Basic assumption	Expression for current distribution (i_z/i_m)	Expression for correction factor, F
Inverse parabolic distribution of resistance	$\sqrt{1-x^2\sin^2\theta}$, where $\frac{\theta}{\sin\theta\cos\theta}=\frac{1+\alpha}{1-\alpha}$	$\frac{1-\alpha}{\cos\theta}$, where $\frac{\theta}{\sin\theta\cos\theta}=\frac{1+\alpha}{1-\alpha}$
Uniform transmission-line theory	$\cos\phi\cos\{(1-x)\phi\}+\sin\phi\sin\{(1-x)\phi\}$, where $\frac{\phi}{\tan\phi}=1-\alpha$	$\frac{\phi}{\sin\phi}$, where $\frac{\phi}{\tan\phi}=1-\alpha$
Parabolic current distribution	$1-\frac{3\alpha}{2+\alpha}\cdot x^2$	$1+\frac{1}{2}\cdot\alpha$
Elliptical current distribution	$\frac{1+\frac{4}{\pi}\cdot\frac{\alpha}{1-\alpha}\cdot\sqrt{1-x^2}}{1+\frac{4}{\pi}\cdot\frac{\alpha}{1-\alpha}}$	$1+\left\{\frac{4}{\pi}-1\right\}\cdot\alpha$

The factor rapidly converges to that given in the table, as the number of turns increases. Thus, for a four-turn square-loop antenna mounted on a side, the exact factor is

$$F=\frac{1+\left(\frac{4}{\pi}-1\right)\alpha}{1+0.011\alpha} \tag{13c}$$

In figure 2 are presented plots of the factor F as a function of (f/f_0), corresponding to the four basic assumptions outlined. The four points of figure 2 designated by cross symbols correspond to

data derived empirically by Bailey on the basis of resistance-distribution measurements. These should check exactly the graph corresponding to inverse parabolic resistance distribution; the slight

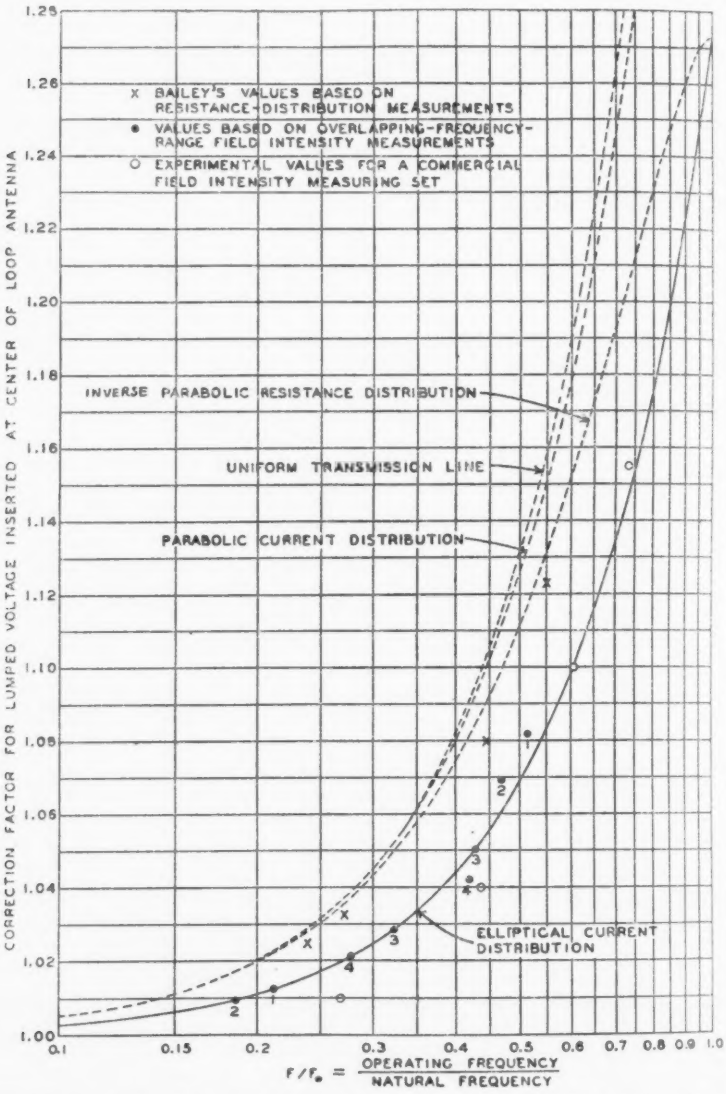

FIGURE 2.—*Graphs showing the derived correction factors for the distributed-capacitance effect corresponding to four assumed distributions of current along the turns of the loop antenna.*

The graph corresponding to elliptical current distribution agrees well with the experimental data.

departure is probably due to experimental errors in measurement. It will be noted from figure 2 that the assumption of elliptical current distribution yields values of F which are materially lower than ob-

tained from the other three theories. An analysis of experimental results to show that this is probably the correct factor will be given in the following section.

Before proceeding to the experimental results, it is of interest to consider the order of agreement of the several assumed current distributions with available published values. In figure 3 are plotted the four current distributions considered; the ordinate scale corresponds to the ratio of the current on specific turns of a loop antenna to the current at the center, while the abscissa scale corresponds to the turns number. The plot is carried out for a 14-turn loop antenna, since Breit published measured current values for such an antenna. Breit's values are shown by the open-circle symbols in figure 3. It will be seen that the curve of elliptical current distribution conforms

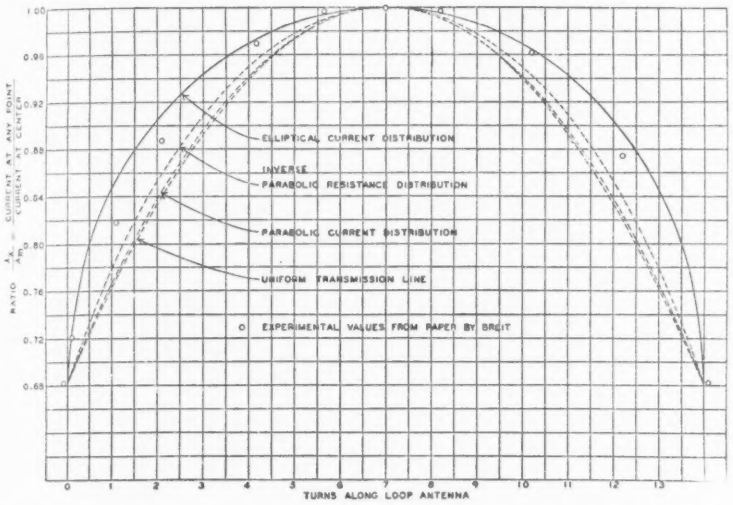

FIGURE 3.—*Graphs showing the current distribution corresponding to the four assumptions treated in the theoretical analysis.*

The open-circle symbols denote experimental values from Breit's papers.

most closely to the measured distribution. Further evidence for the probable correctness of the assumed elliptical current distribution is seen from figure 4. In this figure are plotted graphs corresponding to three of the assumed distributions, showing the variation of the ratio of the current at the center of the loop antenna to the current at its ends as a function of the operating frequency. (Because of the close equivalence of the current distributions for the uniform transmission line theory and the inverse parabolic resistance theory, the graph for the former is not included in fig. 4.) The points having open-circle symbols denote the values of the ratio taken from Breit's published data, while the points having cross symbols are derived values based on Bailey's resistance measurements. It will be observed that the case for elliptical current distribution again agrees most closely with the experimental data.

IV. ANALYSIS OF EXPERIMENTAL DATA ON DISTRIBUTED-CAPACITANCE EFFECT

The ratio of the values of F corresponding to two measured values of (f/f_0) may be determined on the basis of field-intensity measurements with two loop antennas operating in the overlapping portion of their frequency ranges. Four such determinations were made using three loop antennas in each of two field-intensity measuring sets and are plotted in figure 2. Since, for each determination, loop antenna A is operating near its lowest value of (f/f_0) and loop antenna B near its highest value, the ratio of the two field-intensity measurements should represent, to a first approximation, the value of F_B corresponding to $(f/f_0)_B$. A closer value for F_B may be obtained by taking a value for F_A from any of the graphs of figure 2 corresponding to

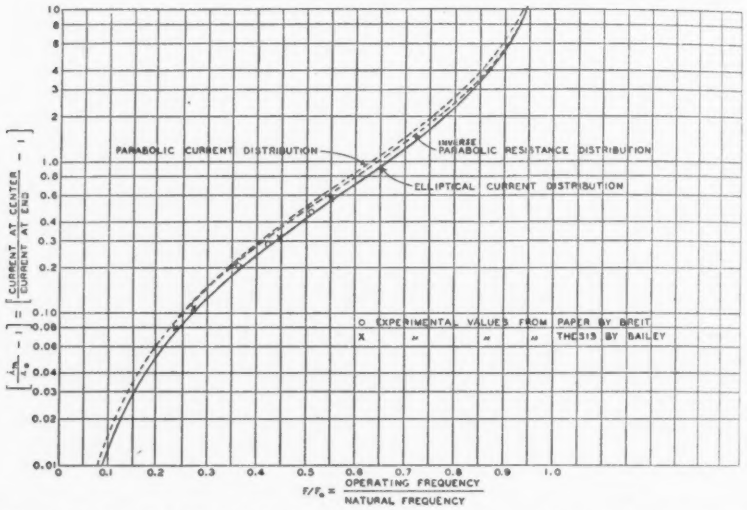
PARABOLIC CURRENT DISTRIBUTION
INVERSE PARABOLIC RESISTANCE DISTRIBUTION
ELLIPTICAL CURRENT DISTRIBUTION
O EXPERIMENTAL VALUES FROM PAPER BY BREIT
X " " " THESIS BY BAILEY
[CURRENT AT CENTER / CURRENT AT END] = [Δn/f0 - 1]
F/F0 = OPERATING FREQUENCY / NATURAL FREQUENCY

FIGURE 4.—*Graphs showing the variation with frequency of the ratio of the current at the center of the loop antenna to the current at its end corresponding to three of the current distributions considered.*

The open-circle points are from Breit's published values and the cross symbols denote values derived from Bailey's resistance measurements.

$(f/f_0)_A$ and increasing the ratio accordingly. In figure 2 the solid circles represent the results of the four determinations adjusted on this latter basis; the values of F_A were in each case chosen from the graph corresponding to elliptical current distribution. The numerals in the illustration serve to identify the two points for each determination. In the first determination (1—1), the ratio of measured field intensities was 1.068 and the values of (f/f_0) for antennas A and B were 0.213 and 0.511, respectively. From the graph, F_A equals 1.013. Hence the value for F_B becomes $1.013 \times 1.068 = 1.082$. It will be noted that the experimental points agree very nicely with the theoretical graph. However, had the values of F_A been chosen from one of the other theoretical graphs, the fit to that graph would not be nearly as good.

The open circles in figure 2 represent the values of the correction factor F at several measured values of (f/f_0) for a commercial apparatus which employs a single loop antenna to cover the frequency range of from 550 to 1,550 kc/s. (The correction factor was found to be very nearly the same for five sets of this manufacture.) The values were obtained from comparative field-intensity measurements with this apparatus and with a standard set corrected for the distributed-capacitance effect on the basis of overlapping frequency-range field-intensity measurements. The experimental data are again seen to fit the theoretical graph for elliptical current distribution.

Added experimental evidence, to show that the graph corresponding to elliptical current distribution probably represents the true correction factor, will be presented in the following section.

V. ΔC METHOD FOR ELIMINATING THE DISTRIBUTED-CAPACITANCE EFFECT

It was first pointed out by Baker and Huxley[4] that the true Q-factor of the antenna for a distributed induced voltage is obtained provided the measurement is carried out by the condenser-variation method. The reason for this is that the effective resistance measured in this method of determining the Q-factor is the average resistance throughout the loop antenna. In 1935 the Federal Communications Commission designed a field intensity measuring set for service as a secondary standard in its survey of clear-channel broadcast frequencies. For use in the conventional voltage-comparator method of measuring field intensity, the set embodied an oscillator, a number of interchangeable plug-in resistors and inductors, and thermoelements of different current ratings, for inserting known lumped voltages at the center of the loop antenna. The same means could be applied to calibrate the radio receiver as a sensitive electron-tube voltmeter. Hence, the Q-factor of each of the loop antennas, corresponding to lumped voltages at the center, could be measured. In addition, the apparatus included a small, calibrated, precision condenser, connected in parallel with the main tuning condenser; this ΔC condenser, in combination with the calibrated tube-voltmeter, permitted the measurement of the Q-factor by the condenser-variation method to a high degree of accuracy. Assuming that the latter determination yields the true value of Q-factor for a distributed field, the ratio of the values obtained by the two methods of measurement should equal the value of F corresponding to the particular value of (f/f_0) for which the measurements were made.

To test the efficacy of the ΔC method for eliminating the distributed-capacitance effect, comparative field-intensity measurements were first made using the three loop antennas of the set (in pairs) at overlapping frequencies. The results showed that the effect was practically eliminated. Next, a series of measurements was made of the Q-factors for distributed and lumped voltages using the two methods just described. The measurements were made for the three antennas of the set for different values of the argument (f/f_0). The ratios of the Q-factors agreed quite closely with the values given by the graph corresponding to elliptical current distribution in figure 2.

[4] W. G. Baker and L. G. H. Huxley, Correction to Field Strength Measurements with Loop Antennae. Radio Research Board of Australia Bulletin 47, Report 1, Melbourne (1931).

Next, a series of measurements was made of the Q-factors by the condenser-variation method using both lumped voltages and distributed fields. For a given antenna and a given value of (f/f_0), the Q-factor was found to be the same whether a lumped voltage or a distributed field was employed.

Finally, a series of comparative field-intensity measurements was made using both the voltage comparator and the ΔC methods in the Federal Communication Commission's set, and also a standard set of the National Bureau of Standards; the latter also had incorporated in it means for measuring intensity by the voltage-comparator method. The results of the intercomparisons are shown in figure 5.

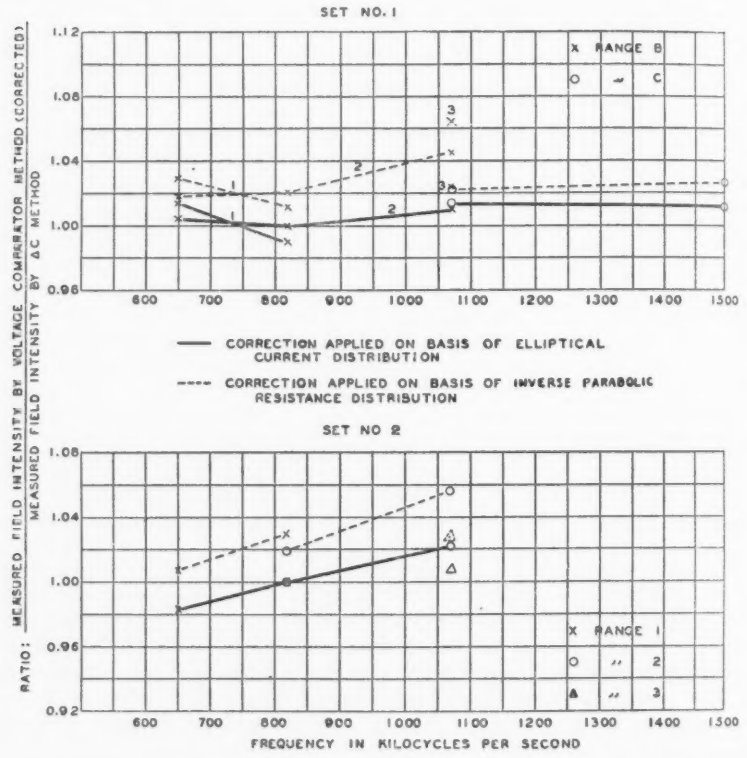

FIGURE 5.—*Graphs showing the comparison of measured values of field intensity by the ΔC and voltage-comparator methods, the latter values being corrected for the distributed-capacitance effect by factors derived on the basis of elliptical current and inverse parabolic resistance distributions.*

In the upper part of figure 5, the Bureau's standard set is compared against the ΔC measurements. The full lines plot the ratios of the field intensities measured with the Bureau's set, corrected in accordance with the factors derived for elliptical current distribution, to the field intensities measured by the ΔC method on the Commission's set. The cross symbols indicate that antenna B was used on the Bureau's set and the open-circle symbols that antenna C was used. The

numbers near the lines indicate, respectively, that antenna 1, 2, or 3 was used on the Commission's set. It will be observed that the agreement was within 2 percent, the limit of accuracy of the measurements.

The dotted lines in figure 5 plot the corresponding ratios of the measured field intensities on the basis that the corrections to the measured values with the Bureau's set are made in accordance with the factors derived for inverse parabolic resistance distribution. (See fig. 2.) This distribution was chosen for a comparison since it represented the least departure from the theoretically correct elliptical current distribution. It will be seen that the agreement is not as good, one point being out by about 6 percent. If no corrections had been applied to the measurements with the Bureau's set, differences up to 6 percent (in the opposite direction) would have been obtained.

In the lower part of figure 5 the measurements with the voltage-comparator and ΔC methods in the Commission's set are compared. The full lines plot the ratios of the field intensities measured with the voltage-comparator method (and corrected in accordance with the factors derived for elliptical current distribution) to the field intensities measured with the ΔC method; the agreement is within 2 percent. Here, again, the dotted lines plot the corresponding ratios of the measured field intensities with the corrections to the voltage-comparator measurements made in accordance with the factors derived for inverse parabolic resistance distribution. The deviation is again up to 6 percent. Had no corrections been applied to the voltage-comparator measurements, differences up to 5 percent (in the opposite direction) would have been obtained.

An explanation of the small errors observed for the distributed-capacitance effect in this intercomparison may be of interest at this point. Both the Bureau's and the Commission's sets were designed to limit this error by employing, respectively, two and three loop antennas for covering the frequency range used. In this way, the upper value of (f/f_0) employed was kept reasonably low, below 0.5 and 0.4, respectively.

It will be seen that all of the experimental evidence points to the fact that the ΔC method is completely free from the distributed-capacitance error.

VI. UNTUNED LOOP ANTENNA

It is of interest to note that the effect of distributed capacitance of the loop antenna on the accuracy of field-intensity measurements may be avoided by the expedient of using an untuned loop antenna, since uniform current distribution is then obtained in the loop antenna, so that the correction factor given by eq 9 is unity. There is, of course, the attendant disadvantage of required high receiver amplification, high set noise, etc. A set embodying this feature was calibrated at the Bureau. The ratio of the measured values of field intensities with this set to the measured values with a standard set (after correction of the latter for distributed-capacitance effect) was found to equal 1.05 ± 0.03, in the frequency range of from 550 to 1,600 kc/s. There was no evidence of a definite trend of variation of this ratio with frequency. Hence, assuming that the 5-percent average difference was caused by some other factor, not determined in the intercompari-

son, the distributed-capacitance effect appears to be avoided with an untuned loop antenna.

VII. SHIELDED LOOP ANTENNA

Another expedient for minimizing the distributed-capacitance effect is to employ a shielded loop antenna. One terminal of the loop antenna is connected to ground through the resistor across which the calibrating voltage is applied. The shield and one side of the tuning condenser are grounded at the same point. The other terminal of the loop antenna and the other side of the tuning condenser are connected to the receiver input. (See fig. 6(a).) The calibrating voltage is thus applied in series with the loop antenna at its grounded end. The current charging the distributed capacitance between the loop antenna and the shield is seen to pass through the calibrating resistor.

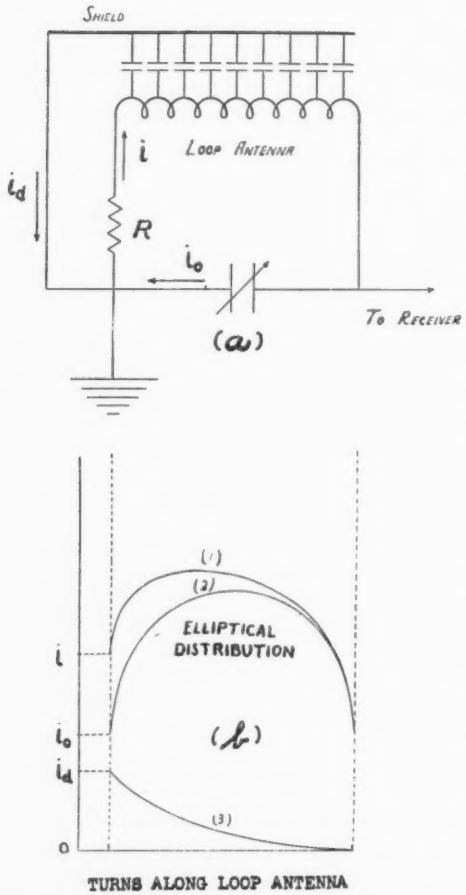

FIGURE 6.—*Sketch and graphs showing the current distribution in an unbalanced shielded loop antenna having the calibrating voltage inserted at its grounded end.*

The current distribution along the turns of the loop antenna now becomes approximately as shown by graph 1 of figure 6 (b). The current in any turn may be considered as being made up in part by the current which would exist if the loop antenna were unshielded and balanced with respect to ground (graph 2) and in part by the charging current for the effective distributed capacitance to the shield of the portion of the loop antenna beyond the turn considered (graph 3). Since the current distribution at resonance is independent of the distribution of voltage, the current distribution of graph 1 will apply for both the distributed field voltage and the lumped calibrating voltage. An analysis of why this type of distribution tends to minimize the effect of the distributed capacitance of the loop antenna follows:

Proceeding as in the derivation of eq 9, the current i_0 through the tuning condenser, which is produced by the voltage e across the calibrating resistor, is

$$i_0 = \frac{e}{\sqrt{R_0 R}}, \tag{14}$$

where R_0 and R are, respectively, the equivalent resistances of the loop antenna at the ungrounded and grounded ends. Hence, when e is adjusted to give the same value of i_0 as produced by the field voltage (see eq 4), it has the magnitude

$$e = \int e_x \sqrt{\frac{R_0}{R_x}} \cdot dx. \tag{15}$$

Hence, when the assumption is made that $e = \int e_x . d_x$, the evaluated field intensity is too high and must be corrected by a factor which comes out to be equal to

$$F = \frac{i}{i_{ave}}. \tag{16}$$

Here i is the current through the calibrating resistor and is greater than the current through the condenser. (See Fig. 6.) Since the current i may be equal to the average current along the loop antenna (if the equivalent distributed capacitance between the loop antenna and the shield is of the correct magnitude) the correction factor, as given by eq 16, may be equal to unity. Furthermore, since the current distribution is a function of the relative magnitudes of two distributed capacitances, the condition of unity correction factor may prove to be independent of the operating frequency.

It is of interest to note that the tendency to minimize the distributed-capacitance effect is produced solely by the unbalanced connection of the loop antenna with respect to ground and not by the shield. The latter controls the value of the current i_d and its distribution and hence determines how closely the condition of unity correction factor is approached. The shield, however, serves the important function of eliminating the vertical or antenna effect. For the case where the loop antenna is balanced and the calibrating voltage is inserted at one end, the currents at the two ends of the loop antenna are equal ($i = i_0$). The current distribution along the loop antenna for this balanced condition is given by eq 12. Substituting these two relationships in eq 16, we have

$$F = 1 - \left(\frac{f}{f_0}\right)^2, \tag{17}$$

which is the correction factor for the calibrating voltage inserted at one end of a *balanced* loop antenna. Here the factor is seen to vary with frequency. See, for comparison, the expressions for the correction factor given in table 1 for the case where the calibrating voltage is inserted at the center of the loop antenna.

The action of the antenna unbalance in minimizing the distributed-capacitance effect was determined in the calibration of a field-intensity measuring set having a shielded loop antenna with the calibrating

voltage applied as indicated in figure 6(a). A switch in the loop antenna permitted using either a 16-turn or a 12-turn connection, as desired. The object of the calibration was to determine the loop-antenna coefficients for the two connections. The results of the calibration are given in table 2. The first column gives the operating frequency, the second column the ratio of the operating frequency to the natural frequency, and the third column the corresponding measured values of the antenna coefficient. The latter is defined in terms of the field intensity, the operating frequency and readings of the output meter and voltage attenuator of the set; it constitutes a lumped factor including the value of the calibrating voltage and the turns area of the antenna. The fourth column of table 2 gives the value this factor would have for a single-turn loop antenna of the same dimensions. The fifth column gives the percentage deviation of the individual determinations from the average measured value. The trend of variation of the antenna coefficient with frequency is seen to be quite small, whereas the operating frequencies employed would appear to require a material correction factor (see eq 17) were it not for the unbalanced current distribution. However, such trend as is noted points to the importance of checking individual designs for possible variation of the antenna coefficient with frequency.

TABLE 2.—*Data showing negligible distributed-capacitance effect for shielded loop antenna*

Frequency (f)	Ratio of operating frequency to natural frequency $\left(\frac{f}{f_0}\right)$	Loop-antenna coefficient $\left(K=\frac{Ef}{MA}\right)$	Equivalent loop-antenna coefficient for one turn (KN)	Percentage deviation from average value of KN
16-TURN CONNECTION OF LOOP ANTENNA				
kc/s				
650	0.29	424	6,780	−0.2
650	.34	425	6,800	+.1
800	.42	415	6,640	−2.2
850	.45	414	6,625	−2.5
1,050	.55	428	6,845	+0.8
1,050	.55	436	6,975	+2.7
1,100	.58	428	6,845	+0.8
12-TURN CONNECTION OF LOOP ANTENNA				
1,050	0.42	568	6,820	+0.4
1,100	.45	552	6,630	−2.4
1,300	.52	564	6,750	−0.6
1,400	.56	575	6,900	+1.7
1,500	.61	575	6,900	+1.7

VIII. PRECAUTIONS FOR ATTAINING MAXIMUM ACCURACY

In section II an estimate was given of the probable absolute accuracy of commercial field-intensity measuring sets at frequencies below about 1,600 kc/s. It was shown that by applying corrections for the several errors likely to occur in the different methods, the absolute

accuracy may be stepped up from not better than 15 or 20 percent to a possible 5 percent. Except for errors of types (g) and (h), the errors encountered are all amenable to correction on the basis of laboratory measurements. As was shown, errors of type (h) may be taken into accurate account by measuring the natural frequency of the loop antenna and applying a theoretical correction factor as a function of the argument (f/f_0). Hence, where care is taken to minimize possible distortion of the field which it is desired to measure, measurements may, in general, be carried out to the 5-percent accuracy

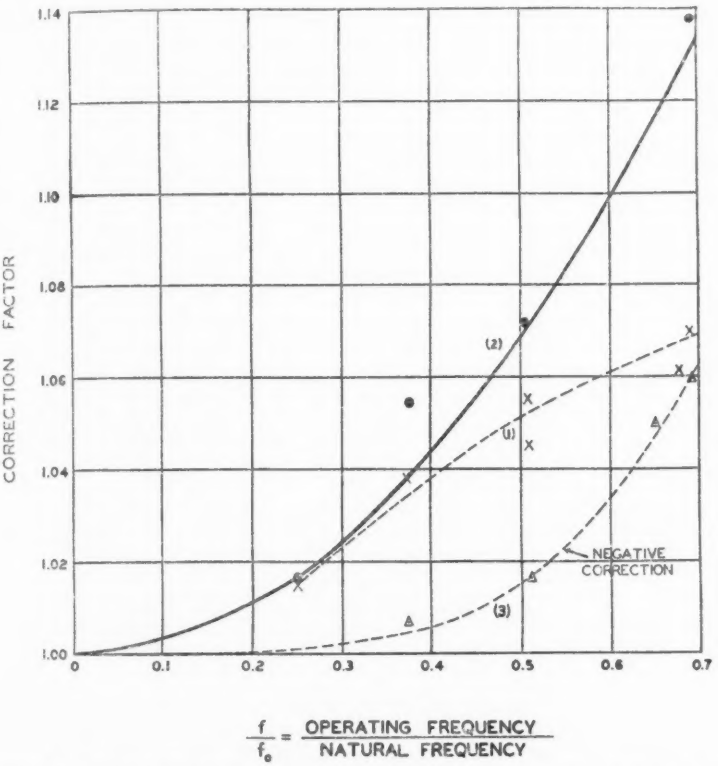

FIGURE 7.—*Graphs showing partial neutralization of the distributed-capacitance effect by an error introduced due to antenna unbalance.*

In the derivation of the correction factor to be applied for the distributed-capacitance effect when the lumped calibrating voltage is inserted at the center of the loop antenna, it was assumed that the loop antenna was in exact balance. The effect of incorrect adjustment of the balancing condenser (see fig. 1) will now be considered.

In one field-intensity measuring set, the variation of the measured values of the correction factor as a function of (f/f_0) was found to be as shown by graph 1 of figure 7. The cross symbols represent the actual observations. The cause for the large departure of the measured values of the correction factor from the values derived theoretically (reproduced as graph 2) was investigated and was found to be

unbalance of the loop antenna. The balancing condenser was found to be set at its minimum value. Upon adjusting it for exact balance (at 1,500 kc/s) the correction factors for several values of (f/f_0) were again determined and are given by the solid-circle symbols in figure 7. Note the excellent agreement with the theoretically derived factors.

The method employed in adjusting the balancing condenser for exact antenna balance seemed to indicate the reason for the difference between graphs 1 and 2. Referring to figure 1, the calibrating voltage was inserted alternately at points 1 and 2 for different settings of the balancing condenser and the corresponding voltages applied to the first detector were measured. With the condenser at minimum, the voltage appearing across the first detector corresponding to position 1 of the calibrating voltage was 10 percent smaller than that corresponding to position 2 of the calibrating voltage. With the condenser at maximum (25 $\mu\mu$f), the voltage corresponding to position 1 was 15 percent larger than that corresponding to position 2. At an intermediate value of the balancing condenser (15 $\mu\mu$f), the input voltages to the detector corresponding to the two positions of the calibrating voltage were equal. This is the setting for exact balance. It is of importance to note that the balance thus obtained differed appreciably at the higher frequencies from the balance determined on the basis of the conventional resonance method. The balance realized on the basis of equality of output voltage is obviously the more fundamental in that it is more intimately related to the actual current distribution. Another interesting relation noted was that the sum of the input voltages to the detector corresponding to the calibrating voltage at the two positions was substantially constant regardless of the setting of the balancing condenser. The significance of this relation will appear below.

The facts determined by the foregoing experiment were (1) the field voltage, being induced in both halves of the loop antenna, produces the same voltage across the detector input regardless of the setting of the balancing condenser; this was checked by actual observations on uniform fields; and (2) the calibrating voltage, being inserted in one-half of the loop antenna, produces different detector voltages depending on the setting of the balancing condenser. At every setting, except that of exact antenna balance, the lead from the center tap of the loop antenna to ground carries current, so that the current distribution along the antenna exhibits a discontinuity at its center. (See the dotted curve in fig. 1(b). As a result an error is introduced by antenna unbalance (additional to the distributed capacitance error) in equating the calibrating voltage to the induced field voltage. This error may be either positive or negative depending on the setting of the balancing condenser and upon the point of insertion of the calibrating voltage.

In the case considered in graph 1 of figure 7, the balancing condenser being set at minimum and the calibrating voltage inserted at position 1, the voltage produced across the detector was less than would have been produced were the condenser at its proper setting. Hence, a negative error was introduced which served to offset, in part, the distributed-capacitance effect. It is obvious that the magnitude of this error varied not only with the degree of antenna unbalance but also with the magnitude of the balancing and tube capacitances in

relation to the tuning condenser and, hence, with (f/f_0). In figure 7, graph 3 was obtained by dividing the points on graph 2 by the corresponding points on graph 1 and should, therefore, show the variation of the error caused by unbalance as a function of (f/f_0). The triangle symbols correspond to direct measurements in this error for several values of (f/f_0). Each measurement consisted in first ascertaining the balance condition in the manner described and then, with the calibrating voltage at position 1, determining the ratio of the voltages produced across the first detector corresponding to balance and minimum setting of the balancing condenser. The agreement with graph 3 is quite good.

Two important conclusions may be drawn from the experiments just outlined. First, it is important to obtain exact antenna balance if the derived correction factors for the distributed-capacitance effect are to be applied. Secondly, a deliberate unbalance of the loop antenna may be introduced to offset automatically a major part of the distributed-capacitance effect. When combined with the use of antennas operating at values of (f/f_0) less than about 0.5, the resultant error may be reduced to the order of a few percent. The agreement of graph 3, which was derived indirectly from two sets of field-intensity measurements, with the laboratory determinations of the error due to antenna unbalance (indicated by the triangle symbols) points to the fact that any vertical or antenna effect introduced by the unbalance had little influence upon the measured field intensities.

To attain maximum accuracy, careful consideration must also be given to possible field distortion (i. e., error (g)). As already noted in section II, errors up to 10 percent were detected because of the distortion of the field by the set container, while errors up to 20 percent were observed by distortion of the field by the car in which the set was installed. Since the distortion is produced by secondary fields radiated from objects placed in the primary field, it is important to keep such objects as small as possible. There is, therefore, a theoretical argument for keeping the set container small, in addition to the practical one of portability. Where it is essential to have a large container or to install the set on an automobile, the loop antenna should be mounted as far as possible above the disturbing metal.

Figure 8 shows the effect of a large set container and the possibility of securing true measurements by placing the antenna outside of the portion of the field which is distorted. At the top of figure 8 is shown the variation in the measured field as a function of the orientation of the loop antenna with respect to the minor axis of the set container. The true value of the field is measured when the plane of the loop antenna coincides with the minor axis (0 to 180 degrees); the measured value is some 10 percent too high when the plane of the loop antenna is along the major axis (90 and 270 degrees). In the middle of figure 8 is shown the variation in the measured field when a small coil antenna is used in place of the loop antenna. The coil, being much nearer to the set container, is within the distorted field caused by the container; hence the error corresponding to the 90- and 270-degree positions is some 25 percent. There is seen to be practically no frequency effect in the amount of field distortion. When an extension fitting, approximately 18 inches long, was used to raise the coil antenna above the set, the true measured value was obtained for all orientations of the

coil with respect to the set. See the graphs at the bottom of figure 8. Obviously, the same treatment may be applied to the mounting of a loop antenna on an automobile, although the height required above the car top may introduce practical difficulties.

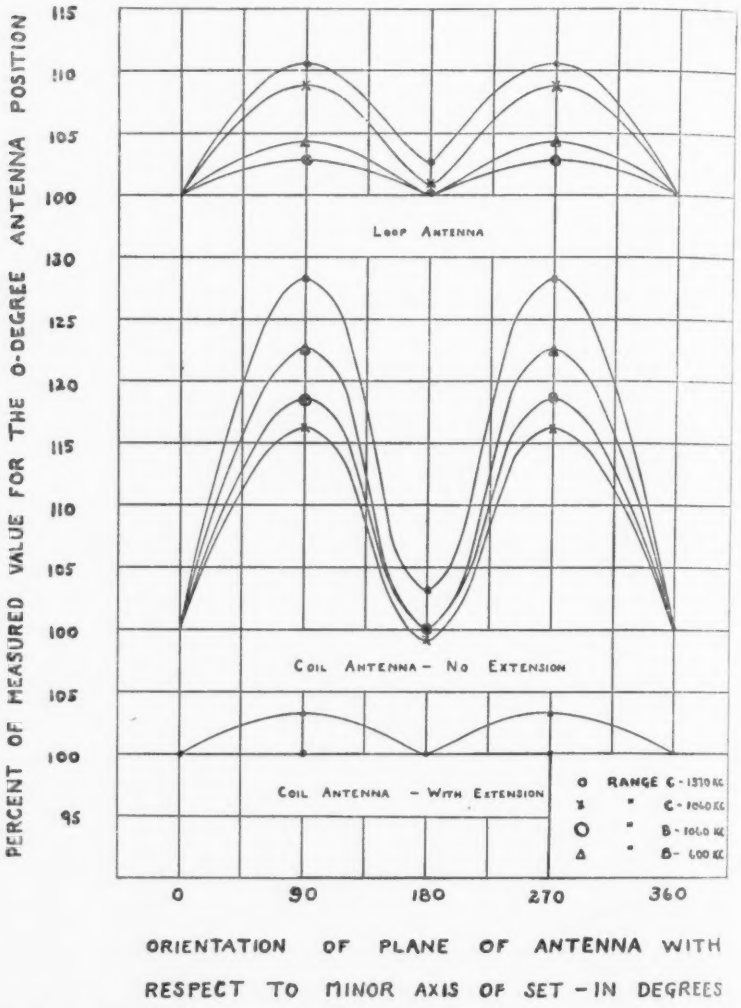

FIGURE 8.—*Graphs showing the effect of distortion of the field by the set container upon the accuracy of field-intensity measurements.*

Removal of the measuring antenna from the distorted field results in true field measurements.

As a final point of interest, figure 9 shows the results of calibration of a set which exhibited errors having a marked variation with frequency. The set was mounted in a car, but since no measurements were made with it outside of the car, there was no evidence to indicate whether or not the errors were due to the car installation. However,

other causes for the variation of the error with frequency may include set regeneration, resonant circuits in the connecting leads from the loop antenna to the set, and induction in the loop antenna from the calibrating oscillator. The observations on this set indicate the importance of preliminary analysis for possible errors before embarking upon actual field-intensity measurements.

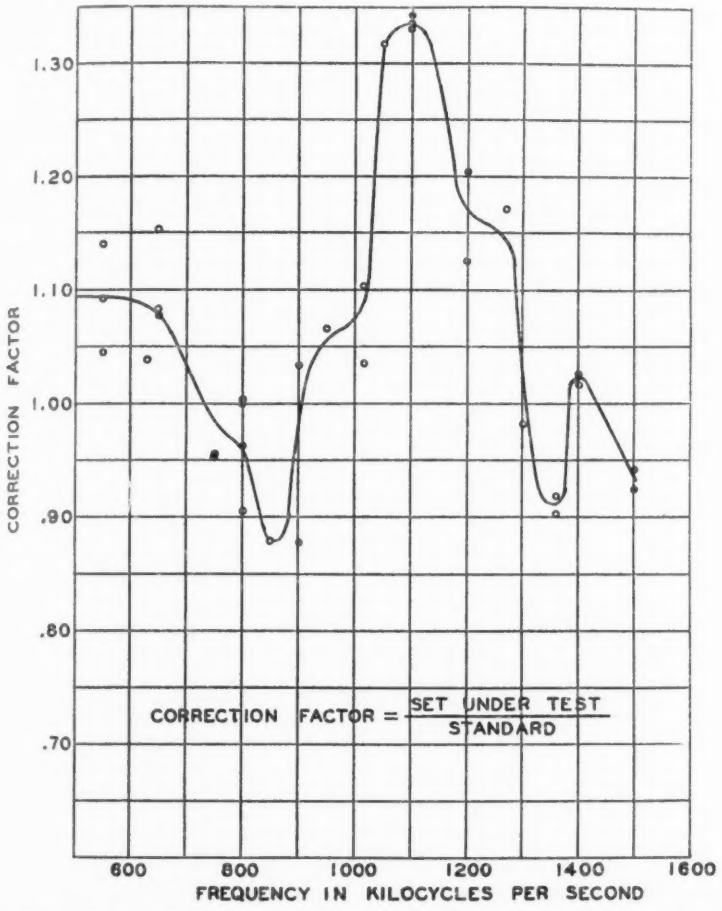

FIGURE 9.—*Calibration of a set showing marked variation of the errors as a function of the operating frequency.*

IX. CONCLUSIONS

Summarizing the data presented in this paper, the following conclusions may be drawn.

1. Commercial equipments designed for field-intensity measurements at frequencies below 1,600 kc/s provide absolute accuracies not greater than 20 percent unless special precautions are taken to correct for the errors enumerated in section I.

2. Of the errors listed, some are common to all the methods of measurement, while others pertain to specific methods. Of the methods discussed, the voltage-comparator arrangement is subject to the least number of errors in the frequency range considered.

3. The error introduced by virtue of the distributed capacitance of the loop antenna is often the most serious of the several errors. Its magnitude may be up to 15 percent in certain sets.

4. This error may be taken into account through the use of a derived correction factor based on the assumption that the distribution of current in the loop antenna is elliptical.

5. The use of the condenser-variation method for measuring the Q-factor of the loop antenna will eliminate this error in the measurement of field intensity. The use of an untuned loop antenna also serves to eliminate this error. The use of an unbalanced shielded loop antenna with the calibrating voltage inserted at the grounded ends tends to reduce this error. The magnitude of this error may also be limited by limiting the frequency range of each loop antenna, and by introducing deliberate unbalance of the loop antenna.

6. With special precautions in calibration, location of the set, provision of large-scale indicating instruments and operating controls, etc., an accuracy of measurement better than 5 percent should be attainable. In several sets the accuracy was found to be within 2 percent.

WASHINGTON, August 25, 1938.

U. S. Department of Commerce National Bureau of Standards

RESEARCH PAPER RP1157

Part of Journal of Research of the National Bureau of Standards, Volume 21, December 1938

CORRELATION OF AN ELECTROLYTIC CORROSION TEST WITH THE ACTUAL CORROSIVENESS OF SOILS

By Irving A. Denison and Robert B. Darnielle

ABSTRACT

The corrosiveness of soils along a 128-mile section of a pipe-line system was estimated from data on the occurrence of leaks and length of line reconditioned and from the results of an electrolytic corrosion test. The development of leaks with time as influenced by reconditioning is illustrated for soils differing in corrosiveness. The corrosiveness of associated soils, as indicated by data on leaks and repairs and the results of the corrosion test, increases as the drainage becomes more deficient and as the soil becomes heavier in texture. The variation of corrosiveness with depth is illustrated for typical soil profiles. A rough linear correlation was observed between the actual corrosiveness of the soils and the results of the electrolytic test. The relative corrosiveness of the soils along approximately 80 percent of the total length of the pipe-line system was correctly indicated.

CONTENTS

	Page
I. Introduction	819
II. Description and classification of soils	820
III. Analysis of data on leaks and reconditioning	821
IV. Influence of soil properties on corrosiveness as indicated by leak frequency and percentage of line reconditioned	824
V. Corrosiveness of soils as measured by an electrolytic corrosion test	826
1. Description of test	826
2. Variation in corrosiveness with depth	826
3. Results of the corrosion test	828
VI. Comparison of actual corrosion on the pipe lines with corrosiveness indicated by the laboratory test	829

I. INTRODUCTION

An electrolytic test for measuring the corrosiveness of soils has been previously described.[1] [2] This test consists in the measurement of the polarization voltage at various current densities of a specially designed corrosion cell, in which the electrodes are steel and the electrolyte is the soil under test. The cell is constructed in such a way that the process of corrosion is similar to that in nature. The average current density corresponding to a definite range of potential is taken as the measure of the relative corrosiveness of the soil.

The results of the corrosion test have been shown to be closely associated with the loss in weight of the anode of the cell over a period

[1] I. A. Denison, J. Research NBS 17, 363 (1936) RP918.
[2] K. H. Logan, S. P. Ewing, and I. A. Denison. Symposium on Corrosion Testing Procedures, p. 95 (Am. Soc. Testing Materials, Philadelphia, Pa.; 1937).

of 2 weeks and also with the results of the long-time field tests on the corrosion of metals in soils that are being conducted by the National Bureau of Standards. The data obtained from these field tests consist of accurate measurements of the loss of weight and depth of pits on 5 or 6 sets of 16 specimens each of wrought ferrous materials removed biennially from each of 47 carefully chosen test sites located in various parts of the United States.[3]

An accurate record of leaks and reconditioning on an extensive pipeline system, which was recently made available to the authors, provided a means of determining the true corrosiveness of the soil types which occur along the pipe lines. By comparing the relative corrosiveness of the soil types estimated by means of the electrolytic test with their actual corrosiveness on the pipe lines, the practical value of the test for locating corrosive soils may be judged by the extent of the correlation.

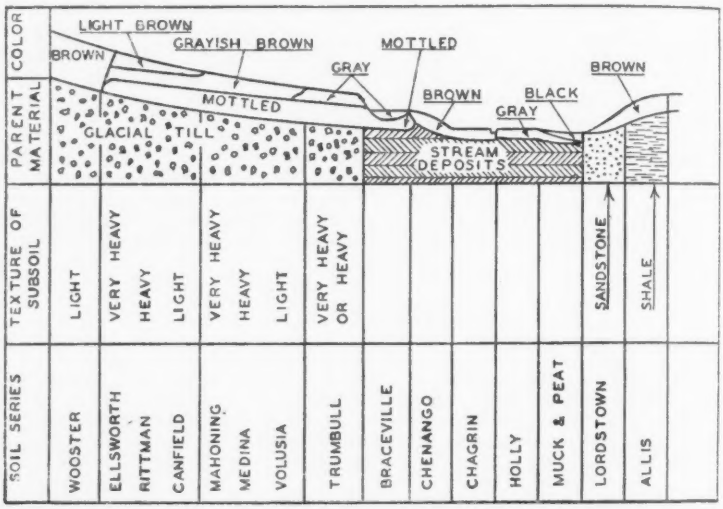

FIGURE 1.—*Characteristics of soils in the region of glaciated sandstones and shales.*

II. DESCRIPTION AND CLASSIFICATION OF SOILS

The pipe lines in the northwestern part of Ohio traverse what is known as the glacial lake region. The soils in this region have resulted chiefly from the weathering of glacial, or ice-laid, deposits and lacustrine, or lake-laid, deposits. Although the glacial drift is derived chiefly from limestone, there is a considerable admixture of shale, which accounts for the extremely heavy nature of the glacial deposits over this area. The very wet, poorly drained condition of much of this region has tended to retard the normal processes of weathering and soil development. The predominating glacial soils of this region belong to the Miami, Brookston, Nappanee, and Clyde series. The important lacustrine soils are those of the Plainfield, Fox, Newton, Toledo, and Wauseon series.

[3] K. H. Logan, J. Research NBS 16, 431 (1936) RP883.

The pipe lines in northeastern Ohio lie wholly in the region of glacial soils derived from sandstone and shale. Where the parent rock is shale, the glacial material from which the soils were formed is a heavy clay. Soils developed from this material are heavy in texture, and consist of clays and clay loams. Where sandstone predominates, the soils are loams or silt loams, which are lighter in texture. As a result of different conditions of topography, drainage, and parent material, numerous soils which differ considerably in their characteristics have been developed. The predominant soils in this region, their distinguishing properties, and their physiographic relation to one another, are shown in figure 1. This figure in a slightly different form was prepared originally by Ewing.[4] Detailed descriptions of these soils, as well as those of northwestern Ohio, have been given by Conrey.[5]

The field work, which was done in connection with previous studies,[6,7] consisted in mapping the soil types occurring along these pipe lines and in the collection of samples for study in the laboratory. Borings were made at intervals of about ½ mile and also wherever there was any question as to the type of soil. Where the soil profile appeared particularly well developed for the type, samples of soil were taken from each layer, or horizon, to a depth of about 36 inches. In general, however, at each location a single sample was taken from the horizon which appeared to be heaviest in texture.

III. ANALYSIS OF DATA ON LEAKS AND RECONDITIONING

The pipe-line system consists of five 8-inch parallel lines which were originally unprotected from corrosion. The pipe lines were laid at different times over a period of 18 years since 1889, and their average age is 33 years. When a leak was reported, the line was uncovered at that point and a temporary repair was made by means of a leak clamp. The date and location of the leak were recorded.

Early in the life of these lines it was observed that, if several leaks occurred in short sections of the line, they were usually followed by other leaks with increasing frequency. Instead of repairing these leaks as they occurred, it was considered more economical to recondition the entire section in which the leak clamps became numerous. Accordingly, such sections were uncovered and the pipe replaced, or if its condition warranted, the pipe was repaired by welding the deeper pits and patching the larger corroded areas. In the severely corrosive locations the pipe was coated after the necessary repairs had been made. The date, location, and length of line reconditioned were recorded as a matter of routine. The fact that reconditioning was often done in sections of only 10 to 20 feet and seldom for more than a few thousand feet at one time, indicates that this work was done only when necessary.

[4] S. P. Ewing, Soil Corrosion and Pipe-Line Protection (American Gas Association, New York, N. Y.) 1938.
[5] G. W. Conrey. Bimonthly Bul. Ohio Agr. Expt. Sta. **11**, 144 (1926), **11**, 233 (1926).
[6] S. P. Ewing, Distribution Committee Report. American Gas Association (1934).
[7] I. A. Denison and S. P. Ewing, Soil Sci. **40**, 287 (1935).

The effect of reconditioning on the occurrence of leaks is illustrated in figures 2 and 3, in which are shown the cumulative leaks per unit area and the cumulative percentage of line reconditioned, each plotted against time for the Mahoning silt loam, a corrosive soil, and for the Wooster loam, a mildly corrosive soil.

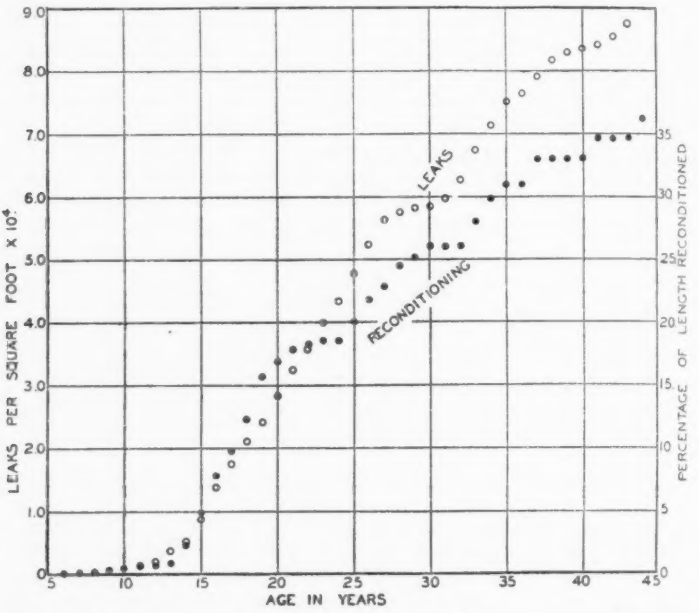

FIGURE 2.—*Effect of time and reconditioning on the occurrence of leaks in the Mahoning silt loam.*

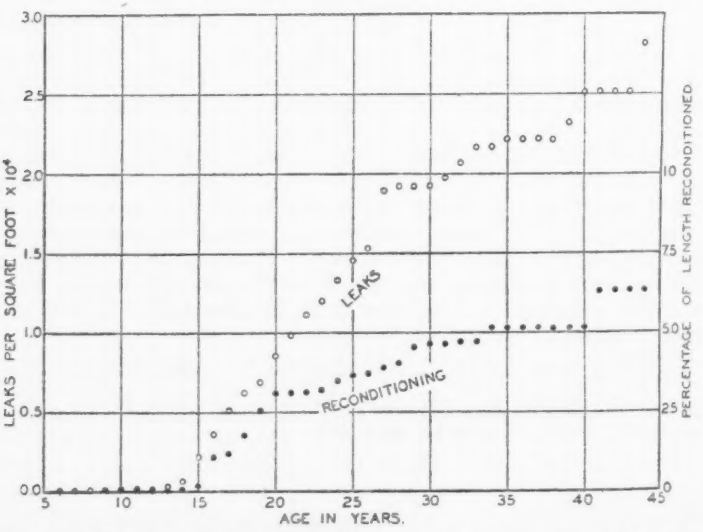

FIGURE 3.—*Effect of time and reconditioning on the occurrence of leaks in the Wooster loam.*

It is seen from figures 2 and 3 that some sections of the lines were reconditioned soon after the first leaks appeared and that the effect of reconditioning on the occurrence of leaks has been very marked even from the beginning. If reconditioning had not been done, the leak curves would have curved upward after approximately 10 years and would have become steeper with time. It will be noted that, after the first 15 years, the curves for both leaks and reconditioning are approximately linear, that is, by doing a constant amount of reconditioning each year the development of leaks is held to a constant rate, which is probably the condition for most economical operation.

The number of leaks which occurred in each soil type and the proportion of the pipe reconditioned in the various soils during the 33-year average period are summarized in table 1. Leaks and repairs within 250 feet of an intersection with a stream, road, or railroad crossing are not included. As the data apply to five parallel pipe lines, the recorded length of pipe is about five times that of the corresponding soil type.

TABLE 1.—*Number of leaks and reconditioned length of pipe lines in the soil type*

Soil		Length of pipe lines in thousands of feet	Number of leaks per 10,000 feet	Reconditioned length	Ratio
Type	Symbol		A	B	B/A
				%	
Wooster fine sandy loam	*Wf*	2.5	28.0	34.5	1.2
Trumbull clay loam	*T*	28.6	20.2	44.1	2.2
Muck	*Mu*	8.0	18.8	32.4	1.7
Genesee silt loam	*G*	6.5	18.5	26.1	1.4
Nappanee clay loam	*N*	47.3	15.9	54.8	3.4
Chagrin silt loam and fine sandy loam	*Ch*	43.3	13.6	21.6	1.6
Mahoning silt loam	*M*	475.7	12.8	19.8	1.5
Wauseon-like soils	*Wa*	46.5	11.8	66.2	5.6
Holly clay loam	*H*	37.4	11.7	22.6	1.9
Lorain clay loam	*Kc*	14.0	10.0	29.2	2.9
Ellsworth silt loam	*E*	49.3	9.6	14.8	1.5
Volusia silt loam	*V*	294.1	8.1	19.0	2.3
Canfield silt loam	*Ca*	132.4	8.1	6.5	.8
Volusia loam	*Vl*	35.5	7.9	6.0	.8
Wauseon fine sandy loam	*W*	19.0	6.9	7.6	1.1
Till	*Ti*	46.6	6.5	12.2	1.9
Canadea silt loam and fine sandy loam	*C*	104.0	6.0	11.0	1.9
Newton fine sandy loam	*Nf*	18.3	6.0	6.5	1.1
Lordstown fine sandy loam	*L*	25.5	5.5	4.5	.8
Crosby silt loam	*Cs*	35.0	4.9	3.4	.7
Sands and sandy loams undifferentiated	*S*	363.0	4.9	3.9	.8
Wooster loam	*Wl*	269.1	4.2	4.6	1.1
Brookston clay loam	*Bc*	245.8	4.0	20.4	5.0
Lorain fine sandy loam	*K*	61.5	3.9	6.9	1.8
Miami silt loam and fine sandy loam	*Ml*	68.5	2.6	2.1	.8
Clyde clay loam	*A*	40.3	2.5	5.3	2.1
Lucas fine sandy loam	*Lf*	14.5	0	0	------
Average	------	------	------	------	1.8

The length of pipe in each type of soil is a rough criterion of the reliability of the data for that soil. Obviously, more weight should be attached to the data for those soils, such as the Mahoning silt loam, Volusia silt loam and the undifferentiated sands, which contain large footages of pipe, than to those soils of slight extent, such as the Wooster

fine sandy loam, muck, and the Genesee silt loam, in which the footage of pipe is relatively small. The soil which was designated as Lorain clay loam in previous papers is designated in this paper as Lorain fine sandy loam and vice versa. Later examination of the field notes and the soil samples, as well as data from other sources, indicated that these soils were originally incorrectly mapped.

Before any comparison can be made between the actual corrosiveness of the soils and the corrosiveness predicted from laboratory tests, it is obviously necessary to decide whether (a) the number of leaks, or (b) the reconditioned length, or (c) some combination of the two, should be taken as the measure of the corrosion that has actually occurred. As both the number of leaks and the proportion of the line reconditioned are dependent upon the corrosiveness of the soils, either one of these factors might be used as the criterion of corrosiveness. In fact, if they are found to be proportional to each other, that is, if they put the soils in the same order, it is immaterial which one is used.

The ratios in the last column of table 1 show that there is a rough proportionality between these two quantities for all but three of the soils, namely, Nappanee clay loam, "Wauseon-like" soils, and the Brookston clay loam, for which the proportionality factor differs from the average by considerably more than 50 percent of the average factor. As the pipe lines in the three soil types mentioned were generally close to roads, reconditioning could be done more cheaply than in less accessible locations. In such soils, the number of leaks is probably a more reliable criterion of relative corrosiveness than is the extent of reconditioning.

Although the ratios in table 1 are only roughly constant, the deviations from constancy are relatively small in comparison with the large differences in the corrosiveness of the soils indicated by the leak frequencies. Hence, it is doubtful whether the greater or less extent of reconditioning done in proportion to the leak frequencies in individual soils would appreciably affect the order of corrosiveness shown by leak frequency alone. For purposes of correlation, the number of leaks per unit length may therefore be taken as a simple, approximate measure of the actual corrosiveness of the soils.

IV. INFLUENCE OF SOIL PROPERTIES ON CORROSIVENESS AS INDICATED BY LEAK FREQUENCY AND PERCENTAGE OF LINE RECONDITIONED

In order to show the effect of soil properties on corrosion, table 2 has been prepared for a group of associated soil types which occur along the eastern part of the lines. The soils are arranged according to the degree of development of the soil profile, which is determined by texture, drainage, and the nature of the material from which the soil is derived. Corrosiveness is indicated by the number of leaks per 10,000 feet which have occurred during the average period of 33 years and by the percentage of the line reconditioned over the same period. If the corrosion data are compared from left to right, it is seen that the corrosiveness of the soils decreases as the drainage improves, as indicated by the color of the surface soil and the depth at which mottling appears. If the values are compared vertically, it is seen that corrosiveness increases as the soils become heavier in texture.

TABLE 2.—*Degree of development of associated soil series and corrosiveness, as indicated by leak density and percentage of line reconditioned in 33 years*

	Degree of development											
	1			2			3			4		
Color of surface soil	Gray			Gray brown			Light brown			Brown.		
Mottling of A_2 horizon	Mottled			Mottled			Mottled			No mottling.		
Mottling of *B* horizon	do			do			do			Do.		
Mottling of *C* horizon	do			do			do			Do.		
Distinguishing characteristics of *B* horizon	Series	Leaks per 10,000 feet	Length reconditioned	Series	Leaks per 10,000 feet	Length reconditioned	Series	Leaks per 10,000 feet	Length reconditioned	Series	Leaks per 10,000 feet	Length reconditioned
			%			%			%			%
Light	Trumbull	20.2	44.1	Volusia	8.1	19.0	Canfield	8.1	6.5	Wooster	4.2	4.6
Heavy				Medina	(a)	(a)	Rittman	(a)	(a)			
Very heavy				Mahoning	12.8	19.8	Ellsworth	9.6	14.8			

[a] Series not identified along pipe line.

The relation shown in table 2 between soil conditions and corrosion can be explained on the basis of our present knowledge of corrosion processes in soils. In addition to the corrosive effect of the greater acidity and conductivity of the heavy and imperfectly drained soils, the relatively large leak frequencies and amounts of pipe repaired in such soils are to be ascribed largely to the fact that under conditions of poor aeration the rate of pitting changes relatively little with time. On the other hand, under conditions of good aeration, there is usually a marked tendency for the rate of pitting to decrease with time.

The relation between the aeration of the soil and depth of pitting is attributed to the inhibiting action of the corrosion products that are precipitated in contact with the corroding areas under conditions of good aeration. The failure of corrosion products to protect under conditions of poor drainage evidently overbalances the opposing effect of the relatively great cathodic polarization that would be expected in poorly drained soils because of the deficiency of oxygen. It should be noted, however, that good aeration is not in itself a sufficient condition for the precipitation of corrosion products. In the presence of a high concentration of salts in many soils, or of extreme acidity, the products of corrosion may remain soluble even when completely oxidized.

The number of leaks, averaging four per 10,000 feet, shown in table 2 to have occurred in the Wooster loam, which is one of the least corrosive soils along the pipe lines, indicates that some leaks may occur even in soils which have properties not ordinarily associated with corrosion. This soil occupies rolling uplands where surface drainage is good. It is coarse in texture, has an open, porous structure, contains very little soluble material (average resistivity—8,000 ohm-cm), and its acidity is normal for the well-weathered soils of the humid regions. Yet a fairly large number of leaks developed in this soil before the line was 15 years old. This same general condition applies likewise to a

large body of coarse, well-drained soils of high resistivity, which are classified as sands. In these soils an average of five leaks per 10,000 feet developed.

A probable explanation for the occurrence of even a small number of leaks in soils in which leaks would not be predicted, is that corrosion did not occur generally throughout that soil type, but was confined to restricted areas of more corrosive soil types, that were too small in their extents to be properly classified.

The occurrence of some leaks in soils which would ordinarily be considered noncorrosive raises the question as to whether any soil types occurring under similar climatic conditions are actually noncorrosive. Since some degree of variability is characteristic of soil types in general, it is difficult to escape the conclusion that in the usual acid soils of the eastern United States, exclusive of certain very well drained or mountainous areas, there are very few soils in which some leaks in a pipe line of average diameter and wall thickness will not develop within 30 years.

V. CORROSIVENESS OF SOILS AS MEASURED BY AN ELECTROLYTIC CORROSION TEST

1. DESCRIPTION OF TEST

The corrosiveness of the soil samples collected along the pipe lines was determined in the laboratory from the relation between current density and potential in a corrosion cell in which the anode and cathode are steel and the electrolyte is the soil under test. By using as the cathode a steel screen which is more readily accessible to air than the anode, the electrodes are aerated differentially and the cell develops its own electromotive force. However, an externally applied electromotive force was used in the tests here described. Current density-potential curves were obtained by plotting the potentials existing in such cells at different current densities. The average current density over the range of voltage between 0 and 0.3 volt was tentatively selected as the criterion of the relative corrosiveness of the soils. The construction of the test cells, preparation of the cells for test, and the method of making the electrical measurements were described in a previous publication.[8]

2. VARIATION IN CORROSIVENESS WITH DEPTH

It is generally recognized that the properties of soils may vary greatly with depth. A familiar example of this variation is the frequent occurrence of a layer of heavy clay below the surface soil. An abrupt change in reaction from high acidity to alkalinity within a few inches is another illustration of the variation which may be encountered between adjacent soil horizons. It was therefore necessary to study the manner in which corrosiveness varied throughout the profiles of the important soil types present.

In table 3 the characteristics of the horizons of 8 soil types are shown, together with the corrosiveness of the various horizons, as indicated by the laboratory test. The profile shown for the "Wauseon-like" soils is typical of rather extensive bodies of soil observed in the glacial

[8] K. H. Logan, S. P. Ewing, and I. A. Denison, Symposium on Corrosion Testing Procedures, p. 95 (Am. Soc. Testing Materials, Philadelphia, Pa.; 1937).

lake region which have not been exactly classified. This profile resembles that of the Wauseon fine sandy loam, but it does not have the dark sandy subsoil extending to about 36 inches, which is typical of the true Wauseon soils.

TABLE 3.—*Relative corrosiveness of horizons of typical soil profiles, as indicated by the electrolytic corrosion test*

SOILS OF NORTHEASTERN OHIO			SOILS OF NORTHWESTERN OHIO		
Depth	Current density	Description	Depth	Current density	Description
WOOSTER SILT LOAM			**MIAMI SILT LOAM**		
in.	*ma/dm²*		*in.*	*ma/dm²*	
0 to 9	1.0	Brown silt loam.	0 to 9	2.0	Brownish-gray silt loam.
9 to 15	2.1	Yellowish-brown silt loam.	9 to 17	6.1	Pale yellowish-brown silt loam.
15 to 27	3.5	Yellowish-brown compact silt loam.	17 to 27	6.8	Dull yellowish-brown silty clay.
Below 27	2.4	Yellowish-brown loam to silt loam.	Below 27	----------	Calcareous clay.
VOLUSIA SILT LOAM			**BROOKSTON CLAY LOAM**		
0 to 7	2.2	Brownish-gray silt loam.	0 to 7	4.1	Gray-black clay loam.
7 to 18	5.7	Mottled-gray and yellowish-brown silt loam.	7 to 22	9.2	Mottled-gray and yellowish-brown clay loam.
18 to 29	10.8	Mottled-gray and yellowish-brown heavy silt loam.	22 to 38	8.1	Mottled yellowish-brown and yellowish gray clay.
Below 29	3.3	Mottled loam to silt loam.	Below 38	7.2	Calcareous clay.
MAHONING SILT LOAM			**NAPPANEE CLAY LOAM**		
0 to 7	2.8	Brownish-gray silt loam.	0 to 8	2.7	Grayish-yellow heavy clay loam.
7 to 13	6.1	Mottled-gray and yellowish-brown silty clay loam.	8 to 25	8.8	Mottled yellowish-brown and gray heavy clay.
13 to 23	11.1	Mottled-gray and yellowish-brown silty clay.	Below 25	7.9	Dull yellowish-brown calcareous clay.
Below 23	11.1	Brownish-drab heavy silty clay.			
TRUMBULL CLAY LOAM			**WAUSEON-LIKE SOILS**		
0 to 9	3.6	Dark-gray clay loam.	0 to 9	2.5	Gray-black fine sandy loam.
9 to 26	4.7	Drab-gray silty clay, mottled with rusty brown.	9 to 28	12.7	Yellowish-brown silty clay loam.
26 to 38	11.2	Drab-gray clay, mottled with rusty brown.	Below 28	5.8	Calcareous clay with decomposed shale.

It will be observed in table 3 that as the soil becomes heavier in texture from the surface downward, the corrosiveness of the soil likewise increases. The upper subsoil is invariably heavier and more corrosive than the surface soil. In several profiles the maximum corrosiveness and heaviest texture occur in the lower subsoil at depths greater than 1 to 2 feet. Increase in corrosiveness with depth throughout the profile is characteristic of those soils which have developed from heavy-textured parent material that is normally acid in reaction, for example, the Mahoning silt loam and the Trumbull clay loam. Soils which have developed from coarse parent material, for example, the Wooster and Volusia silt loams, become less corrosive in the lower part of the profile.

The general tendency, observed in table 3, for corrosiveness to increase as the soil becomes heavier in texture and as the drainage becomes less perfect is in agreement with the conclusions reached after comparing the properties of various soil types with the leak frequency and reconditioned length in these types (table 2). It would seem that in the corrosion cell, as in nature, maintenance of the products of corrosion in the deoxidized, and hence more soluble, condition has a greater effect on the rate of corrosion in the soils studied than has the high cathodic polarization, which is characteristic of heavy, poorly drained soils.

In view of the marked differences in the corrosiveness of certain soils at different depths, it is evident that in sampling soils for corrosion tests, the depth at which the sample is taken must be carefully considered. It is probable that the pipe line will be in contact at some points with soil from the most corrosive horizon of the soil profile, which might therefore logically be selected for the test. The procedure adopted in the present study was to take samples from that horizon which is heaviest in texture, a practice which was supported by the results of the corrosion tests. In general, however, it would be preferable to study in advance of the actual survey the variation with depth in the corrosiveness of each important soil type, using the cell test as a measure of corrosion. From the results of this preliminary study, the depth at which soil samples should be taken could be determined for each soil type.

3. RESULTS OF THE CORROSION TEST

The mean values of the average current density in the potential range from 0 to 0.3 volt are shown in table 4. In general, the number of samples tested in each soil type was about in proportion to the length of pipe contained in that soil. The reliability of the data for a particular soil type depends, therefore, on the length of pipe exposed to that type. Computation of the standard errors of the mean current densities showed that these errors were practically all less than 25 percent of the mean. The latter may therefore be used directly as the measure of corrosiveness determined by the electrolytic test.

TABLE 4.—*Corrosiveness of soils, as indicated by the electrolytic test*

Soil symbol [1]	Number of samples tested	Average current density from 0 to 0.3 v	Soil symbol [1]	Number of samples tested	Average current density from 0 to 0.3 v
		ma/dm²			*ma/dm²*
Mu	2	15.8	*Kc*	2	7.8
Wa	1	12.7	*Ca*	7	4.6
A	3	9.1	*C*	8	4.3
N	3	8.1	*Cs*	2	4.1
Bc	6	8.0	*Ch*	15	3.3
M	38	7.8	*Wl*	12	2.7
H	8	7.2	*K*	3	2.5
E	4	7.1	*Tl*	6	2.4
Ml	4	6.4	*O*	3	2.3
Nf	2	6.3	*Wf*	2	2.2
Vl	5	6.1	*L*	2	1.3
W	2	5.9	*Lf*	2	1.2
T	8	5.8	*S*	2	0.6
V	29	5.7			

[1] For identification of symbols, see table 1, page 823.

In general, the soil types which show the highest values of current density are heavy in texture or poorly drained, or both. Conversely, low values of current density are usually associated with well-drained soils of coarse texture.

VI. COMPARISON OF ACTUAL CORROSION ON THE PIPE LINES WITH CORROSIVENESS INDICATED BY THE LABORATORY TEST

The relation between the corrosiveness of the soil types, as indicated by the laboratory test, and their actual corrosiveness was studied by plotting the mean current densities of the soil types against the corresponding number of leaks per 10,000 feet. It was observed that the points representing extensive soils, for which the laboratory and field data were most reliable, conformed well to a straight line.

In order to decide whether the correlation for the data as a whole was sufficient for the test to be of practical value, the soils were divided into five groups according to successive ranges of leak frequency. The current densities corresponding to these ranges of leak frequency were then calculated from the slope of the line which showed the average relation between the field and laboratory data. The soils were then placed in five groups according to current density, and the agreement between the classifications on the bases, respectively, of leak frequency and of current density was noted. For example, a difference of 0 indicates complete agreement, a difference of +1 means that the electrolytic test places the soil in one group higher (that is, more corrosive) than the group in which it properly belongs, and vice versa. Since the limits of the groups are necessarily arbitrary, an agreement of plus or minus one group is evidence of fair correlation.

TABLE 5.—*Classification of soils according to the electrolytic test*

Group	I	II	III	IV	V
Leaks per 10,000 feet	0 to 4	4.1 to 8	8.1 to 12	12.1 to 16	>16
Current density (ma/dm²)	0 to 2.3	2.4 to 4.6	4.7 to 6.9	7.0 to 9.2	>9.3
	Bc +3 *K* +1 *Mt* +2 *A* +3 *Lf* 0	*Vl* +1 *W* +1 *Tl* 0 *C* 0 *Nf* +1 *L* −1 *Cy* 0 *S* −1 *Wl* 0	*Kc* +1 *E* +1 *V* 0 *Ca* −1 *Wa* +2	*N* 0 *Ch* −2 *M* 0 *H* 0	*Wf* −4 *T* −2 *Mu* 0 *G* −4

Summary	
Difference	Number of soils
0	10
1	9
2	4
3	2
4	2

It is seen in table 5 that 19 of the 27 soils, that is, 70 percent, showed at least fair correlation between the electrolytic test and the reported leaks. Consideration of the length of pipe (or soil) involved, as listed in table 1, shows that on over 80 percent of the actual length of the pipe lines, the electrolytic test would have correctly predicted (that is, ±1 group) the relative corrosiveness of the soil.

The fact that of the four soils (*A*, *Bc*, *G*, and *Wf*) that showed poor correlation, a total of only 14 samples was tested, as compared with a general average of about 7 samples per soil, at least indicates that the samples of these soils may not have been representative. These results indicate that any improvement in the ability to predict soil behavior from the electrolytic test is more likely to result from an improvement in sampling than in the electrolytic test itself.

The authors express their appreciation to S. P. Ewing for the use of certain figures and for many helpful suggestions. They also acknowledge the assistance of I. C. Frost, by whom most of the corrosion tests were made.

WASHINGTON, April 12, 1938.

U. S. Department of Commerce National Bureau of Standards

RESEARCH PAPER RP1158

Part of Journal of Research of the National Bureau of Standards, Volume 21, December 1938

METHOD FOR DETERMINING UNIFORMITY OF TEMPERATURE IN CRYOSTATS

By Martin Shepherd

ABSTRACT

This note reports a sensitive method by which the uniformity of temperature in cryostats (or other constant-temperature baths) may be determined. The method involves the measurement of differences of saturation pressures of a suitable substance (which need not be critically pure) by means of a very easily constructed differential manometer. Such an instrument is capable of differentiating temperature effects at the surface and within the bath, and offers some interesting possibilities in studying low-temperature baths.

The platinum resistance thermometer and the differential thermel, which are normally employed to determine the uniformity of temperature within cryostats (or other constant-temperature baths) are subject to at least one annoying limitation. Neither instrument is well suited for measuring differences of temperature at the surface of the bath. While either instrument may be used in connection with a vapor-pressure thermometer to measure effects of temperature at the surface, the procedure required is relatively complicated and time-consuming.

It is possible to compare the temperatures at any two points within the bath or at its surface simultaneously, with extreme sensitivity and with little or no significant temperature lag, by means of a very simple differential saturation-pressure manometer. This manometer was previously described in connection with the determination of the purity of gases [1] and is illustrated in figure 1 as modified for the present purpose.

Both sides are simultaneously filled with a suitable gas drawn from the same source. The gas used will determine the effective temperature range, which may be extended (with an increase in sensitivity) by filling to a pressure of several atmospheres. If an extended range of temperature must be studied, the manometer may be refilled with other gases, or a set of several permanent manometers can be made. Since the gas used need not be critically pure, and the manometer itself is easily constructed, the instrument possesses the practical advantages of relative cheapness and availability. If greater flexibility is desired, spiral expansion joints can be used to permit movement of the stems, or a flexible metal tubing may be substituted for

[1] BS J. Research **2**, 1156 and 1169 (1929) RP75; **12**, 185 (1934) RP643.

the glass stems. The latter may be attached to the glass by any of the several methods available for making such joints.

A system of shields may be used in the various combinations shown, and the possibilities offered are attractive. For example, if both stems of the manometer are left bare (see 1 of the figure), the differential vapor pressures observed should indicate the combined effect of differences of temperature within the bath and at its surface. The

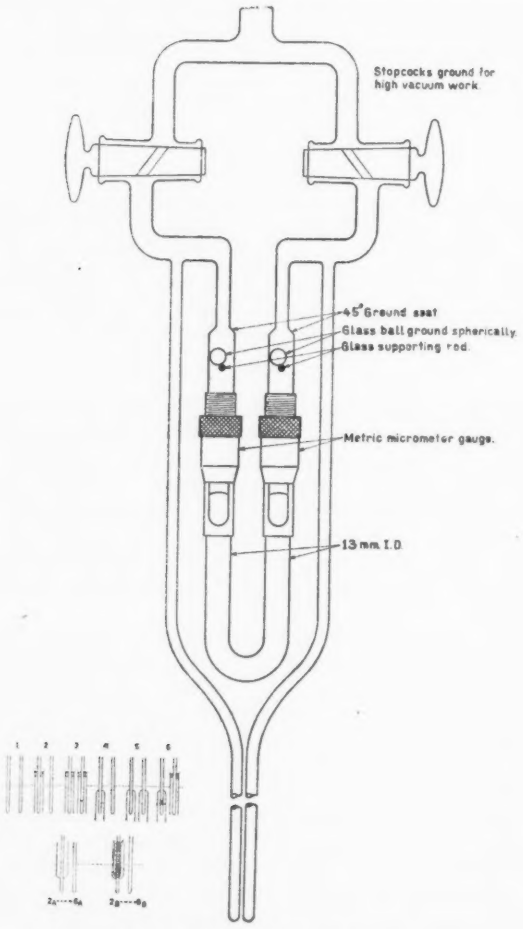

FIGURE 1.—*Detail of differential manometer.*

arrangement shown in 2, 2A, or 2B may be used to determine differences between a point within the bath and the effective temperature as measured by a simple vapor-pressure thermometer. This should immediately disclose the suitability of a bath intended for the comparison of temperatures indicated by a platinum resistance thermometer and a vapor-pressure thermometer. When both stems are shielded (as in 3), differences of temperature between two points

within the bath may be determined. With one stem shielded as in 4, a difference between one spot at the surface and the effective temperature measured by a vapor-pressure thermometer may be indicated. Temperatures at two separate points on the surface may be simultaneously compared if the shields are arranged as in 5. The arrangement shown in 6 may be used to observe differences in temperature between one part of the surface and a point within the bath.

Thus the differential manometer might be used to study the uniformity of temperature more advantageously than is possible with either of the normally employed electrical instruments, since temperatures can be compared both within the bath and at the surface. Moreover, the difference of temperatures between two points is measured simultaneously and with high sensitivity. It is entirely possible to observe some erratic behavior of the bath, which might be missed if a resistance thermometer with a relatively large thermal lag were moved from point to point, by simply allowing the manometer to remain in a fixed position and watching the positions of the mercury menisci. By evacuating one side of the manometer and using it as a simple vapor-pressure thermometer, the constancy as well as the uniformity of temperature may be determined.

In studying the temperatures at the surface of a bath, the differential manometer possesses a unique advantage. It is always *in* the surface itself, even when the surface of the liquid is moving, uneven, and of constantly varying height. The immersed stem of the manometer responds quickly to changes of temperature at the surface. The fullest extent of temperature change will not be realized, since the thin glass stem interposes a heat capacity. But under similar conditions, the platinum resistance thermometer is obviously not suitable. The differential thermel, which does have a low heat capacity, nevertheless has the physical limitation that, if placed at the very surface, it will sometimes be immersed and sometimes not; while, if it is lowered so that constant immersion is achieved, the local effects of the surface may be substantially lost.

The importance of the effects of temperature at the surface of the bath may alone frequently justify the use of the manometer, even if it is employed as an auxiliary to the resistance thermometer or thermel. The extent to which surface temperatures may vary is perhaps not generally realized. The following experiment will illustrate what may sometimes be expected. During the preparation of pure oxygen to be used by this Bureau as a reference point on the International Temperature Scale,[2] the purity of the oxygen was tested by the method described in the previous references (footnote 1). The bulbs of the differential manometer were thin-walled spheres touching one another, and were immersed in a bath of liquid oxygen boiling vigorously within a D'Arsonval tube. Oxygen of high purity was simultaneously condensed from a common source into each bulb.[9] The saturation pressure within each bulb should have been identical, and the manometer should have indicated no difference in pressure, if the temperature of the bath had been uniform. Under these conditions, however, the manometer actually indicated rapidly changing pressures within the

[2] This work was done early in 1933. The present note was originally prepared at the same time, but publication was delayed pending possible experimental work. The opportunity for this work has, unfortunately, never presented itself.

bulbs, in such a manner that first one and then the other bulb exhibited the higher pressure. This dancing behavior was quite erratic; at times the pressures remained steady, while at other times variations of as much as 20 mm (of mercury) were apparent. (At the normal boiling point of oxygen, 10 mm corresponds approximately to 0.13° C.) Stirring the bath of boiling oxygen did not greatly improve the condition. When the bulbs were surrounded with a block of frozen mercury, which extended around the stems and above the surface of the bath, the variations previously observed were effectively eliminated. The author has used such a device for many years in connection with other cryostat baths, and has always found it satisfactory. There has been no breakage of glass when the mercury is frozen around the condensing bulbs. Such an arrangement would seem a logical one to employ in case the temperatures at two points of a bath were required to be accurately the same, as, for example, when calibrating a platinum resistance thermometer against a vapor-pressure thermometer.

The oscillating behavior exhibited by the differential manometer in the case cited may have been caused by variations of temperature within the bath or at the surface. The saturation pressure indicated by a vapor-pressure thermometer will correspond closely to the lowest temperature to which it is exposed, which is usually at the surface of cold baths. Because of these facts, E. F. Mueller of this Bureau suggested the desirability of shielding the stem of this type of thermometer by means of glass envelopes such as are indicated in the figure. He further suggested the possibility of electrically heating the stem within the shield (see series *B*, fig. 1).

It is evident from the foregoing discussion that the differential manometer may be particularly useful in studying baths to be employed for vapor-pressure thermometers, since the effects of surface temperature are so important. It is also evident that the use of the instrument may develop some surprises that have not been indicated in this sort note. Its general applicability and suitability have not been demonstrated or experimentally compared with existing apparatus and methods. The lack of experimental study precludes definite statements, and in the argument between the cryostat and the manometer, it is not possible to predict the certain winner on an estimated score of points. It seems likely, however, that interesting facts concerning both may be revealed; and this seems particularly probable in the field of vapor-pressure thermometry.

WASHINGTON, August 26, 1938.

U. S. Department of Commerce National Bureau of Standards

RESEARCH PAPER RP1159

Part of Journal of Research of the National Bureau of Standards, Volume 21, December 1938

TRENDS OF CHARACTERISTICS OF THE IONOSPHERE FOR HALF A SUNSPOT CYCLE

By Newbern Smith, Theodore R. Gilliland, and Samuel S. Kirby

ABSTRACT

The increase of solar activity from the sunspot minimum of 1933 to 1938 resulted in large increases in the ionization of the upper atmosphere. During this time the ionization densities of the E layer increased by a ratio of approximately 1.55 to 1 and those of the F_2 layer by about 4 to 1. Superposed on this long-period increase were the more or less regular diurnal and seasonal variations. Graphs indicating the long-time variations for the different layers at several different times of day are shown.

CONTENTS

	Page
I. Introduction	835
II. Diurnal and seasonal variations	836
III. Long-period variations	839
IV. Conclusion	845

I. INTRODUCTION

A program of observations extending over the past 5 years has yielded information on the characteristic regular variations of the critical frequencies and virtual heights of the various layers of the ionosphere. These regular variations are diurnal, seasonal, and from year to year. The present paper summarizes this information and indicates the trend and probable cause of the year-to-year variation.

Since the ionization of the earth's upper atmosphere is due, wholly or principally, to energy from the sun, changes in solar activity might be expected to produce corresponding changes in the ionization of the ionosphere. Sunspot numbers are a rough indication of average solar activity. The critical frequencies and virtual heights, which are directly related to the ionization of the ionosphere, might therefore be expected to vary with the sunspot numbers.

Sunspots are but one manifestation of the solar activity influencing the sun's ultraviolet radiation, which is in turn responsible for the ionization of the ionosphere. There is, therefore, no reason to expect detailed correlation between critical frequencies and sunspot numbers. In the absence of a better criterion of solar activity, however, it may be assumed that sunspot numbers give, for long-time averages but not in detail, an index of the intensity of solar radiation. It might, therefore, be expected that the ionosphere critical frequencies

and the sunspot numbers would follow the same trend, but not necessarily show complete correlation.

Regular ionosphere observations of the National Bureau of Standards have covered a period, from 1933 to date (1938), of about half a sunspot cycle.[1] Less regular observations were made from 1930 to 1933. During the half-cycle from 1933 to 1938 the general solar activity, as measured by the sunspot numbers, increased from a minimum in the fall of 1933 to what appears to have been a maximum in 1937, and the ionization of the various layers increased accordingly.

II. DIURNAL AND SEASONAL VARIATIONS

The ionosphere observations of the National Bureau of Standards have indicated the regular diurnal and seasonal characteristics of the critical frequencies and virtual heights of various layers.

Figure 1 shows typical average diurnal curves of critical frequencies and virtual heights for winter and summer conditions, represented by the months of December 1936 and June 1937, respectively. The vertical dashed lines are for the times of sunrise and sunset at the ground (not in the ionosphere). The general diurnal and seasonal variations shown in figure 1 have repeated themselves so consistently as to leave little doubt that they are characteristic of the ionosphere at the latitude of Washington.

No regular diurnal or seasonal variation has been observed in the minimum virtual height of the E region, which appears to be always between 110 and 120 km. The critical frequency, f_E,[2] for the ordinary ray reflected from the E layer, has, however, a regular diurnal and seasonal variation. As may be seen from figure 1, f_E varies synchronously with the altitude of the sun, reaching the diurnal maximum at noon, and having a higher diurnal maximum in the summer than in the winter. This behavior accords with the simple theory of ionization by ultraviolet light from the sun, according to which,[3] assuming recombination to be sufficiently rapid,

$$f_E = K\cos^{1/4}\psi$$

where ψ is the zenith angle of the sun, and K is a factor depending on the intensity of the solar radiation.

It has been established that, for values of ψ not too close to 90°, f_E is proportional to $\cos^{1/4}\psi$, within fairly close limits, throughout the daylight hours of any one day. This would indicate (1) that the E layer is ionized principally by ultraviolet light from the sun, and (2) that K is very nearly a constant throughout the day, that is, the ionizing radiation from the sun does not vary much in the course of a day. It will be noted also, from figure 1, that the f_E begins to rise about a half hour before ground sunrise.

[1] T. R. Gilliland, *Multifrequency ionosphere recording and its significance*, J. Research NBS **14**, 283 (1935) RP769. Proc. Inst. Radio Engrs. **23**, 1076 (1935).
T. R. Gilliland, S. S. Kirby, N. Smith, and S. E. Reymer, *Characteristics of the ionosphere and their application to radio transmission*, J. Research NBS **18**, 645 (1937) RP1001; Proc. Inst. Radio Engrs. **24**, 823 (1937).
T. R. Gilliland, S. S. Kirby, N. Smith, and S. E. Reymer, *Characteristics of the ionosphere at Washington, D. C.* Series of monthly reports beginning in the Sept. 1937 issue of the Proc. Inst. Radio Engrs.

[2] The notation is that used in the second paper of reference 1.

[3] P. O. Pederson, Propagation of Radio Waves. Chap. V. & VI.

[4] S. S. Kirby and E. B. Judson, *Recent studies of the ionosphere*, J. Research NBS **14**, 469 (1935) RP780; Proc. Inst. Radio Engrs. **23**, 733 (1935).

No such simple relation as that given above has characterized the variation of the critical frequencies of the F, F_1, and F_2 layers. As may be seen from figure 1, the daytime critical frequencies of the upper layer are much higher in the winter than in the summer, although the night critical frequencies are somewhat lower. The diurnal maximum of the $f^z_{F_2}$ almost always occurs after noon, and is much later in the day in the summer than in the winter. The post-sunset fall in the night f^z_F is much more rapid in the winter than in the summer; indeed

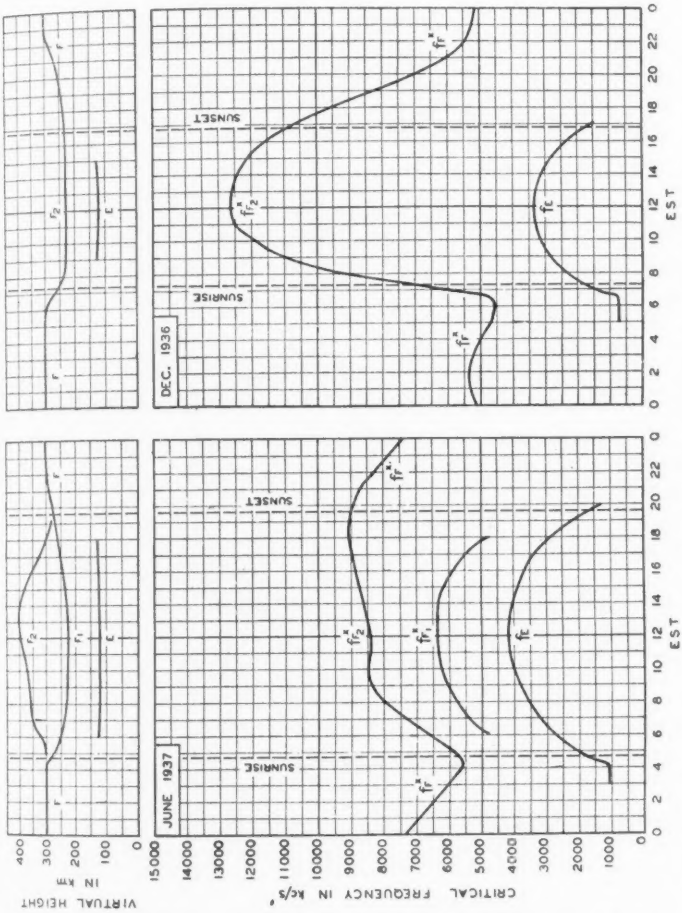

FIGURE 1.—*Typical winter (December 1936) and summer (June 1937) curves of critical frequencies and minimum virtual heights of the ionosphere layers.*

The critical frequency is the frequency which just penetrates a given layer. The virtual height shown is the minimum height measured for a given layer.

the midnight f^z_F in the summer is often as high as or higher than the noon $f^z_{F_2}$. The outstanding characteristics of the f^z_F and $f^z_{F_2}$ are, then, (1) a seasonal variation inverse to that of the f_E, and (2) a diurnal lagging behind the altitude of the sun.

Like the f_E, the f_{F_2} begins to rise from its diurnal minimum about a half hour before ground sunrise. No satisfactory quantitative theory has thus far been advanced to account for this pre-sunrise increase of ionization. It seems possible that the explanation may lie in a scattering of ultraviolet radiation from, or a refraction of this radiation in

the upper ionosphere. Any refraction would have to be caused by some kind of anomalous dispersion, inasmuch as the frequency of the ultraviolet radiation in question lies in a region of absorption for some part of the ionosphere. The fact that both the f_E and f_{F_2} start to increase simultaneously would seem to be evidence in favor of ultraviolet light as the ionizing agent of the F_2 region.

The fact that h_{F_2} is much higher during the summer day than during the winter day is evidence for the existence of a temperature effect

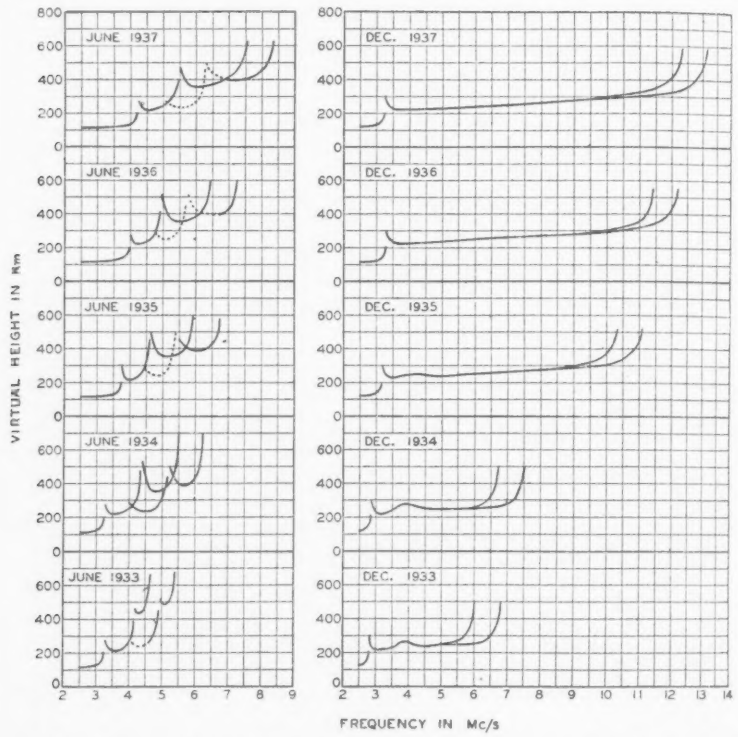

FIGURE 2.—*Average "critical frequency sweeps" or curves of virtual height against frequency, for noon, in June and December, 1933 to 1937.*

A critical frequency is indicated by a cusp on the curve. Where there are two curves, similar in form but separated in frequency by about 800 kc/s, they are the magneto-ionic components, separated because of the earth's magnetic field. The one to the right is the x-component or extraordinary ray; the one to the left is the o-component or ordinary ray. The dotted portions of the curves are those not usually observed because of absorption.

in the F_2 region.[5] It has been pointed out [6] that such a temperature effect may be in part responsible for the lower $f^x_{F_2}$ in the summer than in the winter.

The h_F is usually about 300 km during the night and early morning, both in winter and in summer, and starts to fall to the h_{F_1} level at about the time f^x_F starts to increase, that is, about a half hour before

[5] E. O. Hulburt, *Analysis of recent measurements of the ionosphere*, Phys. Rev. **46**, 822 (1934); *Theory of the ionosphere*, Terr. Mag. **40**, 193 (1935).
[6] L. V. Berkner and H. W. Wells, *Non-seasonal change of F_2 region ion density*, Terr. Mag. **43**, 15 (1935).

sunrise. This pre-sunrise fall is rapid, but the post-sunset rise in h_F is gradual, corresponding to the relatively slow decrease of f_F^2 during the same period.

The stratification of the F layer into F_1 and F_2 layers occurs distinctly only during the summer day, but there is reason to believe that it exists also latently during the winter day.[7] No stratification of the F region into F_1 and F_2 layers has been observed at night.

It should be noted that radio-transmission conditions in general follow the critical frequencies. When the critical frequencies are high the maximum usable frequencies are high and the best frequencies for transmission are also high.

III. LONG-PERIOD VARIATIONS

Figure 2 shows typical average curves of frequency against virtual height for June and December, representing summer and winter conditions, from 1933 to 1937, inclusive. Increase of the critical frequencies with the increase in solar activity has been relatively large for the F_2 region, and smaller but well marked for the E and the F_1 regions. The virtual heights and general form of the curve of frequency against height have remained the same. The chief difference, aside from the magnitude of the critical frequencies, has been a tendency toward disappearance of the daytime F-layer stratification, especially during the winter. It will be noted that the minimum virtual heights have remained about the same during the period from 1933 to 1937.

In order to eliminate seasonal variations, 12-month running averages of critical frequencies were taken for comparison with sunspot numbers. A 12-month running average of sunspot numbers was also taken, in order to eliminate short-time variations and to exhibit the long-time trend in solar activity. The sunspot numbers used are the Zürich provisional numbers.

Another method of eliminating the seasonal variation can be employed in the case of the E region. The factor $K=f_E/\cos^{1/4}\psi$, is the value which f_E would have if measured at the subsolar point. This quantity should thus increase with the intensity of the ionizing radiation from the sun, and should bear the same relation to the general solar activity as does the ionizing radiation. By comparing $f_E/\cos^{1/4}\psi$ with the sunspot numbers, it should be possible to see how well the sunspot numbers indicate the intensity of the ionizing radiation responsible for the E layer.

This has been done in figure 3 for the monthly averages of f_E and sunspot numbers. The solid line in graph b is the monthly average noon f_E plotted for each month since 1933. The dotted line shows the subsolar f_E plotted for the same period as is the regular noon f_E. The correspondence of the subsolar f_E with sunspot numbers is incomplete in some details but nevertheless impressive. It shows that there is in general a fairly close relationship between the cause of the E-layer ionizing energy and the cause or number of sunspots. Over the period covered by the observations, it may be concluded that there is an excellent general correlation, and even a fair amount of agreement in details between the monthly averages of f_E and the sunspot numbers. The day-to-day correlation, however, is small.

[7] T. R. Gilliland, S. S. Kirby, N. Smith, *Characteristics of the ionosphere at Washington, D. C., March 1938*, Proc. Inst. Radio Engrs. **26**, 640 (1938).

The contour diagram at the bottom of figure 3 represents a space model of f_E (indicated in Mc/s) against the time of day and the month of the year, for critical frequencies above 2.6 Mc/s. The regular seasonal variation is quite well marked, the values being higher in the summer than in the winter. It is interesting to note how the contours of equal f_E follow the sunrise and sunset lines. The greater

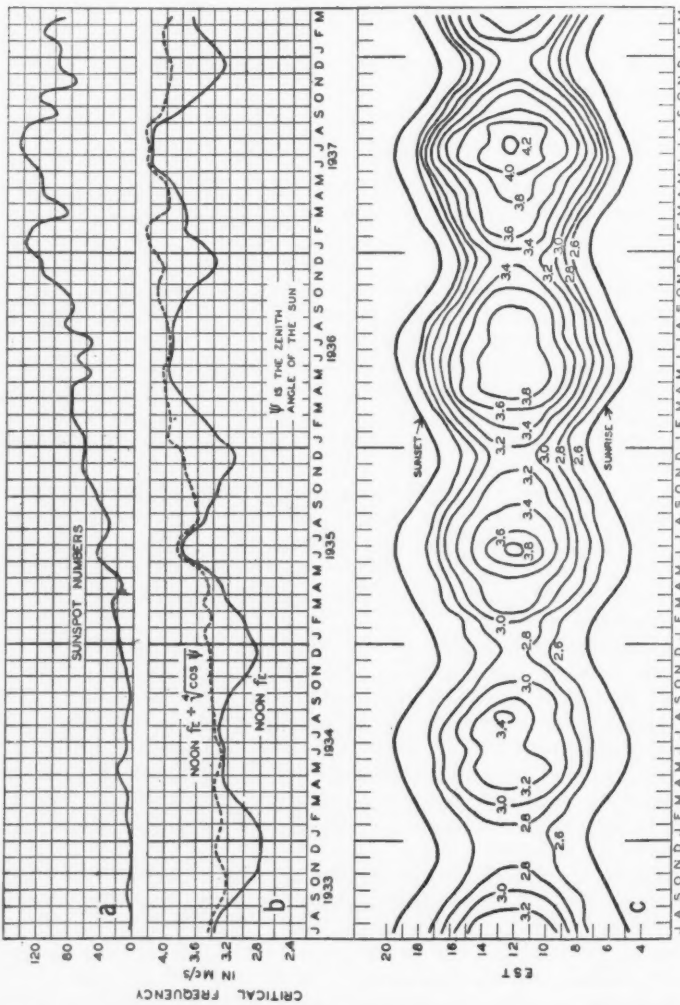

FIGURE 3.—*The critical frequency of the E region.*

Curve *a* is the monthly average of the sunspot numbers. Curve *b* shows the monthly average noon f_E (solid curve) and $f_E \cos^{1/4}\psi$ (dotted curve), where ψ is the noon zenith angle of the sun. Graph *c* is a contour diagram plotted against time of day and month of year, with each contour representing a certain value of the monthly average f_E in Mc/s.

number and closer spacing of contours during the latter part of the period shows how the critical frequencies have risen with the general long-time increase in solar activity.

The F_2 layer presents a more complicated picture, since purely terrestrial influences, such as the temperature of the layer, play an important part. No such simple method therefore exists for eliminating diurnal and seasonal variations as may be done for the E layer.

Because of this difficulty in eliminating the seasonal and diurnal variations of f_{F_2} it is hard to tell whether there is correlation in any considerable detail with sunspot numbers; such as was observed in the case of the *E*-region.

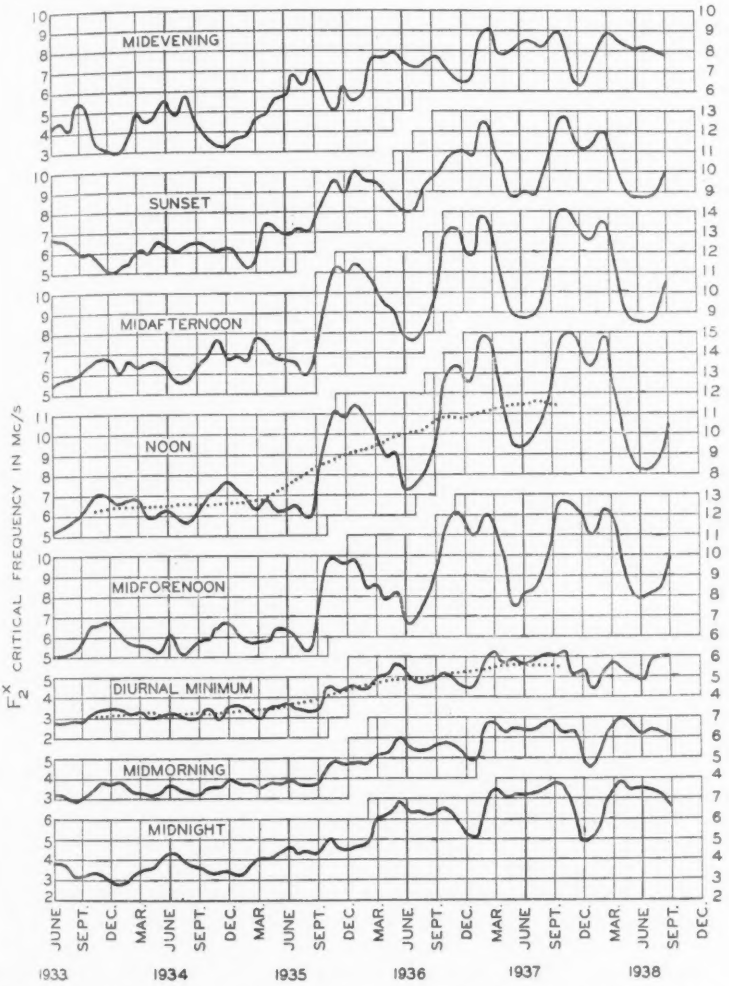

FIGURE 4.—*Monthly average values of f^z_F (night) and $f^z_{F_2}$ (daytime) plotted for the period 1933 to 1938.*

The dotted curves are 12-month running averages for the same hours.

Figure 4 shows the variation, for each month, of the $f^z_{F_2}$ for various parts of the day. The "midmorning" curve is for the time half-way between midnight and sunrise, and the "diurnal minimum" curve is for the time when f^z_F reaches its diurnal minimum, about 30 minutes before ground sunrise. The midforenoon, midafternoon, and mid-

evening, curves are for times half-way between sunrise and noon, noon and sunset, and sunset and midnight, respectively. All of these curves show the general rise in critical frequencies superimposed on the seasonal variation. The amplitude of the seasonal variation is greater for greater solar activity. The high daytime and low evening f_{F_2} in winter and the high evening f_{F_2} in summer stand out. For comparison the 12-month running averages of the noon and diurnal minimum

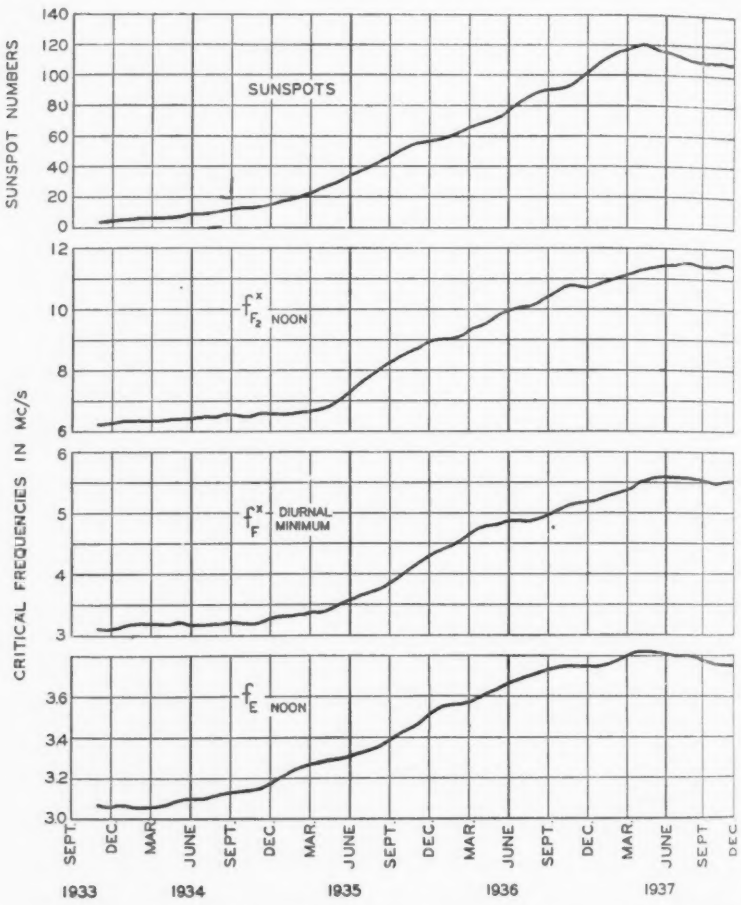

FIGURE 5.—*Twelve-month running averages of critical frequencies and sunspot numbers.*

$f^z_{F_2}$ are shown dotted to indicate the trend and the amplitude of the seasonal variation. The diurnal minimum shows the least seasonal variation; this may be more or less expected, since the direct influence of the sun would be a minimum at this time. The midwinter dip in the daytime f_{F_2} should also be noted.

If we consider the 12-month running averages of the critical frequencies and sunspot numbers, we may see how the trend of f_{F_2} and

f_E follows the trend of the sunspot numbers. Figure 5 shows these averages, for the noon E layer, the noon F_2 layer, and the F layer at the diurnal minimum 30 minutes before sunrise, plotted for the period from 1933 to 1937.

The diagram shows that:

1. The f_E followed the sunspot numbers quite closely. The two quantities began to rise together, reached a maximum together, and began falling together. The rates of change also seemed to vary together.

2. The diurnal minimum $f^z{}_F$ and the noon $f^z{}_{F_2}$ also followed the general trend of the sunspot numbers, but they lagged behind the sunspot numbers in starting to rise, and they kept on rising after the sunspot numbers had started to fall.

3. The sunspot-number curve showed a maximum at about April 1937. This may not indicate the major sunspot maximum of this cycle, but it is the first time since 1933 that the running average showed a decrease.

4. During the half-cycle of sunspot activity the f_E increased by a factor of about 1.25, and the $f^o{}_F$ and $f^o{}_{F_2}$ by a factor of about 2.00. The $f^o{}_F$ and $f^o{}_{F_2}$ represent the ordinary-ray critical frequencies and are about 800 kc/s lower than the $f^z{}_F$ and $f^z{}_{F_2}$, the extraordinary-ray critical frequencies, which are shown in the figures. This corresponds to an increase of E-layer ionization by a factor of about 1.55 and an increase of F- and F_2-layer ionization by a factor of about 4.00. It is interesting that during the rise of the critical frequencies, the amplitude of the seasonal variation of f_E increased by a factor about 1.60 and that of f_{F_2} by a factor of about 4.00; this effect is shown in figures 3 and 4.

Figure 6 is an extension of a curve already published [8] showing the relation between the annual averages of f_E, $f^o{}_{F_1}$, and $f^z{}_{F_2}$ and the sunspot numbers. Most of the points plotted are the same as certain points on the running average curves, except for the $f^o{}_{F_1}$; no running average could be taken of this quantity, since it could be measured only in the summer.

The general correlation between the average of critical frequencies and sunspot numbers is impressive. It indicates that there is on the average a definite relation between sunspot numbers and the solar activity responsible for the ionization of the earth's ionosphere. This relationship seems to be much closer for E-region ionization. In view of the difficulty and wide variations in methods of counting sunspots, together with the lack of any distinction made between active and inactive sunspot groups, close correlation is hardly to be expected.

In order to show the correlation between sunspot numbers and critical frequencies in as complete a manner as possible, the data have been summarized and plotted in figure 7, for which the coordinates are the 12-month running averages of the quantities. It is seen that all the critical frequencies increased with sunspot numbers. The variations of the points from the smooth curves may well be due to an irregular relation between sunspot numbers and the solar activity responsible

[8] E. B. Judson, *Comparison of data on the ionosphere, sunspots, and terrestrial magnetism*, J. Research NBS 17, 323 (1936) RP913; Proc. Inst. Radio Engrs. **25**, 38 (1937).

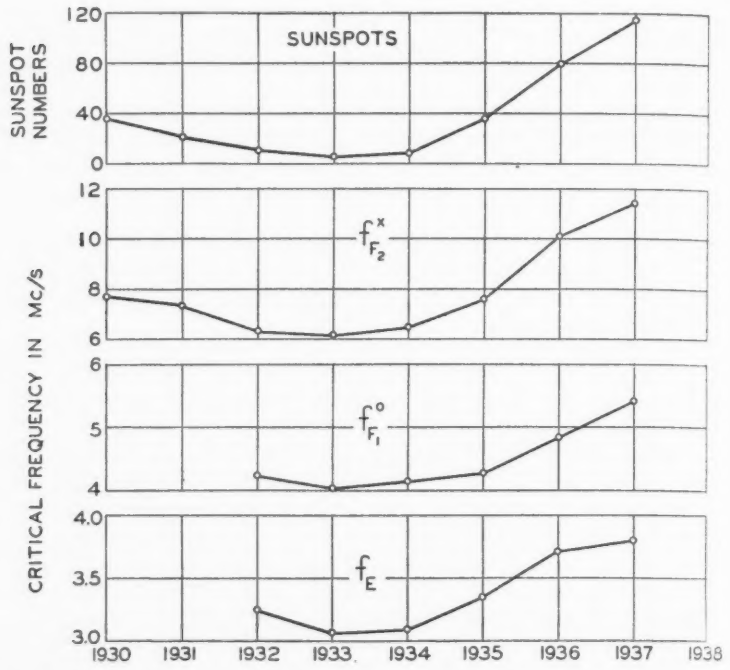

FIGURE 6.—*Comparison of annual averages of sunspot numbers and noon critical frequencies of ionosphere layers.*

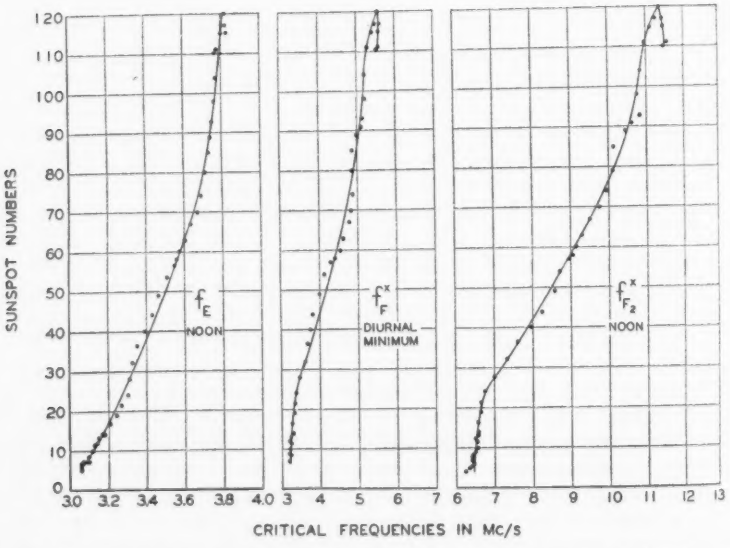

FIGURE 7.—*Twelve-month running averages of critical frequencies plotted against 12-month running average of sunspot numbers.*

for the ionization. It should be noted that the noon f_E, the diurnal minimum $f^z{}_{F}$, and the noon $f^z{}_{F2}$, did not increase as rapidly with sunspot numbers near the maximum.

There is a trace of a lag on both ends of the $f^z{}_{F}$ and $f^z{}_{F2}$ curves, but not on the f_E curve. It remains to be seen whether this effect persists throughout the descending half of the cycle or throughout subsequent cycles. It is well known that terrestrial magnetic disturbances are more frequent and severe following a sunspot maximum than preceding or during it. Since the seat of magnetic storms is principally in the F_2 region [9] this is some indication that such a lag may be reasonable, and that the types of solar radiation responsible for F_2-layer ionization and magnetic storms may be related and may themselves reach a maximum after the sunspot numbers have started to decrease.

IV. CONCLUSIONS

In conclusion, there is a good general correspondence, and, in the case of the E-layer, correlation in considerable detail, between the averages of sunspot numbers and the critical frequencies (or ionization densities), of the various ionosphere layers. This means that the averages of sunspot numbers give a good criterion of the general level of solar activity, and a good index to the general amount of ionizing radiation emitted from the sun. Exact correlation is indeed not to be expected in detail, since sunspots and the ionizing radiation are two different manifestations of solar activity, which follow the same trend in general but not in detail.

The existence of these relations, together with the vast amount of data available on sunspot activity in the past, suggests the possibility of forecasting the average condition of the ionosphere on the descending half of this cycle, and perhaps even in future cycles. Accordingly average radio-transmission conditions and average optimum frequencies for radio communication over different paths can be estimated, months and even years in advance.

WASHINGTON, August 30, 1938.

[9] S. S. Kirby, T. R. Gilliland, E. B. Judson, N. Smith, *The ionosphere, sunspots, and magnetic storms*, Phys. Rev. **48**, 849 (1935).

U. S. Department of Commerce National Bureau of Standards

RESEARCH PAPER RP1160

Part of Journal of Research of the National Bureau of Standards, Volume 21, December 1938

PROPERTIES OF PURIFIED NORMAL HEPTANE AND ISOOCTANE (2,2,4-TRIMETHYLPENTANE)

By Donald B. Brooks

ABSTRACT

Normal heptane and "isooctane" (2,2,4-trimethylpentane) are used universally as the primary standard reference fuels for the knock rating of automotive engine fuels. In developing specifications for these standards, it became apparent that data were needed on the physical properties of samples of the highest possible purity. Material already of high purity was carefully fractionated through columns having an efficiency equivalent to that of 60 theoretical plates. The important properties of the purest fractions obtained thereby were accurately measured. In each case the freezing point of the best material obtained was higher than currently accepted values.

CONTENTS

	Page
I. Origin of investigation	847
II. Source and preparation of materials	847
III. Test apparatus	848
IV. Physical properties	849
V. Calculation of purity	850
VI. References	852

I. ORIGIN OF INVESTIGATION

In 1934 the Cooperative Fuel Research Committee (CFR), representing the automotive and petroleum industries, requested the National Bureau of Standards to develop specifications for *n*-heptane and for "isooctane" (2,2,4-trimethylpentane) which are used as primary standard reference fuels for the knock rating of automotive engine fuels. The investigation of the impurities in the isooctane has been described in this Journal [1].[1] A similar investigation on *n*-heptane is in progress. In addition to knowing the nature and properties of the impurities in the standards, it is necessary to know accurately certain properties of *n*-heptane and isooctane of high purity. To this end the purest available materials were further purified, and the boiling points, freezing points, refractive indices, densities, and certain of their differential coefficients were accurately measured on the resulting materials.

II. SOURCE AND PREPARATION OF MATERIALS

About 7.6 liters of isooctane of high purity had been obtained in the course of the investigation mentioned above. This material was now distilled through fractionating columns packed with locket chain

[1] Figures in brackets indicate the references at the end of this paper.

and having an efficiency equivalent to that of 60 theoretical plates. The forerun (10%) and residue (9%) were discarded and the remaining 81 percent was divided into three roughly equal portions. The boiling points of the individual fractions and the freezing points of the three portions are shown in figure 1.

The center portion of 2,100 and 500 ml of the third portion were combined and again fractionated. The distillate was separated into 10 fractions and the normal boiling point and freezing point of each fraction were measured accurately. The purer fractions were selected for further study.

The source material chosen for the purified *n*-heptane was the purest commercially available material which had been produced at the time this work was done, namely, batch 7 of CFR certified *n*-heptane. About 2.8 liters of this *n*-heptane was fractionated through the columns previously used for the isooctane, and cut into 200-ml fractions. The purer fractions were selected for further investigation.

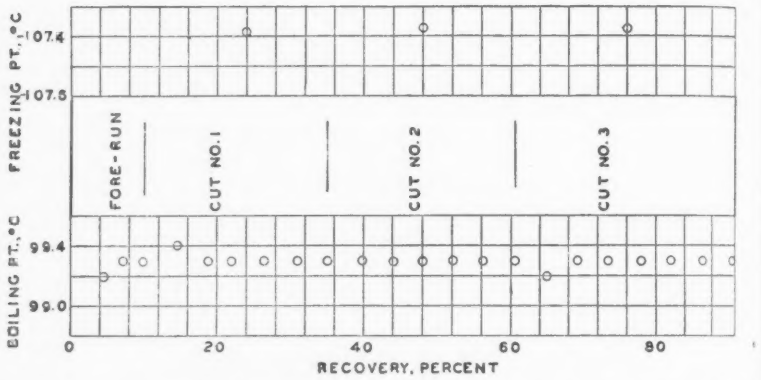

FIGURE 1.—*Boiling- and freezing-points of material obtained after first stage of purification of isooctane.*

III. TEST APPARATUS

The apparatus used in the freezing-point measurements comprised a Pyrex tube containing a platinum resistance thermometer and stirrer, this tube being surrounded to a point above the sample height by a metal tube covered with aluminum foil. A Dewar flask in turn surrounded the above, and was partially immersed in liquid air. In operation, sufficient of the sample was placed in the Pyrex tube to cover the thermometer elements but not to exceed the limit of stirrer travel.

A minor modification which resulted in a material increase in precision was made in the design of the motor-driven stirrer. Stirrers customarily have consisted of a wire helix. The helices employed in the present apparatus were formed on a mandrel and rigidly attached thereto. While rotating the mandrel in a lathe, the helix was ground until the wire comprising it had approximately a semicircular cross section, the flat being on the outer side of the helix. This gave the stirrer a sharp shearing edge. It is believed that the increase of

precision results from the fact that this sharp edge shears microscopic crystals from the walls of the container as soon as they begin to form. Being microscopic, the crystals are rapidly dispersed throughout the liquid, and greatly improve the approach to equilibrium attained during freezing. When a partially frozen sample is removed from this apparatus, it has a milky appearance; as it begins to warm, this milkiness disappears almost instantaneously, indicating very small crystal size.

Boiling points of samples were measured while the samples were being distilled through a 10-inch jacketed column [3], the jacket being externally heated electrically to a temperature such that only slight condensation occurred in the column. A platinum resistance thermometer inserted in the column was used for the temperature measurement. The barometer used for measurement of atmospheric pressure in the determinations on isooctane was a Fuess Standard, readable to 0.01 mm. Reproducibility of results, when corrected to 760 mm Hg, averaged better than 0.002° C, equivalent to 0.04 mm Hg. An inferior Fortin-type barometer, readable only to 0.1 mm, was used in the determinations on *n*-heptane; although it was calibrated after each measurement by determining the boiling point of water, the reproducibility averaged only 0.009° C, equivalent to 0.2 mm Hg.

A Mueller bridge having coils maintained continuously at 35° C and reading directly to 0.0001 ohm, was used in conjunction with a 25-ohm platinum resistance thermometer on both boiling- and freezing-point tests. Both the bridge and the thermometer were calibrated frequently, the latter in accordance with the procedure specified for the International Temperature Scale.

The refractive indices of the carefully dried isooctane, measured by L. W. Tilton [2] of this Bureau, were determined for sodium light by the minimum-deviation method, using a water-jacketed hollow prism which was mounted in a stirred air bath on the spectrometer table. A platinum resistance thermometer was immersed in the sample during index measurements, and the indices were corrected to refer to dry air at the listed temperatures and at a pressure of 760 mm Hg. The probable error in determining the indices is less than 0.000005, and it is thought that the systematic error of the determination did not exceed this value. The indices for *n*-heptane were determined on an Abbe type refractometer (Valentine) graduated to 0.0001 and calibrated against the isooctane.

The densities of the samples, determined by E. L. Peffer of this Bureau, were measured by picnometer. The measured values given for the dry samples are believed to be correct to within ± 0.00001.

IV. PHYSICAL PROPERTIES

The physical properties of isooctane and *n*-heptane found in this investigation are given in table 1, together with the summarized boiling-point data of Smith and Matheson [4], and data from a critical review by Von Grosse and Egloff [5].

It is believed that Smith and Matheson's ebulliometric data on *n*-heptane are decidedly more accurate than those obtained in this investigation. It should be mentioned that their samples were not

the same as those used herein, and that their apparatus also differed materially.

TABLE 1.—*Physical properties of n-heptane and isooctane (2, 2, 4-trimethylpentane)*

[For precision of measurements see text]

Reference [1]	Freezing point	Boiling point 760 mm Hg	dt/dP	Refractive index		dn/dt	Density		dD/dt	Freezing point lowering
				n_D^{30}	n_D^{25}		D^{30}	D^{T}		
ISOOCTANE (2, 2, 4-Me_3PENTANE)										
	°C	°C	°C per mm Hg				g/ml	g/ml	g/ml/°C	°C per mole-percent
Present work	−107.311	99.234	0.04651	1.39146	1.38899	0.000494	0.69182	0.68356[30°]	0.000826	0.2381
Smith and Matheson [4]		99.234	.04651							
Von Grosse and Egloff [5]	−107.41	99.3		1.3916			.6918		.00080	
n-HEPTANE										
Present work	−90.576	98.422	0.04493	1.38777	1.38523	0.000508	0.68372	0.67948[21°]	0.000848	0.2004
Smith and Matheson [4]		98.413	.04485							
Von Grosse and Egloff [5]	−90.62	98.38	.0449	1.38774		.00046	.68365	.67522[20°]	.00084	

[1] See reference [5] for a critical review of the literature.

The data on freezing-point depression were obtained on samples of fairly high purity and are plotted in figures 2 and 3, for isooctane and *n*-heptane, respectively. Freezing curves for the purest samples of isooctane and *n*-heptane are given figures 4 and 5.

V. CALCULATION OF PURITY

From the data in table 1, it follows that if the purity of isooctane is above 97 mole-percent, it can be expressed, relative to that of the present preparation, by the formula

$$P=\frac{131.121+t}{0.2381},$$

where

P=mole-percent 2, 2, 4-trimethylpentane

t=observed freezing point, °C.

The analogous formula for *n*-heptane is

$$P=\frac{110.616+t}{0.2004}$$

where the symbols have a similar meaning.

The assistance of L. W. Tilton and E. F. Peffer in making the refractive index and density measurements is gratefully acknowledged. It is a pleasure to acknowledge also the great assistance rendered by the members of the American Petroleum Institute Project 6, both in consultation and in permitting use of their distillation apparatus for this work.

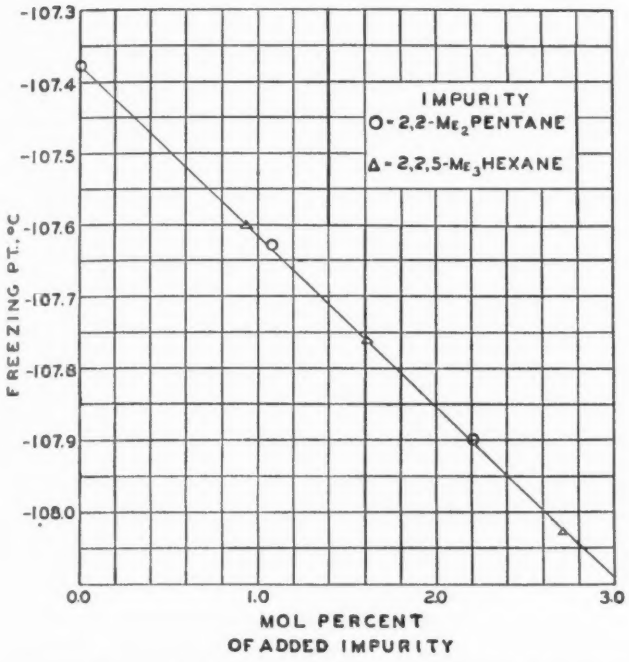

FIGURE 2.—*Effect of impurities on the freezing-point of isooctane.*

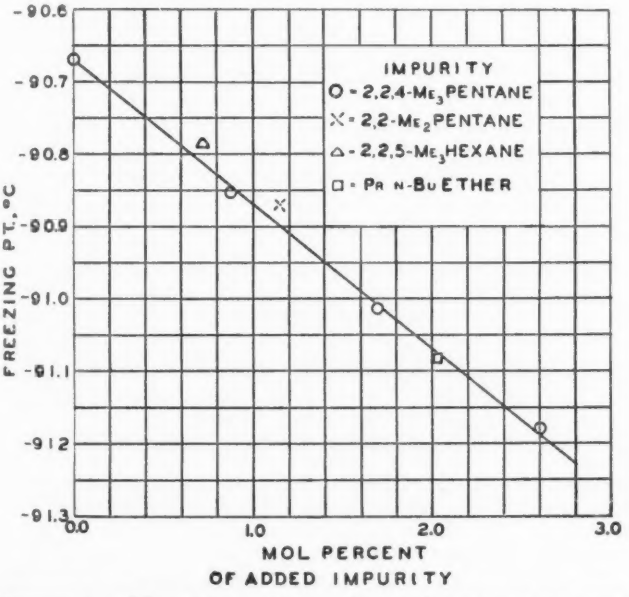

FIGURE 3.—*Effect of impurities on the freezing-point of n-heptane.*

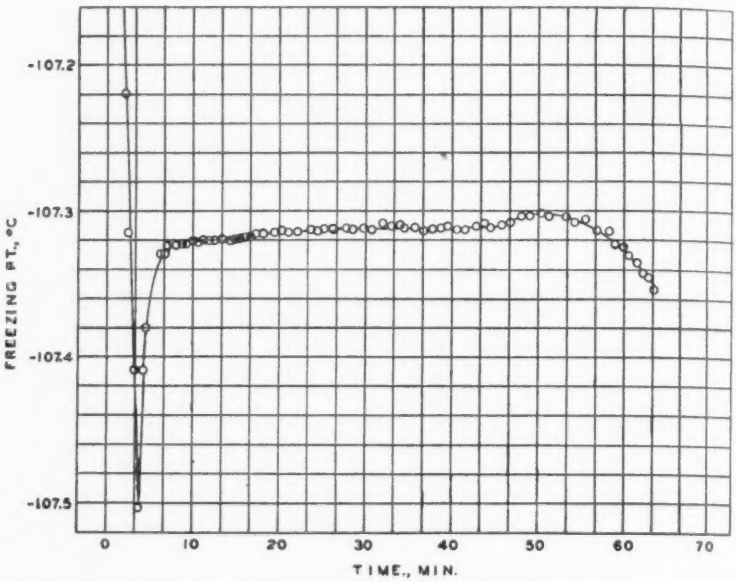

FIGURE 4.—*Freezing-curve of the purest sample of isooctane.*

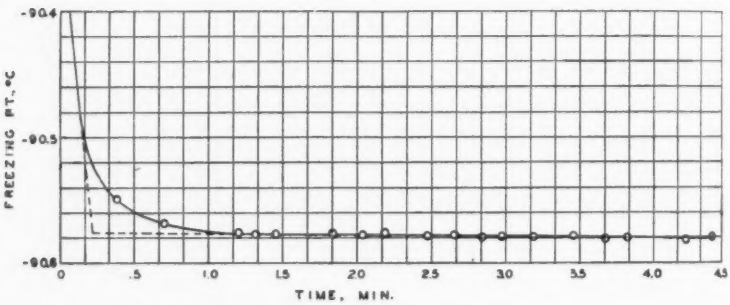

FIGURE 5.—*Freezing-curve of the purest sample of n-heptane.*

VI. REFERENCES

[1] Donald B. Brooks, Robetta B. Cleaton, and Frank R. Carter, J. Research NBS **19,** 319 (1937) RP1027.
[2] Leroy W. Tilton and John K. Taylor, J. Research NBS **20,** 419 (1938) RP1085.
[3] B. J. Mair, BS J. Research **9,** 457 (1932) RP482.
[4] Edgar Reynolds Smith and Harry Matheson, J. Research NBS **20,** 641 (1938) RP1097.
[5] Aristide von Grosse and Gustave Egloff, Physical Constants of Paraffin Hydrocarbons (Universal Oil Products Co. Bul. 219, 1938).

WASHINGTON, October 27, 1938.

U. S. DEPARTMENT OF COMMERCE NATIONAL BUREAU OF STANDARDS

RESEARCH PAPER RP1161

Part of Journal of Research of the National Bureau of Standards, Volume 21, December 1938

STRENGTH OF A RIVETED STEEL RIGID FRAME HAVING A CURVED INNER FLANGE

By Ambrose H. Stang, Martin Greenspan, and William R. Osgood

ABSTRACT

The distribution of stress in the knee of a riveted steel rigid-frame specimen having a curved inner flange was investigated both experimentally and theoretically. A theory was developed which gives the stresses in the knee to the same order of accuracy as the ordinary beam theory gives the stresses in the straight legs of the frame. Reinforcing the outer corner of the knee and stiffening the web were shown to have little effect on the stress distribution in the frame. The maximum load that could be sustained by the specimen was determined.

CONTENTS

	Page
I. Introduction	853
II. Rigid-frame specimen	853
1. Description of the specimen	853
2. Tensile properties of the material	854
III. Testing procedure	855
IV. Measured stresses	856
V. Analytical determination of the stresses	863
VI. Theoretical stresses	868
VII. Maximum load	870
VIII. Conclusions	870
IX. References	871

I. INTRODUCTION

Tests have been made, with the cooperation of the American Institute of Steel Construction, on three steel rigid-frame specimens. The results of tests on a riveted specimen having straight flanges [1][a] have been reported in RP1130. The results of tests on a riveted specimen having a curved inner flange are reported here. This specimen was donated by the American Bridge Co. The results of tests on the third specimen will be reported in a later paper.

II. RIGID-FRAME SPECIMEN

1. DESCRIPTION OF THE SPECIMEN

The rigid-frame specimen is shown in figure 1. It was fabricated from steel plates and angles joined by riveting. The weight as determined by the American Bridge Co. was 2,800 lb. The web of

[a] Numbers in brackets indicate the references at the end of this paper.

the specimen was cut from a single plate. The specimen was symmetrical about a line joining the center of the curved flange and the intersection of the straight flanges.

The outer corner of the specimen was reinforced by a gusset on each side secured to the web by rivets. Additional reinforcement at the outer corner was provided by extra angles and a bent plate. These angles and the plate were secured by bolts turned to a light driving fit in reamed holes, as shown in figure 1, and were removed in some of the tests.

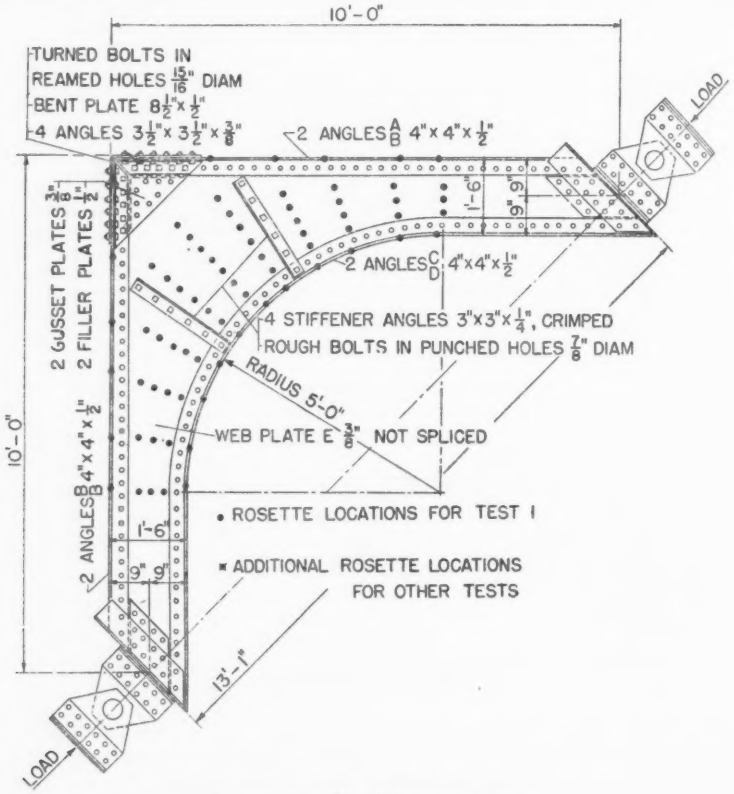
10'-0"
TURNED BOLTS IN REAMED HOLES 15/16" DIAM
BENT PLATE 8 1/2" x 1/2"
4 ANGLES 3 1/2" x 3 1/2" x 3/8"
2 ANGLES A B 4" x 4" x 1/2"
LOAD
2 GUSSET PLATES 3/8"
2 FILLER PLATES 1/2"
1'-6"
9"
9"
2 ANGLES C D 4" x 4" x 1/2"
4 STIFFENER ANGLES 3" x 3" x 1/4", CRIMPED
ROUGH BOLTS IN PUNCHED HOLES 7/8" DIAM
RADIUS 5'-0"
10'-0"
2 ANGLES B 4" x 4" x 1/2"
WEB PLATE E 3/8" NOT SPLICED
• ROSETTE LOCATIONS FOR TEST I
× ADDITIONAL ROSETTE LOCATIONS FOR OTHER TESTS
1'-6"
9"
9"
13'-1"
LOAD

FIGURE 1.—*Rigid-frame specimen.*

The web was stiffened by angles, as shown in figure 1. The lower ends of the stiffener angles were crimped over the connected legs of the inner-flange angles. The stiffener angles were secured to the web and the inner flange of the specimen by rough bolts in punched holes and were removed in one of the tests.

2. TENSILE PROPERTIES OF THE MATERIAL

Samples were taken from the flange angles and web plate before fabrication and marked *A*, *B*, *E*, etc., for identification, as shown in figure 1. The tensile properties of the material were determined from coupons machined from these samples. The coupons were ASTM

8-in.-gage-length tensile specimens for plates, shapes, and flats [2]. The width of the coupons at the reduced section was 1.5 in., and the thickness was that of the material as rolled.

The coupons were tested in a screw-driven, beam-and-poise testing machine having a capacity of 100 kips. The speed of the movable platen of the testing machine was 0.008 in./min until the extensometer was removed from the coupon. Thereafter the speed of the movable platen was 0.4 in./min.

The strains were determined by means of a Ewing extensometer of 8-in. gage length. One division on the scale of this instrument corresponds to a strain of 0.000025. Readings were estimated to 0.1 division.

The yield point was determined by the drop-of-beam method. Young's modulus of elasticity and the proportional limit were determined from difference curves [3].

The tensile properties of the material are given in table 1.

TABLE 1.—*Tensile properties of the material*

Coupon number	Coupon from	Thickness	Young's modulus of elasticity	Proportional limit	Yield point	Tensile strength	Elongation in 8 inches	Reduction of area
		in.	*Kips/in.²*	*Kips/in.²*	*Kips/in.²*	*Kips/in.²*	*Percent*	*Percent*
1	Angle *A*	0.507	28,600	33	36.7	60.3	28.8	57
2	Angle *A*	.502	29,200	36	37.8	61.4	29.8	59
3	Angle *B*	.498	29,400	31	40.2	67.7	27.9	55
4	Angle *B*	.492	27,800	28	40.6	68.2	27.0	62
5	Angle *C*	.497	29,400	31	39.6	65.6	28.3	55
6	Angle *C*	.500	29,600	35	40.8	68.2	28.3	54
7	Angle *D*	.501	29,200	33	40.2	68.5	27.8	55
8	Angle *D*	.495	29,000	33	39.6	67.1	28.8	53
9	Plate *E*	.383	29,600	35	41.0	61.9	29.8	58
10	Plate *E*	.385	28,900	35	40.2	61.7	28.0	53
11	Plate *E*	.390	29,200	35	39.8	61.2	29.9	55
12	Plate *E*	.391	29,000	38	39.7	60.9	29.2	57
Average			29,100					

III. TESTING PROCEDURE

The rigid-frame specimen was loaded in a vertical, screw-driven, beam-and-poise testing machine having a capacity of 600 kips. The load was applied through two pin-connected shoes, shown in figure 1, one attached to each leg of the frame.

Three different tests were made with the load acting along the line indicated in figure 1. For test 1 the bent plate and extra angles at the outer corner and the stiffener angles were bolted to the specimen. For test 2 the bent plate and extra angles at the outer corner were removed, and for test 3 the stiffener angles were also removed. The bolts through the angles were replaced in each case. The gussets at the outer corner were not removed for any of these tests.

Strain-gage readings were taken at rosettes located as shown in figure 1 with Whittemore strain gages having gage lengths of 2 inches. One division on the dial of the strain gage corresponds to a strain of 0.00005. Readings were estimated to 0.1 division. Each rosette consisted of four gage lines intersecting at a point and inclined at 45° to one another.

Each rosette location on the web shown in figure 1 represents two rosettes, one on either side of the specimen; and each rosette location on the angles represents four rosettes, one on the inside and one on the outside of the outstanding leg of each angle.

The specimen is shown in the testing machine for test 1 in figure 2. Before any strain-gage readings were taken, a compressive load of 67 kips was applied and released five times. Strain-gage readings were taken at compressive loads of 5 kips and 65 kips.

IV. MEASURED STRESSES

Stresses computed from the strain-gage readings will be called measured stresses. These stresses were computed from the strains[b] due to the 60-kip increase in load by the methods outlined in RP1130 [1]. The strains in corresponding gage lines of rosettes on opposite sides of the web of the specimen were averaged and the average values used in the computations. In the case of the outstanding legs of the flange angles, the strains in corresponding gage lines of the four rosettes were averaged and the average values used in the computations. The magnitudes and directions of the principal stresses and of the maximum shearing stress for each set of two or four rosettes were computed.

The results of these computations are shown for test 1 in figures 3 to 6, inclusive. Figure 3 is a contour chart of maximum principal stress. Each contour line is a locus of points of equal maximum principal stress in the plane of stress. The contour lines show only the magnitudes of the stress. The directions of the contour lines are not the directions of the maximum principal stresses. The contour lines do not give the values of the stresses in the stiffeners. Similar contour charts of minimum principal stress and of maximum shearing stress are shown in figures 4 and 5, respectively, except that the contour lines of maximum shearing stress in figure 5 were drawn for the three-dimensional state of stress. At any point at which the principal stresses in the plane of stress are of the same sign, the maximum shearing stress occurs in planes at 45° to the plane of stress and is equal to one-half the numerically larger of these principal stresses. The magnitudes and directions of the principal stresses in the plane of stress are shown in figure 6.

The results of tests 2 and 3 are shown in the same way in figures 7 to 14, inclusive.

[b] The greatest deviation of any value of the modulus of elasticity from the average value was about 4.5 percent (table 1). The average value was used for computing the stresses, because it was estimated that the error in the strain-gage readings was greater than 4.5 percent.

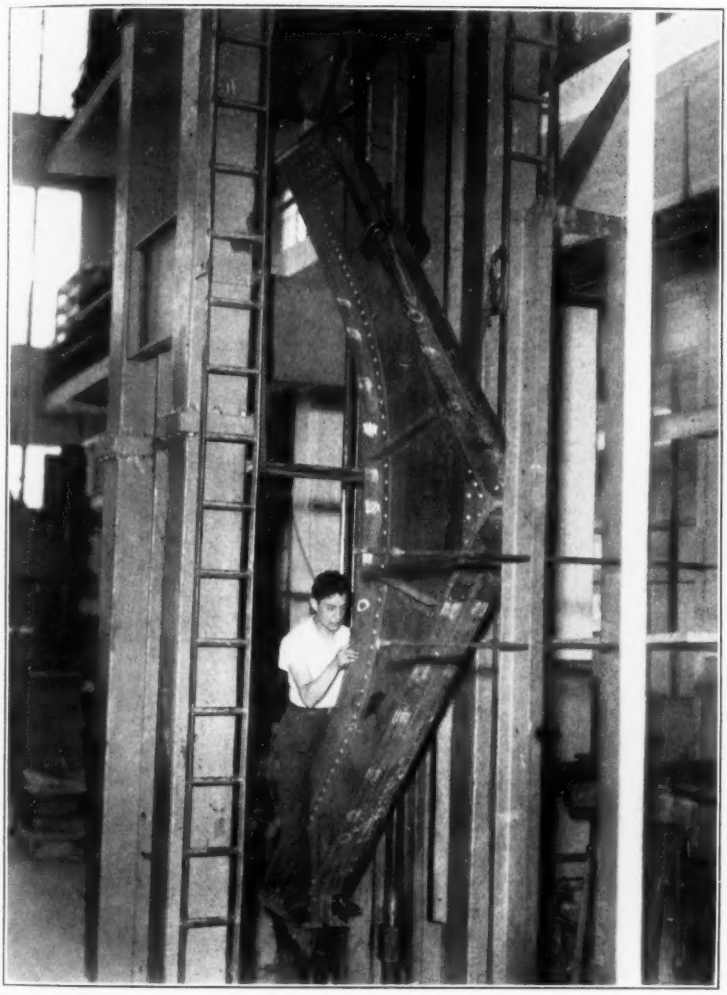

FIGURE 2.—*The rigid-frame specimen in the testing machine.*

UNIV. OF MICH.

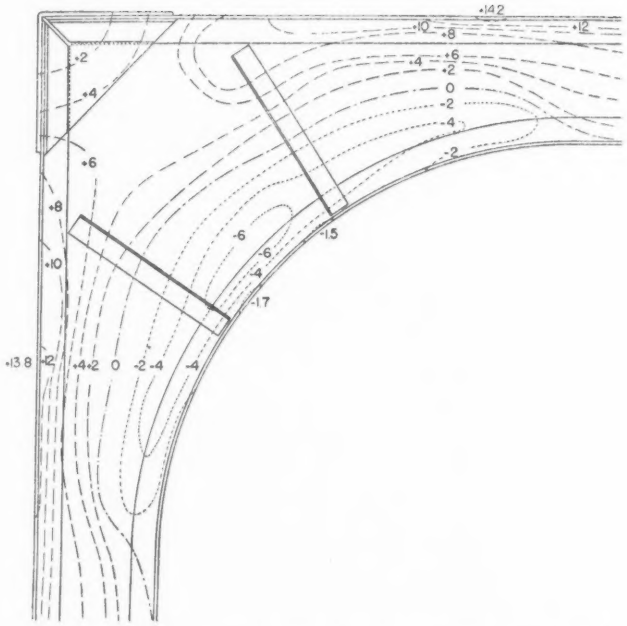

FIGURE 3.—*Test 1.—Maximum principal stress, kips/in*^{2}.

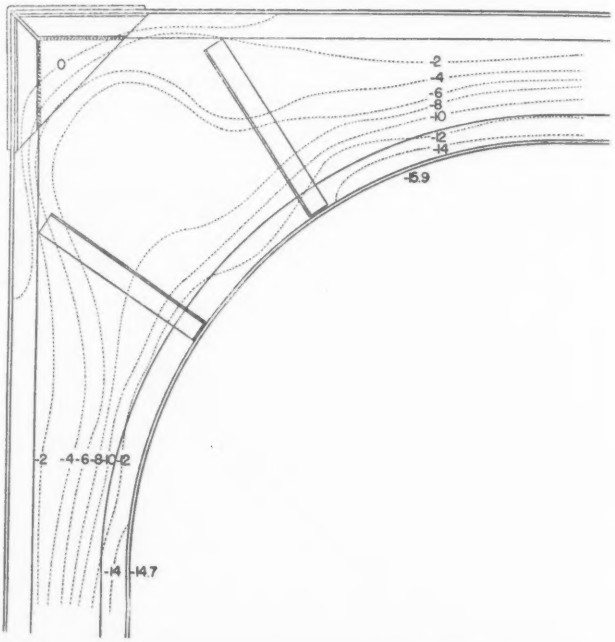

FIGURE 4.—*Test 1.—Minimum principal stress, kips/in*^{2}.

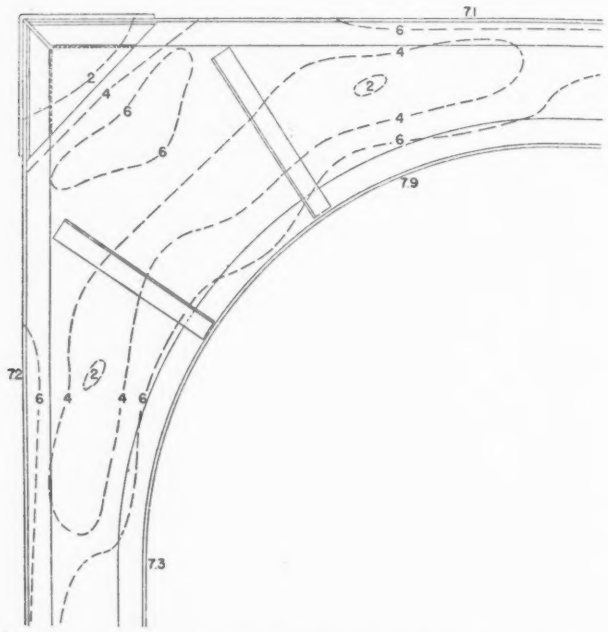

FIGURE 5.—*Test 1.—Maximum shearing stress, kips/in².*

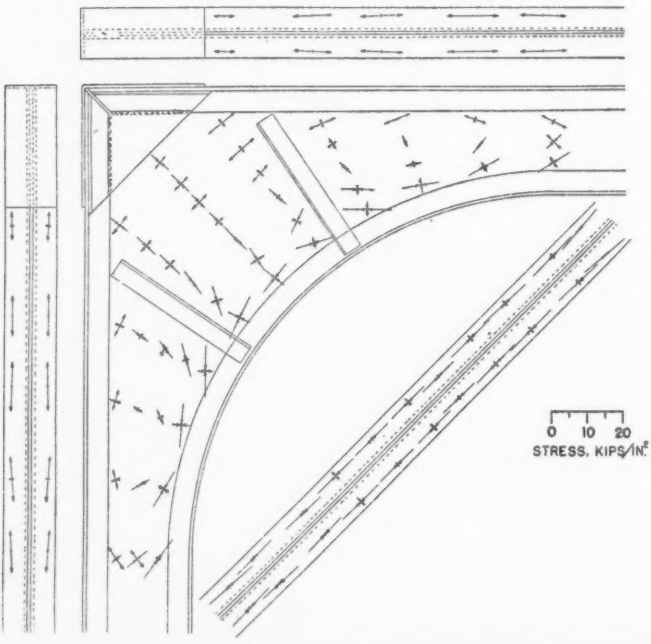

FIGURE 6.—*Test 1.—Magnitude and direction of the maximum and of the minimum principal stresses, kips/in².*

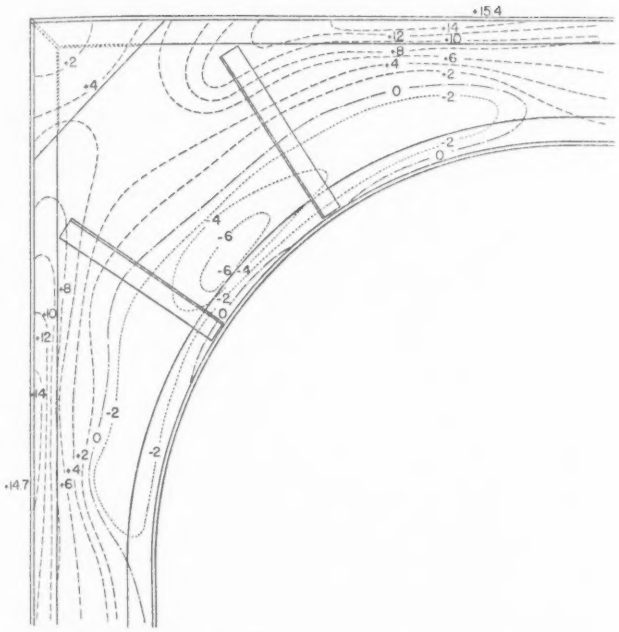

FIGURE 7.—*Test 2.—Maximum principal stress, kips/in².*

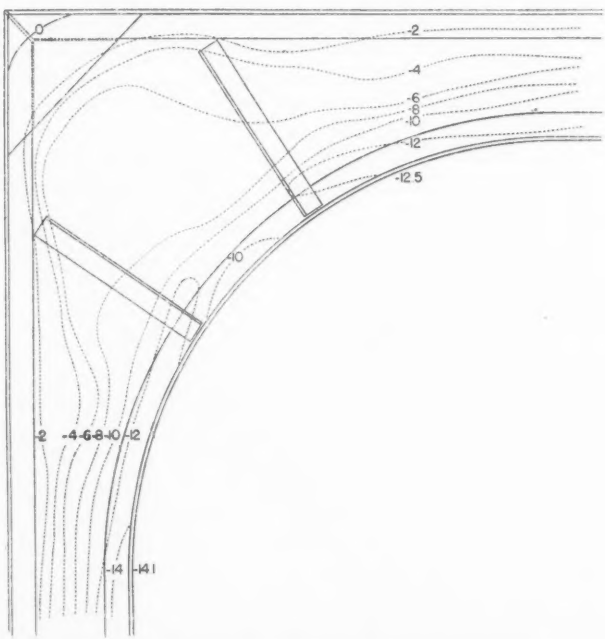

FIGURE 8.—*Test 2.—Minimum principal stress, kips/in².*

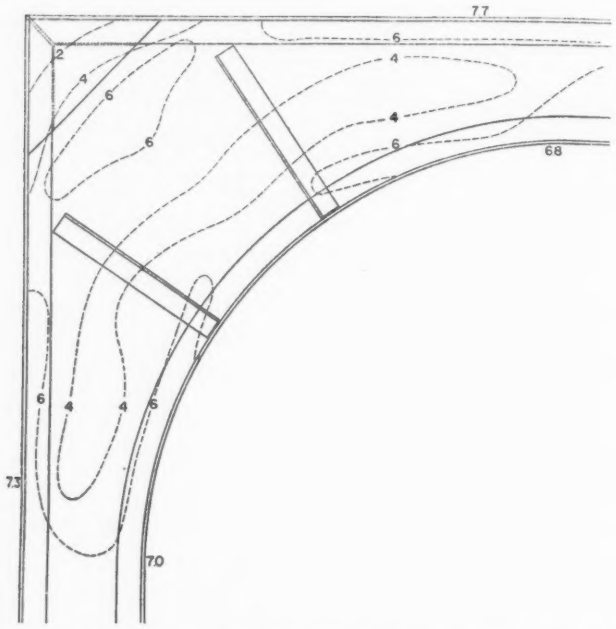

FIGURE 9.—*Test 2.—Maximum shearing stress, kips/in.²*

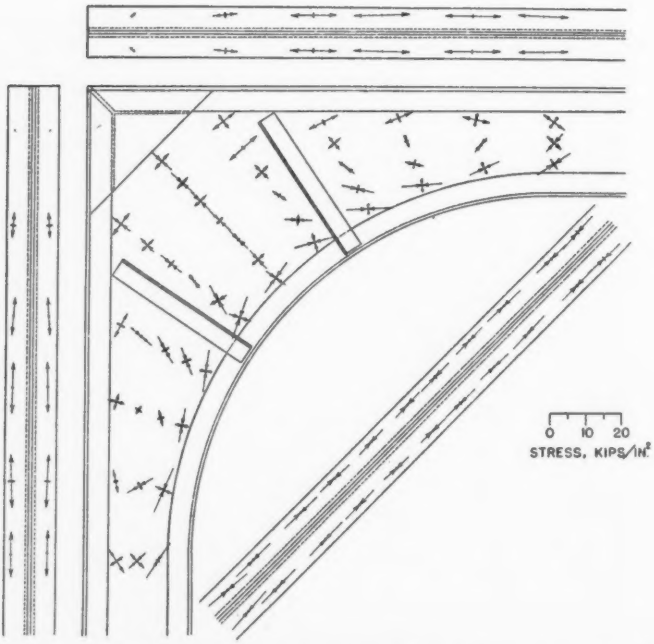

FIGURE 10.—*Test 2.—Magnitude and direction of the maximum and of the minimum principal stresses, kips/in.²*

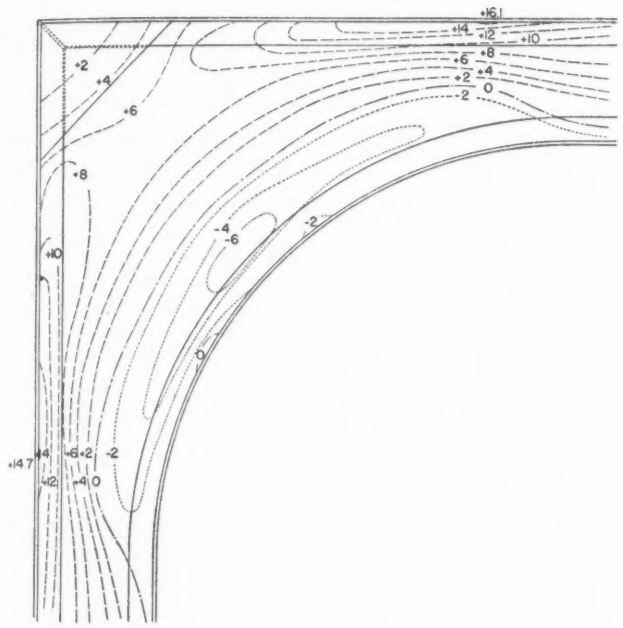

FIGURE 11.—*Test 3.—Maximum principal stress, kips/in*^{2}.

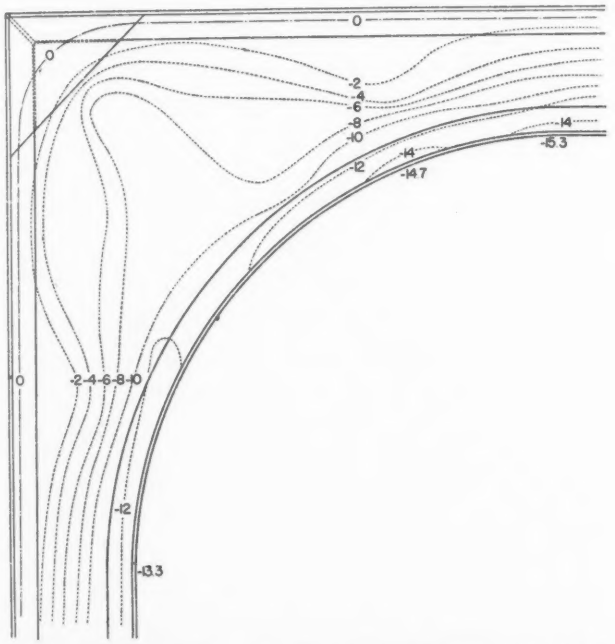

FIGURE 12.—*Test 3.—Minimum principal stress, kips/in*^{2}.

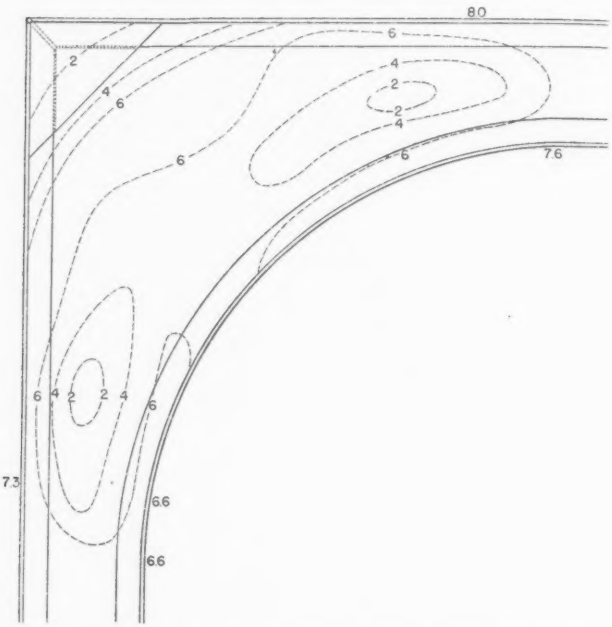

FIGURE 13.—*Test 3.—Maximum shearing stress, kips/in².*

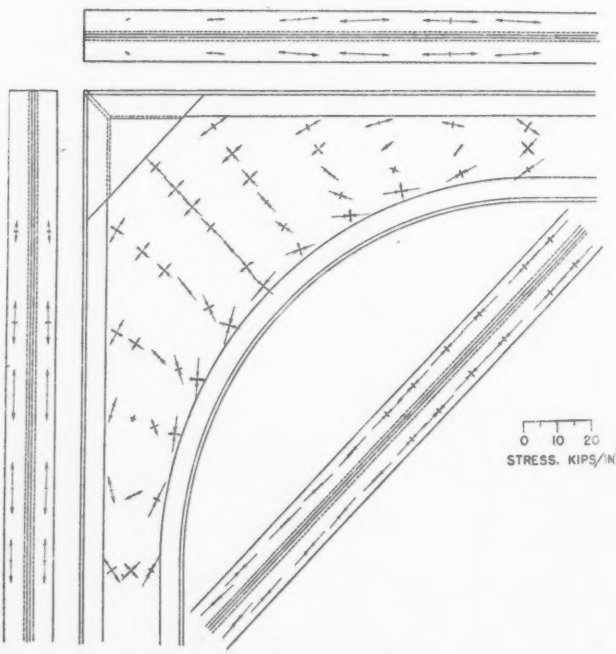

FIGURE 14.—*Test 3.—Magnitude and direction of the maximum and of the minimum principal stresses, kips/in².*

Comparison of the results for the three tests shows that the bent plate and extra angles at the outer corner and the stiffener angles on the web had little effect on the stress distribution in the frame. The stresses at the outer corner were very small.

V. ANALYTICAL DETERMINATION OF THE STRESSES

A rigorous theoretical determination of the state of stress in the knee of a rigid frame with nonparallel curved flanges has not been obtained, but it is possible to determine the stresses semirationally with an accuracy believed to be comparable to that obtained for straight girders by the ordinary formulas used for such girders. Let figure 15 represent the web and the centroidal axes of the flanges of a portion of a rigid frame similar to the specimen tested. Suppose

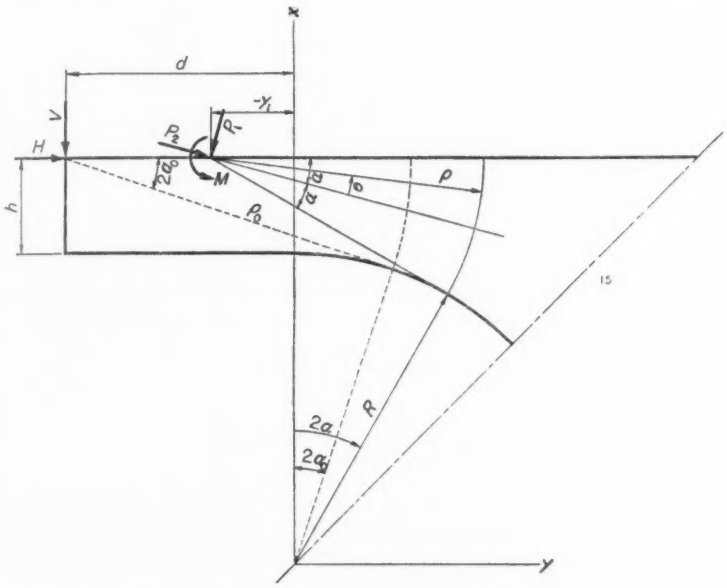

FIGURE 15.—*Web and centroidal axes of flanges of a portion of a rigid frame.*

Determination of circular section and resolution of load at edge of wedge.

the applied load resolved into horizontal and vertical components H and V acting at the centroid of the outer flange at a distance d from the point of tangency of the curved inner flange. Then, with the systems of coordinates shown in the figure, by drawing from any point $(R, 2\alpha)$ of the curved inner flange a tangent intersecting the outer flange at the point $(R+h, y_1)$ it is possible to write semirational expressions for the stresses along the arc, $2\rho\alpha$, swung with center at the intersection, and radius, ρ, equal to the distance between the points $(R+h, y_1)$ and $(R, 2\alpha)$. The radii $\theta=\alpha$, $\theta=-\alpha$, and the arc $2\rho\alpha$ form the boundaries of a wedge, which suggests analysis by means of Airy stress functions. A combination of stress functions is described below by means of which the distribution of stress at the

circular boundary of the wedge may be approximated closely, even though the boundary conditions along the straight boundaries are not all satisfied. The solution for the stresses along the arc $2\rho\alpha$ is very similar to the ordinary one for a girder with parallel flanges and reduces to the latter solution as $\alpha \doteq 0$ ($\rho = \infty$). Its adequacy can be determined only by tests.

In order to obtain the solution, it is convenient to replace the applied load by a force P_1 acting at the point $(R+h, y_i)$ perpendicular to the polar axis $\theta=0$, a force P_2 acting at the same point along the polar axis, and a couple M. These forces and the couple and the radius ρ, which will be required, are easily found to be (see fig. 15)

$$P_1 = V\cos\alpha - H\sin\alpha, \tag{1}$$

$$P_2 = V\sin\alpha + H\cos\alpha, \tag{2}$$

$$M = V\left[d - \frac{h\cos 2\alpha - R(1-\cos 2\alpha)}{\sin 2\alpha}\right], \tag{3}$$

$$\rho = \frac{h+R(1-\cos 2\alpha)}{\sin 2\alpha}. \tag{4}$$

Now assume that the stresses in the wedge due to P_1 can be derived from the stress function [4]

$$\phi_1 = -\frac{c_1}{2} r\theta\cos\theta, \tag{5}$$

where r is the radius vector from the edge, $(R+h, y_i)$, to any point in the wedge. From eq 5

$$(\sigma_r)_1 = \frac{c_1}{r}\sin\theta, \tag{6}$$

$$(\sigma_\theta)_1 = 0, \tag{7}$$

$$(\tau_{r\theta})_1 = 0. \tag{8}$$

To determine the constant c_1, the condition may be used that the component parallel to P_1 of the resultant of the distribution of stress along the arc $2\rho\alpha$ must be equal and opposite to P_1:

$$2A_f\frac{c_1}{\rho}\sin^2\alpha + tc_1\int_{-\alpha}^{\alpha}\sin^2\theta d\theta - P_1 = 0, \tag{9}$$

where the cross-sectional area A_f of each flange is assumed concentrated at $\theta=\alpha$ and $\theta=-\alpha$, respectively, and the thickness of the web plate is denoted by t. From eq 9

$$c_1 = \frac{P_1\rho}{t\rho(\alpha-\sin\alpha\cos\alpha)+2A_f\sin^2\alpha},$$

and the stress $(\sigma_\rho)_1$[c] becomes

$$(\sigma_\rho)_1 = \frac{P_1\sin\theta}{t\rho(\alpha-\sin\alpha\cos\alpha)+2A_f\sin^2\alpha}. \tag{10}$$

[c] Owing to the wide discrepancy between the actual and assumed boundary conditions along the sides of the wedge, none of the computed stresses at $r \neq \rho$ have any significance.

Assume next that the stresses in the wedge due to P_2 can be derived from the stress function [4]

$$\phi_2=\frac{a_1}{2}r\theta \sin \theta, \tag{11}$$

from which

$$(\sigma_r)_2=\frac{a_1}{r}\cos \theta, \tag{12}$$

$$(\sigma_\theta)_2=0, \tag{13}$$

$$(\tau_{r\theta})_2=0. \tag{14}$$

To determine the constant a_1 the condition may be used that the resultant of the distribution of stress along the arc $2\ \rho\alpha$ must hold P_2 in equilibrium:

$$2A_f\frac{a_1}{\rho}\cos^2 \alpha+ta_1\int_{-\alpha}^{\alpha} \cos^2 \theta d\theta+P_2=0. \tag{15}$$

From eq 15

$$a_1=-\frac{P_2\rho}{t\rho(\alpha+\sin\ \alpha \cos\ \alpha)+2A_f \cos^2 \alpha},$$

and the stress $(\sigma_\rho)_2$[4] becomes

$$(\sigma_\rho)_2=-\frac{P_2 \cos \theta}{t\rho(\alpha+\sin\ \alpha \cos\ \alpha)+2A_f \cos^2 \alpha}. \tag{16}$$

Assume, finally, that the stress in the wedge due to M can be derived from the stress function

$$\phi_3=a_0'\theta+d_2' \sin 2\theta, \tag{17}$$

from which

$$(\sigma_r)_3=-\frac{4}{r^2}d_2' \sin 2\theta, \tag{18}$$

$$(\sigma_\theta)_3=0, \tag{19}$$

$$(\tau_{r\theta})_3=\frac{1}{r^2}(a_0'+2d_2' \cos 2\theta). \tag{20}$$

Again, by considering the boundary $2\rho\alpha$ of the wedge, the constants may be determined from the condition of equilibrium of forces perpendicular to the polar axis and the condition of equilibrium of moments (with respect to the edge of the wedge):

$$-2A_f\frac{4}{\rho^2}d_2' \sin 2\alpha \sin\ \alpha-\frac{4t}{\rho}d_2'\int_{-\alpha}^{\alpha} \sin 2\theta \sin \theta\ d\theta$$

$$+\frac{t}{\rho}\int_{-\alpha}^{\alpha}(a_0'+2d_2' \cos 2\theta) \cos \theta\ d\theta=0, \tag{21}$$

$$t\int_{-\alpha}^{\alpha}(a_0'+2d_2' \cos 2\theta)d\theta+M=0. \tag{22}$$

[4] See footnote c.

The solution of the two simultaneous eqs, 21 and 22, for a_0' and d_2' gives

$$a_0'=\frac{M}{t}\frac{\cos 2\alpha-\frac{2A_f}{t\rho}\sin 2\alpha}{\sin 2\alpha-2\alpha\cos 2\alpha+\frac{2A_f}{t\rho}\cdot 2\alpha\sin 2\alpha},$$

$$d_2'=-\frac{M}{2t}\frac{1}{\sin 2\alpha-2\alpha\cos 2\alpha+\frac{2A_f}{t\rho}\cdot 2\alpha\sin 2\alpha},$$

and the stresses $(\sigma_\rho)_3$[e] and $(\tau_{\rho\theta})_3$[f] become

$$(\sigma_\rho)_3=\frac{2M}{t\rho^2}\frac{\sin 2\theta}{\sin 2\alpha-2\alpha\cos 2\alpha+\frac{2A_f}{t\rho}\cdot 2\alpha\sin 2\alpha}, \tag{23}$$

$$(\tau_{\rho\theta})_3=\frac{M}{t\rho^2}\frac{\cos 2\alpha-\frac{2A_f}{t\rho}\sin 2\alpha-\cos 2\theta}{\sin 2\alpha-2\alpha\cos 2\alpha+\frac{2A_f}{t\rho}\cdot 2\alpha\sin 2\alpha}. \tag{24}$$

The final stresses are

$$\sigma_\rho=(\sigma_\rho)_1+(\sigma_\rho)_2+(\sigma_\rho)_3, \tag{25}$$
$$\sigma_\theta=0, \tag{26}$$
$$\tau_{\rho\theta}=(\tau_{\rho\theta})_3. \tag{27}$$

The preceding development makes it possible to determine the state of stress. Of primary practical importance is the determination of the maximum normal and shearing stresses. For any circular section $2\rho\alpha$ the numerically largest normal stress occurs at $\theta=\alpha$ or $\theta=-\alpha$, but the determination of α to make the normal stress a maximum or a minimum is another matter. It is evident that differentiating equation 25 with respect to α, setting the derivative equal to zero, and solving the resulting equation for α involves more than mortal man is likely to accomplish. One must be content with cruder methods. A cantilever girder of uniform strength, with negligible web (latticed construction), loaded only by a transverse force at its end, is triangular in elevation according to the ordinary beam theory. Suppose now that we draw from the point of application of the load in figure 15 a tangent to the curved inner flange, as indicated by the angle $2\alpha_0$. If we neglect the web, it is clear that, by analogy with the girder of uniform strength, the circular section $2\rho_0\alpha_0$ is weaker than any section on either side of it when the effect of only the transverse component, $V\cos\alpha_0-H\sin\alpha_0$, of the applied load is considered. The effect of both the web and the longitudinal component, $V\sin\alpha_0+H\cos\alpha_0$, of the applied load is to shift the weakest section to the left. This shift is likely to be small for most practical cases, but in a questionable case it may be desirable to compute the extreme fiber stresses for $\alpha=0$ (by the ordinary beam theory) and for $\alpha=\alpha_0$ ($M=0$).

[e] See footnote c.
[f] See footnote c.

The stresses for these two values of α are particularly easy to compute and will indicate how rapidly the extreme fiber stress is varying. If the stress for $\alpha=\alpha_0$ is close to the maximum allowable stress, it may be worthwhile to compute the extreme fiber stresses for a value of α intermediate between $\alpha=0$ and $\alpha=\alpha_0$.

The value of α_0 may be obtained by equating the right-hand side of eq 3 to zero and solving for cos 2α:

$$\cos 2\alpha_0=\frac{(h+R)R}{(h+R)^2+d^2}\left[1+\sqrt{1-\frac{(R^2-d^2)[(h+R)^2+d^2]}{R^2(h+R)^2}}\right]. \tag{28}$$

The corresponding value of ρ_0 is obtained by substituting the value of α_0 from eq 28 for α in eq 4.

The analytical determination of the maximum shearing stress involves the same sort of difficulties as arise in connection with the maximum normal stress. It is simply out of the question as a practical matter to differentiate eq 27 with respect to α, set the derivative equal to zero, and solve the resulting equation for α. It is almost evident, however, that the shearing stress becomes a maximum on the section defined by $\alpha=0$, and consequently the equation for maximum shearing stress, τ_{max}, on the cross section of a straight girder applies,

$$\tau_{max}=\frac{3(th+4A_f)V}{2(th+6A_f)th}. \tag{29}$$

The expressions 10, 16, 23, and 24 should give good approximations to the stresses in any beam or girder with equal nonparallel flanges so long as the radii of curvature of the flanges are not too small relative to the depth at the section at which the stresses are desired. The expressions 10, 16, 23, and 24 are closely analogous to those which apply for a straight girder with parallel flanges and reduce to the latter as $\alpha\doteq 0$ ($\rho=\infty$). If numerator and denominator of eq 10 are multiplied by ρ^2, then the quantity $P_1\rho$ may be thought of as the bending moment at the circular section, the quantity $\rho \sin\theta$ is the distance of any fiber from the neutral surface (the polar axis), and the denominator is the moment of inertia of the circular sectional area with respect to the neutral surface. It is obvious then that as $\alpha\doteq 0$ ($\rho=\infty$), eq 10 reduces to the ordinary flexure formula. Similarly, if in eq 16 $\theta\doteq 0$ and $\alpha\doteq 0$ ($\rho=\infty$), the equation reduces to

$$(\sigma_\rho)_2=-\frac{P_2}{th+2A_f},$$

which is the familiar expression for the normal stress due to an axially applied load. Equation 23 may be written for small values of θ and α as

$$(\sigma_\rho)_3=\frac{M\theta}{\frac{2}{3}t\rho^2\alpha^3+2A_f\rho\alpha^2},$$

which, with $\rho\alpha=h/2$ and $\rho\theta=z$, reduces to

$$(\sigma_\rho)_3=\frac{Mz}{\frac{1}{12}th^3+2A_f\left(\frac{h}{2}\right)^2}.$$

This equation is again the ordinary flexure formula. For small values of θ and α eq 24 may be written

$$(\tau_{\rho\theta})_3=-\frac{M}{t\rho^2}\frac{\frac{1}{2}\alpha^2-\frac{1}{2}\theta^2+\frac{A_f}{t\rho}\alpha}{\frac{2}{3}\alpha^3+2\frac{A_f}{t\rho}\alpha^2},$$

which, with $\rho\alpha=h/2$ and $\rho\theta=z$, reduces to

$$(\tau_{\rho\theta})_3=-\frac{\left[\frac{t}{2}\left(\frac{h^2}{4}-z^2\right)+A_f\frac{h}{2}\right]\frac{M}{\rho}}{\left[\frac{1}{12}th^3+2A_f\left(\frac{h}{2}\right)^2\right]t}.$$

This equation is the familiar one giving the transverse or longitudinal shearing stress at any point at the distance z from the neutral axis of a straight girder when the shearing force on the cross section in question is M/ρ. In the present case M and ρ are given by eq 3 and 4, and by forming the ratio M/ρ and allowing α to approach zero, it is easily found that $M/\rho=-V$.

VI. THEORETICAL STRESSES

The theory was applied to the portion of the rigid-frame specimen bounded by nonparallel flanges. This portion may be termed the "knee" of the frame, and half of it is shown in figure 15, included between the positive axes of x and y. A flange was regarded as consisting of two angles and a part of the web plate between them, and the area of the flange was considered concentrated at its centroid, which was taken as the boundary of the web. The location of this boundary was computed for the two 4- by 4- by ½-in. angles and the part of the included ⅜-in. plate which extended from the centroid of the flange to the backs of the flange angles, by the method outlined in RP1130 [1]. The distance between the boundary and the backs of the angles was found to be 1.15 in., and the dimensions (figs. 1 and 15) of the portion of the frame to which the theory was applied were taken as $h=18-2(1.15)=15.7$ in. and $R=60+1.15=61.15$ in.

The load line intersected the centroidal axis of the outer flange at an angle of 45° at the point $(R+h, -d)$, where (fig. 1) $d=120-18-60+h/2=49.85$ in. The load was resolved at this point into components $H=V=60\sqrt{2/2}=42.43$ kips.

With these values of h, R, d, H, and V, eq 1, 2, 3, and 4 for P_1, P_2, M, and ρ were solved for four values of α, and the results were substituted in =25, 26, and 27 for the stresses. The sections taken correspond to the following values of 2α: $2\alpha=0$, for which the theory reduces to the ordinary beam theory; $2\alpha=2\alpha_0=15°\ 9'$ obtained by solution of eq 28 and for which $M=0$; $2\alpha=30°$; $2\alpha=45°$.

A comparison between the theoretical and the measured stresses for test 3 is shown in figure 16. The curves represent theoretical stresses, and the arrows, measured stresses. The measured normal and shearing stresses shown were obtained from the following quantities measured at the rosettes: the maximum principal stresses, σ_u; the minimum principal stresses, σ_v; and the angles, ψ, between σ_u,

and the load line. The values of σ_u at corresponding rosettes on either side of the line of symmetry of the frame were averaged, and from, the averages were interpolated the values of σ_u at the points at which the measured stresses are plotted in figure 16. The values of σ_v and ψ at these points were obtained similarly, and from the values of σ_u, σ_v, and ψ at each point the components of stress in the r- and θ-directions were computed. The normal stresses, σ_ρ, are shown on four circular sections on the lower half of figure 16, and in addition, the normal stresses in the flanges have been plotted at right angles to the directions in which they act, with the centroidal axes of the flanges as base lines, to show more clearly the variation of stress along the

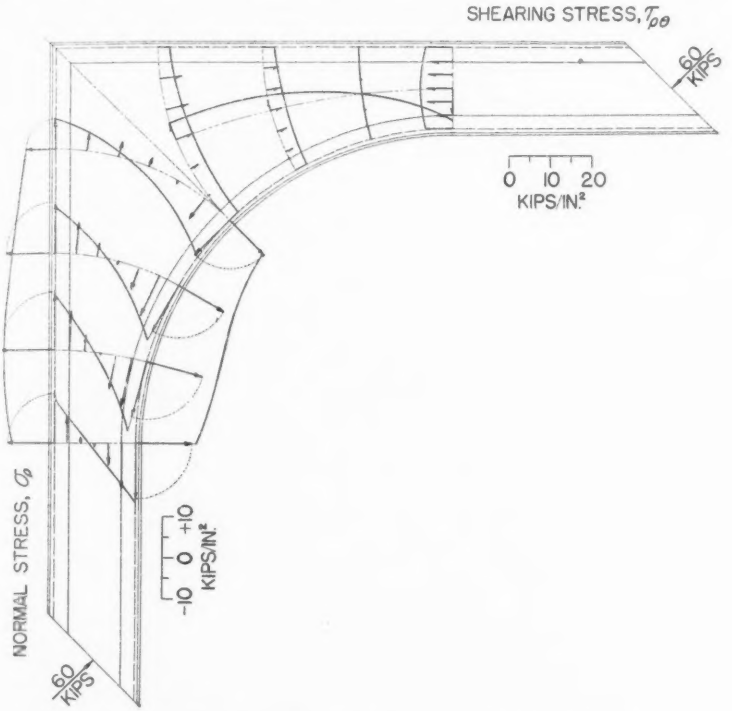

FIGURE 16.—*Test 3.—Theoretical stresses and measured stresses.*
The curves represent theoretical, and the arrows measured, stresses.

flanges. The shearing stresses $\tau_{\rho\theta}$ are plotted on four corresponding sections on the upper half of the figure, and the variation in shearing stress along the center line of the circular sections is also shown.

The agreement between the theoretical stresses and the measured stresses is good, especially for the normal stresses. Except for a few points on the section defined by $2\alpha=45°$, the theory gives stresses to the same order of accuracy as the ordinary beam theory gives the stresses for $2\alpha=0$.

The numerically largest of the measured normal stresses shown in figure 16 occurs at the inner flange on the circular section defined by $\alpha=\alpha_0$. This result is in agreement with the conclusion, drawn

from the theory in section V, that the numerically largest normal stress occurs near the section defined by $\alpha=\alpha_0$. The measured shearing stresses on this section are negligibly small as would be expected from eq 24 and 27, which state that the shearing stresses on this section are everywhere zero.

VII. MAXIMUM LOAD

The rigid-frame specimen is shown in figure 17 in the testing machine for determining the maximum load. The conditions for this test were the same as for test 3, except that lateral deflection of the outer corner of the specimen was prevented, and that the gussets at the outer corner had been removed.[9]

Before loading, the specimen was coated with a cement wash to make Lüders' lines clearly visible where the material was stressed to the yield point.

The maximum load sustained by the specimen was 72,000 lb. Failure occurred suddenly, by lateral deflection of the curved inner portion of the frame with attendant yielding of the web near the inner flange as shown by the Lüders' lines in figure 18. No rivets failed so far as could be observed visually.

For test 3, the ratio of the load to the greatest measured stress in the inner-flange angles was 3.92 kips per kip/in^2. The ratio of the maximum load to the tensile yield point of the angles (see table 1) was only 1.80 kips per kip/in^2. If one assumes linear variation of stress with load up to the yield point and the compressive and tensile yield points to be equal, it is evident that the full compressive strength of the material in the inner-flange angles was not utilized, and that the failure was by elastic instability.

VIII. CONCLUSIONS

The distribution of stress in a riveted steel rigid-frame specimen having a curved inner flange was determined experimentally and theoretically, and the maximum load was measured. The following conclusions were drawn:

1. The stresses at the outer corner of the knee of the specimen were small, and reinforcing the outer corner had a negligible effect on the distribution of stress in the specimen.

2. The stiffeners had a negligible effect on the distribution of stress in portions of the frame not near the stiffeners.

3. The formulas developed give the stresses in the knee to the same order of accuracy as the ordinary beam theory gives the stresses in the straight legs of the frame. These formulas reduce to the ordinary beam theory at the section where the straight and curved parts of the inner flange are tangent.

4. The design was such that the frame failed by elastic instability. The inner-flange angles at failure were stressed to less than half their yield point. This emphasizes the necessity of providing adequate bracing for the inner flange at the knees of rigid frames of this type.

[9] The gussets had been removed in preparation for a contemplated test to determine the stress distribution for this condition.

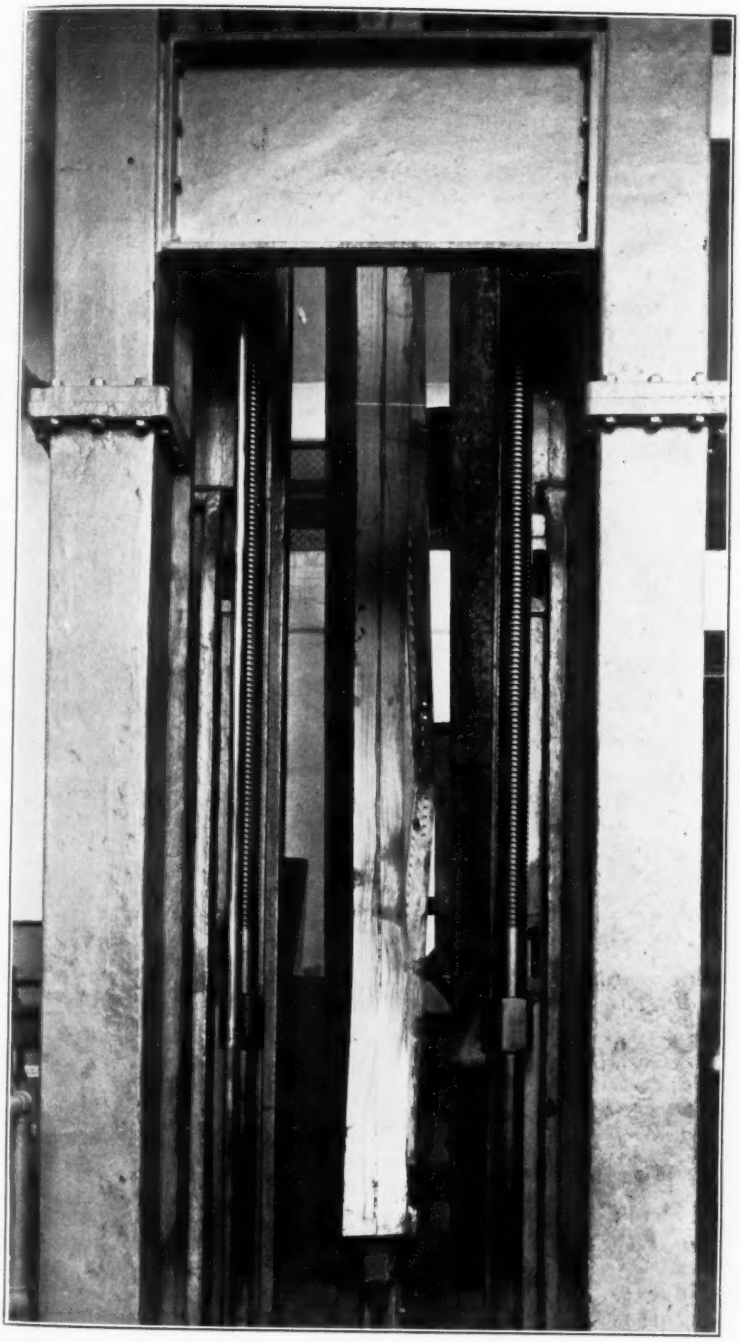

FIGURE 17.—*The rigid-frame specimen under the maximum load of 72,000 lb.*

FIGURE 18.—*Inner portion of the rigid-frame specimen after failure.*
Lüders' lines are visible in a narrow band adjacent to the curved flange.

IX. REFERENCES

[1] Ambrose H. Stang, Martin Greenspan, and William R. Osgood, *Strength of a riveted steel rigid frame having straight flanges.* J. Research NBS **21**, 269 (1938) RP1130.

[2] *Standard specifications for steel for bridges.* Fig. 1, A. S. T. M. Standards, pt. I, 4 (1936).

[3] L. B. Tuckerman, *Discussion on proportional limit.* Proc. Am. Soc. Testing Materials **29**, II, 538 (1929).

[4] S. Timoshenko, Theory of Elasticity (McGraw-Hill Book Co., Inc., 1934).

WASHINGTON, August 5, 1938.

U. S. Department of Commerce National Bureau of Standards

RESEARCH PAPER RP1162

Part of Journal of Research of the National Bureau of Standards, Volume 21, December 1938

RESISTIVITY AND POWER INPUT IN THE CESIUM DISCHARGE AT HIGH CURRENT DENSITY

By Fred L. Mohler

ABSTRACT

Measurements have been made of the potential gradient and the ion current to the tube wall in a tube 5 mm in diameter for current densities ranging from 5 to 20 amp/cm^2 and vapor pressures from 0.0045 mm to 0.33 mm. Potential gradients have also been measured in a 1-mm tube for current densities ranging from 30 to 150 amp/cm^2 and vapor pressures from 0.33 to 2 mm. Published results give electron concentrations and temperatures for this range of conditions. The resistivity agrees approximately with the theoretical value for a completely ionized gas. The power dissipation comes predominantly from wall recombination at low pressures. Above 0.17 mm the radiation is appreciable, and above about 1 cm the radiation would account for most of the power input. Theoretical equations are given for the case where pressure and degree of ionization are so high that the vapor is opaque.

CONTENTS

	Page
I. Introduction	873
II. Experimental results	875
III. Resistivity	877
IV. Power input and loss	879
V. Conclusions	880

I. INTRODUCTION

In another paper [1] data have been given on the electron concentration and electron temperature in cesium discharges with current densities sufficient to give nearly complete single ionization over a wide range of pressures. In connection with these experiments, measurements of potential gradient were made for pressures up to 2 mm of mercury, while values of the positive-ion current density to the tube walls were obtained at pressures up to 0.3 mm. These measurements permit for the first time an experimental investigation of the resistivity and power input in an ionized gas.

A number of physicists have been interested in the theoretical problem of the mean free path and mobility of electrons in an ionized gas. A complication in the problem is that an isolated ion has an infinite effective cross section for electron scattering. However, if there are N_+ ions per cm^3, then an electron is in the field of a single ion over a path less than $1/N_+^{1/3}$ cm, and the scattering cross section has a finite value.

[1] F. L. Mohler, J. Research NBS **21**, 697 (1938) RP1150.

Gvosdover [2] gives the equation for the cross section in square centimeters of a singly charged ion as

$$\sigma^+ = \frac{\pi}{4}\frac{e^4}{k^2 T_e^2} \ln \frac{k^2 T_e^2}{e^4 N_+^{2/3}} = \frac{5.62\times10^{-6}}{T_e^2} \log 0.72\times10^6 \frac{T_e^2}{N_+^{2/3}}, \quad (1)$$

where T_e is the electron temperature, N_+ the ion concentration (equal to electron concentration under discharge conditions), and the other symbols follow conventional usage. Most other derivations give equations of a similar form but with various values for the constants.[3] Gabor, however, has used a very different statistical method of solving the problem and derived a quite different equation.

$$\sigma^+ = \frac{0.8\times10^{-2}}{T_e N_+^{1/3}} \quad (2)$$

Boeckner and the author [4] have shown that scattering of electrons by ions becomes important in a low-pressure discharge with a current density of the order of an ampere per square centimeter. The mean free path at constant pressure decreases with increasing current, and measurements of this decrease give a method of computing the ion-scattering area. The effect of a mixture of ions and atoms is conveniently expressed in terms of the reciprocal of the mean free path, which is the total scattering area per cubic centimeter.

$$1/\lambda = S = N_1\sigma_1 + N_+\sigma_+, \quad (3)$$

where N_1 and σ_1 pertain to the neutral atoms. The resistivity (gradient/current density) in ohms centimeters is

$$X/I = \frac{2.94\times10^9 T_e^{1/2} S}{N_+} \quad (4)$$

Because the scattering area of ions is 20 to 40 times that of neutral atoms, it is practicable to obtain conditions where the scattering by neutral atoms is negligible. Equations 4, 3, and 1 then give

$$X/I = 2.94\times10^9 T_e^{1/2}\sigma^+ \quad (5)$$

$$X/I = \frac{1.48\times10^4}{T_e^{3/2}} \log 0.72\times10^6 \frac{T_e^2}{N_+^{2/3}} \quad (6)$$

In this equation the log term changes so slowly that it is satisfactory to use the form

$$X/I = K/T_e^{3/2}, \quad (7)$$

where K is nearly constant for a range of conditions where $T_e^2/N_+^{2/3}$ remains of the same magnitude. Equation 6 is quite general, for it is assumed to give the limiting value of the resistivity with high currents in any gas or discharge tube, assuming only that the ions are singly ionized.

The energy balance in the positive column can be expressed symbolically

$$\pi a^2 XI = R + H + W, \quad (8)$$

[2] Physik. Z. Sowjetunion **12,** 164 (1937).
[3] Langevin, Ann. chim. phys. **5,** 271 (1905); Thomas, Proc Roy. Soc. (London) [A] **121,** 470 (1928); Landau, Physik. Z. Sowjetunion **10,** 154 (1936); Gabor, Z. Physik **84,** 474 (1933).
[4] BS J. Research **10,** 357 (1933) RP535.

where the term on the left is the power input per centimeter, R is the power radiated by the vapor, H is the power carried to the walls by heat conduction, and W is the power dissipated by recombination of ions and electrons on the walls. The last term can be expressed as follows: [5]

$$W=2\pi aI_+A(V_i+8T_e/11{,}600)=2\pi aI_+AV_R, \tag{9}$$

where $2\pi aI_+$ is the ion current to unit length of the tube wall, V_i is the ionization potential, and $8T_e/11{,}600$ is the kinetic energy of the ion and electron. V_R is the total recombination energy in electron volts and A is an accommodation coefficient to take account of the fact that the neutral atom after recombination will have some kinetic energy. A value nearly equal to one is however to be expected. V_R is of the order of 10-electron volts in these experiments, and it is evident that with 50-percent ionization, H will be only a few percent of W and can safely be neglected. R is probably small compared with W for extreme currents. At low pressures the ratio R/W decreases with increasing current to a value of about 0.5 for a current of 4 amp in a tube 1.8 cm in diameter,[6] but there is no safe basis for predicting the ratio for the conditions here used.

II. EXPERIMENTAL RESULTS

Experimental details have been covered in another paper.[7] At pressures above 0.3 mm of mercury, the electron concentration and temperature in a capillary discharge were measured by measuring the intensity distribution of the continuous recombination spectrum. In one series of experiments the potential difference was measured between two probes near the two ends of a capillary 1 cm long and 1.1 mm in diameter. This potential difference is assumed equal to the gradient in the capillary. The experiments covered a pressure range from 0.3 to 2 mm with current densities from 30 to 150 amp/cm^2. The percentage of ionization ranges from 25 to 98.

Another series of experiments base measurements of T_e and N_e on the characteristics of a probe surface flush with the wall of a 5-mm tube. N_e was derived from the "ion current equation",[8]

$$I_+=0.48\times10^{-16}N_eT_e^{1/2}. \tag{10}$$

The potential gradient was measured between two probes 7 cm apart in the 5-mm tube. These experiments cover a pressure range from 0.0045 mm to 0.3 mm with current densities from 5 to 20 amp/cm^2. The percentage of ionization is not known but is probably of the same magnitude as was found for higher pressures.

Table 1 gives the complete experimental data. Experimental uncertainties are probably of the order of 10 percent for T_e, N_e, and X. It was impossible to attain the precision usually obtained in low current discharges under these extreme conditions. Evolution of foreign gas and thermionic emission from probes from overheating may account for the uncertainty.

[5] Tonks and Langmuir, Phys. Rev. **34,** 876 (1929).
[6] F. L. Mohler, BS J. Research **9,** 25 (1932) RP455.
[7] F. L. Mohler, J. Research NBS **21,** 697 (1938) RP1150.
[8] See footnote 5.

TABLE 1.—*Resistivity and power input*

Vapor pressure	I	X	$\pi a^2 XI$	X/I	T_e	N_e	$aXI/2I_+$	Mean free path
			TUBE DIAMETER, 5 mm					
mm	*amp/cm²*	*v/cm*	*w/cm*	*ohms-cm*	°*K*		*v/ion*	*cm*
0.0045	5	0.60	0.60	0.122	6,600	1.0×10^{13}	10	1.97×10^{-1}
	7.5	.53	.80	.073	8,000	1.22	9.6	2.9
	10	.44	.88	.045	9,500	1.15	10.3	5.5
	12.5	.38	.95	.031	10,800	1.25	9.5	7.8
0.009	5	.8	.80	.163	5,500	1.44	9.9	0.94
	7.5	.87	1.31	.119	6,600	2.54	8.3	.80
	10	.87	1.74	.089	7,800	3.7	6.9	.78
	12.5	.67	1.68	.055	9,100	3.0	7.6	1.70
	15	.54	1.63	.037	10,300	2.3	9.2	3.5
0.0175	5	.86	.86	.175	4,200	1.9	9.1	0.57
	7.5	.99	1.48	.135	5,100	3.2	8.6	.45
	10	1.02	2.04	.104	6,200	4.5	7.7	.49
	12.5	.99	2.48	.081	7,100	5.0	7.8	.62
	15	.98	2.94	.067	8,000	5.0	8.65	.77
	17.5	.90	3.15	.053	8,900	4.7	9.23	1.12
	20	.78	3.12	.040	10,000	3.9	10.4	1.9
0.039	5	1.01	1.01	.206	3,700	2.5	8.5	0.35
	10	1.34	2.68	.136	5,200	6.1	8.0	.25
	12.5	1.42	3.55	.116	5,900	7.7	7.9	.25
	15	1.43	4.29	.098	6,600	9.3	7.5	.26
	17.5	1.59	5.6	.092	7,300	10.8	7 9	.25
	20	1.68	6.72	.085	8,000	12.0	8.2	.25
0.080	5	1.1	1.1	.224	3,400	2.7	9.2	.28
	10	1.53	3.06	.156	4,700	6.9	9.5	.185
	15	1.85	5.55	.127	5,300	12.7	7.8	.132
	17.5	1.89	6.6	.110	5,800	15.1	7.5	.134
	20	1.85	7.4	.094	6,400	17	7.2	.147
0.17	10	1.65	3.30	.168	3,800	0.81×10^{14}	8.7	13.4×10^{-1}
	12.5	1.86	4.65	.151	4,300	1.14	8.15	11.1
	15	2.0	6.0	.136	4,600	1.53	7.6	9.6
	17.5	2.16	7.6	.126	5,000	1.97	7.2	8.4
	20	2.28	9.1	.116	5,300	2.32	7.0	7.9
0.33	10	1.86	3.72	.19	3,400	0.64	13.2	14.1
	12.5	2.0	5.0	.163	3,600	.88	12.2	12.3
	15	2.22	6.66	.151	3,800	1.14	12.2	10.6
	17.5	2.36	8.3	.138	4,100	1.48	11.4	9.2
	20	2.43	9.7	.124	4,200	2.46	8.0	6.2
			TUBE DIAMETER, 1 mm					
0.33	30	7.5	2.25	0.24	3,360	2.8×10^{14}	.....	2.5×10^{-2}
	50	8.8	4.40	.167	3,830	3.6	.....	3.0
	75	9.5	7.14	.12	4,400	3.6	.....	4.5
	100	9.5	9.5	.09	5,050	3.1	.....	7.5
	150	9.0	13.5	.057	6,200	2.7	.....	15.1
0.60	30	8.5	2.54	.27	3,360	4.2	.....	1.51
	50	10.0	5.0	.19	3,830	5.9	.....	1.63
	75	11.6	8.7	.147	4,400	6.6	.....	2.02
	100	11.9	11.9	.113	5,050	6.5	.....	2.8
	150	11.5	17.2	.074	6,200	4.9	.....	6.4
1.1	30	10	3	.32	3,360	6.2	.....	0.85
	50	11.4	5.7	.22	3,830	10.0	.....	.83
	75	13.4	10.1	.17	4,400	13	.....	.88
	100	14.4	14.4	.14	5,050	14	.....	1.07
	150	15.4	23.2	.10	6,200	12	.....	1.93
2.0	30	11.7	3.5	.37	3,360	8.8	.....	0.52
	50	13 1	6.6	.25	3,830	13	.....	.55
	75	15.1	11.3	.19	4,400	18	.....	.59
	100	16.4	16.4	.156	5,050	21	.....	.63

III. RESISTIVITY

It follows from eq. 6 that the resistivity is conveniently expressed as a function of electron temperature. In figure 1 the data in the pressure range 0.0045 to 0.08 mm have been plotted and a single curve drawn through the points. Values tend to increase with decreasing ion concentration, but experimental uncertainties do not justify drawing separate curves through points obtained at different pressures. The theoretical eq. 6 has been plotted as a broken line, using a single mean value of 4.4 for the log term (values range from 5.3 to 3.7).

Figure 2 gives data in the pressure range 0.17 to 2.0 mm. Crosses give values at 0.17 mm in the 5-mm tube; circles for 0.33 mm in the 5-mm tube; dots give data for the 1-mm tube at pressures indicated at the right of each curve. A single theoretical curve has been drawn as a broken line, using a mean value of 3.26 for the log term. Values of the log term decrease from 3.8 to 3.0 as the pressure increases, but the experimental values in the 1-mm tube increase with increasing ion concentration.

Values of the scattering area σ^+ derived from values of X/I by eq 5 range from 0.14×10^{-12} at 10,000° to 1.52×10^{-12} at 3,000° for data of figure 1. Published values[9] based on measurements of the change in total scattering area S of eq 4 with current give somewhat smaller values. Thus at $T_e=4650$, $P=0.0012$, Boeckner and Mohler obtained $\sigma_+=0.60\times10^{-12}$, while the curve of figure 1 gives 0.81×10^{-12}. A complication in measuring the change in S with current is that with increasing current there is an increase in vapor temperature, so that a decrease in $N_1\sigma_1$ of eq 4 partially masks the change in $N_+\sigma_+$. The difference between the two results may come from this effect.

The absolute value of the resistivity from figure 1 is on the average 20 percent less than the value given by Gvosdover's equation (eq 6). Other theoretical equations give higher values and are less satisfactory.

The observed change in resistivity with temperature is somewhat greater than $T_e^{-3/2}$ though the mean curve of figure 1 conceals this trend. The experiments are definitely inconsistent with the Gabor equation (eq 2) both in magnitude and in dependence on T_e and N_+.

In comparing experiment and theory it is to be noted that eq 6 is an ideal equation for a completely ionized gas without boundaries. It does not take into consideration the distribution of current across the tube and the effective current density is not accurately the mean current density, I. This may well account for most of the discrepancy between experiment and theory. The contribution of scattering by neutral atoms to the resistivity is probably small. The scattering area of a neutral atom is about $.03\times10^{-12}$ and with 30 percent ionization the neutral atoms contribute less than 10 percent of the total scattering area. Gvosdover[10] has recently evaluated the contribution of the tube walls to the resistivity. This is small except for long mean free paths and is negligible in these experiments.

Table 1 includes values of the mean free path computed by eq 3 and 4. Except at the lowest pressures the mean free path is much less than the tube diameter. Values decrease with increasing N_e but

[9] Boeckner and Mohler, BS J. Research **10**, 357 (1933) RP535.
[10] Physik. Z. Sowjetunion **13**, 133 (1938).

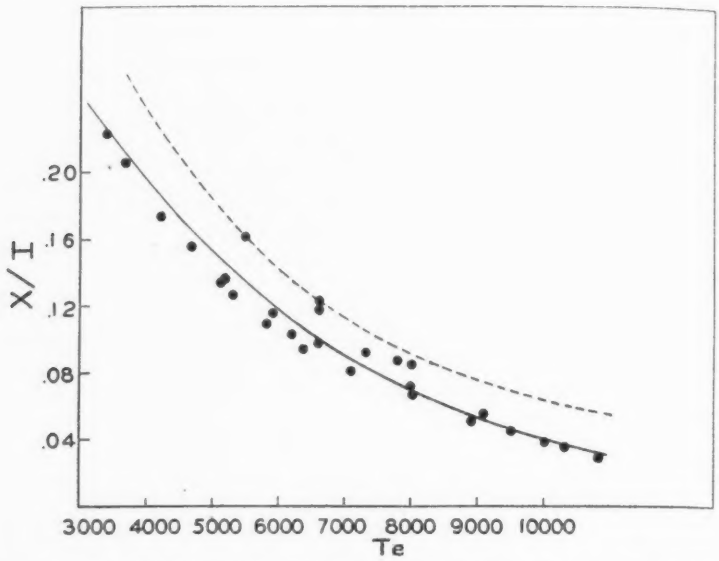

FIGURE 1.—*Resistivity in ohms-centimeters as a function of electron temperature at pressures from 0.0045 to 0.080*

Broken-line curve is eq 6 with a mean value 4.4 for the log term

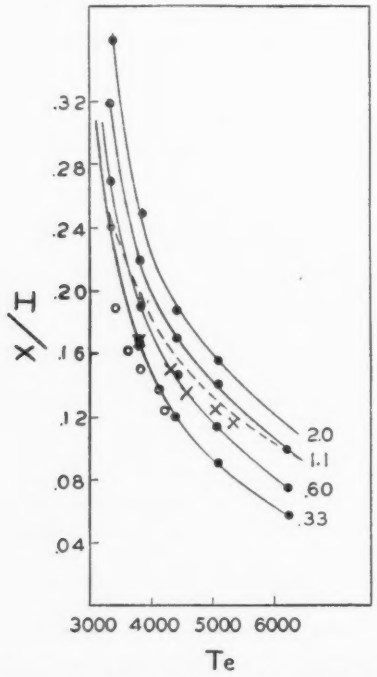

FIGURE 2.—*Resistivity in ohms-centimeters as a function of electron temperature*

Crosses for 5-mm tube at 0.17-mm pressure, circles 5-mm tube at 0.33-mm pressure, dots 1-mm tube at pressures indicated. Broken-line curve is eq. 6 with 3.26 for the log term

begin to increase with increasing current as N_e approaches its maximum value. Theory predicts an increase proportional to T_e^3 for nearly complete ionization.

IV. POWER INPUT AND LOSS

In section I it is shown that recombination on the walls probably accounts for most of the power loss though the power radiated cannot be definitely evaluated. The power input per unit wall current ($aXI/2I_+$ of table 1) is then a quantity that is not much greater than the available recombination energy, AV_R, defined by eq 9. The tabulated values are always of the same magnitude as V_R of eq 9 and at high temperatures definitely less than V_R. A plot of power input per unit wall current versus temperature is given in figure 3. Experimental uncertainties preclude a detailed analysis but some definite conclusions can be drawn. A value of A somewhat less than 1 must

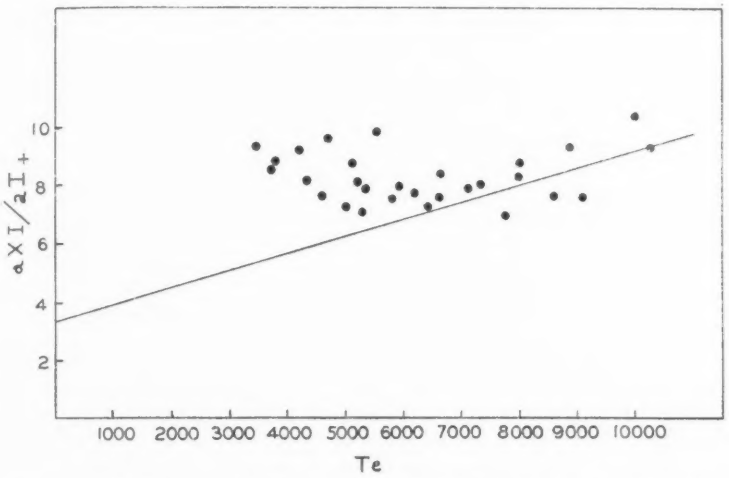

FIGURE 3.—*Power input per ion in electron volts as a function of temperature.*

Pressures from 0.009 to 0.17, inclusive. The straight line is a plot of AV_R of eq 9 with $A=0.85$.

be assumed to fit the high temperature values and the straight line is a plot of AV_R for $A=0.85$. Results are consistent with the assumption that radiation is appreciable only at temperatures less than 6,000° corresponding to lower currents and higher pressures and the vertical distance between the line and the points is the energy radiated per unit ion current. These experiments alone do not exclude the possibility of a lower value of A and more radiation. However, published work[11] on power input and loss at low current densities is inconsistent with a value of A much less than 0.85.

[11] F. L. Mohler, BS J. Research **9**, 25 (1932) RP455.

V. CONCLUSIONS

For the range of conditions covered in table 1, the resistivity, X/I, is nearly equal to the theoretical value for a completely ionized gas, as given by eq 6. It depends primarily on the electron temperature and neither the kind of gas nor the tube radius appears explicitly in the equation.

For a more limited range of conditions the power input is nearly equal to the wall recombination as given by eq 9. That is,

$$XI=\frac{2}{a}I_+A(V_i+8T_e/11{,}600). \tag{12}$$

In contrast to the resistivity, the quantity, XI depends specifically on the tube radius, the kind of gas through V_i, and perhaps on the material of the tube through A. One can eliminate X from eq 6 and 12 and obtain a relation between the electron temperature and the other variables. Since the resulting equation is complicated and cumbersome, a rough approximation will be used to avoid this complexity.

For the resistivity, eq 7 will be used with an experimental value of the constant, K, based on the data of figure 1.

$$X/I=5.2\times10^4/T_e^{3/2}. \tag{13}$$

Data of figure 3 and table 1 show that with few exceptions the power input per unit wall current is within 15 percent of 8.6 v and, hence,

$$XI=17.2I_+/a \tag{14}$$

and by eq 10

$$XI=8.3\times10^{-16}N_eT_e^{1/2}/a. \tag{15}$$

Combining eq 13 and 15 gives the two relations:

$$X^2=4.3\times10^{-11}N_e/T_e a, \tag{16}$$

$$I^2=1.6\times10^{-20}N_eT_e^2/a. \tag{17}$$

It is to be emphasized that these simple relations are rough approximations valid for a limited range. The equations serve merely to give a rough picture of the relation of T_e to other variables under conditions of relatively low pressure and extreme currents. Thus it is of interest that T_e increases with increasing tube radius and constant current density.

Power loss by radiation is evidently appreciable at pressures above 0.3 mm and will be predominant at pressures above a few centimeters in a 5-mm tube for the radiation increases as the square of the pressure for sufficiently high currents. One can obtain relations analogous to eq 16 and 17 for high pressures by a purely theoretical approach. Because there is nearly temperature equilibrium at high pressure, for a given pressure and temperature one can derive N_e by Saha's equation. Equation 6 then gives the resistivity, provided T is sufficiently high to give over 30-percent ionization and the power input is assumed

equal to the total radiation. An approximate theoretical evaluation of the total radiation of ionized cesium would, in general, be complicated. However, for the case that pressure, temperature, and tube diameter are so great that the ionized vapor is nearly opqaue, the radiation approaches that given by the Stefan-Boltzman law, namely, $5.71\times10^{-12}T_e^4$ w/cm^2. The power equation is then simply

$$XI=\frac{11.4}{a}\times10^{-12}T_e^4. \tag{18}$$

This, combined with the resistivity equation, 6, gives

$$X^2=\frac{17\times10^{-8}T_e^{5/2}}{a}\log\frac{0.72\times10^6T_e^2}{N_+^{2/3}}. \tag{19}$$

$$I^2=7.7\times10^{-16}T_e^{11/2}/a\log\frac{0.72\times10^6Te^2}{N_+^{2/3}}. \tag{20}$$

Neglecting the variation in the log term, one has equations of the simple but unusual form,

$$T_e=k_1a^{2/11}I^{4/11}. \tag{21}$$

$$X=k_2a^{-3/11}I^{5/11}. \tag{22}$$

These relations are independent of the pressure except for the variation of the log term. An approximate evaluation of the total radiation has been made for cesium vapor at a pressure of 760 cm of mercury and a temperature of 6,000° K in a tube 0.5 cm in radius. There is approximately 50-percent ionization for these conditions and $N_e=6\times10^{17}$. The total radiation is 80 percent of that of a black body and $XI=2.4\times10^4$ w. $X/I=0.05$ ohms-cm. Hence, X equals 34 v and $I=700$ amp/cm^2. It may be entirely impractical to realize such conditions experimentally, but it remains of some interest to see the relations which must exist under conditions of extreme current density and pressure. Three independent variables in three quite general equations, the Saha equation, the total radiation equation, and the resistivity equation, completely describe the discharge conditions. This is in marked contrast to the complexities encountered under all other discharge conditions. The generality of the Gvosdover resistivity equation for extreme ion concentrations may perhaps be open to question.

The results of the numerical example give what may appear as a low value of X and a correspondingly high value of I, but there is no safe basis of comparison. Very high pressure mercury arcs have been operated at a surface brightness comparable to the above, but the ionization is far from complete, which makes X very much greater and I correspondingly smaller.[12]

WASHINGTON, October 3, 1938.

[12] Elenbaas, Z. Tech. Physik 17, 61 (1936).

107462—38——12

INDEX TO VOLUME 21

A

Page

Acree, S. F., Elizabeth E. Hughes and, Quantitative formation of furfural from xylose, RP1132 ... 327
Aging of leather, RP1128 ... 241
Air capacitor, power factors, RP1138 ... 425
Alloy and simple steels, determination of oxygen in {RP1114 ... 79 / RP1115 ... 87}
Alloys, lead-, tin-, and copper-base, determination of arsenic, antimony, and tin in, RP1116 ... 95
Aluminon, preparation of, and test for aluminum {RP1117 ... 105 / RP1118 ... 113}
Aluminum, colorimetric determination of small amounts, RP1117 ... 105
Ammonium aurintricarboxylate, preparation, RP1118 ... 113
Anthracite cokes, heats of combustion of, RP1139 ... 457
Antimony, distillation and determination, RP1116 ... 95
Arc spectrum of silicon, RP1124 ... 185
Arc spectrum of tungsten, RP1125 ... 207
Arsenic, distillation and determination, RP1116 ... 95
Astin, Allen V., Measurement of relative and true power factors of air capacitors, RP1138 ... 425
Aurin, preparation of, and test for aluminum {RP1117 ... 105 / RP1118 ... 113}
Aurintricarboxylic acid, preparation of, and test for aluminum {RP1117 ... 105 / RP1118 ... 113}
Azeotropic distillation with acetic acid {RP1122 ... 151 / RP1123 ... 167}

B

Beek, John, Jr., Combination of hydrochloric acid and sodium hydroxide with hide, tendon, and bone collagen, RP1119 ... 117
Beij, K. Hilding, Pressure losses for fluid flow in 90° pipe bends, RP1110 ... 1
Bends, pipe, flow in, RP1110 ... 1
Boiling points, determination at low pressures, RP1142 ... 515
Book papers, stability, RP1149 ... 671
Boron, determination in steels and irons, RP1120 ... 125
Branham, Joseph R., Preparation and application of chromous solutions for the absorption of oxygen in volumetric gas analysis, RP1112 ... 45
——, *and Max Sucher,* Displacement of nitrogen from and its solution in certain reagents during volumetric gas analysis, RP1113 ... 63
Bright, Harry A., John L. Hague and, Determination of boron in steel and cast iron, RP1120 ... 125
Brooks, Donald B., Properties of purified normal heptane and isooctane (2,2,4-trimethylpentane), RP1160 ... 847

C

Calcium carbonate, effect on stability of book papers, RP1149 ... 671
Calcium oxide and hydroxide, heat of solution, RP1121 ... 133
Calcium silicate, hydrated, hydrothermal formation of, RP1147 ... 617
Capacitance measurement with Maxwell bridge, RP1137 ... 375
Capacitor, air, RP1138 ... 425
Carbon dioxide, displacement from impure chromic chloride, RP1113 ... 63
Carbon dioxide, free energy of formation, RP1141 ... 491
Carbon dioxide, heat of formation {RP1139 ... 457 / RP1140 ... 475 / RP1141 ... 491}
Cast iron, determination of boron in, RP1120 ... 125
Cement clinker, relation of compositions and heats of solution, RP1135 ... 355
Cement, hydration at elevated temperatures and pressures, RP1147 ... 617
Cement, portland, composition, RP1131 ... 315
Cement, portland, effect of glass content upon heat of hydration of, RP1127 ... 235
Cesium discharge {RP1150 ... 697 / RP1162 ... 873}
Channels, turbulent flow in, RP1151 ... 707
Charlton, Arvid L., George Singer, Lauriston S. Taylor and, Measurement of supervoltage X-rays with the free-air ionization chamber, RP1111 ... 19
——, *Lauriston S. Taylor, George Singer and,* Concrete as a protective material against high-voltage X-rays, RP1155 ... 783
Charts, contour, of stresses in rigid frame {RP1130 ... 269 / RP1161 ... 853}
Chromous solutions for the absorption of oxygen in volumetric gas analysis, RP1112 ... 45
Clay filler, effect on stability of book papers, RP1149 ... 671
Cokes, anthracite, heats of combustion of, RP1139 ... 457
Compositions; relation to heat of solution in cement clinker, RP1135 ... 355
Concrete as an X-ray protective material, RP1155 ... 783
Constants, elastic, for steel, RP1130 ... 269
Copper-base alloys, determination of arsenic, antimony, and tin in, RP1116 ... 95
Corrosion of pipe lines in soils, RP1157 ... 819
Cotton, effect of 1-percent NaOH and concentrated HCl on, RP1146 ... 609
Counter unit, RP1154 ... 779
Craig, D. Norman, Electrolytic resistors for direct-current applications in measuring temperatures, RP1126 ... 225
Critical speeds, rotating propeller blades vibrating flexurally, RP1148 ... 639
Cryostats, measurement of uniform temperature, RP1158 ... 831
Curtis, Harvey L., Charles Moon, and C. Matilda Sparks, A determination of the absolute ohm, using an improved self inductor, RP1137 ... 375
Curtiss, Leon F., Portable Geiger counter unit, RP1154 ... 779

D

Darnielle, Robert B., Irving A. Denison and, Correlation of an electrolytic corrosion test with the actual corrosiveness of soils, RP1157 ... 819
Denison, Irving A., and Robert B. Darnielle, Correlation of an electrolytic corrosion test with the actual corrosiveness of soils, RP1157 ... 819
Density, as affecting the X-ray protective qualities of concrete, RP1155 ... 783
Determination of oxygen in simple and alloy steels {RP1114 ... 79 / RP1115 ... 87}
Dewey, Phillip H., and D. Roberts Harper, 3d, Heats of combustion of anthracite cokes and of artificial and natural graphites, RP1139 ... 457

Page

Diamond, Harry, Kenneth A. Norton, and Evan G. Lapham, On the accuracy of radio field-intensity measurement at broadcast frequencies, RP1156 795
Diamond, heat of combustion of {RP1140 475 / RP1141 491
Distillation of xylose and pentose compounds, RP1132 327
Distribution of stress in rigid frame {RP1130 269 / RP1161 853
Dosage, measurement of X-ray, RP1111 19

E

Electrolytic resistors, RP1126 225
Enamel frits, surface tension, RP1133 337
Expansion effect on inversion of silica crystals, RP1153 773

F

Ferrous metals, corrosion in soils, RP1157 819
Field-intensity measurement, accuracy at broadcast frequencies, RP1156 759
Filling materials, effect on stability of book papers, RP1149 671
Film, photographic, stability, RP1134 347
Film, viscose, stability, RP1134 347
Flexural vibrations in rotating propeller blades, RP1148 639
Flint, Einar P., Edwin S. Newman, J. Arthur Swenson, Herbert Insley and, Relation of compositions and heats of solution of portland cement clinker, RP1135 355
——, *Howard F. McMurdie, and Lansing S. Wells,* Formation of hydrated calcium silicates at elevated temperatures and pressures, RP1147 617
Flow, turbulent, in channels, RP1151 707
Formation of furfural from xylose, RP1132 327
Fractionation of petroleum {RP1122 151 / RP1123 167 / RP1142 515 / RP1143 535 / RP1144 565 / RP1145 581
Frame, rigid, stresses in {RP1130 269 / RP1161 853
Free energy of formation of carbon dioxide, RP1141 491
Freezing and melting of Hevea rubber, optical and dimensional changes, RP1129 257
Fuels, primary standards for knock-rating, RP1160 847
Furfural, quantitative formation from pentose compounds, RP1132 327

G

Gas analysis, error in volumetric {RP1112 45 / RP1113 63
Geiger counter, RP1154 779
George, William D., Production of accurate one-second time intervals, RP1136 367
Gilliland, Theodore R., Samuel S. Kirby, Newbern Smith and, Trends of characteristics of the ionosphere for half a sunspot cycle, RP1159 835
Glass content of portland cement: effect upon heat of hydration, RP1127 235
Glass, devitrified by heat treatment {RP1152 743 / RP1153 773
Graphite, heat of combustion of {RP1139 457 / RP1140 475 / RP1141 491
Greenspan, Martin, William R. Osgood, Ambrose H. Stang and, Strength of a riveted steel rigid frame having a curved inner flange, RP1161 853
——, ——, ——, Strength of a riveted steel rigid frame having straight flanges, RP1130 269

H

Hague, John L., and Harry A. Bright, Determination of boron in steel and cast iron, RP1120 125
Harper, D. Roberts, 3d, Phillip H. Dewey and, Heats of combustion of anthracite cokes and of artificial and natural graphites, RP1139 457

Page

Harrison, William N., and Dwight G. Moore, Surface tension of vitreous enamel frits at and near firing temperatures, RP1133 337
Heat and free energy of transition between graphite and diamond, RP1141 491
Heat effects of inversion in crystalline silica, RP1152 743
Heat of formation of carbon dioxide {RP1139 457 / RP1140 475 / RP1141 491
Heat of hydration of lime and magnesia, RP1121 133
Heat of hydration of portland cement, effect of glass content upon, RP1127 235
Heat of solution of calcium and magnesium oxides and hydroxides, RP1121 133
Heat of solution of portland cement clinker, RP1135 355
Heats of combustion of anthracite cokes and artificial and natural graphites, RP1139 457
Heats of combustion of graphite and diamond {RP1140 475 / RP1141 491
Heptane, normal, properties, RP1160 847
Heuer, Wilson W., Robert T. Leslie and, A continuous high-vacuum still and boiling-point apparatus, and the systematic distillation of a dewaxed lubricant fraction of petroleum, RP1142 515
Hevea rubber, optical and dimensional changes during freezing and melting, RP1129 257
High-voltage X-ray equipment and measurements, RP1111 19
Holm, Vernon C. F., John G. Thompson and, Determination of oxygen in alloy steels, RP1115 87
——, *John G. Thompson and,* Hydrogen-reduction method for the determination of oxygen in steel, RP1114 79
Hughes, Elizabeth E., and S. F. Acree, Quantitative formation of furfural from xylose, RP1132 327
Hydrated calcium silicates, formation at elevated temperatures and pressures, RP1147 617
Hydration, heat of, of cement, effect of glass content on, RP1127 235
Hydraulics, flow in pipe bends, RP1110 1
Hydraulics, open channels, RP1151 707
Hydrocarbons in petroleum {RP1122 151 / RP1123 167 / RP1142 515 / RP1143 535 / RP1144 565 / RP1145 581
Hydrocarbons, paraffin, properties of two, RP1160 847
Hydrochloric acid and sodium hydroxide with hide, tendon, and bone collagen, RP1119 117
Hydrochloric acid, effect on cotton and rayon, RP1146 609
Hydrogen-reduction method for determination of oxygen in simple and alloy steels {RP1114 79 / RP1115 87
Hydrogen sulfide, evolution by chromous sulfate and by chromous chloride {RP1112 45 / RP1113 63
Hydrogenated lubricating oil, physical properties, RP1144 565
Hydrothermal synthesis of hydrated calcium silicates, RP1147 617

I

Inductance, self, computed value of, RP1137 375
Inductor, self, construction, RP1137 375
Insley, Herbert, Arthur Q. Tool and, Observations on crystalline silica in certain devitrified glasses, RP1152 743
——, *Einar P. Flint, Edwin S. Newman, and J. Arthur Swenson,* Relation of compositions and heats of solution of portland cement clinker, RP1135 355
Ionization chamber for measurement of X-rays, RP1111 19
Ionization in high current discharge, RP1150 697
Ionization potential of silicon, RP1124 185
Ionization, upper atmospheric, RP1159 835
Ionosphere characteristics, variations of, RP1159 835
Iron, cast, determination of boron in, RP1120 125

Page

Isooctane (2,2,4-trimethylpentane), properties, RP1160 ... 847
Isopropylbenzene, isolation from petroleum, RP1122 ... 151

J

Jessup, Ralph S., Heats of combustion of diamond and of graphite, RP1140 ... 475
——, *Frederick D. Rossini and*, Heat and free energy of formation of carbon dioxide, and of the transition between graphite and diamond, RP1141 ... 491

K

Kanagy, Joseph R., Accelerated aging of leather in the oxygen bomb at 100° C., RP1128 ... 241
Kennelly-Heaviside layer, RP1159 ... 835
Keulegan, Garbis H., Laws of turbulent flow in open channels, RP1151 ... 707
Kiess, Carl C., Extension and revision of the arc spectrum of silicon, RP1124 ... 185
Kirby, Samuel S., Theodore R. Gilliland, Newbern Smith and, Trends of characteristics of the ionosphere for half a sunspot cycle, RP1159 ... 835
Knock rating, primary reference standards, properties, RP1160 ... 847

L

Lapham, Evan G., Kenneth A. Norton, Harry Diamond and, On the accuracy of radio field-intensity measurement at broadcast frequencies, RP1156 ... 795
Laun, Donald D., Preliminary lists of terms for the arc and spark spectra of tungsten, RP1125 ... 207
Lead equivalent of concrete, RP1155 ... 783
Lead-, tin-, and copper-base alloys, determination of arsenic, antimony, and tin in, RP1116 ... 95
Leather, deterioration, RP1128 ... 241
Ledebur method for oxygen in simple and alloy steels, RP1114 ... 79; RP1115 ... 87
Lerch, William, Effect of glass content upon the heat of hydration of portland cement, RP1127 ... 235
Leslie, Robert T., and Wilson W. Heuer, A continuous high-vacuum still and boiling-point apparatus, and the systematic distillation of a dewaxed lubricant fraction of petroleum, RP1142 ... 515
Levy, Sam, Walter Ramberg and, Calculation of stresses and natural frequencies for a rotating propeller blade vibrating flexurally, RP1148 ... 639
Lime, heat of solution and hydration, RP1121 ... 133
Loop antenna, distributed capacitance, effect on accuracy of field intensity measurements, RP1156 ... 795
Lubricating oil, chemical constitution of, RP1145 ... 581
Lubricating oil, fractionation of, RP1142 ... 515; RP1143 ... 535; RP1144 ... 565; RP1145 ... 581
Lubricating oil fractions, properties of, RP1143 ... 535; RP1144 ... 565; RP1145 ... 581
Lubricating oil, hydrogenation of, RP1144 ... 565
Lüders' lines on rigid frame, RP1130 ... 269; RP1161 ... 853

M

Magnesium oxide and hydroxide, heat of solution, RP1121 ... 133
Mair, Beveridge J., and Charles B. Willingham, Exhaustive fractionation of the "extract" portion of the lubricant fraction from a midcontinent petroleum, RP1143 ... 535
——, ——, *and Anton J. Streiff*, Chemical constitution of the "extract" portion of the lubricant fraction from a midcontinent petroleum, RP1145 ... 581
——, ——, ——, Hydrogenation of the "extract" portion of the lubricant fraction from a midcontinent petroleum, RP1144 ... 565
McMurdie, Howard F., Lansing S. Wells, Einar P. Flint and, Formation of hydrated calcium silicates at elevated temperatures and pressures, RP1147 ... 617

Page

Mease, Ralph T., Ruby K. Worner, and, Effect of purification treatments on cotton and rayon, RP1146 ... 609
Melting of rubber, optical and dimensional changes, RP1129 ... 257
Microstructure, relation to composition of portland cement clinker, RP1135 ... 355
Modes of flexural vibration of rotating propeller blades, RP1148 ... 639
Mogerman, William D., John A. Scherrer and, Improved method for determination of aluminum in certain nonferrous materials by use of ammonium aurintricarboxylate, RP1117 ... 105
Mohler, Fred L. Cesium discharge under conditions of nearly complete ionization, RP1150 ... 697
——, Resistivity and power input in the cesium discharge at high current density, RP1162 ... 873
Moon, Charles, C. Matilda Sparks, Harvey L. Curtis and, A determination of the absolute ohm, using an improved self inductor, RP1137 ... 375
Moore, Dwight G., William N. Harrison and, Surface tension of vitreous enamel frits at and near firing temperatures, RP1133 ... 337
Multivibrators, use in obtaining low frequencies, RP1136 ... 367

N

Natural flexural frequencies for rotating propeller blades, RP1148 ... 639
Newman, Edwin S., J. Arthur Swenson, Einar P. Flint, Herbert Insley and, Relation of compositions and heats of solution of portland cement clinker, RP1135 ... 355
Nitrogen, solubility in certain reagents and transfer during absorption of oxygen, RP1112 ... 45; RP1113 ... 63
Nonferrous metals, test for small amounts of aluminum in, RP1117 ... 105; RP1118 ... 113
Norton, Kenneth A., Evan G. Lapham, Harry Diamond and, On the accuracy of radio field-intensity measurement at broadcast frequencies, RP1156 ... 795

O

Ohm, absolute, determination of, RP1137 ... 375
Oil seal, diffusion of gas through, RP1112 ... 45; RP1113 ... 63
O'Leary, Martin J., Merle B. Shaw and, Effect of filling and sizing materials on stability of book papers, RP1149 ... 671
Optical properties of $K_2O.Al_2O_3$ in the presence of CaO and Fe_2O_3, RP1131 ... 315
Organic matter, destruction, RP1116 ... 95
Oscillators, use in obtaining accurate time intervals, RP1136 ... 367
Osgood, William R., Martin Greenspan, Ambrose H. Stang and, Strength of a riveted steel rigid frame having a curved inner flange, RP1161 ... 853
——, ——, ——, Strength of a riveted steel rigid frame having straight flanges, RP1130 ... 269
Oxygen bomb, aging of leather in, RP1128 ... 241
Oxygen, determination by chromous chloride and by chromous sulfate, RP1112 ... 45; RP1113 ... 63
Oxygen in simple and alloy steels, determination, RP1114 ... 79; RP1115 ... 87
Ozaphane film, stability, RP1134 ... 347

P

Papers, book, effect of filling and sizing materials on stability, RP1149 ... 671
Pentose compounds, distillation, RP1132 ... 327
Petroleum, fractionation of, RP1122 ... 151; RP1123 ... 167; RP1142 ... 515; RP1143 ... 535; RP1144 ... 565; RP1145 ... 581
Pigments, effect on stability of book papers, RP1149 ... 819
Pipe lines, corrosion in soils, RP1157 ... 671
Pipes, flow in bends, RP1110 ... 1
Porcelain enamel, surface tension, RP1133 ... 337

Page

Portland cement clinker, relation of compositions and heats of solution, RP1135 ... 355
Portland cement, effect of glass content upon heat of hydration, RP1127 ... 235
Portland cements, composition, RP1131 ... 315
Potassium hydroxide, solubility of nitrogen in, RP1113 ... 63
Power factors of air capacitors, measurement, RP1138 ... 425
Power input in the cesium discharge at high current density, RP1162 ... 873
Pressure losses in pipe bends, RP1110 ... 1
Propeller vibrations, effect of rotation, RP1148 ... 639

R

Radio, field-intensity measurements at broadcast frequencies, RP1156 ... 795
Radium detector, RP1154 ... 779
Ramberg, Walter, and Sam Levy, Calculation of stresses and natural frequencies for a rotating propeller blade vibrating flexurally, RP1148 ... 639
Rayon, effect of 1-percent NaOH on, RP1146 ... 609
Rectifiers, high-voltage, RP1111 ... 19
Resistance, determination of, in terms of time and inductance, RP1137 ... 375
Resistivity in the cesium discharge at high current density, RP1162 ... 873
Resistors, electrolytic, RP1126 ... 225
Rigid frame, stresses in {RP1130 ... 269; RP1161 ... 853}
Riveted rigid frame, stresses in {RP1130 ... 269; RP1161 ... 853}
Rose, Frank W., Jr., and Joseph D. White, Separation, by distillation with acetic acid, of the aromatic hydrocarbons from the fraction of a midcontinent petroleum boiling between 154° and 162° C, RP1123 ... 167
——, ——, Separation of isopropylbenzene from a midcontinent petroleum by adsorption with silica gel and distillation with acetic acid, RP1122 ... 151
Rossini, Frederick D., and Ralph S. Jessup, Heat and free energy of formation of carbon dioxide, and of the transition between graphite and diamond, RP1141 ... 491
Rotation, effect on propeller vibrations, RP1148 ... 639
Rubber, optical and dimensional changes during freezing and melting, RP1129 ... 257

S

Sand-lime brick, cementing material in, RP1147 ... 617
Saturation pressures, device for assuring uniformity temperatures around two thermometers, RP1158 ... 831
Saunders, James B., Arthur Q. Tool and, Expansion effects on the inversion of silica crystals in certain devitrified glasses, RP1153 ... 773
Saylor, Charles Proffer, W. Harold Smith and, Optical and dimensional changes which accompany the freezing and melting of Hevea rubber, RP1129 ... 257
Scherrer, John A., Determination of arsenic, antimony, and tin in lead-, tin-, and copper-base alloys, RP1116 ... 95
——, *and W. Harold Smith*, Preparation of ammonium aurintricarboxylate, RP1118 ... 113
——, *and William D. Mogerman*, Improved method for determination of aluminum in certain nonferrous materials by use of ammonium aurintricarboxylate, RP1117 ... 105
Shaw, Merle B., and Martin J. O'Leary, Effect of filling and sizing materials on stability of book papers, RP1149 ... 671
Shepherd, Martin, Method for determining uniformity of temperature in cryostats, RP1158 ... 831
Shielded-loop antenna, use in field-intensity measurements, RP1156 ... 795
Silica crystals in devitrified glass {RP1152 ... 743; RP1153 ... 773}
Silicon spectrum, RP1124 ... 185
Singer, George, Arvid L. Charlton, Lauriston S. Taylor and, Measurement of supervoltage X-rays with the free-air ionization chamber, RP1111 ... 19
——, *Lauriston S. Taylor, and Arvid L. Charlton*, Concrete as a protective material against high-voltage X-rays, RP1155 ... 783
Sizing materials, effect on stability of book papers, RP1149 ... 671
Smith, Newbern, Theodore R. Gilliland, and Samuel S. Kirby, Trends of characteristics of the ionosphere for half a sunspot cycle, RP1159 ... 835
Smith, W. Harold, and Charles Proffer Saylor, Optional and dimensional changes which accompany the freezing and melting of Hevea rubber, RP1129 ... 257
——, *John A. Scherrer and*, Preparation of ammonium aurintricarboxylate, RP1118 ... 113
Sodium hydroxide, effect on cotton and rayon, RP1146 ... 609
Soil corrosion, RP1157 ... 819
Solar-radio correlations, RP1159 ... 835
Sookne, Arnold M., and Charles G. Weber, Stability of the viscose type of Ozaphane photographic film, RP1134 ... 347
Spark spectrum of tungsten, RP1125 ... 207
Sparks, C. Matilda, Charles Moon, Harvey L. Curtis and, A determination of the absolute ohm, using an improved self inductor, RP1137 ... 375
Spectrum of silicon, RP1124 ... 185
Spectrum of tungsten, RP1125 ... 207
Stability of book papers, RP1149 ... 671
Stang, Ambrose H., Martin Greenspan, and William R. Osgood, Strength of a riveted steel rigid frame having a curved inner flange, RP1161 ... 853
——, ——, ——, Strength of a riveted steel rigid frame having straight flanges, RP1130 ... 269
Steam treatment of cement and calcium silicates, RP1147 ... 617
Steel, corrosion in soils, RP1157 ... 819
Steel, determination of boron in, RP1120 ... 125
Steels, simple and alloy, determination of oxygen in {RP1114 ... 79; RP1115 ... 87}
Still, continuous high-vacuum, for lubricating oil, RP1142 ... 515
Strain readings on rigid frame {RP1130 ... 269; RP1161 ... 853}
Streiff, Anton J., Charles B. Willingham, Beveridge J. Mair and, Chemical constitution of the "extract" portion of the lubricant fraction from a midcontinent petroleum, RP1145 ... 581
——, ——, ——, Hydrogenation of the "extract" portion of the lubricant fraction from a midcontinent petroleum RP1144 ... 565
Stress distribution in rigid frame {RP1130 ... 269; RP1161 ... 853}
Stresses in rotating propellers vibrating flexurally, RP1148 ... 639
Stresses in wedge, RP1161 ... 853
Sucher, Max, Joseph R. Branham and, Displacement of nitrogen from and its solution in certain reagents during volumetric gas analysis, RP1113 ... 63
Sunspots and radio transmission, RP1159 ... 835
Surface tension of vitreous enamels, RP1133 ... 337
Swenson, J. Arthur, Einar P. Flint, Edwin S. Newman, Herbert Insley and, Relation of compositions and heats of solution of portland cement clinker, RP1135 ... 355

T

Tannins, oxidation, RP1128 ... 241
Taylor, Kenneth, and Lansing, S. Wells, Studies of heat of solution of calcium and magnesium oxides and hydroxides, RP1121 ... 133
Taylor, Lauriston S., Arvid L. Charlton, George Singer and, Concrete as a protective material against high-voltage X-rays, RP1155 ... 783
——, *George Singer, and Arvid L. Charlton*, Measurement of supervoltage X-rays with the free-air ionization chamber, RP1111 ... 19
Taylor, William C., Phase equilibria studies on mixtures of the compounds $4CaO.Al_2O_3.Fe_2O_3$–$2CaO.Fe_2O_3$–$K_2O.Al_2O_3$, RP 1131 ... 315
Temperature measurements with electrolytic resistors, RP1126 ... 225
Terms of arc and spark spectra of tungsten, RP1125 ... 207
Terms of silicon, RP1124 ... 185
Textiles, purification of cellulose fibers in, RP1146 ... 609
Thermal data relative to mixtures of CaO, Al_2O_3, Fe_2O_3, and K_2O, RP1131 ... 315

Page

Thompson, John G., and Vernon C. F. Holm, Determination of oxygen in alloy steels, RP1115 87
——, ——, Hydrogen-reduction method for the determination of oxygen in steel, RP1114 79
Time intervals, production of accurate, RP1136 367
Tin, distillation and determination, RP1116 95
Titanium dioxide pigments, effect on stability of book papers, RP1149 671
Tool, Arthur Q., and Herbert Insley, Observations on crystalline silica in certain devitrified glasses, RP1152 743
——, *and James B. Saunders,* Expansion effects on the inversion of silica crystals in certain devitrified glasses, RP1153 773
Tungsten spectra, RP1125 207
Turbulent flow in channels, RP1151 707

V

Vacuum-fusion method for oxygen { RP1114 79 / RP1115 87 } in simple and alloy steels
Vacuum pump for high-voltage X-ray tube and rectifier, RP1111 19
Vapor pressures, device for assuring uniformity of temperatures around two thermometers, RP1158 831
Vibrations in rotating propeller blade, RP1148 639
Viscose photographic film, stability, RP1134 347
Vitreous enamels, surface tension, RP1133 337

W

Wave lengths of silicon, RP1124 185
Wave lengths of tungsten, RP1125 207
Weber, Charles G., Arnold M. Sookne, and, Stability of the viscose type of Ozaphane photographic film, RP1134 347
Wedge, stresses in, RP1161 853
Wells, Lansing S., Howard F. McMurdie, Einar P. Flint and, Formation of hydrated calcium silicates at elevated temperatures and pressures, RP1147 617

Page

Wells, Lansing S., Kenneth Taylor and, Studies of heat of solution of calcium and magnesium oxides and hydroxides, RP1121 133
White, Joseph D., Frank W. Rose, Jr., and, Separation, by distillation with acetic acid, of the aromatic hydrocarbons from the fraction of a midcontinent petroleum boiling between 154° and 162° C, RP1123 167
——, ——, Separation of isopropylbenzene from a midcontinent petroleum by adsorption with silica gel and distillation with acetic acid, RP1122 151
Whittemore strain-gage measurements { RP1130 269 / RP1161 853 }
Willingham, Charles B., Anton J. Streiff, Beveridge J. Mair and, Chemical constitution of the "extract" portion of the lubricant fraction from a midcontinent petroleum, RP1145 581
——, ——, ——, Hydrogenation of the "extract" portion of the lubricant fraction from a midcontinent petroleum, RP1144 565
——, *Beveridge J. Mair and,* Exhaustive fractionation of the "extract" portion of the lubricant fraction from a midcontinent petroleum, RP1143 535
Worner, Ruby K., and Ralph T. Mease, Effect of purification treatments on cotton and rayon, RP1146 609

X

X-ray protection, RP1155 783
X-rays, measurement of high-voltage, RP1111 19
Xylose, distillation, RP1132 327

Z

Zeeman effect for tungsten, RP1125 207
Zinc sulfide pigments, effect on stability of book papers, RP1149 671

○

UNITED STATES DEPARTMENT OF COMMERCE
HARRY L. HOPKINS, Secretary
NATIONAL BUREAU OF STANDARDS
Lyman J. Briggs, Director

✦

Journal of Research

of the

National Bureau of Standards

✦

Volume 21
July to December 1938
Research Papers 1110 to 1162

UNITED STATES
GOVERNMENT PRINTING OFFICE
WASHINGTON : 1939

Corrections to be noted in volume 21 of the Journal of Research of the National Bureau of Standards

Page	Line	Now reads in part	Should read
96	Heading	1. In babbitt metals, type metals, and solders.	1. In babbitt metals, type metals, and solders (method *A*).
98	do	2. In tin-base alloys	2. In tin-base alloys (method *B*).
98	do	3. In copper-base alloys	3. In copper-base alloys (method *C*).
146	Table 10, column 4	15.57 ±0.88	15.57 ±0.08.
188	11130.37	$3d\,^3F_4^\circ - 4f\,^3G_4^\circ$	$3d\,^3F_4^\circ - 4f\,^3G_5^\circ$
188	10015.33	$4p\,^1S_0 - 5d\,^1P_1^\circ$	$4p\,^1S_0 - 7s\,^1P_1^\circ$
189	8898.97	$3d\,^3F_4^\circ - 5f\,^3F_4^\circ$	$3d\,^3F_4^\circ - 5f\,^3F_4^\circ$
189	8791.28	$3d\,^3F_4^\circ - 5f\,^3F_3^\circ$ $4p\,^1D_2 - 5d\,^1F_3^\circ$	$4p\,^1D_2 - 5d\,^1F_3^\circ$ $3d\,^3F_4^\circ - 5f\,^3F_3^\circ$
189	8579.15		$4p\,^3D_3 - 5d\,^3P_2^\circ$
203	8766.24	Delete entire line	
203	8511.40	do	
203	8198.48	do	
203	8145.61	$4p\,^1S_0 - 7d\,^1P_1^\circ$	$4p\,^1S_0 - 9s\,^1P_1^\circ$
203	7976.65	Delete entire line	
203	7518.50	do	
204	7410.14	do	
204	7365.16	do	
219	2315.02	(0.561/05) 0.81, 1.40. 2.04	(0.56, 1.05) 0.81, 1.40, 2.04
227	Table 1, column 8	$P_0°C - P_{20}°C$	$P_0°C/P_{20}°C$
249	Illustration is figure 4.		
250	Illustration at top of page is figure 3.		
268	Reference [5]	N. Bekkedahl	N. Bekkedahl and H. Matheson.
298	7	eq 10	eq 13.
507	Paragraph 2, 2d line	Hidnert [58]	Hidnert [58] and Hidnert and Sweeney [57].
637	Table 11, last column, 3d line from bottom.	No	Yes.
718	eq 39	$\frac{a}{a_e} =$	$\frac{u}{u_e} =$
836	Line 1, last paragraph	It has been established that,	It has been established[4] that
838	Footnote 6	(1935)	(1938).
868	Line 10 from bottom	in =25, 26, and 27	in eq 25, 26, and 27.

RESEARCH PUBLICATIONS

of the

NATIONAL BUREAU OF STANDARDS

1904–1919:

(*a*) *Bulletin of the Bureau of Standards.* A quarterly journal. The *Bulletin* contained all research papers until, in 1910, it was limited to scientific papers; see (*f*) for technical papers.

(*b*) Reprints [1] from (*a*). *Scientific Papers* S1 to S329.

(*c*) Volumes [2] of (*a*), cloth bound, consecutively paged and indexed. Volumes 1 to 14.

1919–1928:

(*d*) *Scientific Papers* [1] *of the Bureau of Standards* (separates continuing series (*b*), nos. S330 to S572).

(*e*) Volumes [2] of (*d*), cloth bound, consecutively paged and indexed. Volumes 15 to 22.

1910–1928:

(*f*) *Technologic Papers* [1] *of the Bureau of Standards*, T1 to T370. Prior to T203 issued only as separates.

(*g*) Volumes [2] of (*f*) cloth bound, beginning with T203, volume designated No. 16, to volume 22; consecutively paged and indexed.

1928:

(*h*) *Bureau of Standards Journal of Research* (issued under new title "*Journal of Research of the National Bureau of Standards*" beginning with the July 1934 number, volume 13, no. 1); (monthly), continuing and consolidating series (*d*) and (*f*). Subscription $3.50 per year, United States, Canada, Colombia, Cuba, Dominican Republic, Ecuador, Guatemala, Honduras, Mexico, Newfoundland (including Labrador), Panama, and Venezuela; $4.50, elsewhere.

(*i*) Volumes [3] of (*h*), cloth bound (six monthly issues), consecutively paged and indexed.

(*j*) Separates [1] of (*h*) issued under new series title, *Research Papers.*

Circular C24 contains a list of (*a*) to (*g*), inclusive, from 1901 to June 30, 1925, accompanied by a short summary of each paper and a subject index. Two supplements continue this list, and with the Circular, give a complete list of all publications to June 30, 1936. A mimeographed insert furnished with the second supplement brings the list practically up to date. Copies of this Circular and the supplements should be found at Government depository libraries having files of the Bureau publications.

Copies of the separate or complete lists may be purchased from the Superintendent of Documents, Government Printing Office, Washington, D. C., as follows:

Circular C24, 7th edition (covering the period 1901 to June 30, 1925)	25 cents.
1925–1931 Supplement to C24 (covering the period July 1, 1925, to Dec. 31, 1931)	25 cents.
1932–1936 Supplement to C24 (covering the period Jan. 1, 1932, to June 30, 1936)	5 cents.
Complete list	55 cents.

[1] For prices and other information, see Circular C24 and Supplements thereto.

[2] Volumes 1 to 21, $2 each; 22, $3. Volumes 1, 2, and 8 of the Bulletin and volumes 15, 16, 19, and 20 of the Scientific Papers are out of print. Special prices for set, address Superintendent of Documents, Government Printing Office, Washington, D. C.

[3] Volumes 1 to 6, $2.75 each; 7 to 20, $3 each. For shipment to foreign countries, add 50 cents to the cost of the volume.

Separate copies of the Research Papers listed herein may be purchased from the Superintendent of Documents, U. S. Government Printing Office, Washington, D. C., at the prices indicated beginning on page V, or at a discount of 25 percent for 100 copies or more. Remittance should be in the form of a post-office money order, coupons (issued by the Superintendent of Documents for the specific purpose of purchasing Government publications), express money order, New York draft, or cash at sender's risk.

CONTENTS OF VOLUME 21

Vol. 21—July 1938—No. 1

RP		Page
1110.	Pressure losses for fluid flow in 90° pipe bends. K. Hilding Beij. [Price 10c]	1
1111.	Measurement of supervoltage X-rays with the free-air ionization chamber. Lauriston S. Taylor, George Singer, and Arvid L. Charlton. [Price 10c]	19
1112.	Preparation and application of chromous solutions for the absorption of oxygen in volumetric gas analysis. Joseph R. Branham. [Price 5c]	45
1113.	Displacement of nitrogen from and its solution in certain reagents during volumetric gas analysis. Joseph R. Branham and Max Sucher. [Price 5c]	63
1114.	Hydrogen-reduction method for the determination of oxygen in steel. John G. Thompson and Vernon C. F. Holm. [Price 5c]	79
1115.	Determinations of oxygen in alloy steels. John G. Thompson and Vernon C. F. Holm. [Price 10c]	87
1116.	Determination of arsenic, antimony, and tin in lead-, tin-, and copper-base alloys. John A. Scherrer. [Price 5c]	95
1117.	Improved method for determination of aluminum in certain nonferrous materials by use of ammonium aurintricarboxylate. John A. Scherrer and William D. Mogerman. [Price 5c]	105
1118	Preparation of ammonium aurintricarboxylate. John A. Scherrer and W. Harold Smith. [Price 5c]	113
1119.	Combination of hydrochloric acid and sodium hydroxide with hide, tendon, and bone collagen. John Beek, Jr. [Price 5c]	117

Vol. 21—August 1938—No. 2

1120.	Determination of boron in steel and cast iron. John L. Hague and Harry A. Bright. [Price 5c]	125
1121.	Studies of heat of solution of calcium and magnesium oxides and hydroxides. Kenneth Taylor and Lansing S. Wells. [Price 5c]	133
1122.	Separation of isopropylbenzene from a midcontinent petroleum by adsorption with silica gel and distillation with acetic acid. Joseph D. White and Frank W. Rose, Jr. [Price 5c]	151
1123.	Separation, by distillation with acetic acid, of the aromatic hydrocarbons from the fraction of a midcontinent petroleum boiling between 154° and 162° C. Frank W. Rose, Jr., and Joseph D. White. [Price 5c]	167
1124.	Extension and revision of the arc spectrum of silicon. Carl C. Kiess. [Price 5c]	185
1125.	Preliminary lists of terms for the arc and spark spectra of tungsten. Donald D. Laun. [Price 5c]	207

RP Page

1126. Electrolytic resistors for direct-current applications in measuring temperatures. D. Norman Craig.....[Price 10c] 225
1127. Effect of glass content upon the heat of hydration of portland cement. William Lerch.....[Price 10c] 235
1128. Accelerated aging of leather in the oxygen bomb at 100° C. Joseph R. Kanagy.....[Price 5c] 241

Vol. 21—September 1938—No. 3

1129. Optical and dimensional changes which accompany the freezing and melting of Hevea rubber. W. Harold Smith and Charles Proffer Saylor.....[Price 10c] 257
1130. Strength of a riveted steel rigid frame having straight flanges. Ambrose H. Stang, Martin Greenspan, and William R. Osgood.....[Price 15c] 269
1131. Phase equilibria studies on mixtures of the compounds $4CaO.Al_2O_3.Fe_2O_3$–$2CaO.Fe_2O_3$–$K_2O.Al_2O_3$. William C. Taylor.....[Price 5c] 315
1132. Quantitative formation of furfural from xylose. Elizabeth E. Hughes and S. F. Acree.....[Price 5c] 327
1133. Surface tension of vitreous enamel frits at and near firing temperatures. William N. Harrison and Dwight G. Moore [Price 10c] 337
1134. Stability of the viscose type of Ozaphane photographic film. Arnold M. Sookne and Charles G. Weber.....[Price 5c] 347
1135. Relation of compositions and heats of solution of portland cement clinker. Herbert Insley, Einar P. Flint, Edwin S. Newman, and J. Arthur Swenson.....[Price 10c] 355
1136. Production of accurate one-second time intervals. William D. George.....[Price 10c] 367

Vol. 21—October 1938—No. 4

1137. A determination of the absolute ohm, using an improved self inductor. Harvey L. Curtis, Charles Moon, and C. Matilda Sparks.....[Price 15c] 375
1138. Measurement of relative and true power factors of air capacitors. Allen V. Astin.....[Price 10c] 425
1139. Heats of combustion of anthracite cokes and of artificial and natural graphites. Phillip H. Dewey and D. Roberts Harper, 3d.....[Price 5c] 457
1140. Heats of combustion of diamond and of graphite. Ralph S. Jessup.....[Price 5c] 475
1141. Heat and free energy of formation of carbon dioxide, and of the transition between graphite and diamond. Frederick D. Rossini and Ralph S. Jessup.....[Price 5c] 491
1142. A continuous high-vacuum still and boiling-point apparatus, and the systematic distillation of a dewaxed lubricant fraction of petroleum. Robert T. Leslie and Wilson W. Heuer.[Price 10c] 515

Vol. 21—November 1938—No. 5

1143. Exhaustive fractionation of the "extract" portion of the lubricant fraction from a midcontinent petroleum. Beveridge J. Mair and Charles B. Willingham.....[Price 10c] 535

RP Page

1144. Hydrogenation of the "extract" portion of the lubricant fraction from a midcontinent petroleum. Beveridge J. Mair, Charles B. Willingham, and Anton J. Streiff.....[Price 5c] 565
1145. Chemical constitution of the "extract" portion of the lubricant fraction from a midcontinent petroleum. Beveridge J. Mair, Charles B. Willingham, and Anton J. Streiff.....[Price 10c] 581
1146. Effect of purification treatments on cotton and rayon. Ruby K. Worner and Ralph T. Mease.....[Price 5c] 609
1147. Formation of hydrated calcium silicates at elevated temperatures and pressures. Einar P. Flint, Howard F. McMurdie, and Lansing S. Wells.....[Price 10c] 617
1148. Calculation of stresses and natural frequencies for a rotating propeller blade vibrating flexurally. Walter Ramberg and Sam Levy.....[Price 10c] 639
1149. Effect of filling and sizing materials on stability of book papers. Merle B. Shaw and Martin J. O'Leary.....[Price 10c] 671
1150. Cesium discharge under conditions of nearly complete ionization. Fred L. Mohler.....[Price 10c] 697

Vol. 21—December 1938—No. 6

1151. Laws of turbulent flow in open channels. Garbis H. Keulegan. [Price 10c] 707
1152. Observations on crystalline silica in certain devitrified glasses. Arthur Q. Tool and Herbert Insley.....[Price 10c] 743
1153. Expansion effects on the inversion of silica crystals in certain devitrified glasses. Arthur Q. Tool and James B. Saunders.. [Price 5c] 773
1154. Portable Geiger counter unit. Leon F. Curtiss.....[Price 5c] 779
1155. Concrete as a protective material against high-voltage X-rays. George Singer, Lauriston S. Taylor, and Arvid L. Charlton.. [Price 5c] 783
1156. On the accuracy of radio field-intensity measurement at broadcast frequencies. Harry Diamond, Kenneth A. Norton, and Evan G. Lapham.....[Price 10c] 795
1157. Correlation of an electrolytic corrosion test with the actual corrosiveness of soils. Irving A. Denison and Robert B. Darnielle.....[Price 5c] 819
1158. Method for determining uniformity of temperature in cryostats. Martin Shepherd.....[Price 5c] 831
1159. Trends of characteristics of the ionosphere for half a sunspot cycle. Newbern Smith, Theodore R. Gilliland, and Samuel S. Kirby.....[Price 5c] 835
1160. Properties of purified normal heptane and isooctane (2,2,4-trimethylpentane). Donald B. Brooks.....[Price 5c] 847
1161. Strength of a riveted steel rigid frame having a curved inner flange. Ambrose H. Stang, Martin Greenspan, and William R. Osgood.....[Price 10c] 853
1162. Resistivity and power input in the cesium discharge at high current density. Fred L. Mohler.....[Price 5c] 873

Index to volume 21 (July 1938 to December 1938) Research papers RP1110 to RP1162..... 883